3-1-2022 9:00 AM

# Optimization of Advanced Building Integrated Photovoltaic and Thermal System with Dual Working Fluid

Barilelo E. Nghana, *The University of Western Ontario*

Supervisor: Bitsuamlak, Girma, *The University of Western Ontario*
Co-Supervisor: Tariku, Fitsum, *British Columbia Institute of Technology*
A thesis submitted in partial fulfillment of the requirements for the Doctor of Philosophy degree in Civil and Environmental Engineering

# Abstract

A direct exchange building integrated photovoltaic and thermal (BIPV/T) heat pump system is proposed where the heat extracted from the BIPV is used to drive the heat pump. To ensure a more stable diurnal system performance, especially at low solar conditions, air flow is instituted in the cavity between BIPV façade and the insulated inner wall. The airflow is directed from the heated or cooled space into the air channel and can be exhausted or returned to the space depending on the building operating conditions. The flow and geometrical parameters of the BIPV/T façade are optimized such that more than 40% of the peak performance is recovered by the airflow in the channel off-peak conditions. Also, BIPV façade surface temperature is reduced by up to 10°C compared to air based BIPV/T and the wall heat gain is reduced by up to 46%. A case study scenario is considered where the BIPV/T heat pump system is installed as supplemental heating for an electric water heater and the annual energy saving is quantified. A surrogate model of the BIPV/T heat pump system is developed and implemented in EnergyPlus. The annual energy analysis suggests the Domestic hot water (DHW) heating energy demand was reduced by up to 40.4% for a wall integrated system and 44.2% for a roof integrated system.



## Keywords

Building integrated photovoltaic and thermal systems (BIPV/T), Building integrated photovoltaic systems (BIPV), Natural convection, Forced convection, Roughness, Energy Efficiency, Turbulence, Convective heat transfer coefficient, Computational Fluid Dynamics (CFD), Multiphase Flow, EnergyPlus

# Summary for Lay Audience

The building sector is responsible for a considerable amount of energy use largely due to the space heating requirements. Of course, this translates to significant green house gas emissions. To curb this, several passive techniques have been introduced, of which the most common is the increasing the Insulation in the walls. However, there is the diminishing returns of adding more insulation. Beyond an optimum insulation level, the cost outweighs the heat loss reduction. A more sustainable approach is to incorporate renewable technology like photovoltaics in buildings in an integrated fashion such that the cladding is substituted with PV modules. This improves the cost effectiveness of integrating renewable technology in buildings in that the PV cells perform multiple functions. However, by integrating PV cells, in the building envelope there is potential to overheat since typical PV efficiencies are less than 20%. As such, 80% of the solar energy is converted to waste heat that can increase the temperatures. To maintain appropriate operational temperatures a thermal management system is proposed to extract the waste heat and utilize it for other domestic purposes like space heated, domestic water heating, etc. The potential of the system is investigated, and the energy savings quantified for a system that utilizes the waste heat for DHW. The findings suggest that the combined electrical and thermal energy extracted can offset at least 44.2% of the hot water energy demand depending on the climate and orientation of the building integrated photovoltaic concept.

# Co-Authorship Statement

This thesis has been prepared in accordance with the regulation for an Integrated-Article format thesis prepared by the Western University Graduate and Postgraduate studies and has been co-authored as:

**Chapter 2**: *Assessing ventilation cavity design impact on the energy performance of rainscreen wall assemblies: A CFD study* is published in the *Journal of Building and Environment* under the co-authorship of Barilelo Nghana, Fitsum Tariku, and Girma T. Bitsuamlak.

**Chapter 3**: *BIPV with transverse rib roughened air channel - Parametric analysis of the effect of transverse roughness shape, roughness height (e/D), roughness spacing (p/e), and channel angle (θ) on the turbulent natural convection heat transfer* will be submitted for publication under the co-authorship of Barilelo Nghana, Fitsum Tariku, and Girma T. Bitsuamlak.

**Chapter 4**: *BIPV/T with transverse rib roughened air channel - Parametric analysis of the effect of transverse roughness shape, roughness height (e/D), and roughness spacing (p/e) on the turbulent forced convection heat transfer* will be submitted for publication under the co-authorship of Barilelo Nghana, Fitsum Tariku, and Girma T. Bitsuamlak.

**Chapter 5**: *A novel BIPV/T façade concept with coupled air and refrigerant heat extraction system – Validation of the coupled air and refrigerant flow CFD model* will be submitted for publication under the co-authorship of Barilelo Nghana, Fitsum Tariku, and Girma T. Bitsuamlak.

**Chapter 6**: *BIPV/T façade concept with coupled air and refrigerant heat extraction system – Parametric analysis on the impact of the geometry and flow variables on the overall thermal efficiency* will be submitted for publication under the co-authorship of Barilelo Nghana, Fitsum Tariku, and Girma T. Bitsuamlak.

**Chapter 7**: *Energy Performance of BIPV/T Façade system Coupled with Heat Pump Technology for Domestic Hot Water* will be submitted for publication under the co-authorship of Barilelo Nghana, Fitsum Tariku, and Girma T. Bitsuamlak.

# Acknowledgments

First, I am extremely grateful to the Almighty God without whom nothing is possible.

I would like to specially thank my supervisors; Dr. Fitsum Tariku and Dr. Girma Bitsuamlak, for all the time, energy and effort invested in me during this PhD study. I am sincerely grateful. I have cherished our conversations as they have been extremely inspirational during my research and I'm sure will be in the future.

I would like to specially thank the Alan G. Davenport wind-engineering group, the staff and faculty of Department of Civil and Environmental Engineering at Western University, and the Department of Mechanical and Materials Engineering at Western University, and the Building Science Center of Excellence (BSCE) at British Columbia Institute of Technology (BCIT). I would like to acknowledge the financial support from Natural Sciences and Engineering Research Council of Canada (NSERC) Collaborative Research Development, and BCIT. I would like to thank the SharcNet and Compute/Calcul Canada for the High-Performance Computation (HPC) facility and excellent support from their technical staff.

The support of my research team (Ahmed, Zoheb, Tibebu, Anwar, Meseret, Matiyas, Abiy, Tsinuel, Anant, Kimberly, Chris, Eric, Hang, Hadil, Matthew, Muna, Tewodros, Thomas, Ameyu, Dagimawi, Tsigereda, Tsegaye, Misrak, Kate, Clara, and Elias) was immense. Thank you for all your contributions to this research and for making this journey more pleasant.

To my parents, this journey started 13 years ago when you decided it was best for me to pursue my university education in Canada. I am thankful for all the love and care you've shown throughout and continue to show. Thanks for not letting me give up through the tough times of my academic pursuit. To my sisters, thank you for your emotional support and inspiring me to always be better.

# Table of Contents

# List of Tables

# List of Figures

# Chapter 1

# 1 Introduction

## 1.1 Background

The building envelope or building enclosure is the part of the building that separates the interior from the exterior (Straube, 2006). It includes the walls (above and below grade), roofs, floors, and openings (windows and doors). These enclosure components harmonize to maintain a safe and stable indoor environment by categorically providing the basic control, support, finish, and distribution functions (Figure 1-1).

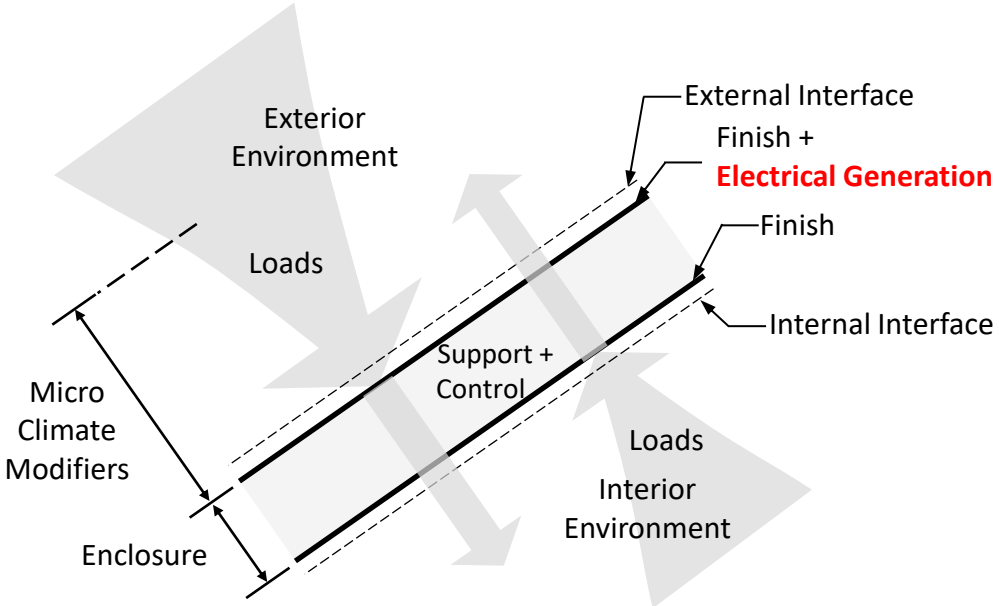


Figure 1-1: The building envelope and its functions (Straube, 2006)

In view of sustainability, these functions can be extended to generate and harness energy as in Figure 1-1 (Mora et al., 2011). Hence, sustainable development demands creation of advanced innovative building envelope systems. This is the premise for design and adoption of solar facades (including roofs). Solar facades are advanced building enclosure systems that can be used to reject, absorb and reutilize solar heat (Lai and Hokoi, 2015). Based on the solar heat treatment, solar facades can be classified as Building Integrated Photovoltaic systems (BIPV), building integrated solar thermal systems (BIST) and building integrated photovoltaic and thermal systems (BIPV/T).

BIPV/T systems have a higher solar utilization ratio due to electrical energy conversion and thermal energy extraction.

## 1.2 Literature Review

A review of the advancement in BIPV/T systems is presented. The brief historical development of the concept is first discussed. Following, previous studies on BIPV/T systems are presented. Lastly, the potential for integration with heat pump technology is outlined.

### 1.2.1 Historical Development

BIPV/T systems have come about because of deficiencies in PV technology. Commercially available PV cells have conversion efficiencies in the range of 10 – 20% (Verma et al., 2021). Hence, most of the solar radiation received is wasted as heat, which can increase the cell temperature. The temperature rise reduces the cell efficiency as seen in Figure 1-2 and can inflict structural damage due to thermal stressing (Chow, 2010).

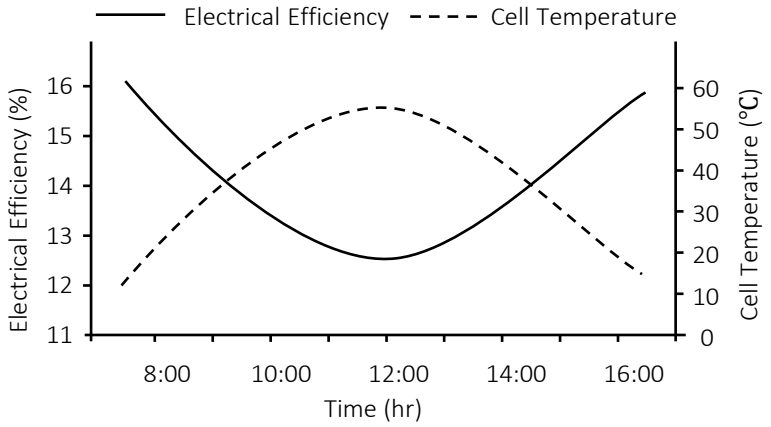


Figure 1-2: Illustration of PV efficiency on cell temperature (Lai & Hokoi, 2015)

The temperature dependent electrical efficiency is given in Equation 1-1:

$$\boldsymbol{\eta_c = \eta_{ref}\left[1 - \beta_{ref}\left(T_c - T_{ref}\right)\right]} \qquad \text{Equation 1-1}$$

where $\eta_{ref}$ and $\beta_{ref}$ are the cell efficiency and temperature coefficient given at standard test conditions ($T_{ref}$ = 25°C and $I_{rad}$ = 1000 W/m$^2$) and $T_c$ is the cell temperature. Since the cell efficiency should be indirectly related to the temperature, it is necessary to maintain a low

temperature by waste heat extraction and possibly utilizing the thermal energy. Waste heat extraction are by means of Photovoltaic/Thermal Systems (PV/T).

PV/Ts are devices that convert solar energy into thermal energy and electrical energy simultaneously. In effect, PV/Ts combine the functions of solar thermal collectors and PV panels. The advantages of PV/Ts are a reduction in the demand for physical space, decrease in cost and increase in energy production per unit area (Bloem et al., 2012; Shahsavar et al., 2011; Evola & Marletta, 2014; Sarhaddi et al., 2010). Generally, PV/Ts can be classified into air based and liquid (typically water) based systems (Hazi & Hazi, 2014). The PV/T classifications are illustrated in Figure 1-3.

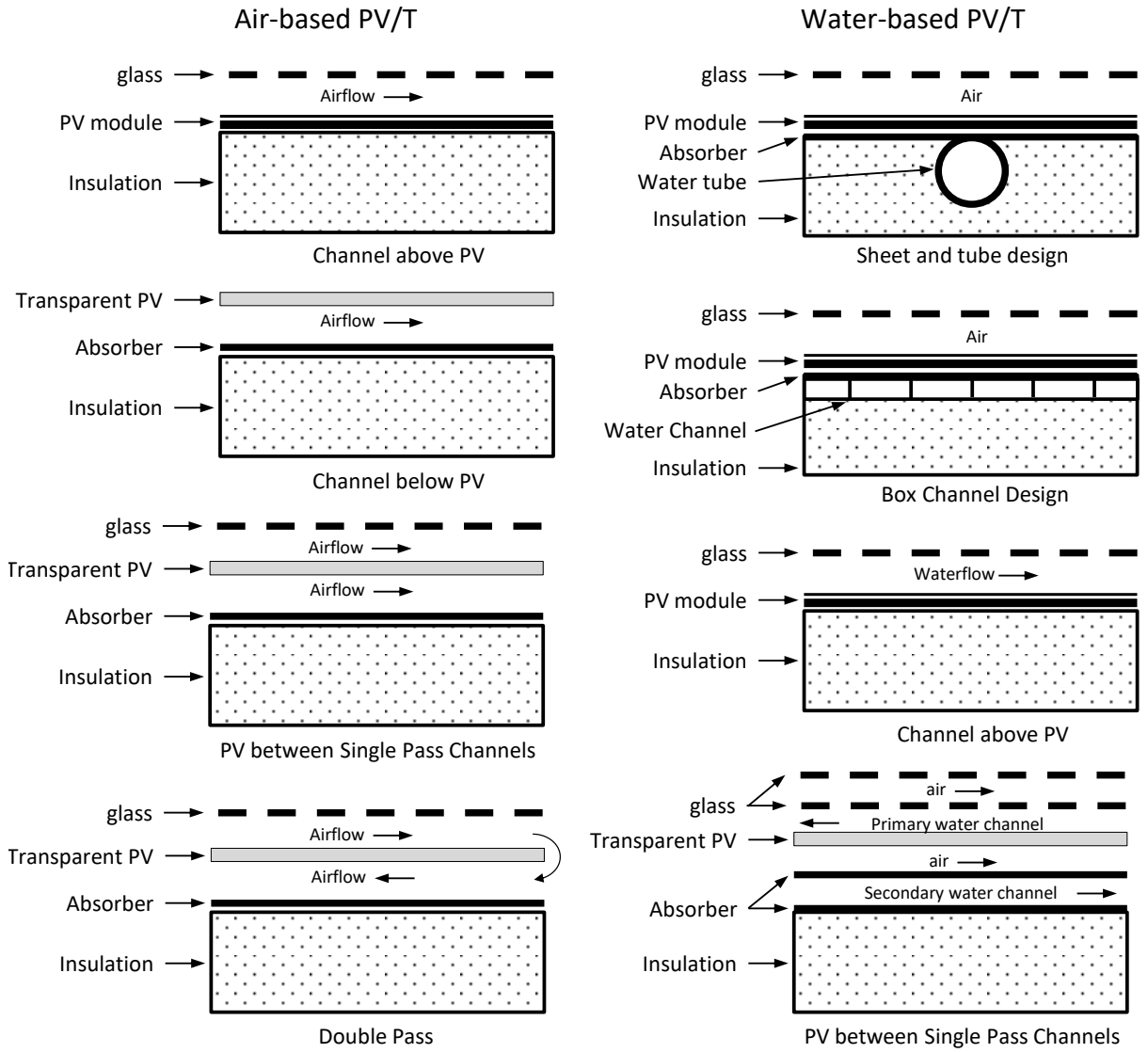


Figure 1-3: Illustration of the typical air and water based photovoltaic and thermal systems

Air-based PV/T systems (PV/Ta) are preferred to water-based PV/T systems (PV/Tw) because of simplicity and economics (Mojurnder et al., 2016, Naveed et al., 2006; Daghigh et al., 2011). However, PV/Tw systems are more efficient than PV/Ta systems due to their high thermo-physical properties (Hussain et al., 2013).

Research on PV/T started in the mid 1970's. Boer (1974) and Wolf (1976) first demonstrated the potential of PV/T systems to offset building thermal and electrical energy demand. Further work in the 70's and 80's focused on extending the Hottel-Whillier model for thermal analysis of flat plate collectors to the analysis of PV/T collectors. (Florschuetz, 1979; Raghuraman, 1981). In the 90's, research was focused on parametric analysis (Bhargava et al., 1991; Agarwal & Garg, 1994; Prakash, 1994; Garg & Adhikari, 1995, 1997, 1998), new collector designs (Sopian et al., 1995) and proposing new PV/T performance measures (Fujisawa & Tani, 1997; Huang et al., 2001).

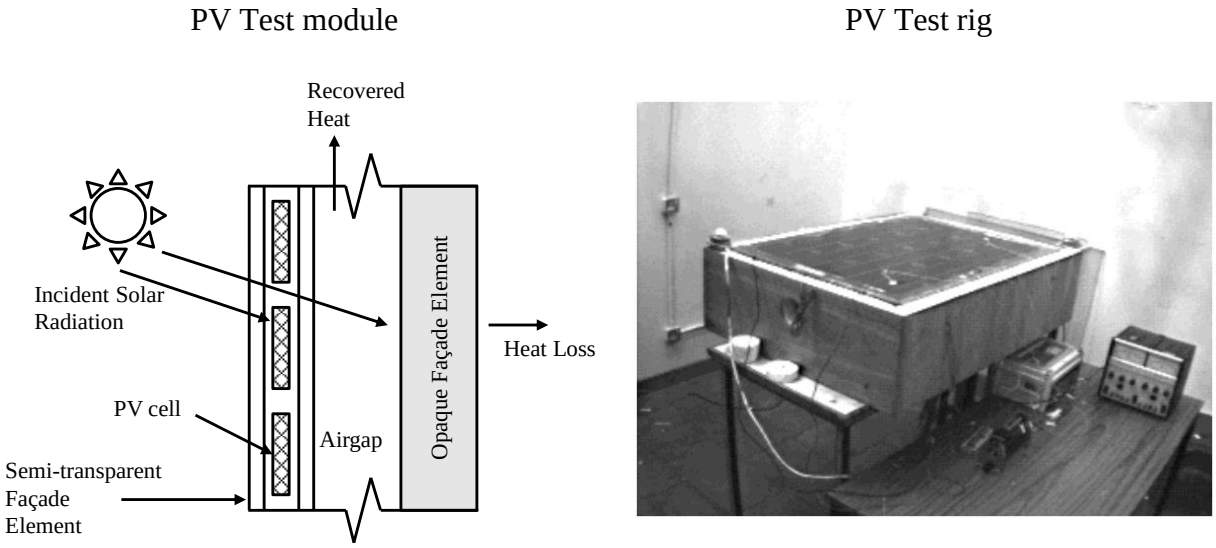


Figure 1-4: Laboratory testing and characterization of a PV-integrated façade (Clarke et al., 1996)

During this period, Clarke et al. (1996) subjected a PV-façade to laboratory testing and computer simulation to characterize its thermal and electrical performance as seen in Figure 1-4. This work pioneered the integration of PV in the building enclosure. These systems are called Building integrated photovoltaic/thermal systems (BIPV/T). In effect, the BIPV/T transforms buildings from energy consumers into active power generators and is important to promote sustainable development in the building sector (Ho et al., 2013). BIPV/T combines the functionalities of the

building enclosure, solar cells, and thermal collector in one product. This increases the cost effectiveness of the PV module (Sarhaddi et al., 2010; Pantic et al., 2010; Agrawal & Tiwari, 2010; Wilson & Paul, 2011) and the overall output of the system (Wu et al., 2011).

### 1.2.2 Building Integrated Photovoltaic/Thermal Systems

Presently, the development trend for solar energy systems is building integration (Buker & Riffat, 2015). BIPV/T's typically consist of the PV cladding, the building inner wall and an airflow cavity as shown in Figure 1-5. Depending, on the heat transfer medium instituted for thermal regulation of the PV cladding, the airflow in the cavity can be driven by natural convection or forced convection. The airflow in the cavity is mostly driven by natural convection or forced convection in air based and liquid (e.g., water) based BIPV/T systems respectively. For a special case when the airflow cavity in the BIPV/Tw system is driven by forced convection, the system is regarded as a bi-fluid BIPV/T façade system.

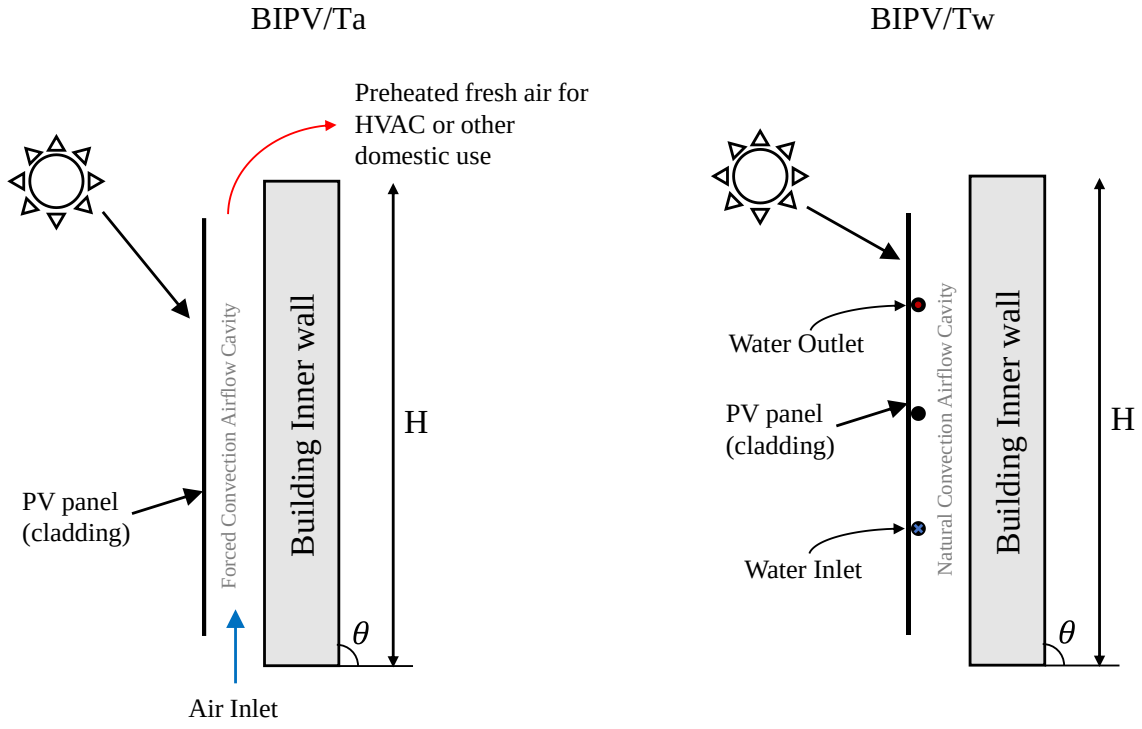


Figure 1-5: Schematic of air cooled (Left) and water cooled (Right) Building Integrated Photovoltaic and Thermal Systems

BIPV/Ta systems are more common than BIPV/Tw systems especially in cold climate when freezing is a major concern for BIPV/Tw systems. Also, BIPV/Ta systems are more easily integrated with the building envelope and heating, ventilation, and air conditioning (HVAC) systems. An air-based PV integrated building façade was numerically investigated by Zoguo & Stapountzis (2011a). The thermal mass increase of the building was noted, and the air heated in the duct could supply 22% of the total heating load during the heating season for a typical office building. Further field study of the concept under different modes of natural and forced convection revealed an enhancement of the convective heat transfer coefficient as well as an alteration of the inlet flow conditions under forced convection (Zoguo & Stapountzis, 2011b). The enhancement in heat transfer coefficient was quantified in a CFD study and a convective heat transfer correlation was derived (Zogou & Stapountzis, 2012). Nagano et al., (2003) presented a more unique BIPV/Ta façade integration which incorporated PV cells directly on the exterior wallboards. It was shown that the system has the potential to cover half of the heating demand.

BIPV/Ta façade integration is beneficial since more area coverage is available but in most cases, it does not provide the optimum angle for solar capture. As a rule of thumb, it is advisable to incline the collector in the latitude of the location. A deviation of +/- $10^{o}$ doesn't significantly affect the solar capture (Chow & Chan, 2004). This favours roof integration, although overheating may pose a greater concern for the solar cells in this configuration. The performance of an open loop roof integrated BIPV/Ta system was investigated by Pantic et al. (2010). Specifically, the effect of glazing was considered. It was shown that the unglazed system provided the best configuration for electricity generation due to the convective heat loss by wind that helped to further cool down the PV surface temperature. However, the glazed system displayed the best thermal efficiency. Further, Chen et al. (2010a; 2010b) thermally coupled a BIPV/Ta roof system with a ventilated concrete slab and domestic hot water (DHW) in a low energy house. The full-scale monitored data showed a possible temperature rise of $40^{o}$C across the roof. Convective heat transfer correlations (CHTC) were also developed from experimental data and 2D steady state system representations. Lin et al. (2014) presented a novel BIPV/Ta ventilation system integrated with Phase change materials (PCMs) and effective control system to allow for heating, cooling and thermal storage based on comfort requirements.

For considerable long channel lengths, especially for façade integrated systems, a significant amount of heat can be extracted. However, this causes substantial temperature variations on the surface of the PV panels. This PV surface temperature variation limits the electrical yield of system as demonstrated by Ghani et al. (2012). Yang and Athienitis (2015) presented a multiple inlet BIPV/Ta system to realize a more uniform PV surface temperature distribution as well as recover some of the exterior convective heat loss. The idea was to break the boundary layer and enhance heat transfer. Significant thermal efficiency improvement was observed when compared to a single inlet system. A façade integrated BIPV/Ta combined with an unglazed transpired collector (UTC) was also investigated by Athienitis et al. (2011). The novel install of the PV on the corrugated sheet promoted turbulence that enhanced the convective cooling of the PV panels. Field experimental monitoring show that the air flow cooled the PV by up to 8.1$^{o}$C. Further CFD studies demonstrated the slope length and the wavelength of the UTC as having the most dominant impact on the thermal performance (Li & Karava, 2014). CHTC were also determined for the combined BIPV/Ta and UTC system incorporating weather and design parameters (Li et al., 2014).

As earlier mentioned, although air systems are simpler to implement, water systems are more efficient heat carriers. A BIPV/Tw façade system for DHW was presented in Chow et al. (2007; 2009). This building envelope integration increased the thermal mass as was reflected in the reduced building cooling load and peak load time shift by up to 3 hours. Further studies by Ji et al. (2006a, 2006b, 2007), and Chow et al. (2009) investigated the effect of key design parameters (packing factor, flow rate, water delivery pipe size, flow channel dimensions, glazing transmissivity, PV cell efficiency, ratio of water mass in storage tank to aperture area) and environmental parameters (solar radiation, ambient temperature and wind) on the thermal and electrical performance.

### 1.2.3 Building Integrated Photovoltaic/Thermal System Energy Utilization: Heat Pump Coupling

The heat energy extracted by PV/T systems is low grade energy. Integration with heat pumps provide a suitable technology to upgrade this low-grade heat. Another premise for the adoption of the PV/T-HP technology is the mismatch between required outlet temperature and PV working efficiency especially for closed loop water heating systems. Per Wilson & Paul (2011), combining PV/T collector and heat pump is a very promising and attractive concept.

The concept of incorporating solar thermal collectors with heat pumps is not a new concept. Solar assisted heat pumps have been around for some time. However, the main advantage of incorporating PV/T collectors with heat pumps is that the systems can be self-sufficient and the high temperature evaporation which has the potential to improve the coefficient of performance. Chow et al. (2010), Xu et al. (2009), Zhao et al. (2011), Pei et al. (2008), and Keliang et al. (2009) investigated a direct exchange PV-solar assisted heat pump system. It is worth mentioning that only system presented by Zhao et al. (2011) is building integrated.

A limitation to the direct exchange PV/T collector/evaporator configuration is that, for sufficiently low solar radiation, the collector will be ineffective. This issue has been resolved by having a back-up air evaporator in parallel with the PV/T evaporator and having an appropriate control system to coordinate the operation of the evaporators (Ji et al., 2009; Pei et al., 2008; Fu et al., 2012; Ji et al., 2008). Another alternative is to use the heat recovered from the PV/T collector to drive the heat pump in an indirect heat exchange configuration. (Kamel and Fung (2014) and Manzolini et al. (2016) used PV/Ta collectors to drive the heat pump while Bai et al. (2012) and Bakker et al. (2005) used PV/Tw collectors as the evaporator heat source.

## 1.3 Research Gap

### 1.3.1 Few research on the performance of Direct exchange BIPV/T collector/evaporator and heat pump systems

From the review of literature, there is limited research on BIPV/T integrated with heat pump. Chow et al. (2010), Xu et al. (2009) Pei et al. (2008), Keliang et al. (2009), Ji et al. (2009), Pei et al. (2008), Fu et al. (2012), Ji et al. (2008), and Kamel and Fung (2014) investigated stand-alone PV/T heat pump systems. Bakker et al. (2005) studied a building applied system i.e., mounted on the cladding. Zhao et al. (2011) and Manzolini et al. (2016) presented a detailed study of BIPV/T and heat pump coupling. Manzolini et al. (2016) reported a modest COP improvement and was attributed to the reliance on buoyancy to drive the air flow over the evaporator. Also, a back-up evaporator will be required in the concept presented by Zhao et al. (2011). The cost implications of having a back-up evaporator may be one of the determents of exploring refrigerant based BIPV/T and heat pump system. These systems are important because refrigerant based BIPV/T's

have a high solar utilization rate in that compared to air and water the boiling and condensation heat transfer coefficients are significantly higher than the convective heat transfer coefficients.

### 1.3.2 Limitation on full-scale numerical and experimental studies

As suggested by Zogou and Stapountzis (2012), design optimization for this type of BIPV/T applications must be based on sound understanding of flow and heat transfer characteristics. This is possible through a detailed numerical simulation with fully monitored experiments instrumented to measure the inflow conditions, outflow conditions, surface temperatures of the corresponding layers, heat flow, flow characteristics and weather data, with sufficient measurement intervals to capture weather changes. Manzolini et al. (2016) and Zhao et al. (2011) used steady state models that were validated with experimental data from small scale experiments or data from literature. Athienitis et al. (2011) performed experiments with 1 h measurement intervals so as not to capture the unsteady weather conditions. Chow et al. (2007, 2009), Zoguo and Stapountzis (2011b), and Nagano et al. (2003) used simplified system models. Pantic et al. (2010) validated their simplified model with few hours data. Li et al. (2014) performed detailed 3D CFD simulations with experimental validation, however, the error margins were significant, and radiation was ignored. Zoguo & Stapountzis (2011b) did not validate the numerical simulation. It is apparent that full scale experiments for validation of numerical simulations are lacking, especially in BIPV/T-HP applications. Full-scale experiments are important to demonstrate the long-term performance as well as encourage development and spreading of the concept. Also, more detailed numerical simulations with flow visualizations and consideration given to all modes of heat transfer like computational fluid dynamic packages are required for effective design optimization.

### 1.3.3 Limited work on simultaneous exploration of climatic, design and operational parameters influencing the performance of BIPV/T integrated with heat pump

Figure 1-6 shows the cross-section of a Direct Exchange BIPV/T façade evaporator concept and its components. The BIPV/T façade consists of the glazed PV/T evaporator, a ventilated airgap, and the opaque inner wall. The performance of PV/T systems, which is a subset of the BIPV/T evaporator is well documented in literature. Table 1-1 summarizes the climatic, design and operational parameters that affect the performance of PV/T systems.

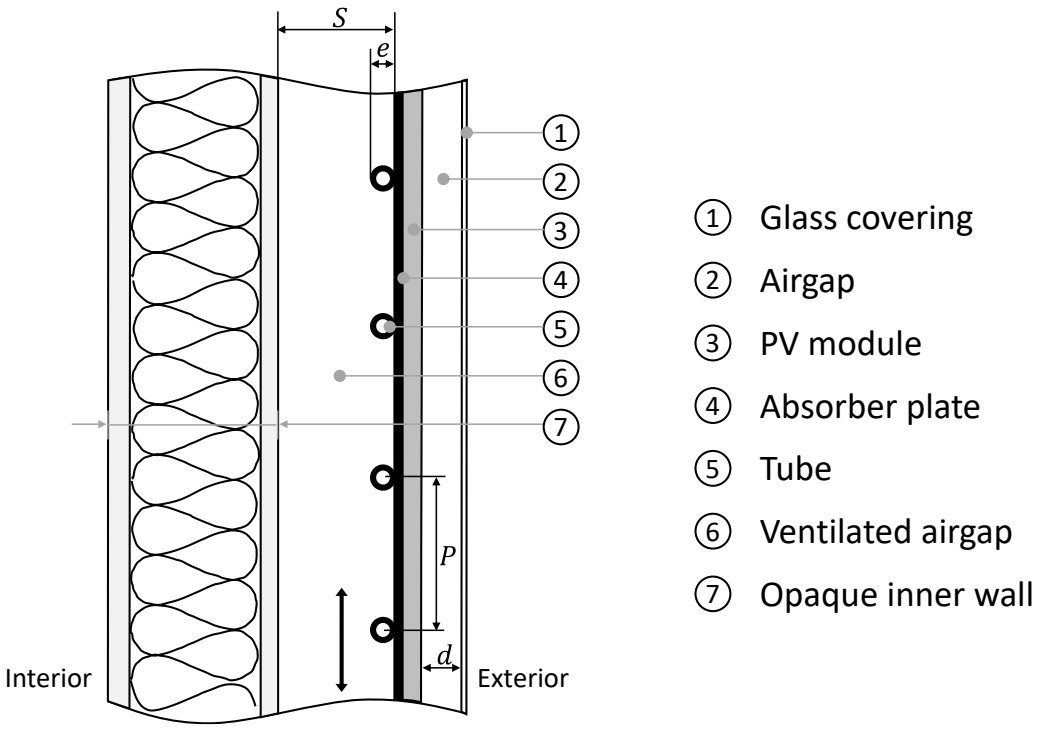


Figure 1-6: Illustration of the components of the Direct Exchange BIPV/T facade concept design parameters

While Table 1-1 is not an exhaustive list, it highlights the complexities in assessing the thermal and electrical yield of the PV/T collector. As such, optimizing the performance of the PV/T collector requires investigating the relative contributions of the different parameters on the overall thermal and electrical yield. There is extensive research on the impact of these parameters on the thermal and electrical yield. Ji et al. (2006a, 2006b, 2007), and Chow et al. (2009) conducted parametric analysis to optimize the geometry and operating conditions of PV/T systems. Significant geometric, design and environmental parameters were investigated as earlier mentioned. However, these parameters were not investigated simultaneously, neither were these systems building integrated.

Table 1-1: Factors and parameters affecting the PV/T collector performance (Elbreki et al., 2016)

| Category | Variables |
|---|---|
| Climate | Solar Irradiance, Ambient temperature, and Wind speed |
| Design | PV/T aspect ratio (Duct length, duct width), channel depth, PV module type, Number of glazing and glazing thickness, distance of glazing above PV surface, anti-reflection coating (location: on glazing vs on solar cells), low-e coating (location on glazing), number of tubes, tube material, riser configuration (tube shape), thermal insulation (type and thickness), absorber material (conductivity, absorptivity and thickness), Effect of fins, roughness element (Length and interspacing and shape), emissivity (Channel top and bottom), absorber thickness, and Number of collectors. |
| Operational | Mass flow rate, inlet fluid temperature, packing factor, and effect of fans (air speed). |

Building integration further complicates the problem in that more variables need to be explored such as global orientation, envelope inclination, thermal mass of the supporting wall (for hot climate), insulation thickness (for a cold climate), and wall assembly ventilation type. Further, the heat pump system design parameters have not been considered. These include the evaporation temperature, the condensation temperature, the flow rate, and thermal characteristics of the heat transfer media. Hence, to maximize the thermal and electric yield, an optimization of the system is necessary considering simultaneously the global and local parameters.

### 1.3.4 Lack of simplified optimization tools for BIPV/T application: Proper selection of convective heat transfer coefficients

The performance of BIPV/T systems is strongly correlated to the climate; hence, it is important to develop tools to optimize system design for different climates. Currently, a limited amount of work has been done to develop systematic optimization procedures or tools to improve the overall performance of BIPV/T collectors for different climate (Charron & Athienitis, 2006). This will require development of reduced order simplified models that have been sufficiently validated/calibrated to within reasonable error bounds. The major source of error is in the choice of appropriate convective heat transfer coefficient as applied to BIPV/T systems (Shan et al.,

2014). This is due to complexities arising from heating asymmetries, high aspect ratios, non-consistent heat fluxes, non-uniform wall temperatures and non-developed flow conditions (Canadanedo et al., 2011; Dehra, 2009). Significant research has focused on developing convective heat transfer correlations. Zogou and Stupountzis (2012) compared various CHTC and reported a wide range of predictions which indicate a lack of understanding of the flow and heat transfer behavior. Hence, a deeper understanding of the convective coefficients is necessary for the more accurate prediction of simplified thermal models.

## 1.4 Problem Statement

Hence, the question is, how feasible is it to come up with a BIPV/T collector concept that combines the advantages of the high temperature evaporative cooling of the refrigerant based PVT and an air/water evaporator? In other words, a bi-fluid PV/T collector as in (Bakar et al., 2014), however, with refrigerant rather than water and integrated with the building envelope (see Figure 1-6). This is important because refrigerant based PV/T enhances solar utilization rate compared to air and water as working fluid since the boiling and condensation heat transfer coefficients are significantly higher than the CHTC. Currently, there are few works on examining the performance of BIPV/T systems using refrigerant as the working fluid (Charron & Athienitis, 2006).

## 1.5 Proposed Research

Based on the literature review and research gap discussed, the present research aims to

- Investigate the natural convection heat transfer in a double skin opaque wall assembly
- Optimize three BIPV/T façade systems:
    - BIPV/T with natural convection air cooling
    - BIPV/T with forced convection air cooling
    - BIPV/T with dual refrigerant and air-cooling heat removal system, and
- Quantify the energy impacts of the BIPV/T with dual refrigerant and air-cooling heat removal system coupled with heat pump technology for domestic hot water heating

## 1.6 Organization of the thesis

This thesis has been prepared in an "Integrated-Article" format. In Chapter 1, the historical development of BIPV/T systems and the associated energy benefits are provided. As well, the opportunities to further the implementation of the BIPV/T systems that will be investigated in this thesis are provided. The objectives of the thesis are addressed in detail in the following chapters.

### 1.6.1 Parametric characterization of the air channel design and its impact on the natural convection heat transfer in an opaque wall assembly

In this chapter, the impact of the ventilation cavity design on the energy performance of the rainscreen wall assembly was numerically investigated in CFD. The ventilated cavity design parameters considered were the cladding material type (i.e., Fiber cement, brick, and metal cladding), the sheathing membrane emissivity coefficient (i.e., 0.1 - 0.9), the ventilated cavity height (i.e., 1$H$ and 2$H$) and the air gap width (i.e., 13 $mm$ – 50 $mm$). The CFD model was validated with experimental data and a dynamic simulation for a typical hot day and cold day is performed. The heat flux through the wall assembly was compared amongst the design alternatives. A numerical baseline for comparison of the energy performance of the BIPV/T wall assembly is established in this study.

### 1.6.2 BIPV with transverse rib roughened air channel - Parametric analysis of the effect of transverse roughness shape, roughness height (e/D), roughness spacing (p/e), and channel angle (θ) on the turbulent natural convection heat transfer

In this chapter, the effect of varying rib geometry on the turbulent natural convective heat transfer coefficient in a BIPV air channel was assessed numerically. The CFD model is validated with experimental data from the literature to within reasonable accuracy. The study investigates parameters such as the rib shape (i.e., square, triangle and semi-circle), relative rib height, relative pitch ratio, and heat flux. A new natural convective heat transfer correlation is developed for different geometry and flow conditions.

### 1.6.3 BIPV/T with transverse rib roughened air channel - Parametric analysis of the effect of transverse roughness shape, roughness

### height (e/D), and roughness spacing (p/e) on the turbulent forced convection heat transfer

In this chapter, the flow characteristics and gain of heat transfer associated with addition of ribs in the BIPV/T flow channel using CFD. The geometric and flow parameters are the relative roughness pitch, relative roughness pitch and Reynolds number. A new forced convective heat transfer correlation is developed for different flow conditions and roughness geometry within the transitionally rough and fully rough flow paradigm. Further, the near-wall vortex flow structures are investigated and categorized based on detailed wall shear stress data derived from CFD. The optimal geometry and flow parameters that maximized the thermohydraulic performance is provided. Further, a parametric study is conducted to understand the impacts of roughness shape, roughness height, roughness pitch, and Reynolds number on the thermo-hydraulic performance. A forced convective heat transfer correlation is developed for different flow conditions and roughness geometry.

### 1.6.4 A novel BIPV/T façade concept with coupled air and refrigerant heat extraction system – Validation of the coupled air and refrigerant flow CFD model

In this chapter, a novel BIPV/T concept is proposed with dual fluid flow thermal management system. A CFD approach to quantifying the useful heat gain for the BIPV/T façade is proposed and validated. Some of the difficulties in saturated flow boiling (i.e., two-phase flow) are emphasized.

### 1.6.5 BIPV/T façade concept with coupled air and refrigerant heat extraction system – Parametric analysis on the impact of the geometry and flow variables on the overall thermal efficiency

In this chapter, BIPV/T façade concept is optimized using the validated CFD model in Chapter 5. A parametric analysis is conducted to numerically investigate the impact of certain geometry and flow parameters on the thermal efficiency of the BIPV/T façade evaporator concept. The parameters considered are the relative tube height (e/D), relative tube pitch (p/e), tube shape, and relative flow ratio ($Re_{ref}/Re_{air}$). The relative flow ratio is the ratio of the dimensionless flow rates in the refrigerant tubes and the air channel.

### 1.6.6 Energy Performance of BIPV/T Façade system Coupled with Heat Pump Technology for Domestic Hot Water

In this chapter, the annual performance of the proposed BIPV/T façade concept coupled with heat pump is numerically investigated. A simulation methodology is employed that involves four distinct phases: weather data analysis, detailed CFD simulation, Regression analysis, and BES. In the weather data analysis, representative days for each month with varying levels of solar radiation are determined. The determined outdoor conditions were inputted as boundary conditions for the detailed CFD simulation to determine the heat gain and electrical efficiency. In the regression analysis, the heat gain and electrical efficiency are correlated with the outdoor temperature, solar radiation, wind speed and cloud cover. The derived multi-variable polynomial expression is then implemented in EnergyPlus via the Energy Management System to dynamically predict the heat added to the storage tank per hour of operation of the BIPV/T coupled heat pump system. Following, the energy impacts on the DHW energy usage are quantified for different wall orientations and climatic conditions across Canada by considering a typical residential DHW consumption profile.

Finally, in Chapter 7, the overall conclusion of the present study and venues of future research are discussed.

## 1.7 References

Agarwal, R. K., & Garg, H. P. (1994). Study of a photovoltaic-thermal system—thermosyphonic solar water heater combined with solar cells. Energy conversion and management, 35(7), 605-620.

Agrawal, B., & Tiwari, G. N. (2010). Optimizing the energy and exergy of building integrated photovoltaic thermal (BIPVT) systems under cold climatic conditions. Applied Energy, 87(2), 417-426.

Athienitis, A. K., Bambara, J., O'Neill, B., & Faille, J. (2011). A prototype photovoltaic/thermal system integrated with transpired collector. Solar Energy, 85(1), 139-153.

Bakar, M. N. A., Othman, M., Din, M. H., Manaf, N. A., & Jarimi, H. (2014). Design concept and mathematical model of a bi-fluid photovoltaic/thermal (PV/T) solar collector. Renewable Energy, 67, 153-164.

Bhargava, A. K., Garg, H. P., & Agarwal, R. K. (1991). Study of a hybrid solar system—solar air heater combined with solar cells. Energy Conversion and Management, 31(5), 471-479.

Bhuvaneswari, M. C. (Ed.). (2014). *Application of Evolutionary Algorithms for Multi-objective Optimization in VLSI and Embedded Systems*. Springer.

Bloem, J. J., Lodi, C., Cipriano, J., & Chemisana, D. (2012). An outdoor test reference environment for double skin applications of building integrated photovoltaic systems. Energy and Buildings, 50, 63-73

Böer, K. W. (1974). Solar One: The Delaware Solar House and Results Obtained during the First Year of Operation. DELAWARE UNIV NEWARK INST OF ENERGY CONVERSION.

Buker, M. S., & Riffat, S. B. (2015). Building integrated solar thermal collectors–a review. Renewable and Sustainable Energy Reviews, 51, 327-346.

Candanedo, L. M., Athienitis, A., & Park, K. W. (2011). Convective heat transfer coefficients in a building-integrated photovoltaic/thermal system. Journal of Solar Energy Engineering, 133(2), 021002.

Chen, F., & Yin, H. (2016). Fabrication and laboratory-based performance testing of a building-integrated photovoltaic-thermal roofing panel. Applied Energy, 177, 271-284.

Chen, Y., Athienitis, A. K., & Galal, K. (2010). Modeling, design and thermal performance of a BIPV/T system thermally coupled with a ventilated concrete slab in a low energy solar house: Part 1, BIPV/T system and house energy concept. Solar Energy, 84(11), 1892-1907.

Chen, Y., Galal, K., & Athienitis, A. K. (2010). Modeling, design and thermal performance of a BIPV/T system thermally coupled with a ventilated concrete slab in a low energy solar house: Part 2, Ventilated Concrete Slab. Solar Energy, 84(11), 1892-1907.

Chow, T. T. (2010). A review on photovoltaic/thermal hybrid solar technology. Applied energy, 87(2), 365-379.

Chow, T. T., Chan, A. L. S., Fong, K. F., Lin, Z., He, W., & Ji, J. (2009). Annual performance of building-integrated photovoltaic/water-heating system for warm climate application. Applied Energy, 86(5), 689-696.

Chow, T. T., He, W., & Ji, J. (2007). An experimental study of facade-integrated photovoltaic/water-heating system. Applied Thermal Engineering, 27(1), 37-45.

Clarke, J. A., Hand, J. W., Johnstone, C. M., Kelly, N., & Strachan, P. A. (1996). Photovoltaic-integrated building facades. Renewable energy, 8(1-4), 475-479.

Daghigh, R., Ruslan, M. H., & Sopian, K. (2011). Advances in liquid based photovoltaic/thermal (PV/T) collectors. Renewable and Sustainable Energy Reviews, 15(8), 4156-4170.

Dehra, H. (2009). A two dimensional thermal network model for a photovoltaic solar wall. Solar Energy, 83(11), 1933-1942.

Elbreki, A. M., Alghoul, M. A., Al-Shamani, A. N., Ammar, A. A., Yegani, B., Aboghrara, A. M., ... & Sopian, K. (2016). The role of climatic-design-operational parameters on combined PV/T collector performance: A critical review. *Renewable and Sustainable Energy Reviews*, *57*, 602-647.

Evola, G., & Marletta, L. (2014). Exergy and thermoeconomic optimization of a water-cooled glazed hybrid photovoltaic/thermal (PVT) collector. Solar Energy, 107, 12-25.

Florschuetz, L. W. (1979). Extension of the Hottel-Whillier model to the analysis of combined photovoltaic/thermal flat plate collectors. Solar energy, 22(4), 361-366.

Fujisawa, T., & Tani, T. (1997). Annual exergy evaluation on photovoltaic-thermal hybrid collector. Solar Energy Materials and Solar Cells, 47(1), 135-148.

Garg, H. P., & Adhikari, R. S. (1997). Conventional hybrid photovoltaic/thermal (PV/T) air heating collectors: steady-state simulation. Renewable Energy, 11(3), 363-385.

Garg, H. P., & Adhikari, R. S. (1998). Transient simulation of conventional hybrid photovoltaic/thermal (PV/T) air heating collectors. International journal of energy research, 22(6), 547-562.

Garg, H. P., & Agarwal, R. K. (1995). Some aspects of a PV/T collector/forced circulation flat plate solar water heater with solar cells. Energy Conversion and Management, 36(2), 87-99.

Ghani, F., Duke, M., & Carson, J. K. (2012). Effect of flow distribution on the photovoltaic performance of a building integrated photovoltaic/thermal (BIPV/T) collector. Solar energy, 86(5), 1518-1530.

Hazi, A., & Hazi, G. (2014). Comparative study of indirect photovoltaic thermal solar-assisted heat pump systems for industrial applications. Applied Thermal Engineering, 70(1), 90-99.

Ho, C. J., Jou, B. T., Lai, C. M., & Huang, C. Y. (2013). Performance assessment of a BIPV integrated with a layer of water-saturated MEPCM. Energy and Buildings, 67, 322-333.

Huang, B. J., Lin, T. H., Hung, W. C., & Sun, F. S. (2001). Performance evaluation of solar photovoltaic/thermal systems. Solar energy, 70(5), 443-448.

Hussain, F., Othman, M. Y. H., Sopian, K., Yatim, B., Ruslan, H., & Othman, H. (2013). Design development and performance evaluation of photovoltaic/thermal (PV/T) air base solar collector. Renewable and Sustainable Energy Reviews, 25, 431-441.

Ibrahim, A., Fudholi, A., Sopian, K., Othman, M. Y., & Ruslan, M. H. (2014). Efficiencies and improvement potential of building integrated photovoltaic thermal (BIPVT) system. Energy Conversion and Management, 77, 527-534.

Ji, J., Han, J., Chow, T. T., Han, C., Lu, J., & He, W. (2006). Effect of flow channel dimensions on the performance of a box-frame photovoltaic/thermal collector. Proceedings of the Institution of Mechanical Engineers, Part A: Journal of Power and Energy, 220(7), 681-688.

Ji, J., Han, J., Chow, T. T., Yi, H., Lu, J., He, W., & Sun, W. (2006). Effect of fluid flow and packing factor on energy performance of a wall-mounted hybrid photovoltaic/water-heating collector system. Energy and Buildings, 38(12), 1380-1387.

Ji, J., Liu, K., Chow, T. T., Pei, G., He, W., & He, H. (2008). Performance analysis of a photovoltaic heat pump. Applied Energy, 85(8), 680-693.

Ji, J., Lu, J. P., Chow, T. T., He, W., & Pei, G. (2007). A sensitivity study of a hybrid photovoltaic/thermal water-heating system with natural circulation. Applied Energy, 84(2), 222-237.

Lai, C. M., & Hokoi, S. (2015). Solar façades: A review. *Building and Environment*, *91*, 152-165.

Li, S., & Karava, P. (2014). Energy modeling of photovoltaic thermal systems with corrugated unglazed transpired solar collectors–Part 2: Performance analysis. Solar Energy, 102, 297-307.

Li, S., Karava, P., Currie, S., Lin, W. E., & Savory, E. (2014). Energy modeling of photovoltaic thermal systems with corrugated unglazed transpired solar collectors–Part 1: Model development and validation. Solar Energy, 102, 282-296.

Lin, W., Ma, Z., Sohel, M. I., & Cooper, P. (2014). Development and evaluation of a ceiling ventilation system enhanced by solar photovoltaic thermal collectors and phase change materials. Energy conversion and management, 88, 218-230.

Lin, W., Ma, Z., Sohel, M. I., & Cooper, P. (2014). Development and evaluation of a ceiling ventilation system enhanced by solar photovoltaic thermal collectors and phase change materials. Energy conversion and management, 88, 218-230.

Manzolini, G., Colombo, L. P., Romare, S., & Fustinoni, D. (2016). Tiles as solar air heater to support a heat pump for residential air conditioning. Applied Thermal Engineering, 102, 1412-1421.

Mojumder, J. C., Ong, H. C., Chong, W. T., & Shamshirband, S. (2016). Application of support vector machine for prediction of electrical and thermal performance in PV/T system. Energy and Buildings, 111, 267-277.

Mora, R., Bitsuamlak, G., & Horvat, M. (2011). Integrated life-cycle design of building enclosures. *Building and Environment*, *46*(7), 1469-1479.

Nagano, K., Mochida, T., Shimakura, K., Murashita, K., & Takeda, S. (2003). Development of thermal-photovoltaic hybrid exterior wallboards incorporating PV cells in and their winter performances. Solar Energy Materials and Solar Cells, 77(3), 265-282.

Naveed, A. T., Kang, E. C., & Lee, E. J. (2006). Effect of unglazed transpired collector on the performance of a polycrystalline silicon photovoltaic module. Journal of Solar Energy Engineering, 128(3), 349-353.

Pantic, S., Candanedo, L., & Athienitis, A. K. (2010). Modeling of energy performance of a house with three configurations of building-integrated photovoltaic/thermal systems. Energy and buildings, 42(10), 1779-1789.

Prakash, J. (1994). Transient analysis of a photovoltaic-thermal solar collector for co-generation of electricity and hot air/water. Energy Conversion and Management, 35(11), 967-972.

Raghuraman, P. (1981). Analytical predictions of liquid and air photovoltaic/thermal, flat-plate collector performance. Journal of solar energy engineering, 103(4), 291-298.

Sarhaddi, F., Farahat, S., Ajam, H., & Behzadmehr, A. (2010). Exergetic performance assessment of a solar photovoltaic thermal (PV/T) air collector. Energy and Buildings, 42(11), 2184-2199.

Sarhaddi, F., Farahat, S., Ajam, H., Behzadmehr, A. M. I. N., & Adeli, M. M. (2010). An improved thermal and electrical model for a solar photovoltaic thermal (PV/T) air collector. Applied Energy, 87(7), 2328-2339.

Shahsavar, A., Salmanzadeh, M., Ameri, M., & Talebizadeh, P. (2011). Energy saving in buildings by using the exhaust and ventilation air for cooling of photovoltaic panels. Energy and Buildings, 43(9), 2219-2226.

Shan, F., Cao, L., & Fang, G. (2013). Dynamic performances modeling of a photovoltaic–thermal collector with water heating in buildings. Energy and Buildings, 66, 485-494.

Shan, F., Tang, F., Cao, L., & Fang, G. (2014). Dynamic characteristics modeling of a hybrid photovoltaic–thermal solar collector with active cooling in buildings. Energy and buildings, 78, 215-221.

Sopian, K., Yigit, K. S., Liu, H. T., Kakac, S., & Veziroglu, T. N. (1996). Performance analysis of photovoltaic thermal air heaters. Energy Conversion and Management, 37(11), 1657-1670.

Straube, J. (2006). The building enclosure. *Building Science Digest*, *18*, 1-14.

Verma, S., Mohapatra, S., Chowdhury, S., & Dwivedi, G. (2021). Cooling techniques of the PV module: A review. Materials Today: Proceedings, 38, 253-258.

Wang, Z., Qiu, F., Yang, W., Zhao, X., & Mei, S. (2016). Experimental investigation of the thermal and electrical performance of the heat pipe BIPV/T system with metal wires. Applied Energy, 170, 314-323.

Wang, Z., Zhang, J., Wang, Z., Yang, W., & Zhao, X. (2016). Experimental investigation of the performance of the novel HP-BIPV/T system for use in residential buildings. Energy and Buildings, 130, 295-308.

Wilson, M. J., & Paul, M. C. (2011). Effect of mounting geometry on convection occurring under a photovoltaic panel and the corresponding efficiency using CFD. Solar Energy, 85(10), 2540-2550.

Wolf, M. (1976). Performance analyses of combined heating and photovoltaic power systems for residences. Energy Conversion, 16(1-2), 79-90.

Wu, S. Y., Zhang, Q. L., Xiao, L., & Guo, F. H. (2011). A heat pipe photovoltaic/thermal (PV/T) hybrid system and its performance evaluation. Energy and buildings, 43(12), 3558-3567.

Yang, T., & Athienitis, A. K. (2015). Experimental investigation of a two-inlet air-based building integrated photovoltaic/thermal (BIPV/T) system. Applied Energy, 159, 70-79.

Yin, H. M., Yang, D. J., Kelly, G., & Garant, J. (2013). Design and performance of a novel building integrated PV/thermal system for energy efficiency of buildings. Solar Energy, 87, 184-195.

Zhao, X., Zhang, X., Riffat, S. B., & Su, Y. (2011). Theoretical study of the performance of a novel PV/e roof module for heat pump operation. Energy conversion and Management, 52(1), 603-614.

Zogou, O., & Stapountzis, H. (2011). Energy analysis of an improved concept of integrated PV panels in an office building in central Greece. Applied Energy, 88(3), 853-866.

Zogou, O., & Stapountzis, H. (2011). Experimental validation of an improved concept of building integrated photovoltaic panels. Renewable energy, 36(12), 3488-3498.

Zogou, O., & Stapountzis, H. (2012). Flow and heat transfer inside a PV/T collector for building application. Applied energy, 91(1), 103-115.

# Chapter 2

# 2 Parametric characterization of the air channel design and its impact on the natural convection heat transfer in an opaque wall assembly

The National Building Code of Canada (2015) and the British Columbia Building Code (2018) specify a rain-screen wall with a minimum of 10 *mm* air gap for exterior walls in climate zones with high rain load. The impact of the air gap on the moisture transport has been extensively studied since the 60's (Garden, 1963; Killip & Cheetham, 1984; Baskaran, 1994; Tariku & Iffa, 2019). The air gap creates a capillary break between the cladding and the structural inner wall and the airflow through the cavity further short circuits inward moisture drive. The relative contribution of the capillary break created by the air gap and the cavity ventilation to the overall moisture control performance of rain-screen systems was experimentally investigated in Tariku & Iffa (2019). The hygrothermal analysis showed the capillary break had more influence on the moisture control performance. However, the added drying potential due to ventilation manifested as lower sheathing wall temperatures that may have contributed to the building heating and cooling load.

The impact of ventilation on the energy flows in the wall assembly is an active research area. Significant reduction in the building cooling load during summer and increase of the building heating load during winter due to cavity ventilation has been reported (Alberto et al., 2017; Hashemi et al., 2010; Giancola et al., 2012; Fallahi et al., 2010; Chan et al., 2009). Girma & Tariku (2021) reported that by increasing the air gap from 19 mm to 152 mm, the heat gain is reduced by up to 40%. The cavity ventilation introduces cooler ambient air into the cavity, which may be detrimental to the energy consumption during winter but have a positive impact on the cooling load during summer (Tariku & Iffa, 2019). Dampers are recommended during the heating season to limit airflows and enhance the thermal buffer effect (Andelkovic et al., 2015).

The effect of cavity ventilation on the thermal performance of the wall assembly is dependent on the climatic conditions, configuration type, thermophysical and optical material properties, façade orientation, and geometry (Patania et al., 2010; Aparicio-Fernandez et al., 2014; Gagliano et al., 2016). As such, natural ventilated facades have complex and difficult to predict cavity airflow

(Falk & Sandin, 2013). Langmans et al., (2016) performed experiments to quantify the airflows in the cavity for different cladding materials. Also, various simplified numerical approaches have been reported in literature (Marques da Silva et al., 2015; Kuznik et al., 2011; Ghadimi et al., 2013). These simplified approaches are limited in that the cavity airflows are not effectively captured and result in significant errors in quantifying the energy performance. Jiru & Haghighat (2008) reported errors of up to 5°C for a simplified model based on a zonal approach at peak solar conditions. For a detailed study of ventilation in the air cavity in which one is interested in understanding airflow in the cavity including the impact of the external boundary conditions; which are dynamic in nature, a detailed numerical model is necessary such as those based on computational fluid dynamics – CFD (Jiru and Haghighat, 2008; Seferis et al., 2011; Fuliotto et al., 2010). The potential of ventilated façade for energy saving was investigated using the CFD approach and significant energy savings were achieved (Gagliano et al., 2016; Sanchez et al., 2016; Suarez et al.,2011).

Although, the energy saving potential of ventilated facades has been explored, dynamic modelling is still crucial for the thermal performance of a ventilated wall assembly (Wang et al., 2016). Studies focussing on opaque ventilated cavity are scarce even though more than 60% of the housing stock by building type in the residential sector is dominated by opaque construction (NRC Canada). This is also important because of the increasingly stringent energy codes and the demand for high performance building envelope. Further, the energy performance of ventilated wall assemblies is influenced by geometric and climatic parameters, hence, it is necessary to understand the contributions of these parameters to the overall energy performance. The aim of this study is to numerically quantify the impact of ventilated cavity on the energy performance of an opaque wall assembly for typical summer and winter periods. The numerical simulation based on CFD is validated in comparison with in-house generated experimental data. Following, a parametric analysis is conducted to determine the impact of the air cavity height, air gap thickness, cladding material, and radiation properties of the sheathing membrane on the heat flux through the wall assembly.

## 2.1 Methodology

The numerical simulation is conducted using computational fluid dynamics (CFD) and validated using in-house generated experimental data. The experimental data is derived from long term

monitoring of a typical rain-screen 2 x 6 wood-frame wall assembly with fibre cement cladding to assess the impact of air cavity ventilation on the hygrothermal performance. The wall assembly is instrumented with thermocouples; to measure the interstitial surface temperatures of the different wall layers at different heights (Figure 2-1). The Omni-directional Anemometer measures the mid-cavity air velocity and temperature. The indoor and outdoor conditions are monitored by an on-site weather station. To validate the numerical model, the temperature within the interstitial layers of the wall assembly, the temperature at different heights in the air cavity and the mid cavity air velocity are compared with the experimental data. Refer to Tariku & Iffa (2019) for a detailed description of the experimental setup.

Following the CFD validation, a parametric analysis is conducted to understand the impact of various variables on the heat flux through the wall assembly. The variables considered in this paper are air gap width, sheathing membrane emissivity, wall height and cladding material type. The variables are chosen based on variations in typical construction practice. There exist multiple cladding materials, each have recommendations as per code. For example, the BCBC recommends a minimum of 10 *mm*, however, for brick cladding, a minimum of 25.4 *mm* to prevent the mortar that fall behind the cladding from obstructing the path of airflow. The sheathing membrane emissivity may vary from 0.9 (i.e., Building paper) to lower than 0.2 (i.e., low emissivity Tyvek Thermawrap LE). Further, the ventilated cavity may extend over multiple stories. The variables considered are summarized in Table 2-1. The impact of the variables listed in Table 2-1 on the wall heat flux will be investigated for a typical hot and cold day.

Table 2-1: Variables examined in the numerical study

| Parameter | Iterations |
|---|---|
| Air gap width, *mm* | 13, 19, 25, 50, … |
| Emissivity of the inner wall | 0.1, 0.3, 0.6, 0.9 |
| Air Channel height, *mm* | 1H, 2H* |
| Type of cladding | Fiber cement, Brick, Metal |

*where H = 8ft, the typical floor height

## 2.2 Validation of the Numerical model

The typical thermal loading of a rain-screen wall assembly is complex due to dynamic nature of the heat transfer mechanisms occurring simultaneously. This poses a conjugate heat transfer problem that is solved by implementing the unsteady Reynolds Averaged Navier-Stokes and Energy equations. The radiation heat exchange is modeled using the Discrete Ordinate method (DOM). Turbulence is modeled using the standard low reynolds number k-epsilon turbulence model as it is suitable for natural convection flows (Siemens, 2018).

### 2.2.1 Numerical Simulation Setup

The details of the numerical setup including the computational domain, boundary conditions, mesh generation and solution strategy are presented in this section.

#### 2.2.1.1 Computational Domain

The two-dimensional representation of the solution domain is seen in Figure 2-1. A 2D modeling approach is employed since it was reported that switching from a 2D to a 3D computational domain did not show appreciable improvement in results (Pasut & Carli, 2012; Fuliotto et al., 2010). The computational domain consists of the wall assembly, the foundation wall, and the immediate external environment (i.e., the soil and outdoor air).

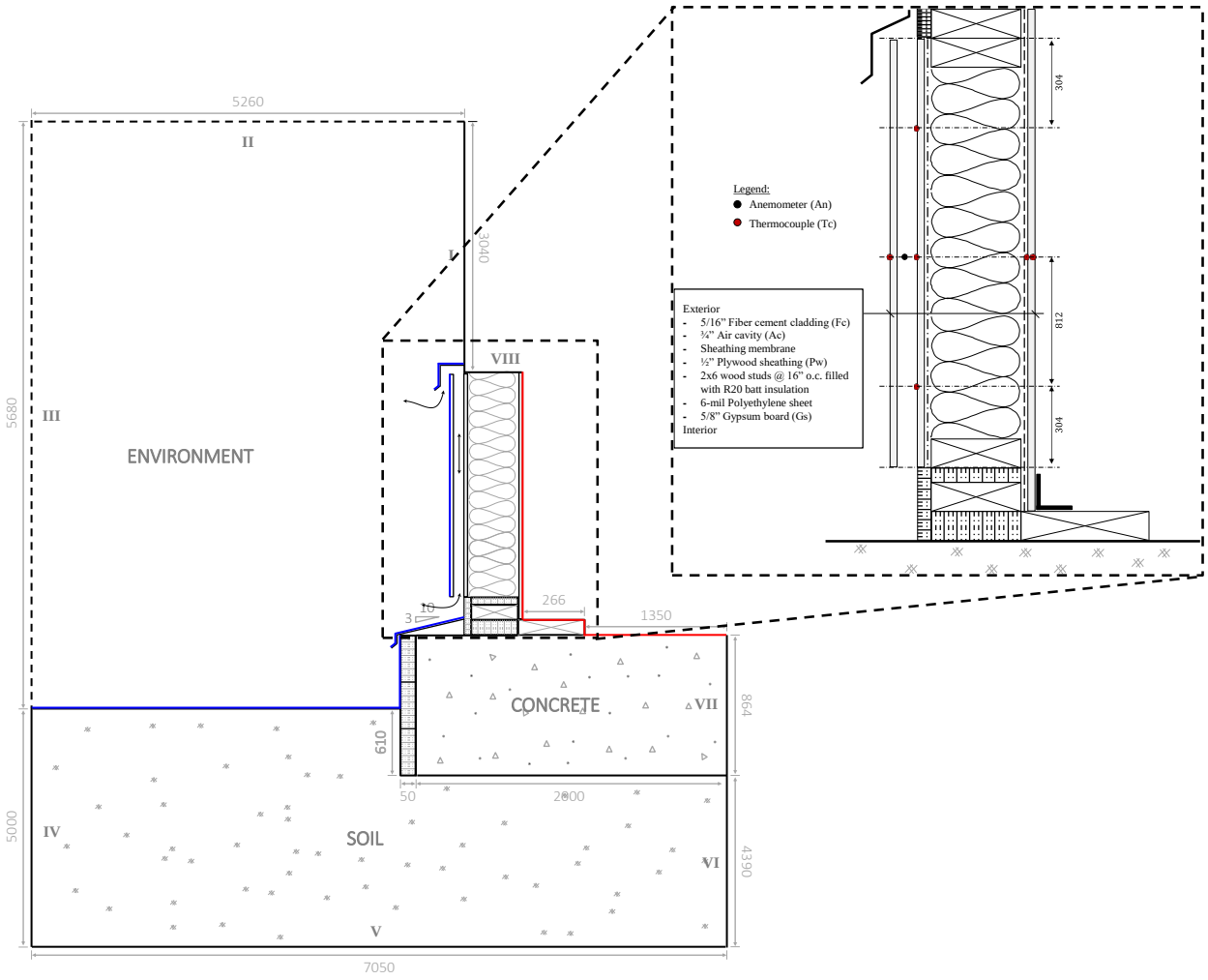


Figure 2-1: The 2D computational domain (NTS)

The computational domain is extended to include the foundation wall and the external environment to deal with the uncertainty in specification of the inlet air temperature. The inlet air temperature is typically specified as the outdoor air temperature; however, it has been determined in experimental studies that this assumption is inaccurate (Eicker et al., 2008; Saelens et al., 2004). This uncertainty in specification of the inlet air temperature can lead to errors in the prediction of the thermal and flow field in the air cavity. Extending the computational domain to include the adjacent ground, building structures, and surrounding space will allow the inlet air temperature to develop naturally. This will potentially enhance the accuracy of the numerical model.

The computational domain is extended 5260 *mm* to the right of the cladding material and 3040 *mm* above the wall assembly. The foundation wall or concrete block is 864 *mm* high and 2000 *mm*

wide. The right edge of the concrete block extends 1620 *mm* from the interior surface of the wall assembly. The concrete block is 610 *mm* beneath the soil surface and insulated with 50 *mm* rigid insulation on the exterior side. The soil layer is modeled to a depth of 4390 *mm* below the concrete block and 5000 *mm* below the ground surface where the ground temperature is sufficiently stable (Gold & Williams, 1976). The thermophysical properties of the concrete block and the soil are given in Table 2-2.

The wall assembly is numerically represented to be like the experimental setup. The wall height is 2240 *mm* and the overall wall thickness including the 13 *mm* thick air cavity is 186 *mm*. The elbow at top of the air cavity is included to account for the impact of the flashing in the experimental design. The elbow extends about 25 *mm* down the top of the fiber cement cladding. All the layers of the inner wall are modeled as individual solid domains except the air and vapour control layers (i.e., Tyvek Housewrap and 6-mil polyethylene), since their effect on the conduction heat transfer through the wall assembly is negligible. However, the effect of the sheathing membrane (i.e., Tyvek Housewrap) on the radiation exchange in the air cavity is accounted for by specifying 0.2 as the emissivity. The emissivity of the cladding is 0.5. The specified emissivity values are verified in Section 3.2. Other key material properties of the wall layers including the density ($kg/m^3$), thermal conductivity ($W/m/K$) and specific heat capacity ($J/kg/K$) are given in Table 2-2.

Table 2-2: Material properties of the components of the wall assembly[a]

| Material | $\rho$ | $\lambda$ | $c_p$ |
|---|---|---|---|
| Fiber Cement | 1400 | 0.25 | 840 |
| Plywood | 460 | 0.14 | 1880 |
| Wood Block[b] | 400 | 0.09 | 1630 |
| Aluminum | 2702 | 237 | 903 |
| Gypsum Board | 640 | 0.16 | 1150 |
| Batt Insulation | 12 | 0.043 | 800 |
| EPS | 64 | 0.029 | 1700 |
| Concrete | 2240 | 1.59 | 840 |
| Ground[c] | 1500 | 1.3 | 800 |
| Air[d] | - | - | - |
| Brick | 1920 | 0.72 | 835 |
| Metal | 7854 | 60.5 | 434 |

[a]material properties adopted from ASHRAE Handbook of fundamentals, 2017
[b]spruce wood
[c]dry packed soil from ANSI/ASHRAE Standard 140-2001
[d]temerature dependent air properties

#### 2.2.1.2 Boundary Conditions

The outer boundaries of the computational domain (Figure 2-1) are identified with roman numerals: I – VII. The physical boundaries are represented with solid lines and the artificial boundaries are represented with broken lines. The interior and exterior boundaries of the wall assembly are represented with red and blue lines respectively. The specifications for the labelled boundaries of the computational domain are given in Table 2-3.

Table 2-3: Specification of boundary conditions for the computational domain

| No. | Boundary Condition | Comment |
|---|---|---|
| I | Temperature BC | Representative of the building second floor, which has a similar temperature as the test wall cladding. |
| II & III | Pressure Outlet | Boundary specified at outdoor air temperature and atmospheric pressure. The turbulent kinetic energy and turbulent specific dissipation rate at the pressure outlet boundaries are initialized to 0 *J/kg* and 0 $m^2/s^3$ respectively. |
| IV & VI | Adiabatic | No lateral heat transfer. |
| V | Temperature BC | A deep ground temperature of 10℃ is assumed (ANSI/ASHRAE Standard 140-2001). |
| VII & VIII | Symmetry | No lateral heat transfer. |

The interior boundary (i.e., the red line in Figure 2-1) is specified as a combined convection and radiation heat flux boundary as given in Equation 2-1.

$$\boldsymbol{Q_{comb,int} = h_{comb,int}(T_s - T_{int})} \qquad \text{Equation 2-1}$$

where, $T_s$ is the surface temperature, $T_{int}$ is the measured indoor air temperature and $h_{comb,int}$ is the combined convection and radiation heat transfer coefficient which is given as 8.29 $W/m^2K$ for the vertical oriented surface and 6.13 $W/m^2K$ for the horizontal surface with downward heat flow (AHSRAE HOF, 2017).

The exterior heat flux (i.e., the blue line in Figure 2-1) is specified as heat flux boundary. The heat flux specification for the other wall boundary is given in Equation 2-2.

$$\boldsymbol{Q_{total} = Q_{rad} + Q_{conv,ext} + Q_{sky}} \qquad \text{Equation 2-2}$$

where, $Q_{rad}$ is the horizontal or vertical solar radiation intensity depending on the surface orientation, $Q_{conv,ext}$ is convective heat loss or gain due to wind and $Q_{sky}$ is the sky radiation. The convective heat transfer with the outdoor air is expressed in Equation 2-3.

$$\boldsymbol{Q_{conv,ext} = h_{conv,ext}(T_s - T_{ext})} \quad \text{Equation 2-3}$$

where, $h_{conv,ext}$ is the exterior convective heat transfer coefficient, and $T_{ext}$ is the outdoor air temperature. The exterior convective heat transfer coefficient is calculated in accordance with the ESP-r implementation of the McAdams model (Mirsadeghi et al., 2013) for rough surfaces (Equation 2-4).

$$\boldsymbol{h_{c,ext} = 3.8\, V_{10} + 7.4} \quad \text{Equation 2-4}$$

where, $V_{10}$ is the on-site measured wind speed. The impact of wind on the flow in the cavity is minimal but its impact on the wall temperature is important (Tariku & Iffa, 2019). The sky radiation is expressed in Equation 2-5 (Algarni & Nutter, 2015):

$$\boldsymbol{Q_{sky} = \varepsilon_s \sigma F_{ss}\left(T_s^4 - T_{sky}^4\right)} \quad \text{Equation 2-5}$$

where, $\varepsilon_s$ is the surface emissivity (i.e., 0.5 for the cladding material, 0.88 for the ground surface, and 0.9 for the other materials), $\sigma$ is the Stefan Boltzmann constant (5.67 x $10^{-8}$ W/m$^2$/K$^4$), $F_{ss}$ is the sky view factor (i.e., 0.5 for a vertical surface and 1.0 for a horizontal surface), and $T_{sky}$ is the sky temperature. The sky temperature is estimated according to Equation 2-6.

$$\boldsymbol{T_{sky} = \gamma\, T_{sky,cloudy} + (1 - \gamma) T_{sky,clear}} \quad \text{Equation 2-6}$$

where, $\gamma$ is the sky index (See Table 2-4), $T_{sky,cloudy}$ is the cloudy sky temperature (Equation 2-7) and $T_{sky,clear}$ is the clear sky temperature (Equation 2-8 - Algarni & Nutter, 2015).

$$\boldsymbol{T_{sky,cloudy} = T_{ext}} \quad \text{Equation 2-7}$$

$$\boldsymbol{T_{sky,clear} = 0.0555 T_{ext}^{\,1.5}} \quad \text{Equation 2-8}$$

Table 2-4: Sky index value assigned for cloud cover

| Cloud Cover | Sky Index, $\gamma$ |
|---|---|
| Clear | 0.0 |
| Mainly Clear | 0.2 |
| Partially Cloudy | 0.5 |
| Mostly Cloudy | 0.8 |
| Cloudy | 1.0 |

### 2.2.1.3 Numerical Solution Strategy

Simcenter STAR-CCM+ uses the finite volume method to solve the governing equations for Newtonian fluids. The governing equations are discretized in space and time and the resulting linear equations are then solved with the algebraic multigrid solver. In the time coordinate, the solution of the governing equations is obtained using the Euler implicit scheme; a first order temporal scheme. The time step size is derived from the experimental data using the reciprocal of the Brunt Vaisala frequency as seen in Equation 2-9.

$$\Delta \boldsymbol{t} = \frac{\mathbf{1}}{\boldsymbol{\beta g}(\boldsymbol{\Delta T}/\boldsymbol{L})^{\mathbf{2}}} \qquad \text{Equation 2-9}$$

where, $\beta$ is the volumetric thermal expansion coefficient, $g$ is the gravitational acceleration, $\Delta T$ is the temperature difference in the solution domain and $L$ is the characteristic length. The optimal time step is derived to be 300*s*. In the space coordinate, the conservation equations of mass and momentum are solved using the implicit unsteady pressure-based approach. The pressure-based approach is implemented as the Segregated Flow Model. The steady segregated solver employs the SIMPLE (Semi-Implicit Pressure Linked Equation) pressure-velocity coupling algorithm. The Second-Order Upwind (SOU) scheme is used to discretize the governing equations. The solution is converged for all residuals (i.e., continuity, velocity components and energy) less than $10^{-4}$.

### 2.2.1.4 Mesh Generation

The typical meshing scheme consists of 377,232 grid cells as shown in Figure 2-2. The computational domain is discretized with an unstructured polyhedral mesh. Five prism layer meshes are employed to capture the near wall viscous dominated flow. A physics controlled

meshing scheme is specified that concentrates the finer grid elements in the air cavity to effectively capture the fluid flow physics. The grid size is progressively increased from the finer grids in the air cavity to the solid domains farther from the air cavity by specifying a surface growth ratio.

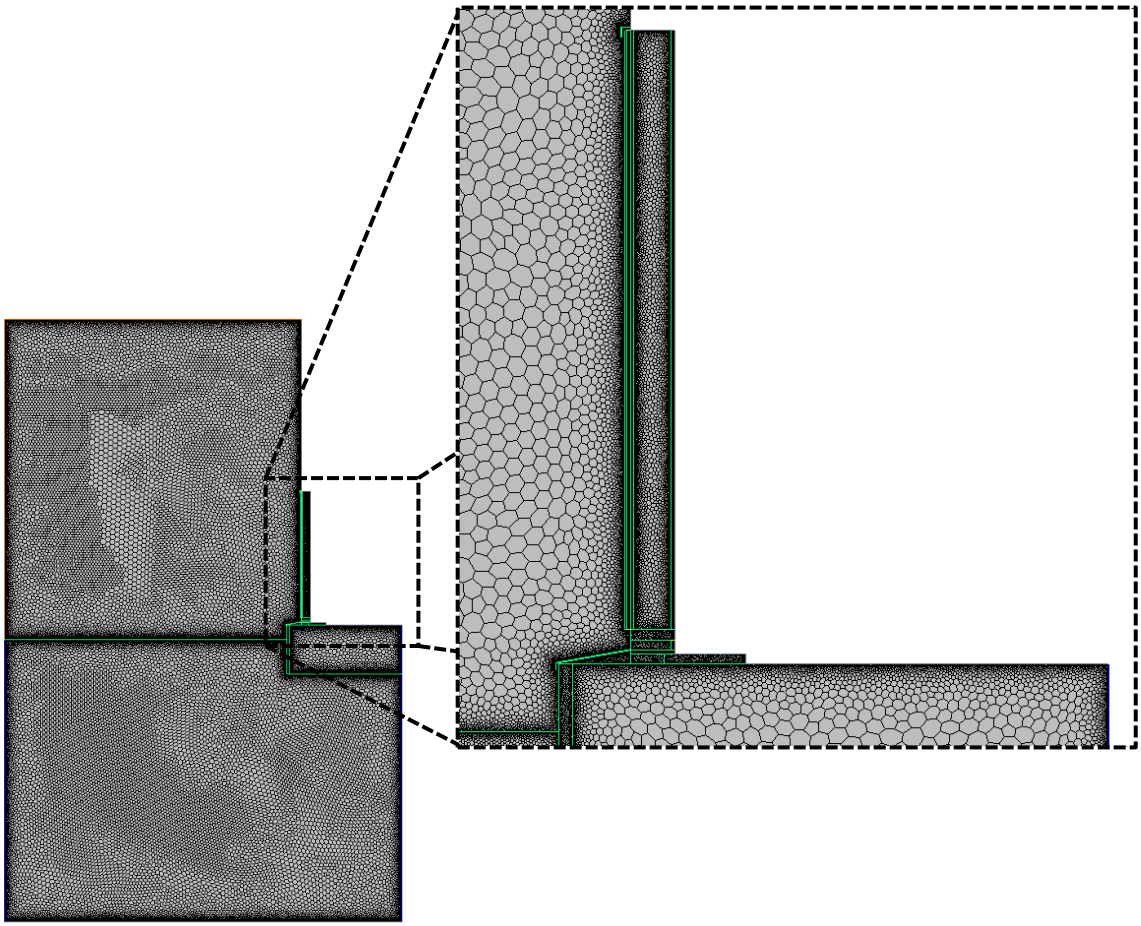

Figure 2-2: The typical mesh of computational Domain

Grid sensitivity study is conducted with a coarse and fine mesh. The computational domain is discretized with 251,784 and 602,491 grid cells for the coarse and fine mesh respectively. The mesh independency study is carried out for the outdoor conditions given in Figure 2-3. The peak solar radiation intensity is 665 $W/m^2$. The maximum and minimum outdoor air temperature are 9.52℃ and -0.83℃, respectively. The average wind speed is 0.48 *m/s* with a peak of 1.46 *m/s* that occurs at 2:00 pm.

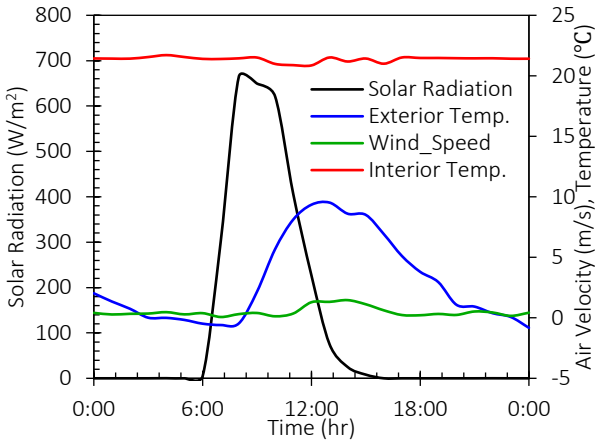


Figure 2-3: Exterior climate parameters on February 4th

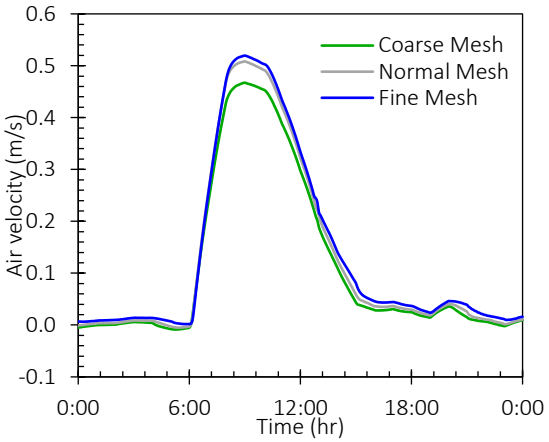


Figure 2-4: The effect of mesh refinement on the solution convergence of the mid-cavity air velocity

Figure 2-4 compares the predictions of the mid-cavity air velocity for the coarse mesh, normal mesh, and fine mesh. As the mesh is refined from the coarse mesh to the normal mesh, the peak velocity increases from 0.467 *m/s* to 0.508 *m/s* (i.e., an 8.7% increase). A subsequent refinement of the mesh from the normal mesh to the fine mesh increases the peak velocity by 0.90% (i.e., from 0.508 *m/s* to 0.520 *m/s*). The relative change is marginal; hence, the normal mesh is deemed sufficient to capture the airflow characteristics in the ventilated cavity.

### 2.2.2 CFD Validation Results

The results from the CFD model validation are presented in this section. The Root mean square error (*RMSE*) given in Equation 2-10 is adopted to quantify the numerical error (Chai & Draxler, 2014).

$$\boldsymbol{RMSE} = \sqrt{\frac{\mathbf{1}}{\boldsymbol{n}}\sum_{\boldsymbol{i=1}}^{\boldsymbol{n}}\left(\boldsymbol{y_{sim}} - \boldsymbol{y_{exp}}\right)^{\mathbf{2}}} \qquad \text{Equation 2-10}$$

#### 2.2.2.1 Interior and Exterior Boundary Conditions

Figure 2-5a and Figure 2-5b compare the CFD prediction of the interior wallboard temperature and cladding temperature with the experimental data. The mini-wall sketch shows the respective sensor locations. There is good agreement between the numerical prediction and the experimental data. The RMSE for the numerical prediction of the temperature on the interior wallboard and cladding is 0.29ºC and 1.93ºC respectively.

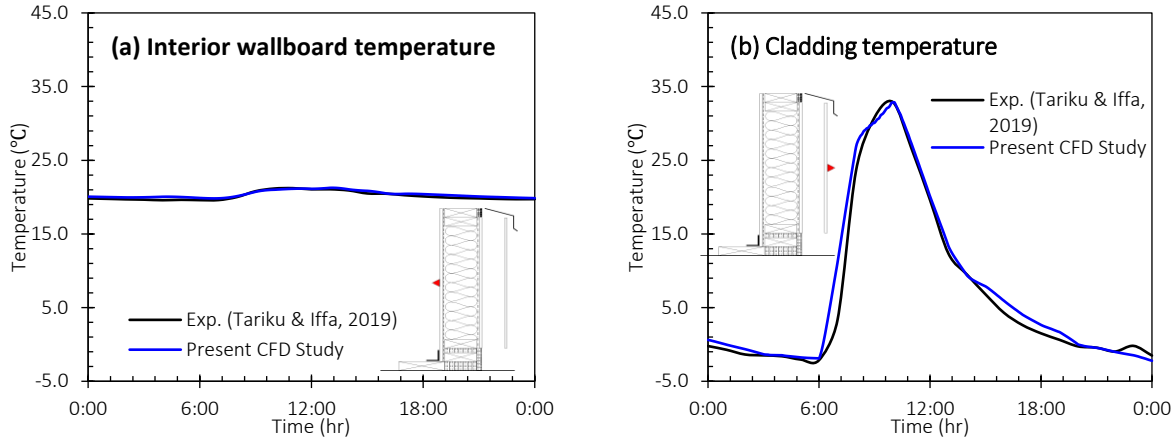


Figure 2-5: Comparison of the CFD prediction of the (a) interior wallboard temperature and (b) cladding temperature, with experimental data

The error in predicting the cladding temperature may be attributed to the uncertainties in determining the sky radiation because of the numerical transformation of the cloud cover. Also, the interpolation method between time steps may also contribute to the numerical error. This manifests as a phase lead of the CFD predicted cladding temperature compared with the experimental data especially at the morning solar rise (i.e., 6am). However, the errors are consistent with literature on airflow in a ventilated cavity. Kuznik et al. (2011) reported errors

within 1.5℃ of the experimental data. Jiru & Haghighat (2008) predicted temperatures with errors of more than 5℃. Seferis et al. (2011) reported mean and maximum temperature prediction errors of 2.19℃ and 6℃ respectively.

#### 2.2.2.2 Ventilated Cavity Thermal and Flow Characteristics

The mid-cavity air velocity and the temperatures at different heights are then assessed to validate the cavity flow and thermal characteristics. Figure 2-6a compares the CFD prediction of the mid-cavity air velocity with the experimental data. As seen in Figure 2-6a, there is good agreement between the numerical model prediction and the experimental data, although, the peak velocity is slightly overestimated. Further, the discrepancy may be attributed to the phase difference between the predicted value and the experimental data. The *RMSE* is 0.056 *m/s*.

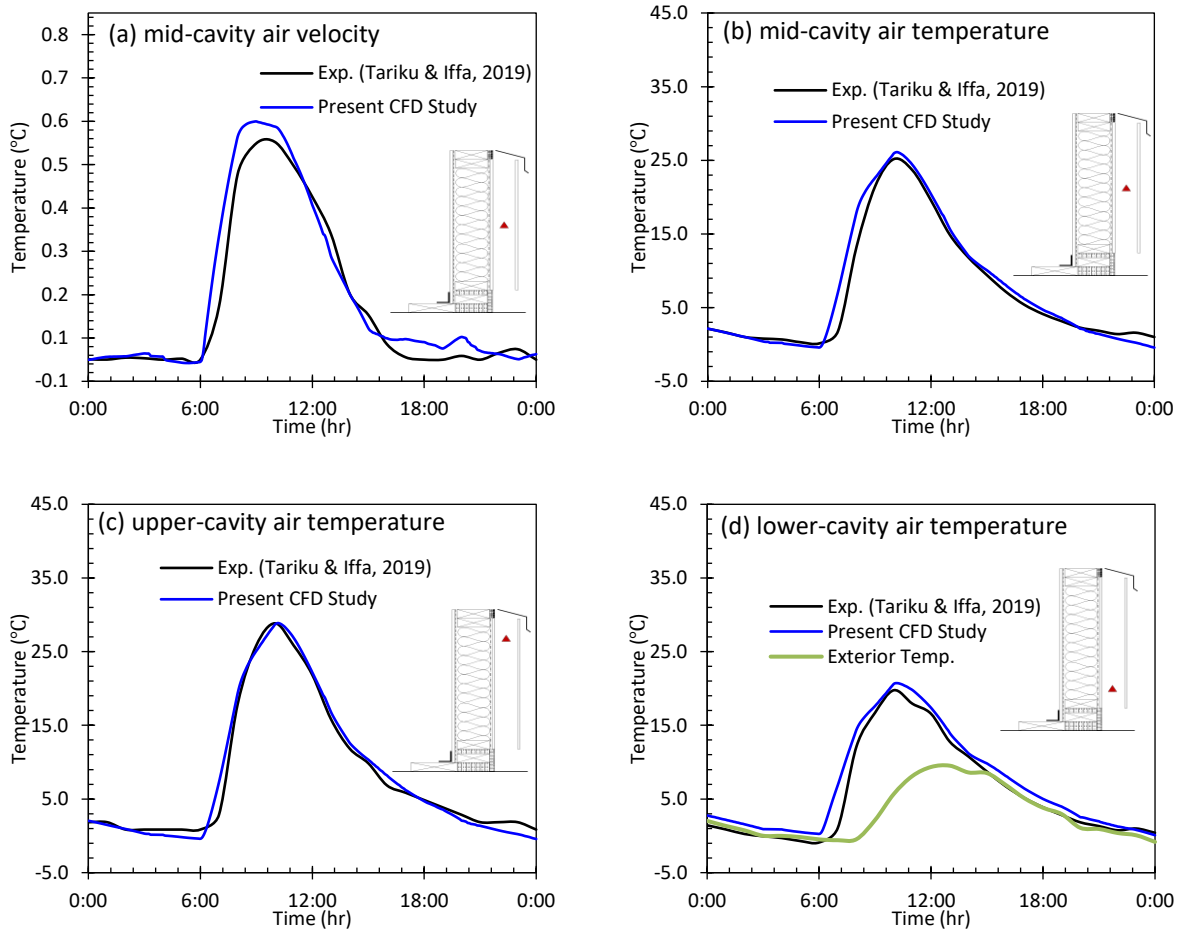


Figure 2-6: Comparison of the CFD prediction and experimental data for the (a) mid-cavity air velocity, (b) mid-cavity air temperature, (c) upper-cavity air temperature, and (d) lower-cavity temperature

Figure 2-6b, Figure 2-6c and Figure 2-6d compare the CFD prediction of mid-cavity temperature, upper-cavity temperature and lower-cavity temperature. The *RMSE* in predicting the mid-cavity temperature, upper-cavity temperature and lower-cavity temperature is 1.28℃, 1.76℃ and 1.60℃ respectively. Hence, numerical model can be relied upon to sufficiently capture the enthalpy gain of the airflow in the cavity.

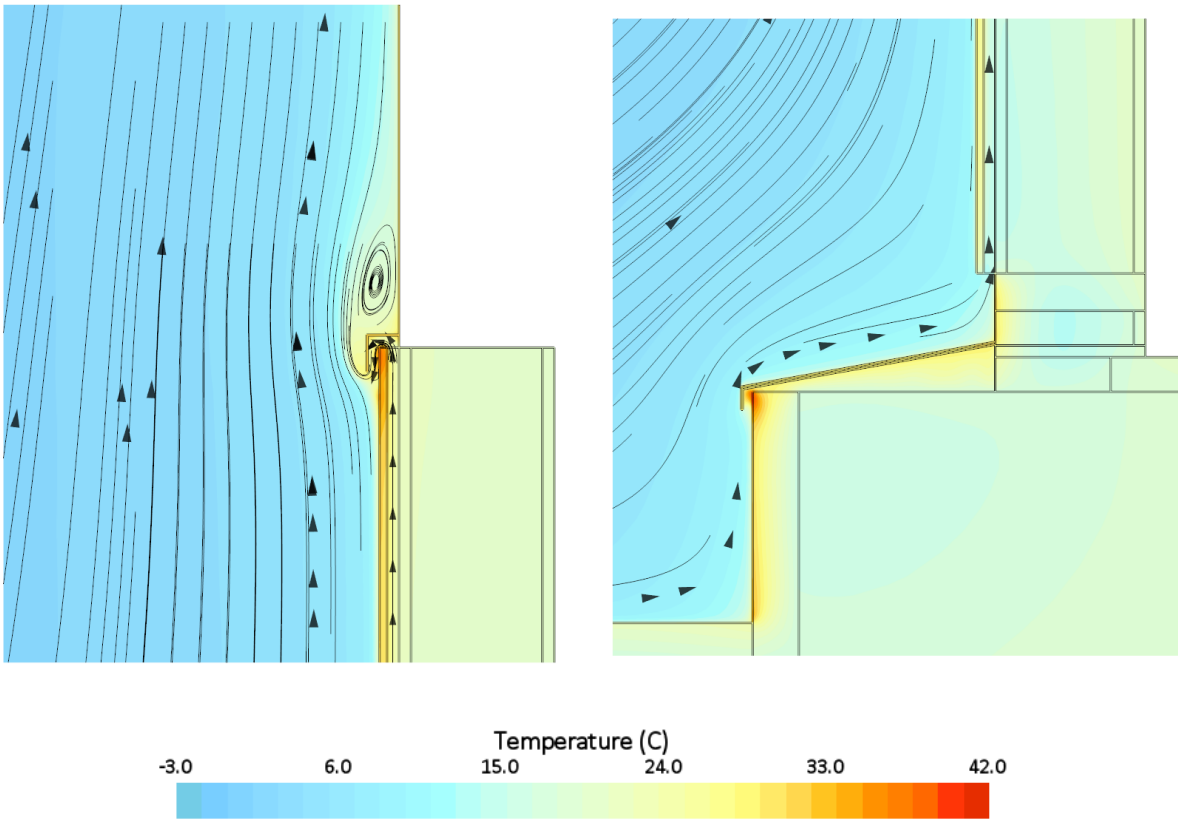


Figure 2-7: Streamlines of velocity and temperature contours for the (a) top flashing and (b) bottom flashing at peak solar conditions

In Figure 2-6d, the influence of the flashing on the inlet air can be seen. The inlet air temperature is cooler than the outdoor temperature at night-time due to sky radiation and warmer than the exterior temperature during the day. The flow structure in Figure 2-7 further asserts the impact of the bottom flashing on the air flow in the ventilated cavity for the hottest hour of the day. The elevated temperature of the cladding, bottom flashing and the ground in the immediate wall surrounding induces an upward flow in the ventilated cavity. The top flashing impedes the upward

fluid motion which creates a negative pressure gradient in the immediate upstream and results in flow recirculation as shown by the flow streamlines.

### 2.2.2.3 Interstitial Temperature Profile

Figure 2-8a - d compares the interstitial temperature profile for the numerical model and the experimental data. Particularly, the sheathing temperature adjacent to the ventilated cavity at the middle, top and bottom location is compared with experiment. The interior wall board temperature is also considered.

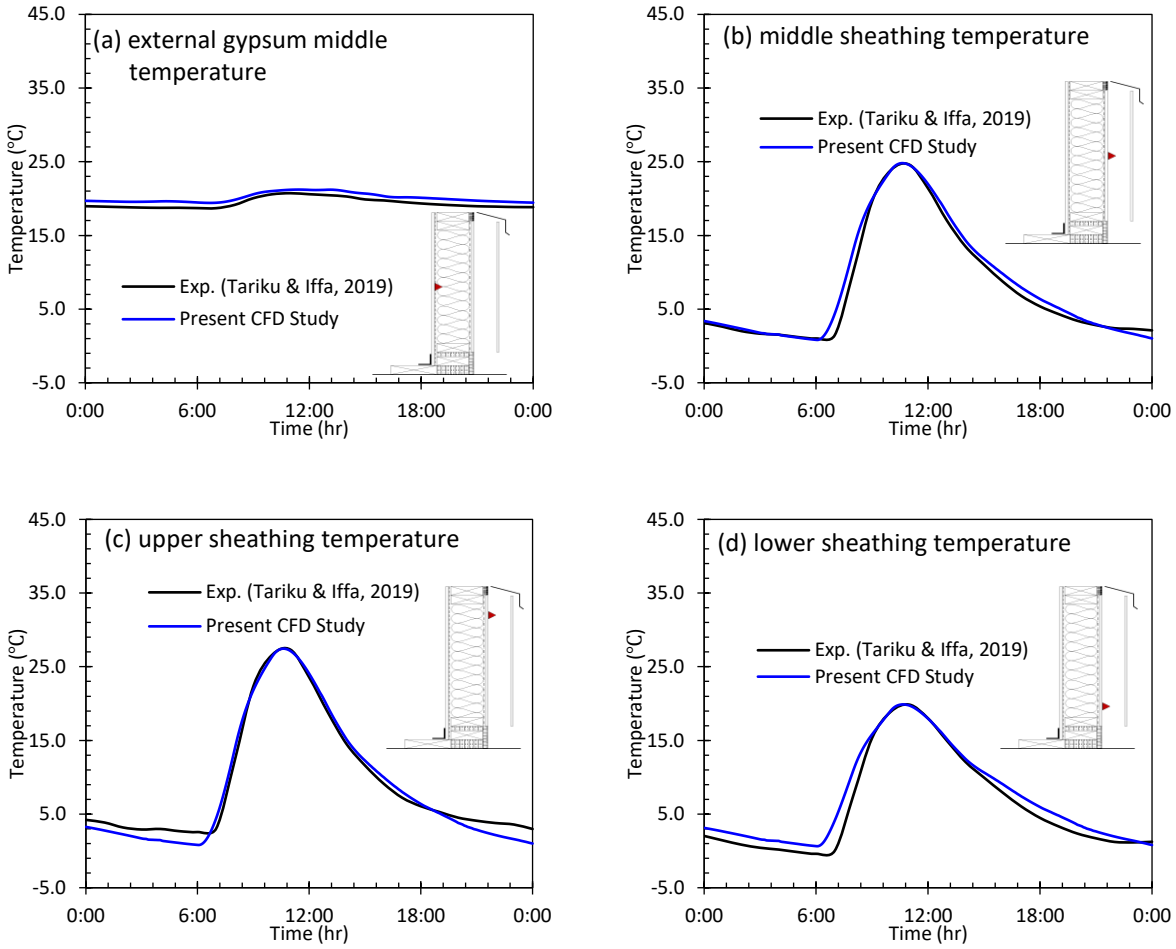


Figure 2-8: Comparison of the CFD prediction and experimental data for the (a) external gypsum middle temperature, (b) middle sheathing temperature, (c) upper sheathing temperature, and (d) lower sheathing temperature

The *RMSE* for predicting the interior wallboard temperature (Figure 2-8a) is 0.72℃. The error may be attributed to the uncertainty in the thermophysical properties of the interior wall board. Also, there may be thermal contact resistance effects that are not captured in the numerical simulation. The *RMSE* for predicting the middle, top and bottom sheathing temperatures are 1.39℃, 1.78℃ and 1.41℃ respectively. This error is more pronounced when the solar radiation intensity is low as seen in Figure 2-8b-d. The middle sheathing temperature is predicted with the least error of the three locations. This is expected since the influence of the top and bottom openings are not prominent.

## 2.3 PARAMETRIC ANALYSIS - Results and Discussions

The parameters considered were the sheathing membrane emissivity, the air gap width, the channel height, and the cladding material type. The climate and interior conditions for typical cold and hot days of the 2012 calendar year are presented in Section 2.3.1. The weather data is derived from in-house weather station; however, the cloud cover is derived from archived Environment Canada data for the Vancouver Int'l Airport weather station. The impact of the parameters earlier listed are compared to a reference wall assembly with no airgap. The heating and cooling load for the reference wall assembly has been determined to be -158 $kWh/m^2$ and 66.1 $kWh/m^2$ for the typical cold and hot day respectively.

### 2.3.1 Exterior climate and Interior Conditions

The parametric analysis is carried out for a cold day and hot day, which are representative of winter and summer performance respectively. The solar radiation, wind speed, and outdoor air temperature are given in Figure 2-9a for the typical cold day (i.e., January 18$^{th}$, 2012) and Figure 2-9b for the typical hot day (i.e., August 17$^{th}$, 2012). The average outdoor air temperature is -6.8℃ and 24.2℃ for the cold and hot day respectively. Wind speeds of up to 1.67 *m/s* and 1.27 *m/s* are seen on the cold and hot day respectively. The simulation period is extended to include January 17$^{th}$ for the cold day simulation and August 16$^{th}$ for the hot day simulation to limit the influence of the initial conditions. The interior temperature is assumed to be maintained at 21℃ and 23℃ for the cold and hot day simulation respectively.

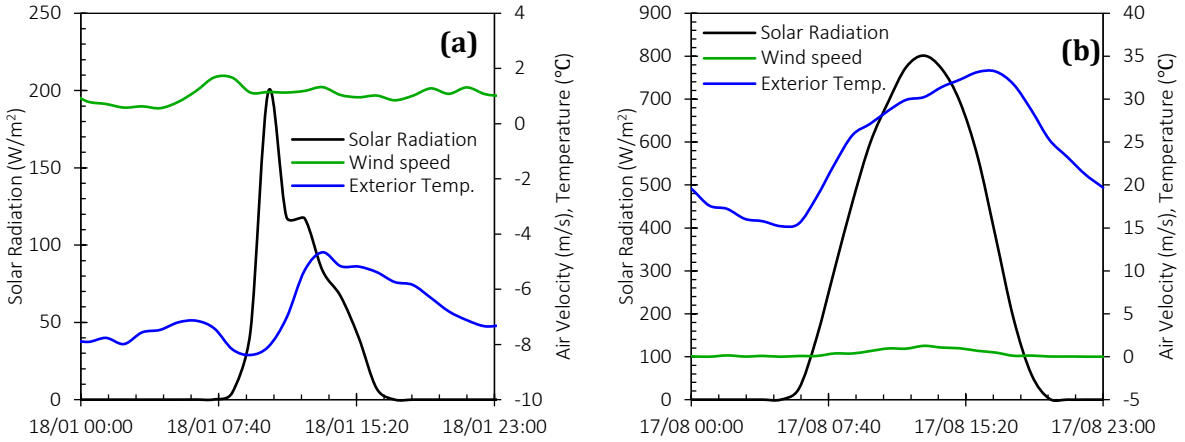


Figure 2-9: The exterior climate parameters for the typical (a) cold day, and (b) hot day

### 2.3.2 Impact of sheathing membrane emissivity

The sheathing membrane emissivity is varied as in Table 2-1. In all instances, the air gap width is 13 *mm* with fiber cement cladding and a 1-storey channel height (i.e., 2440 *mm*). Figure 2-10a-i & Figure 2-10a-ii show the cladding and sheathing temperature for the emissivity values considered under cold outdoor conditions. The cladding temperature is similar for the range of emissivity values considered (i.e., 0.1, 0.3, 0.6, and 0.9). The cladding temperature fluctuates between 0.84°C and -7.62°C. The cladding temperature is always higher than the outdoor air temperature even at night because the cloudy sky cover, limits the intensity of the sky radiation. As seen in Figure 2-10a-ii, the higher the emissivity the lower the sheathing temperature which is more pronounced at night. The higher sheathing temperature translates to a higher induced mid-cavity air velocity especially at night for the sheathing membrane emissivity of 0.1 as seen in Figure 2-10a-iii. The induced air flow enhances convective heat loss and is shown by the higher air temperature for $\varepsilon$ = 0.1 compared with 0.9 in Figure 2-10a-iv. There is a conflicting influence of the radiation heat exchange and the convection heat exchange in the air cavity. The relative impact of both means of heat exchange on the heat transfer across the wall assembly is assessed by quantifying the energy flows. The wall heat fluxes for the case with the sheathing membrane emissivity of 0.1, 0.3, 0.6, and 0.9 are -144 $kWh/m^2$, -146 $kWh/m^2$, -148 $kWh/m^2$, and -149 $kWh/m^2$ respectively. It is then deduced that the heating load is respectively reduced by 8.86%, 7.59%, 6.33%, and 5.70% compared with the reference wall assembly. This increasing heat flux with emissivity implies that

the heat loss associated with long-wave radiation is more dominant than the heat loss associated with convection due to the increase of the air flow for the lower emissivity wall.

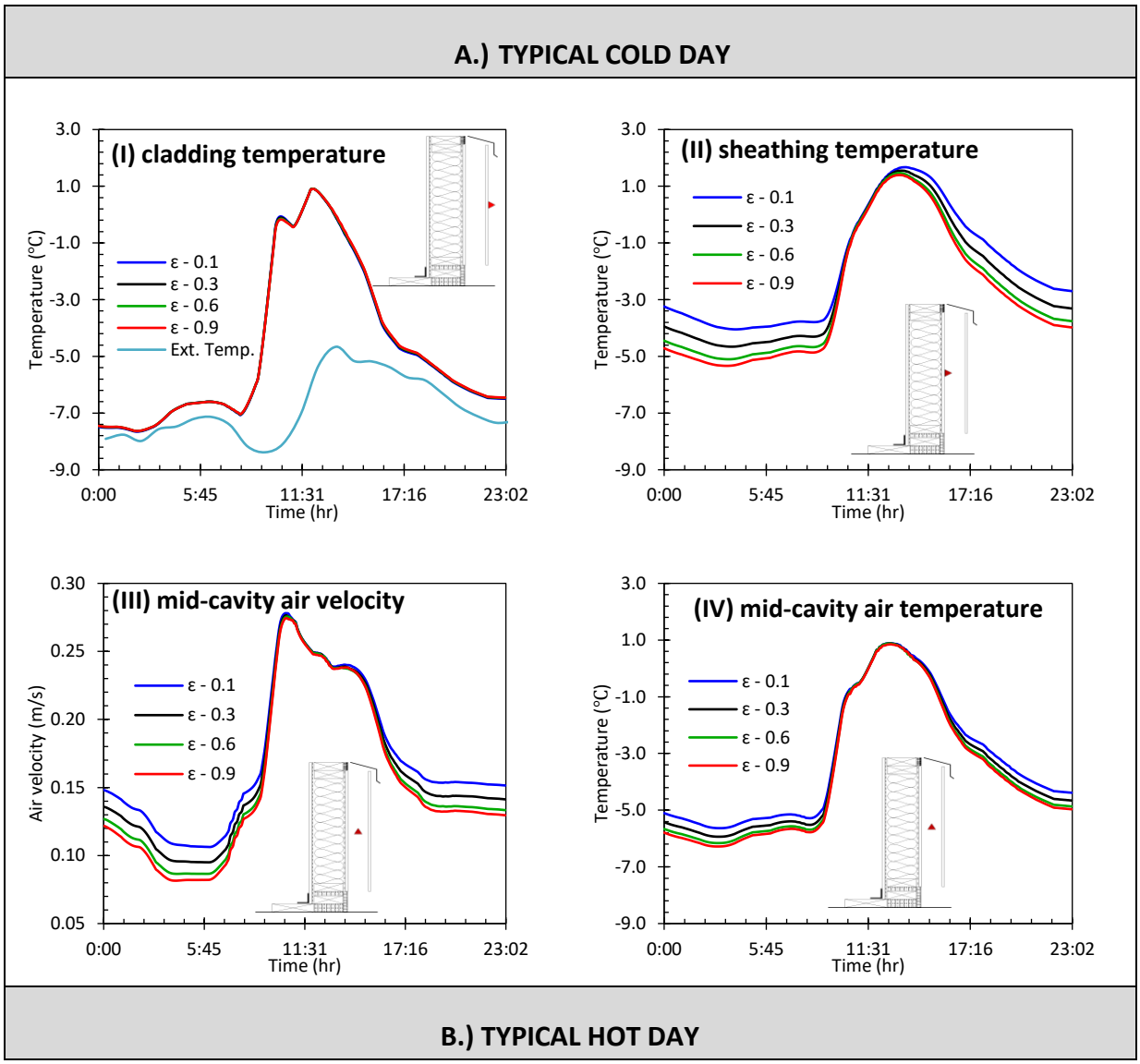

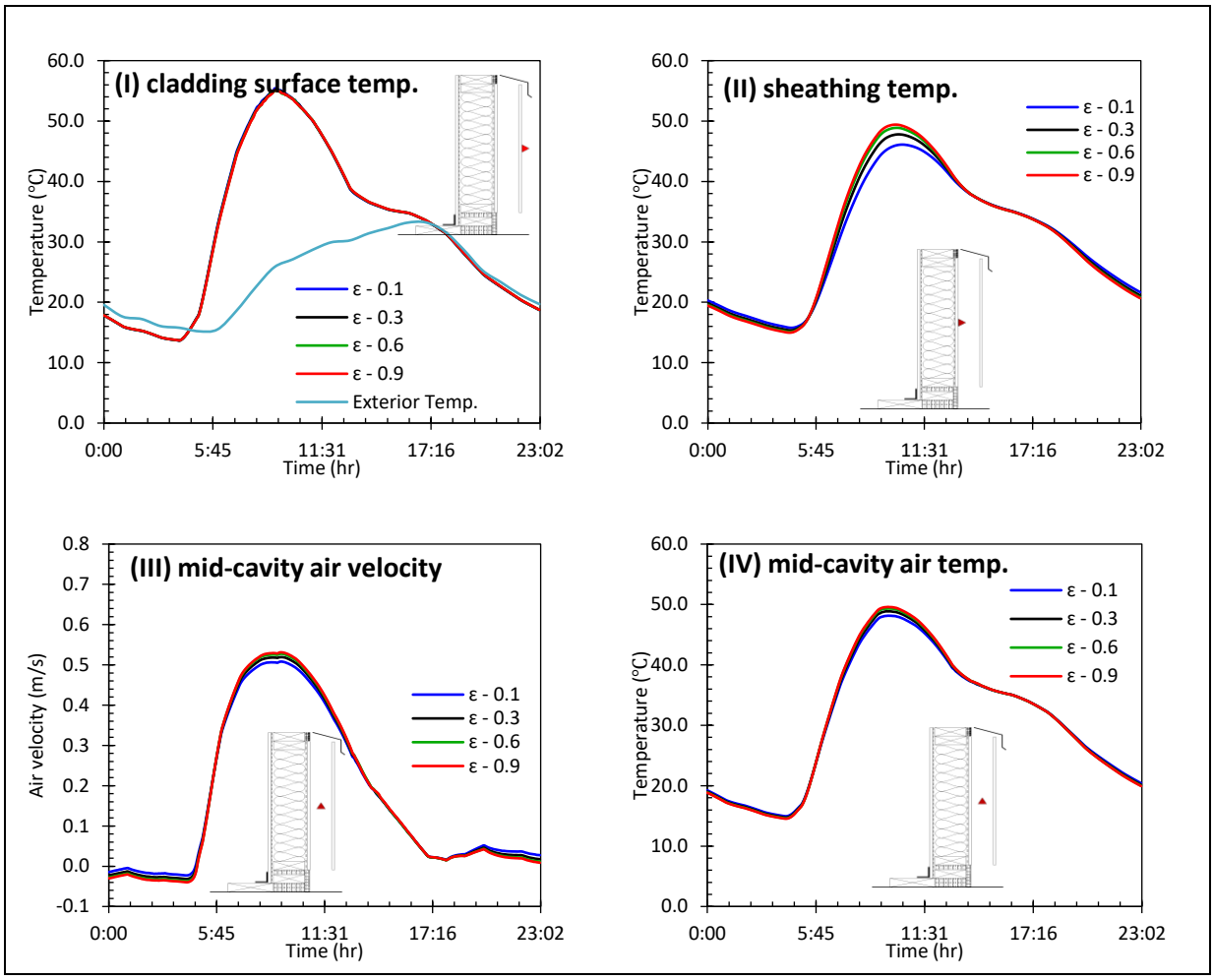


Figure 2-10: The effect of varying the sheathing membrane emissivity on the (I) cladding surface temperature, (II) sheathing temperature, (III) mid-cavity air velocity, and (IV) mid-cavity air temperature

For the hot day case study, the cladding temperature is significantly hotter than the cold day study as seen in Figure 2-10b-i. The temperature fluctuates between 14°C and 55°C. The sheathing temperature follows the same trend as the cladding surface temperature; however, there is a noticeable offset between the peak temperatures of the cladding and the sheathing that correlates with the sheathing membrane emissivity. As seen in Figure 2-10b-ii, the peak sheathing temperatures are 46.0°C, 47.8°C, 48.9°C, and 49.4°C for the emissivity values of 0.1, 0.3, 0.6, and 0.9 respectively. The increasing peak temperatures with emissivity is attributed to the higher intensity of long wave radiation exchange in the channel. The induced velocity in the ventilated cavity is significantly higher in Figure 2-10b-iii for the hot day case study compared to the cold

day case study (See Figure 2-10a-iv), which is attributed to the higher temperature difference with the outdoor air.

The induced airflow in the ventilated cavity is similar for the emissivity values considered. The peak air velocity is 0.51 *m/s*, 0.52 *m/s*, 0.53 *m/s*, and 0.53 *m/s* for the emissivity values of 0.1, 0.3, 0.6, and 0.9 respectively. As such, the air temperature in the ventilated cavity is also similar (Figure 2-10b-iv). The wall heat flux for the case with the sheathing membrane emissivity of 0.1, 0.3, 0.6, and 0.9 is 52.7 $kWh/m^2$ (-20.3%), 54.8 $kWh/m^2$ (-17.1%), 56.2 $kWh/m^2$ (-15.0%), and 56.8 $kWh/m^2$ (-14.1%) respectively. Note that the values in parenthesis signify the performance compared to the reference wall. This convention is followed throughout. The heat gain increases by 7.78% as the emissivity is increased from 0.1 to 0.9. The increase in heat gain attributed to the increase of the sheathing membrane emissivity is small for $\varepsilon > 0.6$. The sheathing membrane emissivity has more impact on the wall heat flux during summer than winter.

### 2.3.3 Impact of air gap width

Initially, the air gap width is varied from 13 – 50 *mm*. In all cases, the sheathing membrane emissivity is 0.2 with fiber cement cladding and a 2440 *mm* channel height. Figure 2-11a shows the cladding temperature for the different air gap widths during the cold day case study. The cladding temperature is similar in all cases. The sheathing temperature decreases with the air gap width especially at peak solar conditions (Figure 2-11b). The peak sheathing temperature is 1.59℃, 0.90℃, 0.53℃, and 0.07℃ for the air gap widths of 13 *mm*, 19 *mm*, 25 *mm*, and 50 *mm* respectively. This is attributed to the change in the flow characteristics with increase in gap width. Figure 2-11c shows that the mid-cavity velocity increases with increase in gap width for $\delta \leq 25$ *mm* and reduces for $\delta > 25$ *mm*. The modified Rayleigh number, $Ra_s(\delta/H)$ in Figure 2-11e shows that the airflow in the cavity changes from a fully developed flow (i.e., $Ra_s(\delta/H) \leq 10$) for $\delta \leq 13$ *mm* to an isolated plate flow (i.e., $Ra_s(\delta/H) \geq 100$) for $\delta > 25$ *mm*. The natural convective mixing in the mid-cavity significantly diminishes for the isolated plate flow as reflected in the deviation from the parabolic velocity profile for $\delta > 25$*mm* (See *Figure 2-11g*).

The diminished natural convective mixing is demonstrated in Figure 2-11d and Figure 2-11h. As the air gap increases, the mid-cavity temperature decreases as well as the enthalpy gain along the channel height. Consequently, the plywood sheathing temperature is lower for higher cavity widths

as seen in Figure 2-11b. The energy implication of varying the airgap is seen in Figure 2-11f. The peak heat flux increases slightly and occurs one hour later compared with the reference case with no airgap. The heat loss at night for the reference wall is significantly lower than the cases with the airgap. This suggests the air gap affords an additional thermal resistive value. Hence, the diurnal variation of the heat flux for the reference case is more significant than the cases with the air gap. This yields a reduction in the heating load of 8.23%, 8.23%, 7.59%, and 6.33% for $\delta$ values of 13 *mm*, 19 *mm*, 25 *mm*, and 50 *mm* respectively.

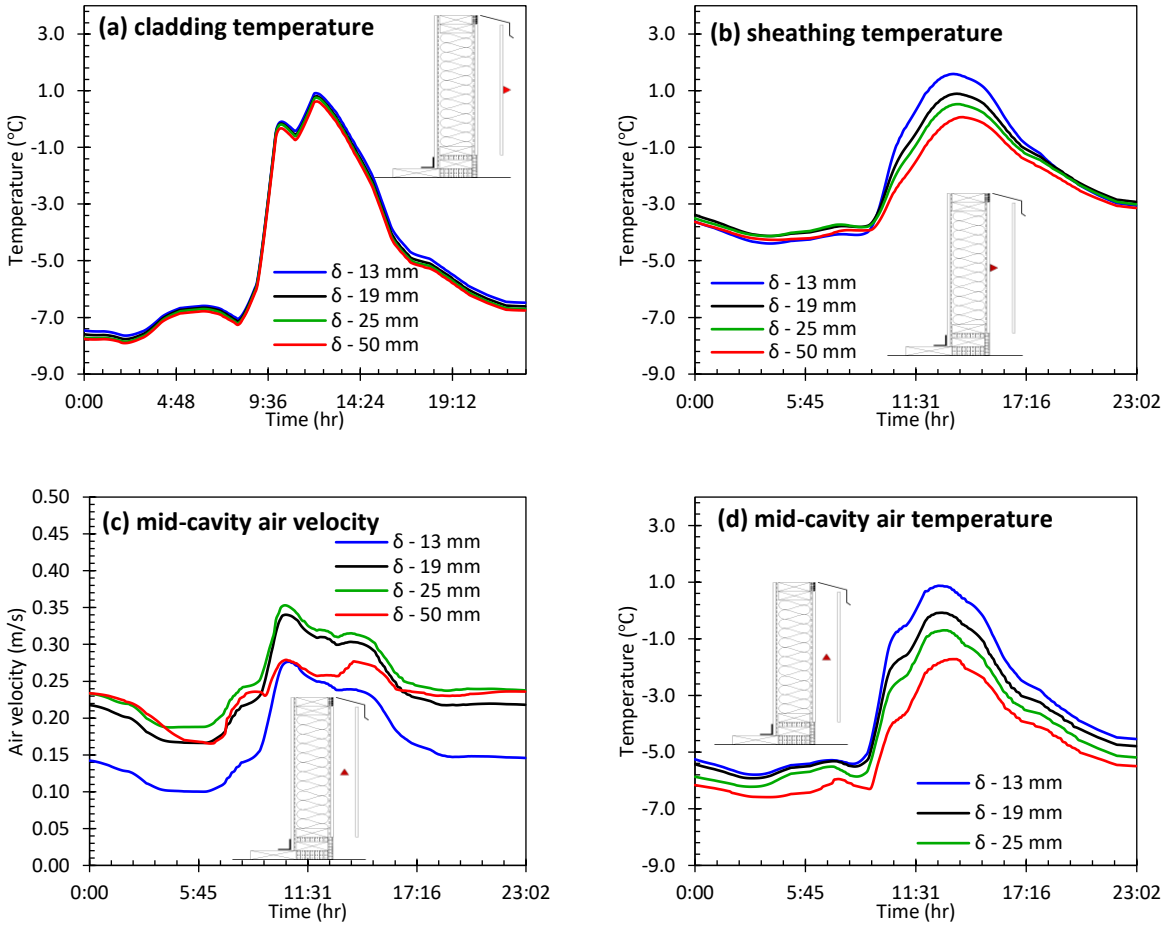

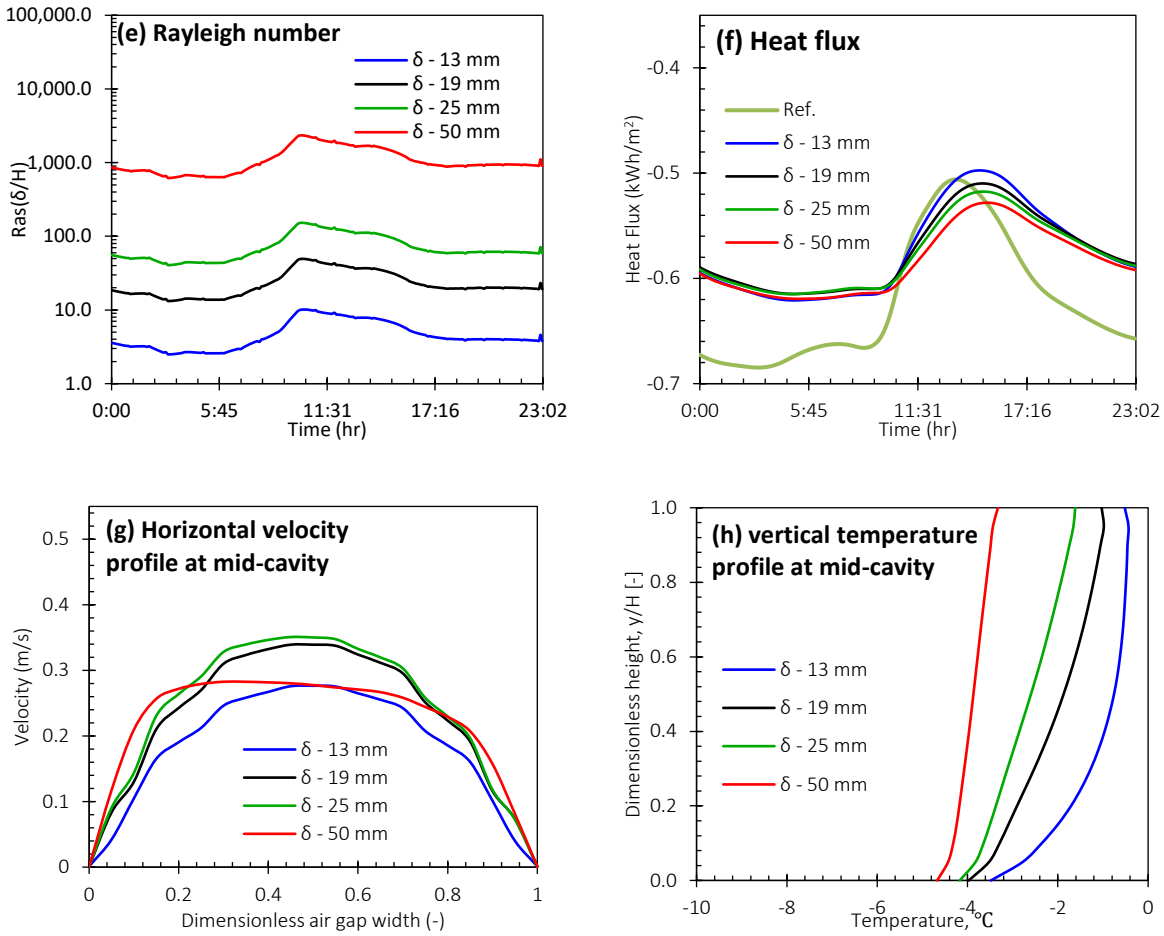


Figure 2-11: The effect of varying the air gap width on the (a) cladding temperature, (b) sheathing temperature, (c) mid-cavity air velocity, (d) mid-cavity air temperature, (e) Rayleigh number, (f) Heat flux, (g) Velocity profile across the cavity at peak conditions, and (h) Temperature along the height for the cold day case study

In the hot day case study, more elevated surface conditions are expected as evidenced by the cladding temperature in Figure 2-12a. The cladding temperature is lower than the outdoor air temperature at nighttime due to night sky radiation cooling. This induces back flow in the air cavity as shown by the slightly negative air velocity in Figure 2-12c. However, at peak solar radiation intensity, the induced air velocity is up to 0.51 *m/s*, 0.57 *m/s*, 0.56 *m/s* and 0.46 *m/s* for the gap widths of 13 *mm*, 19 *mm*, 25 *mm*, and 50 *mm* respectively. The decrease in the mid-cavity air velocity for $\delta$ > 25 *mm* is attributed the change in the flow structure from a boundary layer flow to an isolated plate flow. This is illustrated by the modified Rayleigh number in Figure 2-12e. The maximum modified Rayleigh number is 19, 89, 271 and 4120 for gap widths of 13 *mm*, 19 *mm*,

25 *mm*, and 50 *mm* respectively. Similar to the flow observation for the typical cold day, the enthalpy gain associated with airflow in the cavity reduces with increase in the air gap width as seen in Figure 2-12h.

In simple terms, the volumetric flow increases with increase in the air gap width. This reduces the strength of the buoyancy drive in the cavity for the same solar heat flux intensity. This is reflected in the deviation from the parabolic velocity profile for $\delta$ > 25 *mm* at peak conditions as seen in Figure 2-12g. In fact, by comparing the sheathing temperature (Figure 2-12b) and the mid-cavity temperature (Figure 2-12d), it is seen that the peak mid-cavity temperature is higher than the peak sheathing temperature for $\delta$ = 13 *mm* (*i.e., mostly fully developed flow regime*). The peak mid-cavity temperature and the peak sheathing temperature are similar for $\delta$ = 25 *mm (i.e., on-set of isolated plate flow)* and the sheathing temperature is higher than the mid-cavity temperature for $\delta$ = 50 *mm.* The relatively higher sheathing temperature for $\delta$ = 50 *mm* is sustained by the long-wave radiation exchange in the air cavity. The peak sheathing temperature is 47℃, 43℃, 41℃, and 39℃ for the air gap widths of 13 *mm*, 19 *mm*, 25 *mm*, and 50 *mm* respectively. This translates to a significant heat gain reduction for higher air gap widths as seen in Figure 2-12f. The wall heat fluxes for $\delta$ values of 13 *mm*, 19 *mm*, 25 *mm*, and 50 *mm* are reduced by 18.5%, 28.1%, 33.0% and 38.9% respectively compared to the reference wall.

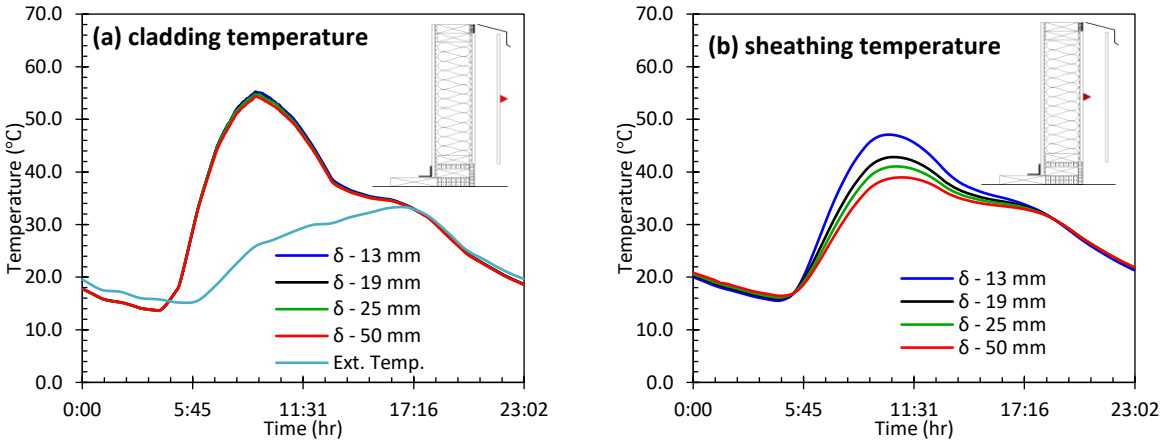

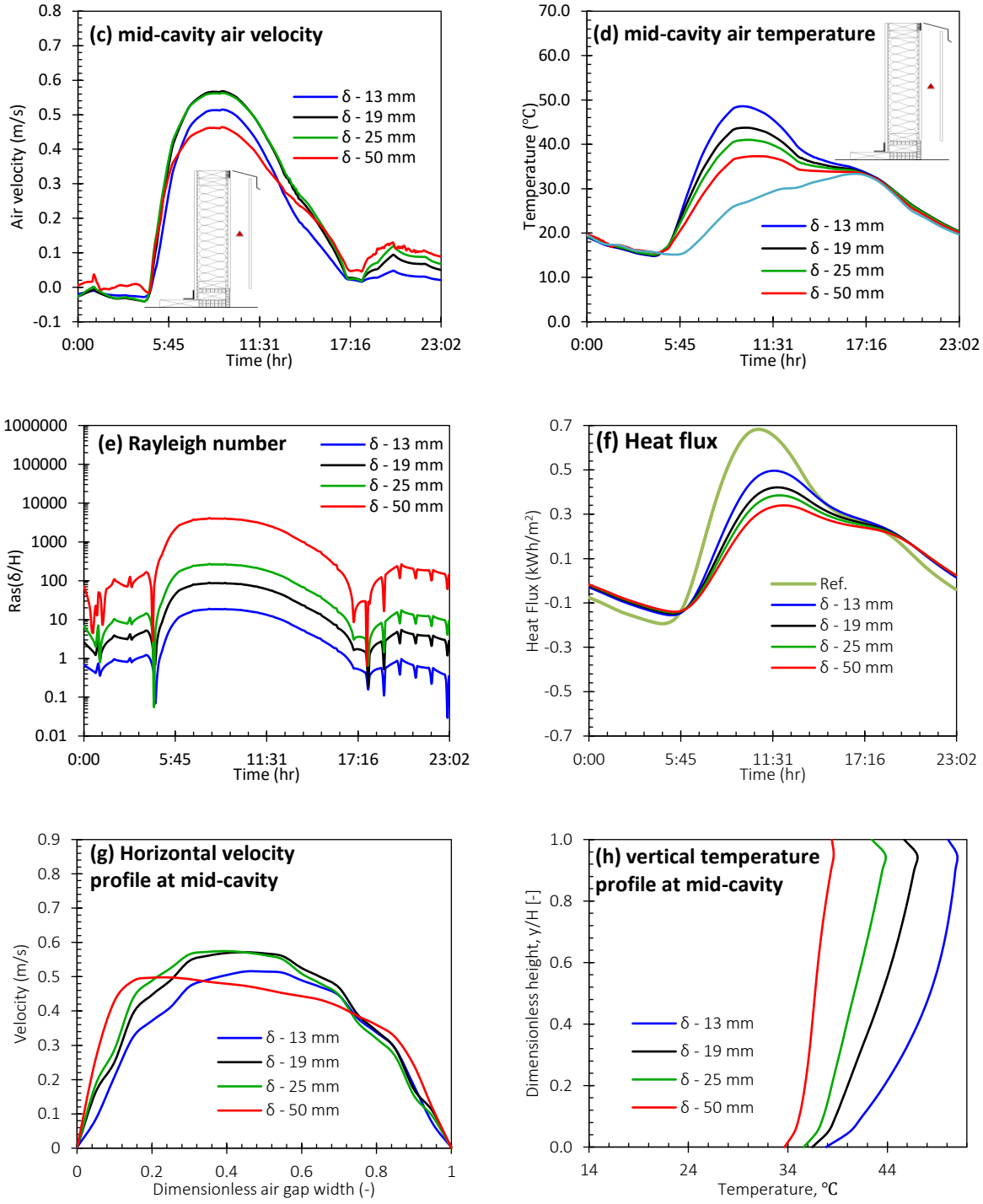


Figure 2-12: The effect of varying the air gap width on the (a) cladding temperature, (b) sheathing temperature, (c) mid-cavity air velocity, (d) mid-cavity air temperature, and (e) Rayleigh number, (f) Heat flux (g) Velocity profile across the cavity at peak conditions, and (h) Temperature variation with height for the hot day case study

It was shown that the flow changed from a fully developed flow to an isolated plate flow for $\delta$ = 25 *mm.* Further, the air gap is increased up to 381 *mm* (i.e., 15 *in*), to understand the optimal air gap configuration to minimize the building heating and cooling load. Figure 2-13 shows the impact of varying the air gap width on the heat gain and heat loss for the typical hot and cold day. It can be seen from Figure 2-13a, $\delta$ = 13 *mm (*i.e., 0.5 *in)* minimizes the winter heat loss. Also, *Figure 2-13b* shows that increasing the air gap width beyond 127 *mm (i.e.*, 5 *in*) has negligible additional heat gain reduction benefits.

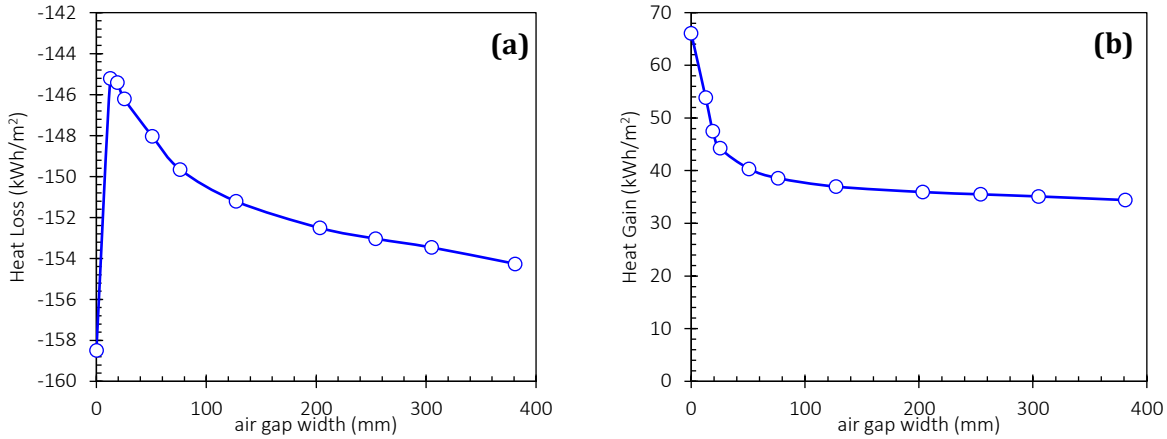


Figure 2-13: The impact of varying the air gap width on (a) winter heat loss, and (b) summer heat gain.

### 2.3.4 Impact of channel height

The channel height is doubled and its impact on the energy is assessed. For the single and double height channels, the air gap width is 13 *mm*, the sheathing emissivity is 0.2, and the cladding is fiber cement. Figure 2-14a shows the impact of doubling the height of the wall assembly on the heat transfer and flow dynamics in the ventilated cavity for the cold day case study. The sensor probe locations have been scaled accordingly with the height ratio factor for the double height wall.

## A. TYPICAL COLD DAY

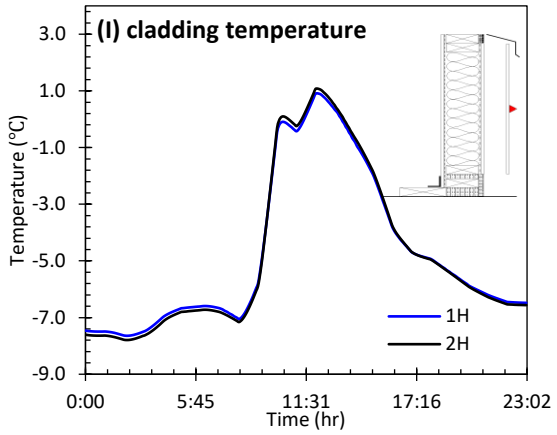


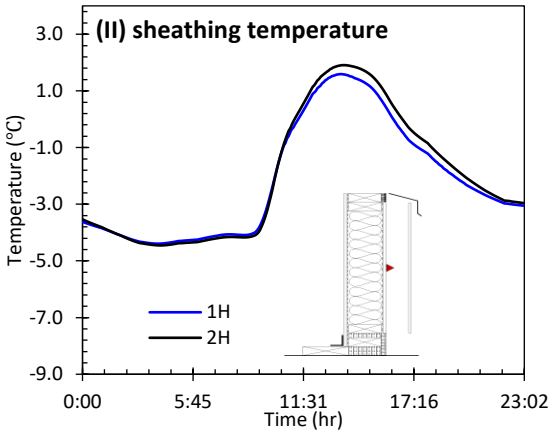


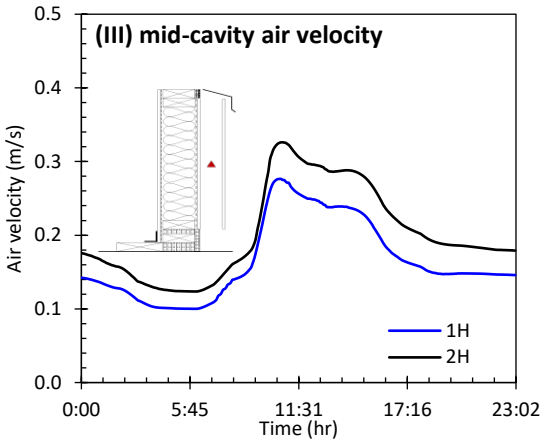


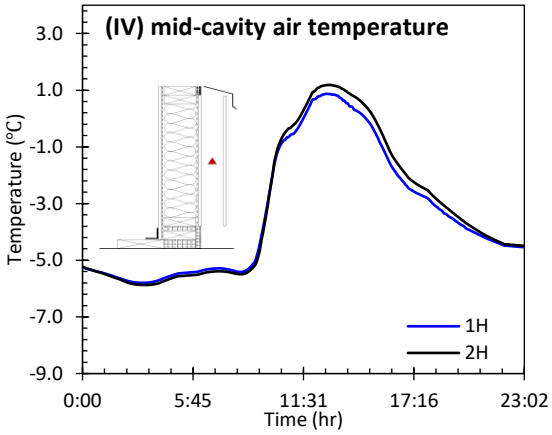


## B. TYPICAL HOT DAY

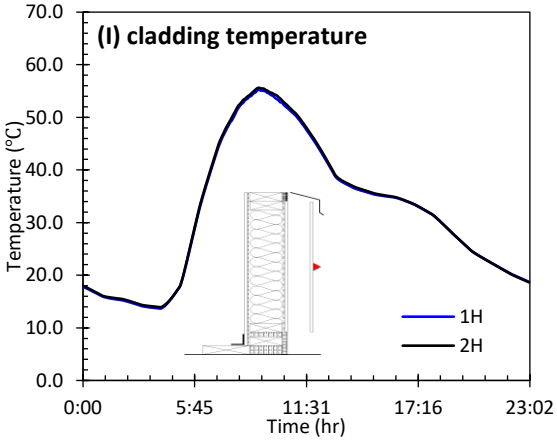


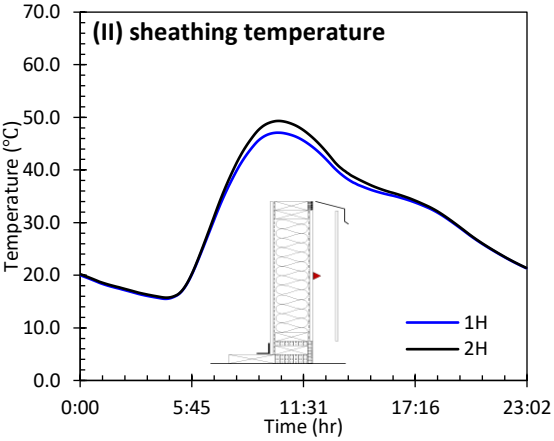

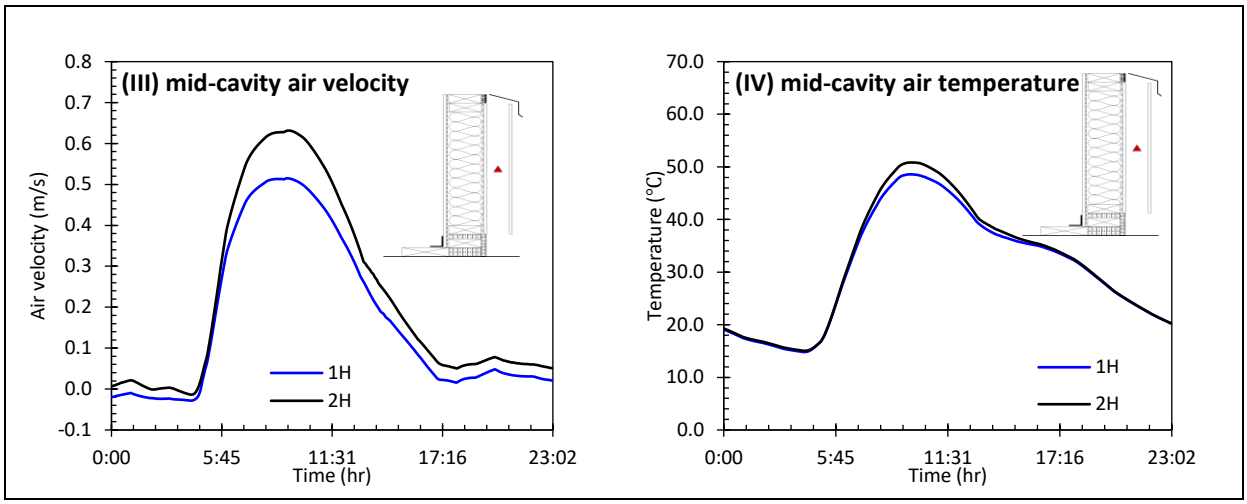


Figure 2-14: The effect of varying the channel height on the (I) cladding temperature, (II) sheathing temperature, (III) mid-cavity air velocity, and (IV) mid-cavity air temperature

The cladding temperature (Figure 2-14a-i) is similar for the wall heights considered. However, as seen in Figure 2-14a-iii, the induced velocity is higher for the 2-storey wall than the 1-storey wall. The maximum velocity for the cold day case study is 0.28 *m/s* and 0.33 *m/s* for the 1-storey and 2-storey wall respectively. This is because the pressure difference in the air channel due to the normal stack effect is proportional to the height of the air channel. Although, the mid-cavity velocity is higher for the 2-storey wall height, the sheathing temperature and the mid-cavity air temperature for both channel heights are similar as seen in Figure 2-14a-ii and Figure 2-14a-iv respectively. The peak sheathing temperature for the 1-storey and 2-storey wall height is 1.59℃ and 1.91℃ respectively while the peak mid-cavity temperature is 0.87℃ and 1.19℃ respectively. The temperature difference is attributed to the continuous heating of the air along the height of the air channel such that at point of interest (i.e., sensor location), the 2-storey wall is slightly warmer than the 1-storey wall. The impact on the wall heat transfer is negligible as the wall heat flux is reduced from -145 $kWh/m^2$ (-8.23%) to -144 $kWh/m^2$ (-8.86%).

Similarly, the effect of doubling the height on the heat gain for the hot day case study can be seen in Figure 2-14b. As seen in Figure 2-14b-i, the cladding temperature for the 1-storey and 2-storey ventilated cavity are similar. The peak velocity is increased from 0.51 *m/s* for the 1-storey cavity to 0.63 *m/s* for the 2-storey cavity as seen in Figure 2-14b-iii. This is suggestive of non-linearity between the channel height and the temperature increase of the air in the channel. As such, the sheathing and mid-cavity temperature for the 2-storey ventilated cavity are not significantly higher

than the 1-storey cavity as seen in Figure 2-14b-ii and Figure 2-14b-iv respectively. The peak sheathing temperature for the 1-storey and 2-storey cavity is 47.1℃ and 49.3℃ respectively while the peak mid-cavity temperature is 48.6℃ and 50.8℃ respectively. This higher sheathing temperature translates to a 5.94% increase in the heat gain for the 2-storey wall from 53.9 $kWh/m^2$ (-18.5%) to 57.1 $kWh/m^2$ (-13.6%).

### 2.3.5 Impact of cladding material

The cladding materials considered are fibre cement board, brick, and metal. To maintain congruency amongst the cladding alternatives, the cladding and sheathing emissivity are 0.5 and 0.2 respectively, the air gap width is 25 *mm* and the channel height is 2440 *mm* for all instances. Figure 2-15a-i compares the cladding temperature for the cladding materials investigated under cold outdoor conditions. Initially, the brick cladding temperature is the warmest due to the sensible heat stored up from the previous day. Eventually, the stored heat diminishes, and the cladding surface temperatures are similar at 5:00am. Then the solar radiation intensity increases after 6:00am as seen from the increase in cladding temperature. There is attenuation of the peak cladding temperature for the brick cladding due to the higher thermal storage capacity. The peak cladding temperature is 0.76℃, -0.98℃, and 0.69℃ for the fiber cement, brick, and metal cladding respectively. The impact of the higher thermal mass of the brick cladding on the sheathing temperature can be seen in Figure 2-15a-ii. The peak sheathing temperature is attenuated and shifted 1.75 hours compared to the other cladding materials. The peak sheathing temperature is 0.53℃, -0.05℃, and 0.68℃ for the fiber cement, brick, and metal cladding respectively.

Also, notice that the nighttime temperature for the brick cladding is higher than the other sheathing materials which should contribute considerably to energy flows through the wall. As seen in Figure 2-15a-iv, the air temperature in ventilated cavity follows the same trend as the sheathing temperature. The air velocity is more stable in the wall assembly with brick cladding as seen in Figure 2-15a-iii and is attributed to the heat storage and release in the day and nighttime respectively. The energy flows are equal for the fiber cement and metal cladding (i.e., -146 $kWh/m^2$ ≡ -7.59%). However, the heat loss is reduced by 1.32% for the brick cladding (i.e., -144 $kWh/m^2$ ≡ -8.86%).

## A. TYPICAL COLD DAY

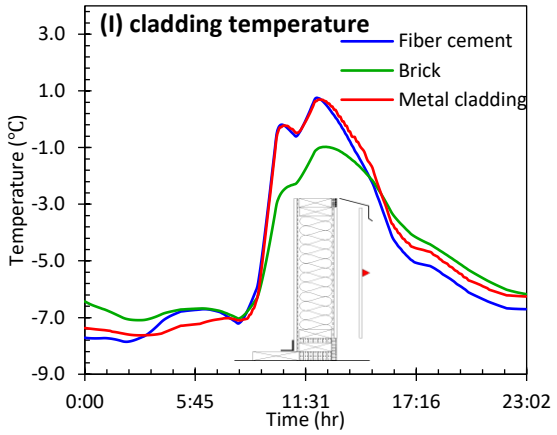


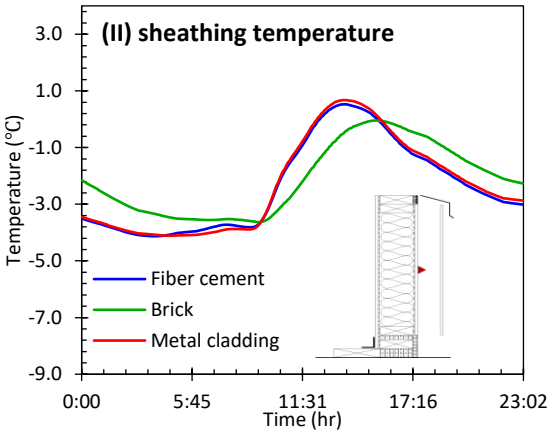


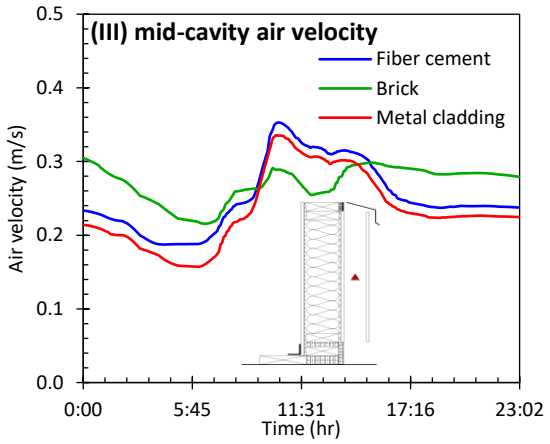


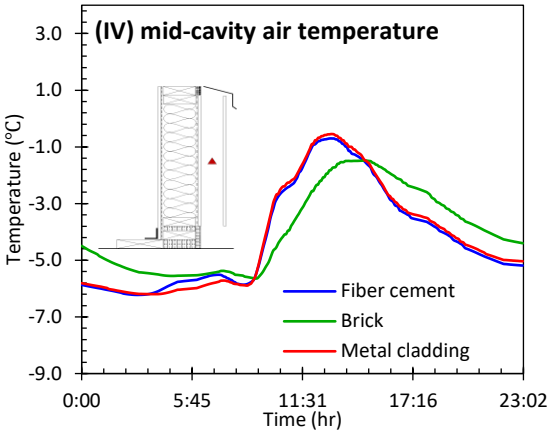


## B. TYPICAL HOT DAY

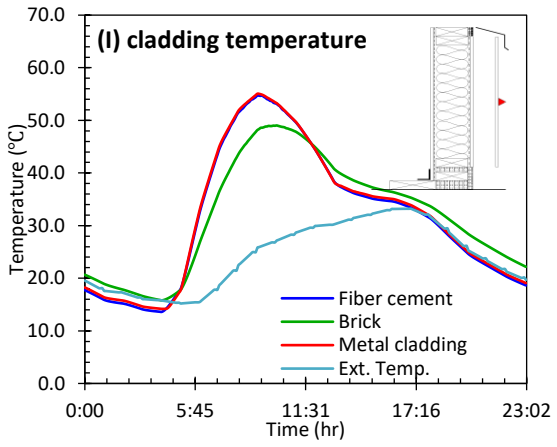


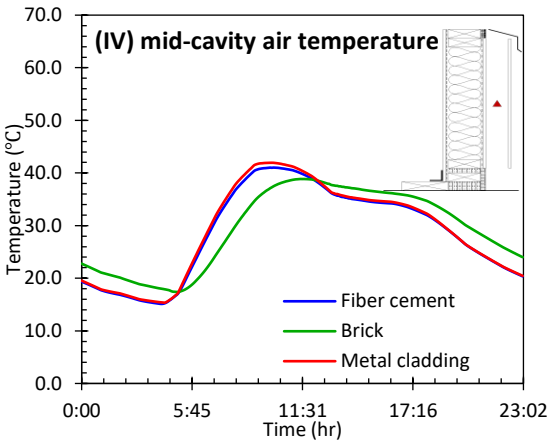

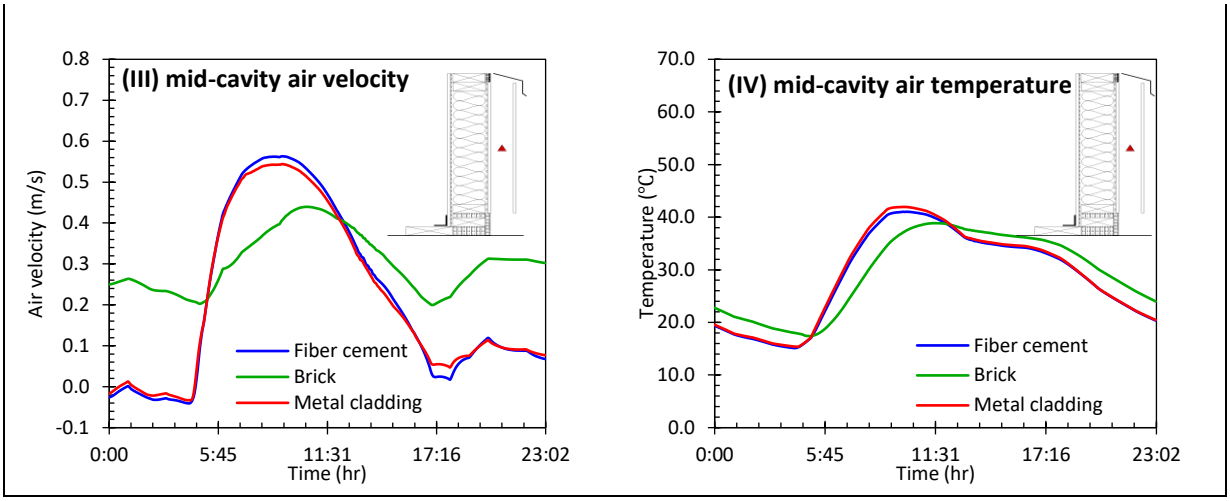


Figure 2-15: The effect of varying the cladding material on the (I) cladding surface temperature, (II) sheathing temperature, (III) mid-cavity air velocity, and (IV) mid-cavity air temperature

Figure 2-15b-i compares the cladding temperature for the cladding materials investigated under warmer outdoor conditions. The impact of the thermal mass on the cladding temperature can be seen and manifests as peak attenuation and trough increase with brick cladding. The peak cladding temperature is 55°C, 49°C, and 55°C for the fiber cement, brick, and metal cladding respectively. Similarly, as seen in Figure 2-15b-ii, the peak sheathing temperature is 41.0°C, 37.9°C, and 42.1°C for the fiber cement, brick, and metal cladding respectively. The minimum sheathing temperature for the hot day case study is 16.1°C, 18.3°C, and 16.3°C for fiber cement, brick, and metal cladding respectively. The mid-cavity air temperature also follows the same trend as the sheathing temperature (see Figure 2-15b-iv). Again, the air velocity for the full day simulation is more stable for the brick cladding as seen in Figure 2-15b-iii. The peak attenuation of the sheathing temperature with brick cladding results in a 4.29% heat gain reduction from 44.3 $kWh/m^2$ (-33.0%) for the fiber cement cladding to 42.4 $kWh/m^2$ (-35.9%). Similarly, the heat gain increases by 4.29% for the metal cladding to 46.2 $kWh/m^2$ (-30.1%).

## 2.4 CONCLUSION

The effect of the ventilated channel design parameters on the energy flows across the wall assembly of the typical rainscreen wall assembly was studied numerically using CFD. The CFD model was first validated with in-house experimental data to a reasonable degree of accuracy. Following, the influence of the air gap, sheathing membrane emissivity, ventilation channel height,

and cladding material on the wall heat flux are investigated. The heat transfer assessment is carried out for a typical hot and cold day, which are representative of summer and winter performance respectively.

The results show that the higher the emissivity of the sheathing membrane, the higher the heat gain during summer and heat loss during winter. As the air gap width is increased, the flow structure changes from a boundary layer flow to an isolated plate flow. The increased volume flow associated with the isolated plate flow ensures that the cavity air temperature is close to the outdoor air temperature. As such, the heat loss is enhanced slightly by up to 8.23% during winter and the heat gain is reduced by up to 38.9% during summer for the range of air gap widths investigated.

Increasing the channel height has negligible impact on the heat loss in winter, however, the heat gain for the hottest day is increased by 5.94% as the channel height is doubled. This is attributed to the continues heating of the air with height which potentially increases the sheathing temperature. Alternative cladding materials were investigated, namely: Fiber cement, brick, and metal cladding. The wall assembly with brick cladding showed the least heat loss for the cold day case study while the fibre cement and metal cladding showed similar heat loss. The thermal massing of the brick reduced the summer heat gain by 35.9% due to its better thermal regulation characteristics. The metal cladding recorded the highest heat gain of 4.29%.

## 2.5 REFERENCES


Alberto, A., Ramos, N. M., & Almeida, R. M. (2017). Parametric study of double-skin facades performance in mild climate countries. *Journal of Building Engineering*, *12*, 87-98.

Algarni, S., & Darin Nutter PhD, P. E. (2015). Survey of sky effective temperature models applicable to building envelope radiant heat transfer. ASHRAE Transactions, 121, 351.

Anđelković, A. S., Gvozdenac-Urošević, B., Kljajić, M., & Ignjatović, M. G. (2015). Experimental research of the thermal characteristics of a multi-storey naturally ventilated double skin facade. *Energy and Buildings*, *86*, 766-781.

Aparicio-Fernández, C., Vivancos, J. L., Ferrer-Gisbert, P., & Royo-Pastor, R. (2014). Energy performance of a ventilated façade by simulation with experimental validation. *Applied Thermal Engineering*, *66*(1-2), 563-570.

ASHRAE. (2017). 2017 ASHRAE Handbook: Fundamentals. ASHRAE.

ANSI/ASHRAE Standard 140-2001, Standard Method of Test for the Evaluation of Building Energy Analysis Computer Programs. (2001). Atlanta, GA: American Society of Heating, Refrigerating, and Air-Conditioning Engineers.

Baskaran, A. (1994). A numerical model to evaluate the performance of pressure equalized rainscreen walls. Building and Environment, 29(2), 159-171.

Chai, T., & Draxler, R. R. (2014). Root mean square error (RMSE) or mean absolute error (MAE)?–Arguments against avoiding RMSE in the literature. Geoscientific model development, 7(3), 1247-1250.

Chan, A. L. S., Chow, T. T., Fong, K. F., & Lin, Z. (2009). Investigation on energy performance of double skin facade in Hong Kong. *Energy and Buildings*, *41*(11), 1135-1142.

Eicker, U., Fux, V., Bauer, U., Mei, L., & Infield, D. (2008). Facades and summer performance of buildings. Energy and Buildings, 40(4), 600-611.

Falk, J., & Sandin, K. (2013). Ventilated rainscreen cladding: Measurements of cavity air velocities, estimation of air change rates and evaluation of driving forces. *Building and Environment*, *59*, 164-176.

Fallahi, A., Haghighat, F., & Elsadi, H. (2010). Energy performance assessment of double-skin façade with thermal mass. *Energy and Buildings*, *42*(9), 1499-1509.

Fuliotto, R., Cambuli, F., Mandas, N., Bacchin, N., Manara, G., & Chen, Q. (2010). Experimental and numerical analysis of heat transfer and airflow on an interactive building facade. *Energy and Buildings*, *42*(1), 23-28.

Gagliano, A., Nocera, F., & Aneli, S. (2016). Thermodynamic analysis of ventilated façades under different wind conditions in summer period. *Energy and Buildings*, *122*, 131-139.

Garden, G. K. (1963). Rain penetration and its control. In Canadian building digest 1-100 (pp. 4-4).

Ghadimi, M., Ghadamian, H., Hamidi, A. A., Shakouri, M., & Ghahremanian, S. (2013). Numerical analysis and parametric study of the thermal behavior in multiple-skin façades. *Energy and Buildings*, *67*, 44-55.

Giancola, E., Sanjuan, C., Blanco, E., & Heras, M. R. (2012). Experimental assessment and modelling of the performance of an open joint ventilated façade during actual operating conditions in Mediterranean climate. *Energy and Buildings*, *54*, 363-375.

Girma, G. M., & Tariku, F. (2021). Experimental investigation of cavity air gap depth for enhanced thermal performance of ventilated rain-screen walls. Building and Environment, 107710.

Gold, L. W., & Williams, G. P. (1976). Ground temperatures. Canadian Building Digest; no. CBD-180.

Hashemi, N., Fayaz, R., & Sarshar, M. (2010). Thermal behaviour of a ventilated double skin facade in hot arid climate. *Energy and Buildings*, *42*(10), 1823-1832.

Jiru, T. E., & Haghighat, F. (2008). Modeling ventilated double skin façade—A zonal approach. *Energy and Buildings*, *40*(8), 1567-1576.

Killip, I. R., & Cheetham, D. W. (1984). The prevention of rain penetration through external walls and joints by means of pressure equalization. Building and Environment, 19(2), 81-91.

Kuznik, F., Catalina, T., Gauzere, L., Woloszyn, M., & Roux, J. J. (2011). Numerical modelling of combined heat transfers in a double skin façade–full-scale laboratory experiment validation. *Applied thermal engineering*, *31*(14-15), 3043-3054.

Langmans, J., Desta, T. Z., Alderweireldt, L., & Roels, S. (2016). Field study on the air change rate behind residential rainscreen cladding systems: A parameter analysis. *Building and Environment*, *95*, 1-12.

Marques da Silva, F. M., Gomes, M. G., & Rodrigues, A. M. (2015). Measuring and estimating airflow in naturally ventilated double skin facades. *Building and Environment*, *87*, 292-301.

Mirsadeghi, M., Costola, D., Blocken, B., & Hensen, J. L. (2013). Review of external convective heat transfer coefficient models in building energy simulation programs: Implementation and uncertainty. Applied Thermal Engineering, 56(1-2), 134-151.

National Research Council. (2012). British Columbia Building Code 2012. Victoria, BC: The Province of British Columbia.

Pasut, W., & De Carli, M. (2012). Evaluation of various CFD modelling strategies in predicting airflow and temperature in a naturally ventilated double skin façade. Applied Thermal Engineering, 37, 267-274.

Patania, F., Gagliano, A., Nocera, F., Ferlito, A., & Galesi, A. (2010). Thermofluid-dynamic analysis of ventilated facades. *Energy and Buildings*, *42*(7), 1148-1155.

Saelens, D., Roels, S., & Hens, H. (2004). The inlet temperature as a boundary condition for multiple-skin facade modelling. *Energy and Buildings*, *36*(8), 825-835.

Sanchez, E., Rolando, A., Sant, R., & Ayuso, L. (2016). Influence of natural ventilation due to buoyancy and heat transfer in the energy efficiency of a double skin facade building. *Energy for Sustainable Development*, *33*, 139-148.

Seferis, P., Strachan, P., Dimoudi, A., & Androutsopoulos, A. (2011). Investigation of the performance of a ventilated wall. *Energy and Buildings*, *43*(9), 2167-2178.

Siemens, P. (2018). Simcenter STAR-CCM+ User Guide V13. 04. Siemens PLM.

Spalart, P.R. and Rumsey, C.L. 2007. "Effective Inflow Conditions for Turbulence Models in Aerodynamic Calculations", AIAA Journal, 45(10), pp. 2544-2553.

Suárez, C., Joubert, P., Molina, J. L., & Sánchez, F. J. (2011). Heat transfer and mass flow correlations for ventilated facades. *Energy and Buildings*, *43*(12), 3696-3703.

Tariku, F., & Iffa, E. (2019). Empirical model for cavity ventilation and hygrothermal performance assessment of wood frame wall systems: Experimental study. Building and Environment, 157, 112-126.

Wang, Y., Chen, Y., & Zhou, J. (2016). Dynamic modeling of the ventilated double skin façade in hot summer and cold winter zone in China. *Building and Environment*, *106*, 365-377.

# Chapter 3

# 3 BIPV with transverse rib roughened air channel - Parametric analysis of the effect of transverse roughness shape, roughness height (*e/D*), roughness spacing (*p/e*), and channel angle (*ϑ*) on the turbulent natural convection heat transfer

Building integrated Photovoltaic and Thermal (BIPV/T) Systems enhance the economical feasibility of solar panels. BIPV/Ts replace conventional building materials in certain parts of the building envelope (Agathokleous & Kalogirou, 2016). This multi-functionality of BIPV/Ts increases the cost effectiveness of integrating photovoltaics in buildings (Peng et al., 2011). However, overheating is a concern with BIPV since about 80% of the incident solar radiation is wasted as heat and manifests as an increase in the cell temperature. It is well known that the electrical conversion efficiency reduces with increase in cell temperature. In extreme cases (i.e., $T_c > 100$ ℃), the elevated temperature can lead to damage from thermal stressing.

BIPVs are typically installed on the building envelope with an air gap for thermal regulation. The air flow in the gap is driven actively or passively. In an active configuration, air flow in the channel is driven by fans. The advantage of the active system is its operational flexibility. It can be directly integrated with the heating, ventilation and air conditioning (HVAC) or the domestic hot water (DHW) system since the flow rates are predictable and mildly affected by the environmental conditions. Although, higher convective heat transfer coefficients can be achieved with forced air cooling, the passive thermal regulation is simple and cost effective (Yilmaz & Fraser, 2007). In the passive system, the air flow is driven by natural convection. The effectiveness of natural convection as an effective BIPV thermal regulation strategy has been demonstrated in literature. Up to 20℃ reduction in PV surface temperature was achieved which was accompanied by a significant increase in the electrical output (Brinkworth et al., 1997). An increase in the annual electrical generation of up to 4% was attributed to the natural ventilation of the PV façade (Shahrestani et al., 2017). Han et al. (2019) found that the maximum PV surface temperature decreased by 8℃ due to free convection. Further, it was shown that mounting the BIPV with a narrow channel can reduce the operating temperature of the photovoltaic panel by up to 10℃ (Hamed et al., 2019; Tonui & Tripanagnostopoulos, 2008).

The effectiveness of natural convection cooling of BIPV is limited by the lower heat transfer coefficients associated with the low flow rates in the air channel. The heat transfer effectiveness can be enhanced by appending roughness elements on one or both surfaces of the vertical channel (Abidi-Saad et al., 2017). The roughness could induce disturbances in the laminar boundary layer thus causing premature transition to turbulence. Also, the roughness elements, if heated, add an extra heat transfer surface area (Sarper et al., 2018). The induced turbulent mixing can increase the heat transfer coefficient considerably (Brinkworth & Sandberg, 2006; Sinha & Dash 2014). This manifests as lower surface temperatures in the ribbed wall duct compared with the smooth channel (Brinkworth & Sandberg, 2006). However, the presence of numerous large ribs can reduce the flow. As such, some authors have reported lower heat transfer coefficients for the ribbed duct compared with the smooth duct (Desrayaud & Fichera, 2002; Cavazzuti & Corticelli, 2008; Ambrosini et al., 2005). In fact, up to 44% reduction in the heat transfer coefficient is possible (Tanda, 1997).

From the review of literature, there is limited research on the impact of ribs on the natural convection heat transfer coefficient in channels (Abidi-Saad et al., 2017). The available research has been focused on laminar natural convection and suggests a deficiency of theoretical work on the turbulent natural convection in vertical parallel-plate channel (Sanvicente et al., 2013; Federov & Viskanta, 1997). Also, most research investigated only the square shaped ribs with fixed geometry (Desrayaud & Fichera, 2002). Hence, further developments on the influence of parametric changes in the obstacle geometry are required. The aim of this study is to numerically investigate the impacts of the ribs design on the turbulent natural convection heat transfer coefficient in BIPV channels with emphasis on the effect of rib shape, blockage ratio, rib spacing and channel inclination angle.

## 3.1 METHODOLOGY

The numerical study is conducted using computational fluid dynamics (CFD) and validated using experimental data from literature. The experimental study investigated natural convection airflows in an asymmetric heated vertical parallel channel, which is the typical heating configuration for a BIPV/T air channel (Yilmaz & Fraser, 2007). The brief description of the experimental data is given in *Section 3.3.1*. To validate the numerical model, the temperature, velocity, and kinetic

energy profiles at different height locations in the open-air channel are compared with the experimental data.

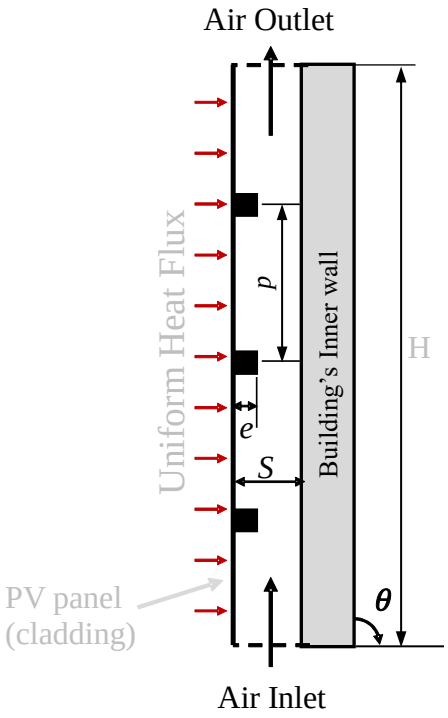


Figure 3-1: Illustration of the BIPV air channel roughened with transverse square ribs

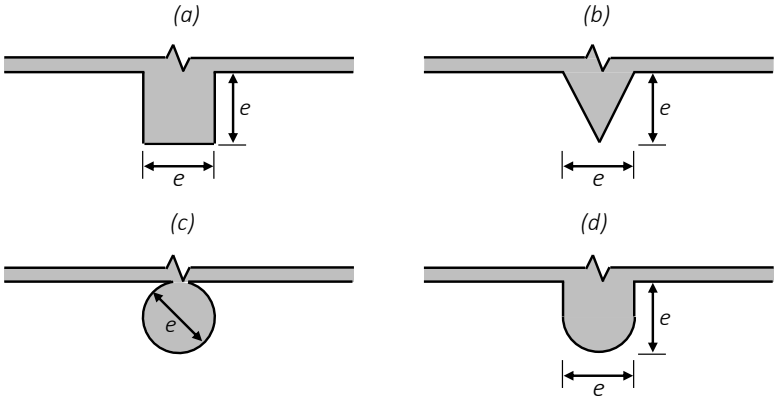


Figure 3-2: The roughness geometries considered in the study: (a) square (b) triangle (c) circle and (d) semi-circle

Following the CFD validation, a parametric analysis is conducted to understand the impact of various geometric and flow parameters on the convective heat transfer on the heated wall. The variables considered in this paper are rib shape, blockage ratio, rib spacing, channel inclination angle, and Rayleigh number (See Figure 3-1 and Figure 3-2). The simulation matrix for the variables considered is summarized in Table 3-1.

Table 3-1: Variables examined in the numerical study

| Parameter | Iterations |
|---|---|
| Heat Flux, W/m$^2$ | 100, 400, 700, 1000 |
| Rib shape | Square, semi-circle and triangle |
| Blockage ratio (*e/D*) | 0.01, 0.03, 0.05, 0.08, 0.11, 0.20, and 0.30 |
| Relative rib pitch (*p/e*) | 5, 7.5, 10, 15, 20, 30, and 50 |
| Channel inclination angle ($\vartheta$) | 0, 45, 60, and 75 degrees |

## 3.2 Governing Equations

The governing equations for the two-dimensional conjugate heat transfer natural convection problem adopted in this work are given in Equation 3-1, Equation 3-2, Equation 3-3, and Equation 3-4.

Continuity equation:

$$\frac{\partial(\overline{\rho}\overline{u})}{\partial x}+\frac{\partial(\overline{\rho}\overline{v})}{\partial y}=0 \qquad \text{Equation 3-1}$$

x-component of momentum equation:

$$\frac{\partial(\overline{\rho}\overline{u}\overline{u})}{\partial x}+\frac{\partial(\overline{\rho}\overline{u}\overline{v})}{\partial y}=-\frac{\partial P}{\partial x}+\frac{\partial}{\partial x}\left[\mu\frac{\partial\overline{u}}{\partial x}\right]+\frac{\partial}{\partial y}\left[\mu\frac{\partial\overline{u}}{\partial y}\right] \qquad \text{Equation 3-2}$$

y-component of momentum equation:

$$\frac{\partial(\overline{\rho}\overline{v}\overline{u})}{\partial x}+\frac{\partial(\overline{\rho}\overline{v}\overline{v})}{\partial y}=-\frac{\partial P}{\partial y}+\frac{\partial}{\partial x}\left[\mu\frac{\partial\overline{v}}{\partial x}\right]+\frac{\partial}{\partial y}\left[\mu\frac{\partial\overline{v}}{\partial y}\right]+(\overline{\rho}-\rho_\infty)g \qquad \text{Equation 3-3}$$

Energy equation:

$$\frac{\partial(\bar{\rho}\bar{u}\bar{T})}{\partial x}+\frac{\partial(\bar{\rho}\bar{v}\bar{T})}{\partial y}=+\frac{\partial}{\partial x}\left[\Gamma\frac{\partial\bar{T}}{\partial x}\right]+\frac{\partial}{\partial y}\left[\Gamma\frac{\partial\bar{T}}{\partial y}\right]+S_h \qquad \text{Equation 3-4}$$

An important feature of a buoyant flow in a rectangular cavity is the concurrent occurrence of laminar, transitional, and turbulent regimes along the vertical walls (Lau et al., 2013). Hence, Equation 3-1 to Equation 3-4 are solved directly for the laminar region. However, Γ and μ are substituted with $\Gamma_{eff}$ (i.e., $\Gamma + \Gamma_t$) and $\mu_{eff}$ (i.e., $\mu + \mu_t$) respectively in the turbulent region. In Equation 3-4, the source term (i.e., $S_h$) is derived from the radiative transfer equation (RTE). Radiation is modeled using the Discrete Ordinate Method (DOM). Turbulence is modeled using the standard low reynolds number k-epsilon turbulence model as it is suitable for the natural convection flows (Siemens, 2018). The transport equations for the turbulent kinetic energy, $k$, and the turbulent dissipation rate, $\varepsilon$ are given in Equation 3-5 and Equation 3-6 respectively.

$$\begin{aligned}(\bar{\rho}\bar{u})\frac{\partial k}{\partial x}+(\bar{\rho}\bar{v})\frac{\partial k}{\partial y}&\\ =\frac{\partial}{\partial x}\left[\left(\mu+\frac{\mu_t}{\sigma_t}\right)\frac{\partial k}{\partial x}\right]+\frac{\partial}{\partial y}\left[\left(\mu+\frac{\mu_t}{\sigma_t}\right)\frac{\partial k}{\partial y}\right]&\\ +\left(P_k-\rho(\varepsilon-\varepsilon_0)\right)&\end{aligned} \qquad \text{Equation 3-5}$$

$$\begin{aligned}(\bar{\rho}\bar{u})\frac{\partial \varepsilon}{\partial x}+(\bar{\rho}\bar{v})\frac{\partial \varepsilon}{\partial y}=\frac{\partial}{\partial x}\left[\left(\mu+\frac{\mu_t}{\sigma_t}\right)\frac{\partial \varepsilon}{\partial x}\right]+\frac{\partial}{\partial y}\left[\left(\mu+\frac{\mu_t}{\sigma_t}\right)\frac{\partial \varepsilon}{\partial y}\right]&\\ +\frac{1}{T_e}C_{\varepsilon1}P_\varepsilon-\rho C_{\varepsilon2}f_2\left(\frac{\varepsilon}{T_e}-\frac{\varepsilon_o}{T_o}\right)&\end{aligned} \qquad \text{Equation 3-6}$$

In Equation 3-1 to Equation 3-6, $\rho$ is fluid density, $\bar{u}$ and $\bar{v}$ are $x$ and $y$ compponens of velocity respectively, $\mu$ is dynamic viscosity, $\mu_t$ is turbulent dynamic viscosity, $P_k$ and $P_\varepsilon$ are production terms, $f_2$ is damping function, $T_o$ is specific time scale, and $k_0$ and $\varepsilon_0$ are ambient turbulence values that offset turbulence decay. The model coefficients are: $C_\mu$ = 0.09, $\sigma_k$ = 1, $\sigma_\varepsilon$ = 1.3, $C_{\varepsilon2}$ = 1.92, $C_{\varepsilon2}$ = 1.44.

## 3.3 Validation of Numerical Model

The numerical model is validated in this section. The experimental data is first presented, then the numerical simulation setup is outlined.

### 3.3.1 Experiment Data

The experiment is situated in a laboratory (Yilmaz & Fraser, 2007) and is designed to study natural convection air flows in an asymmetric heated vertical parallel channel. The flow channel is 3 *m* high and 1 *m* wide with an aspect ratio of depth to height (*S/H*) of 0.0333. The flow channel is formed by a heated front wall, a glass back wall and Perspex side walls. The heated wall consists of the 6.35 *mm* aluminum plate, serpentine graphite electric resistance heaters, 25 *mm* fiber insulation material and 19 *mm* plywood backing. The aluminum plate is highly polished to limit radiative heat transfer in the flow channel. The aluminum plate is fitted with thermocouples to monitor the surface temperature. The thermocouples are installed at the centerline of the plate at 0.30 *m* intervals such that the dimensionless height (i.e., *y/H*) is 0.03, 0.27, 0.50, 0.80, and 0.98. Velocity measurements in the flow channel are by means of a Laser-doppler anemometry (LDA) system. The velocity readings are taken across the air channel at the same height as the temperature readings.

### 3.3.2 Numerical Simulation Setup

#### 3.3.2.1 Computational Domain

The two-dimensional computational domain is shown in Figure 3-3. A two-dimensional approach is taken since varying the aspect ratio had negligible impacts on the convective heat transfer coefficient (Desrayaud & Fichera, 2002). The BIPV panel is represented by a 5 *mm* thin aluminum material. The air channel is modelled as a rectangular cross-section that consists of the entrance section (0.5 *m*), ribbed section (2.0 *m*) and exit section (0.5 *m*). The thermophysical properties of air and aluminum are given in Table 3-2. The entrance section ensures a relaminarized flow before the ribbed section. Similarly, the exit section ensured negligible effects of the top opening. In the ribbed section, transverse ribs are attached to the hot wall (i.e., the right surface) and are of the same material as the BIPV (i.e., Aluminum). The contact resistances between the transverse ribs and the BIPV are not considered. The square ribs have been shown for illustrative purposes,

however, the channel with triangular rib and the semi-circular rib have similar geometry. In all rib shape instances, the blockage ratios (i.e., *e/D*) are equal. The channel depth is 0.1 m to ensure adequate airflow on naturally ventilated systems and ensure low PV temperatures to avoid efficiency decrease (Agathokleous & Kalogirou, 2018; Fossa et al., 2008).

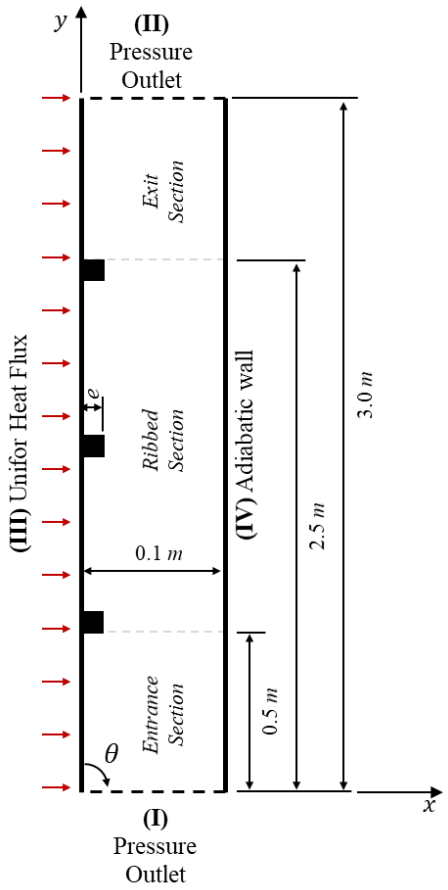


Figure 3-3: The 2D computational domain and boundary conditions

The ribs in the channel are sized such that the blockage ratio (i.e., *e/D*) varies from 0.01 – 0.30, the relative pitch ratio (i.e., *p/e*) varies from 5 – 50, and the inclination angle of the channel varies from 0 – 90 degrees. Refer to Table 3-1 for the discrete values within the range of parameters investigated. A uniform heat flux is considered on the PV surface, which is representative of the net heat gain on the BIPV surface.

Table 3-2: Material properties of the components of the wall assembly[a]

| Material | Density $[kg/m^3]$ | Thermal Conductivity $[W/mK]$ | Specific Heat $[J/kg/K]$ |
|---|---|---|---|
| Aluminum | 2702 | 237 | 903 |
| Air[b] | - | - | - |

[a]material properties adopted from ASHRAE Handbook of fundamentals, 2017
[d]temerature dependent air properties

### 3.3.2.2 Mesh Generation

The computational domain is discretized with a polygonal and prism layer mesh. The typical mesh size is 4.0 *mm* (i.e., $\frac{1}{25}S$); however, the mesh is refined around the rib elements in the ribbed section to effectively capture the recirculation flow. The mesh is 0.4 *mm* (i.e., $\left(\frac{1}{10}\right)\frac{1}{25}S$) around the rib elements. Five prism layer meshes with a total thickness of 0.4 *mm* and geometric stretching factor of 1.5 are employed to capture the near wall viscous dominated flow. The smooth transition from the finer cells around the roughness elements to the relatively coarse grid cells in the entrance and exit sections is ensured by specifying a surface growth ratio of 1.3. The typical meshing is shown in Figure 3-4.

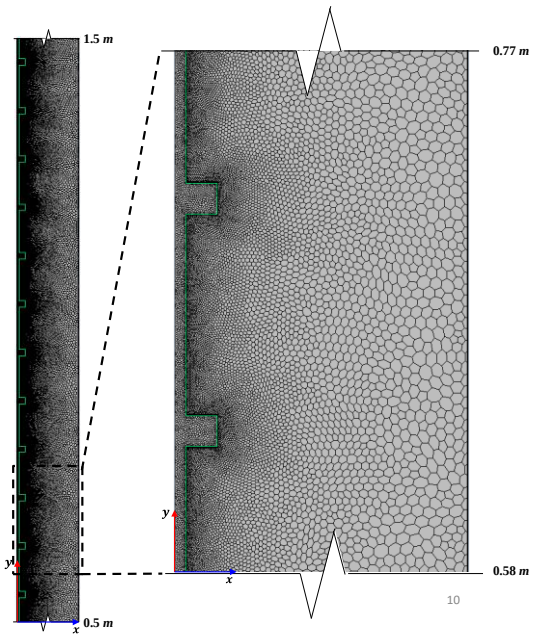


Figure 3-4: Mesh of the computational domain for *e/D* = 0.11 and *p/e* = 7.5 – Normal mesh

Grid sensitivity study is conducted with two additional meshing architypes. A Coarse mesh and Fine mesh with the typical mesh size of $\frac{1}{5}S$ and $\frac{1}{50}S$ respectively. For consistency, the other mesh parameters are scaled with respect to the typical mesh size. The grid sensitivity study is conducted for a typical solution domain with $e/D$ – 0.11, $p/e$ – 7.5, $\theta$ – 0 degrees, and $q$" – 400 $W/m^2$. The rate of change of the average Nusselt number with further mesh refinement is monitored to assess mesh independency. Table 3-3 shows that refinement of the mesh beyond the normal mesh has negligible impact on the Nusselt number. Hence, the normal mesh is enough to capture the flow characteristics.

Table 3-3: Summary of mesh independency study

| No. | Mesh | Typical Grid size* | *Nu* | % Increase in *Nu* |
|---|---|---|---|---|
| 1 | Coarse | 0.20*S* | 19.225 | - |
| 2 | Normal | 0.04*S* | 18.330 | -4.7% |
| 3 | Fine | 0.02*S* | 18.256 | -0.38% |

*Where *S* is the channel depth

### 3.3.2.3 Boundary Conditions and Solution Strategy

The boundaries of the computational domain (Figure 3-3) are identified with roman numerals I – IV. The specifications for the boundaries of the computational domain are given in Table 3-4.

Table 3-4: Specification of boundary conditions for the computational domain

| No. | Boundary Condition | Coordinates | Description |
|---|---|---|---|
| I | Pressure Outlet | *x: 0 ≤ x ≤ S*<br>*y: 0* | Boundary specified at ambient air temperature (23°C) and atmospheric pressure. The turbulent Intensity is initialized to 15% as per Tkachenko et al. (2016). |
| II | Pressure Outlet | *x: 0 ≤ x ≤ S*<br>*y: H* | Boundary specified at ambient air temperature and atmospheric pressure. The turbulent kinetic energy and turbulent specific dissipation rate are initialized to 0 *J/kg* and 0 $m^2/s^3$ respectively. |
| III | Uniform Heat Flux | *x: 0*<br>*y: 0 ≤ y ≤ H* | $\frac{\partial T}{\partial y} = q''$; where *q*" varies from 100 $W/m^2$ – 1000 $W/m^2$. No slip boundary condition. |
| IV | Adiabatic wall | *x: S*<br>*y: 0 ≤ y ≤ H* | No lateral heat transfer. No slip boundary condition. |

The 2D natural convection problem is solved in Simcenter STAR-CCM+ that uses the finite volume method. The solution is converged for all residuals less than $10^{-6}$.

### 3.3.2.4 Performance Indicators

The average Nusselt number gives an indication of the convective heat transfer effectiveness (Equation 3-7)

$$\boldsymbol{Nu = f(Ra_s^*) = \frac{h\,D}{k}} \qquad \text{Equation 3-7}$$

where, $D$ is the channel depth, $k$ is the thermal conductivity of air, $h$ is the average convective heat transfer coefficient, and $Ra_s^*$ is the modified Rayleigh number defined in Equation 3-8.

$$\boldsymbol{Ra_s^* = \frac{g\beta q'' S^4}{k\alpha v}} \qquad \text{Equation 3-8}$$

The fluid properties in Equation 3-7 and Equation 3-8 are evaluated at the film temperature $(T_{surf} + T_{ref})/2$). The heat transfer enhancement or Nusselt number ratio attributed to the presence of the rib in the air channel is given in Equation 3-9.

$$\boldsymbol{Nu_{enh}} = {\boldsymbol{Nu_r}}/{\boldsymbol{Nu_s}} \qquad \text{Equation 3-9}$$

In Equation 3-9, $Nu_r$ and $Nu_s$ are the Nusselt number and friction factor for the roughened channel and the smooth channel respectively. The heat transfer augmentation is more significant than the system pressure loss for $Nu_{enh}$ > 1 and vice versa.

### 3.3.3 Validation Results

The validation results are presented in this section. The temperature and velocity at different locations are compared with the experimental data. The accuracy of the numerical model is assessed by comparing the *NRMSD* (Equation 3-10).

$$\boldsymbol{NRMSD} = \frac{\sqrt{\frac{\boldsymbol{1}}{\boldsymbol{n}}\sum_{\boldsymbol{i=1}}^{\boldsymbol{n}}\left(\boldsymbol{y_{sim}} - \boldsymbol{y_{exp}}\right)^{\boldsymbol{2}}}}{\boldsymbol{y_{exp,max}} - \boldsymbol{y_{exp,min}}} \qquad \text{Equation 3-10}$$

where, $y_{exp}$ and $y_{sim}$ are the experimental data and numerical predictions respectively, *n* is the number of data points. $y_{exp,max}$ and $y_{exp,min}$ are the maximum and minimum data points attained in the experiment.

#### 3.3.3.1 Temperature Comparison

Figure 3-5 compares the temperature across the channel at different heights (i.e., *y/H* - 0.03, 0.27, 0.50, 0.80, and 0.98) for the numerical simulation and experimental data.

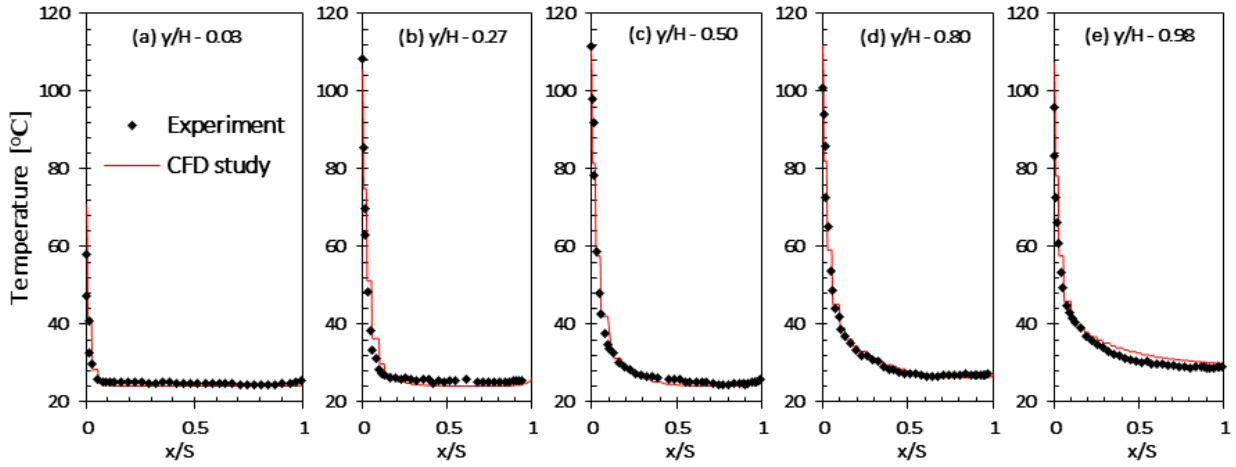


Figure 3-5: Comparison of the CFD prediction of the temperature across the air channel with experiment

In Figure 3-5, $x/S$ = 0 is the hot wall and $x/S$ = 1 is the cold wall. The temperature on the cold wall is close to the ambient temperature (23.0℃) which may be due to the negligible radiation heat exchange in the air channel or the much larger width of the cavity. However, the increase in the wall temperature with height is evident in the cold wall (i.e., $x/S$ = 1) and hot wall (i.e., $x/S$ = 0). The temperature at $x/S$ =1 for $y/H$ values of 0.03, 0.27, 0.50, 0.80, and 0.98 are 24.4℃, 25.8℃, 26.8℃, 27.1℃, and 30.0℃ respectively. The temperature at $x/S$ =0 (i.e., the hot wall) for $y/H$ values of 0.03, 0.27, 0.50, 0.80, and 0.98 is 71.0℃, 105.6℃, 112.0℃, 112.0℃, and 107.4℃ respectively. The hot wall temperature profile (i.e., $x/S$ = 0) is explicitly shown in Figure 3-6. The temperature increases from near ambient at the inlet to up to 112℃ at the middle of the channel and decreases at the outlet of the channel. The temperature decrease at the channel outlet in the numerical simulation is not as pronounced as the experiment. The discrepancy is attributed to radiation effects that are not adequately captured in the numerical model (Brinkworth & Sandberg, 2006; Sanvicente et al., 2013). The *NRMSD* for predicting the temperature across the air channel for $y/H$ values of 0.03, 0.27, 0.50, 0.80, and 0.98 is 7.3%, 4.4%, 2.6%, 4.0%, and 5.1% respectively. The error is more pronounced at the channel inlet and may be attribute to geometrical entrance effects. The prediction improves along the height of the channel which may be due to the change of the flow characteristics from laminar to turbulent flow.

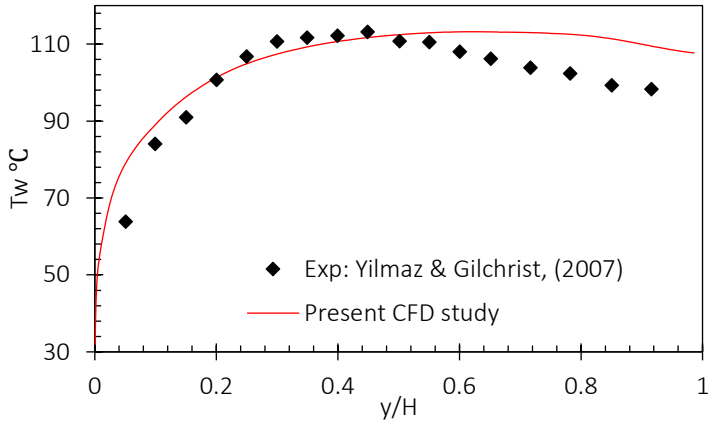


Figure 3-6: Variation of the surface temperature of the heated wall with height

### 3.3.3.2 Velocity Comparison

Figure 3-7 compares the velocity for the numerical simulation and experiment at different heights across the air channel. There is generally a good agreement between the numerical prediction and experimental data for the all the heights. At $y/H$ = 0.03 (i.e., the entrance), the velocity profiles show a good match for $x/S < 0.6$. for $x/S > 0.6$, the CFD model overpredicts the velocity in the air channel. This may be attributed to the entrance effects not captured in the CFD model. The error is more pronounced closer to the cold wall in that the strength of the buoyancy drive does not out-weigh the entrance effect (i.e., $x/S = 0$). The maximum velocity for the numerical prediction and experimental data of the peak velocity at $y/H$ = 0.03 is 0.52 *m/s* and 0.50 *m/s* respectively. In the mid-section of the air channel depicted by $y/H$ values of 0.27, 0.50 and 0.80, the velocity is higher close to the hot wall as expected because of the elevated surface temperature. This is the case in the experimental data and the numerical prediction. The maximum velocity from experiment at $y/H$ values of 0.27, 0.50 and 0.80 is 0.61 *m/s*, 0.73 *m/s* and 0.86 *m/s* respectively. The maximum velocity for numerical prediction at $y/H$ values of 0.27, 0.50 and 0.80 is 0.71 *m/s*, 0.89 *m/s* and 0.97 *m/s* respectively. The deviation between the experimental and numerical prediction may attributed to the occurrence of both laminar and turbulent flow air channel for the height considered and 3D effects that may not be captured in the CFD model. The maximum error occurs at $y/H$ = 0.50 and may be an indication of the transition flow which is difficult to predict. At the outlet (i.e., y/H = 0.98), the flow air velocity shows a better match with the experimental data. This may be because the flow is fully turbulent at that point. The peak velocity is 0.86 *m/s*, and 0.92 *m/s* for the

numerical and experimental data. The *NRMSD* for predicting the velocity for *y/H* values of 0.03, 0.27, 0.50, 0.80, and 0.98 is 13.5%, 9.8%, 10.2%, 7.3%, and 6.7% respectively.

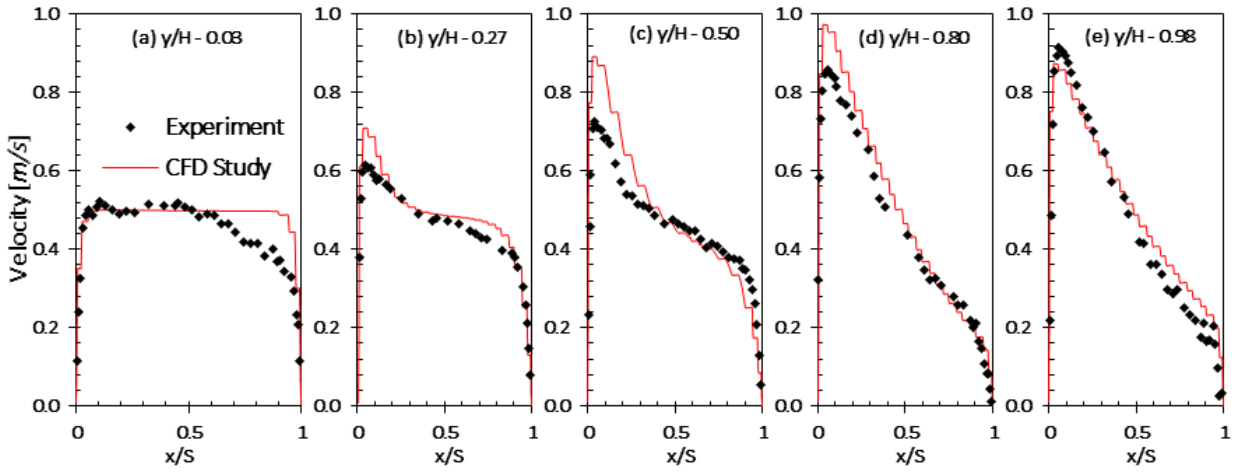


Figure 3-7: Comparison of the CFD prediction of velocity across the air channel with experiment

The errors in predicting the temperature and velocity along the height of the channel are consistent or better than literature. The numerical errors with reference to the experimental data are in the order of 15 - 20% (Wu & Lei, 2015; Yilmaz & Gilchrist, 2007). However, the numerical errors in the present CFD for the higher channel heights (i.e., Turbulent natural convection) are better predicted (i.e., lower than 10.2%). The numerical errors are acceptable and the CFD model can capture the heat transfer and flow characteristics in the BIPV channel.

## 3.4 PARAMETRIC ANALYSIS RESULTS AND DISCUSSION

The results from the parametric analysis are presented in this section. The effect of the roughness shape, roughness height (*e/D*), roughness spacing (*p/e*) and channel angle ($\theta$) is assessed. In each case the heat flux is varied from 100 $W/m^2$ to 1000 $W/m^2$. The parameters are assessed by comparing the average Nusselt number and the heat transfer enhancement.

### 3.4.1 Effect of shape

Figure 3-8*a* shows the effect of varying the transverse rib shape on the convective heat transfer coefficient in the air channel. The square rib, triangle rib and semi-circular rib are compared. To maintain congruency in results between the different rib profiles, the blockage ratio is similar for all the shape instances considered as well as the width of the roughness elements.

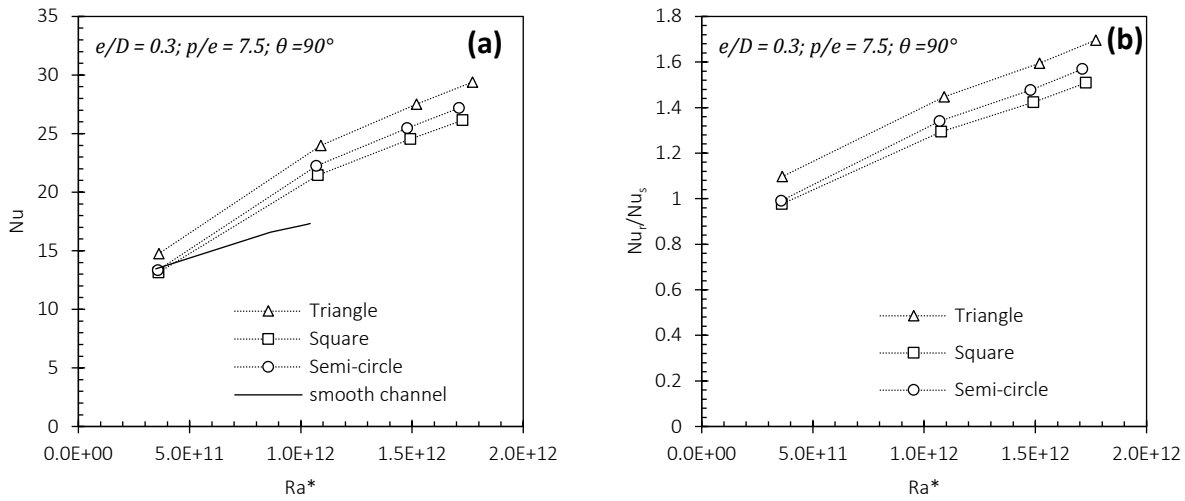


Figure 3-8: The effect of varying the rib cross-sectional profile on the (a) Nusselt number and (b) Nusselt number ratio

In Figure 3-8*a*, Nusselt number increases with increase in Rayleigh number for all simulated cases. Using the triangular rib as case study, the Nusselt number increases from 14.8 to 29.4 as the modified Rayleigh number, $Ra_s^*$ is increased from $3.62 \times 10^{11}$ to $1.77 \times 10^{12}$. This occurs because of the higher induced velocity at higher Rayleigh numbers. The heat transfer enhancement afforded by appending roughness elements in the air channel can be seen in Figure 3-8*a* for a vertical channel (i.e., $\theta = 90°$) with the roughness geometry of $e/D = 0.3$ and $p/e = 7.5$. For instance, the average Nusselt number at the modified Rayleigh number of $1.09 \times 10^{12}$ is 17.1, 20.6, 21.4 and 29.4 for the smooth channel, square rib roughened channel, semi-circle rib roughened channel and triangle rib roughened channel. The enhancement in heat transfer is attributed to the breaking of the boundary layer that develops on the wall of the smooth channel due to the presence of the roughness elements. The boundary layer acts as a thermal resistive layer that impedes heat transfer. The heat transfer enhancement is more pronounced in the channel with the triangular transverse rib. This is explained with the aid of the streamlines in Figure 3-9.

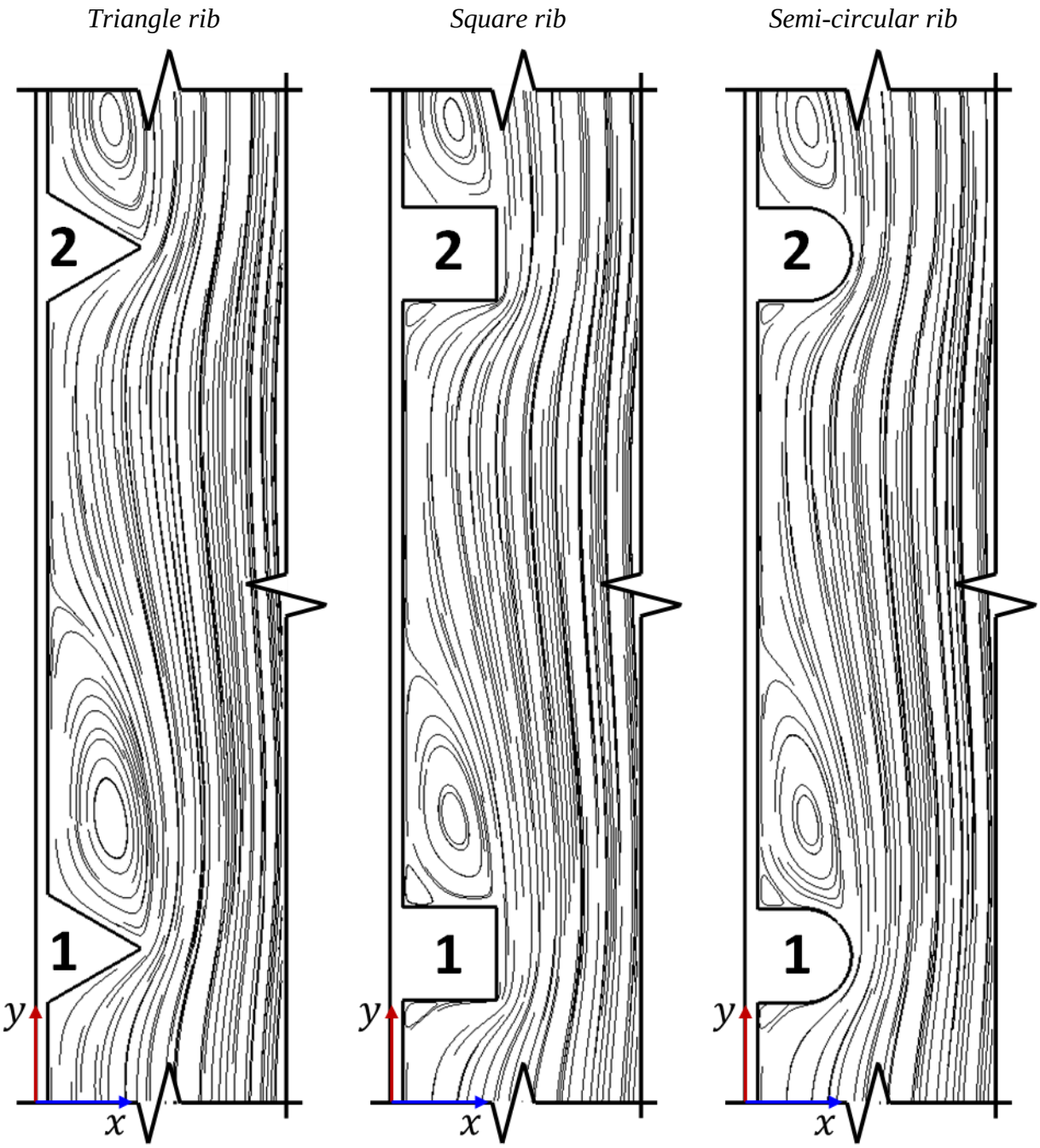


Figure 3-9: Streamlines for the different transverse rib roughness for *e/D* = 0.30 and *p/e* = 7.5 for flow in the +y direction

The roughness elements enhanced mixing in the air channel is evident by the distorted streamlines in Figure 3-9. The vortices formed in the immediate upstream and downstream of consecutive rib elements can be seen and is more pronounced in the square and semi-circular rib. The number of

vortices and the direction of rotation of each vortex can be inferred from the wall shear stress profile in Figure 3-10.

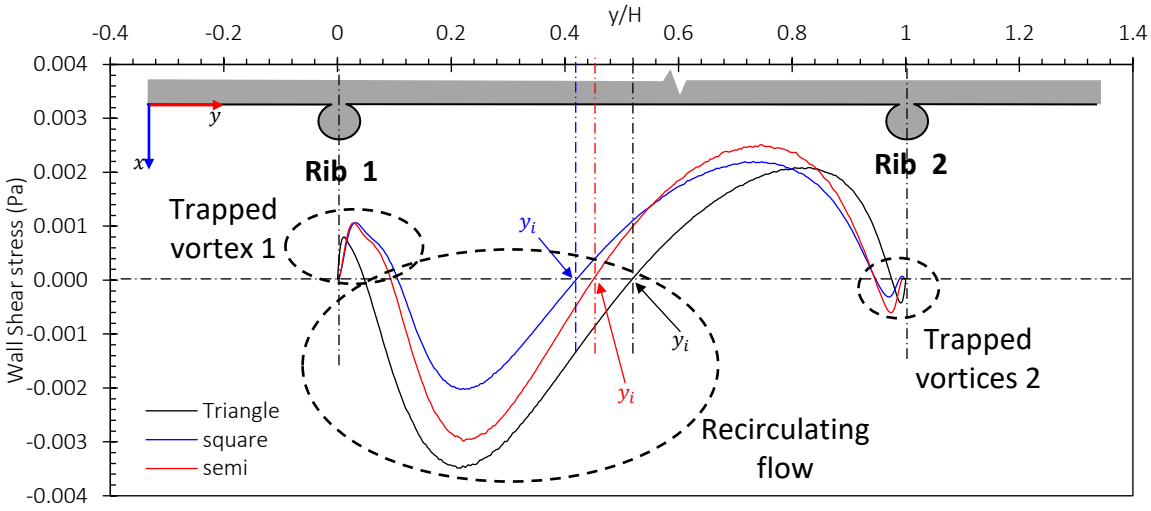


Figure 3-10: Comparison of the typical wall shear stress profiles for different transverse roughness shapes for *e/D* = 0.30 and *p/e* = 7.5

In Figure 3-10, the positive shear stress is associated with a clockwise rotating vortex or reattached flow and the negative shear stress is associated with recirculation or counterclockwise rotating vortex. it can be inferred from Figure 3-10 that there are four (4) vortices per rib element for the square and semi-circular rib, and three (3) vortices for the triangular rib. This is attributed to the obtuse angle in the triangular rib that allows for a more effective vortex shedding. The effect of the trapped vortex is a local increase in temperature or hot spots which are more pronounced in the immediate downstream of the rib elements. This hot spot problem can be seen in Figure 3-10. The local temperature increase is more pronounced in the square rib and as seen in Figure 3-10, the region labeled “trapped vortex 1” covers 10% of the pitch length. Conversely, the region labeled “trapped vortex 1” covers 5% of the pitch length for the triangular rib element, hence, the hot spot problem is not as evident compared with the other rib elements. Thus, the triangular roughness rib provides the most heat transfer enhancement. Up to 1.70 heat transfer enhancement is afforded with the triangular ribs as seen in Figure 3-8b.

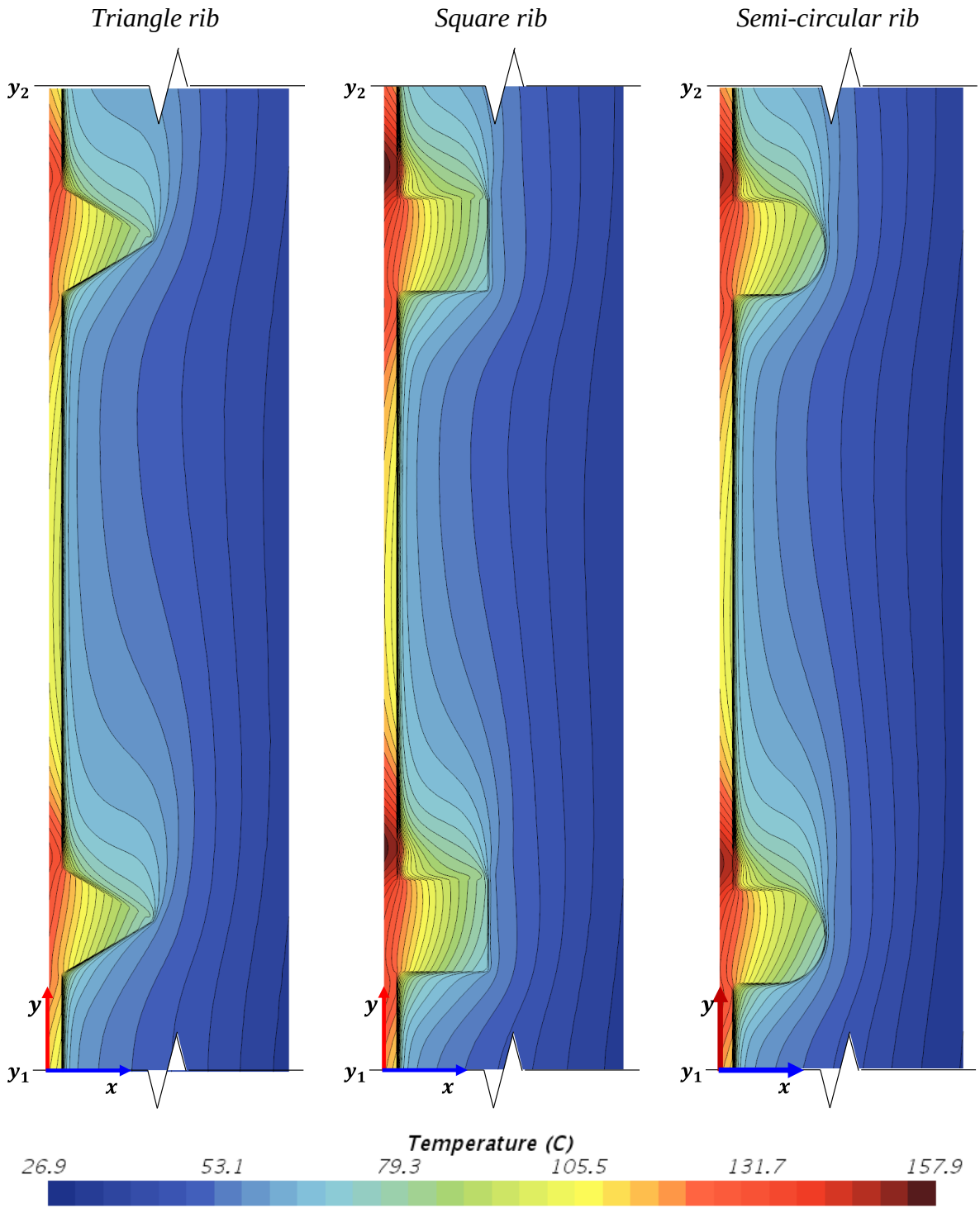


Figure 3-11: Temperature contours for the different transverse rib roughness for *e/D* = 0.30 and *p/e* = 7.5

### 3.4.2 Effect of relative roughness height (*e/D*)

The triangular rib demonstrated the most effective convective heat transfer; hence the effect of the relative roughness height (i.e., *e/D*) is assessed for the vertical channel roughened with triangular rib. Figure 3-12*a* shows the effect of varying the relative roughness height on the Nusselt number for different flow conditions. The Nusselt number increases with increase in the relative roughness height up till $e/D = 0.20$. Further increase in the roughness height has negligible impact on the Nusselt number as evident by the curve plateau for $e/D > 0.2$ in Figure 3-12*a*. The convective heat transfer coefficient is also maximized at $e/D = 0.20$ for $p/e = 10$ such that the Nusselt number ratio of up to 1.74 is attainable (Figure 3-12b).

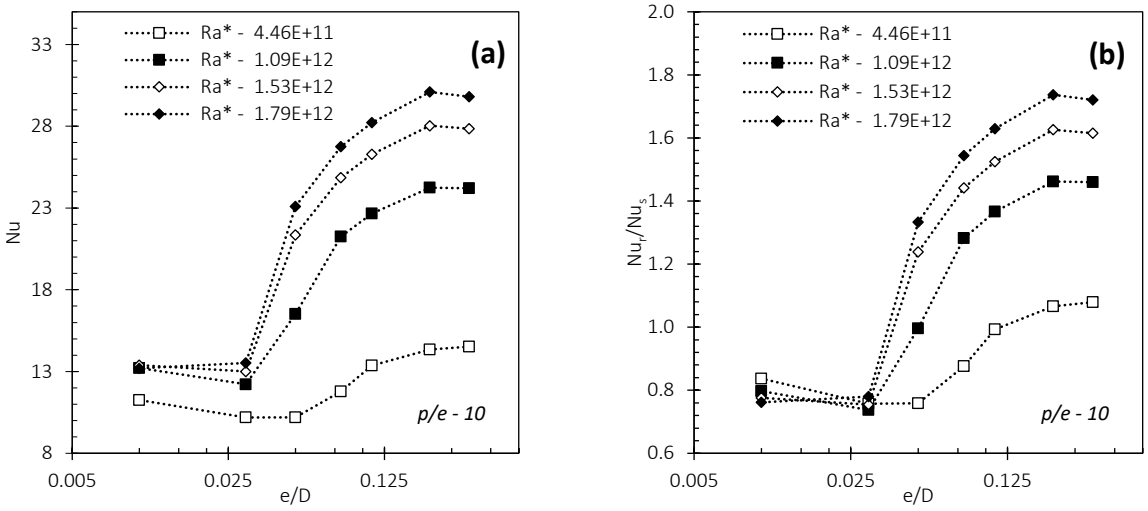


Figure 3-12: The effect of varying the relative roughness height on the (a) Nusselt number and (b) Nusselt number ratio

Figure 3-12a and Figure 3-12b can be explained by observing the wall shear stress profiles in Figure 3-13 and the dimensionless temperature profiles in Figure 3-14. The dimensionless temperature is given in **Error! Reference source not found.**.

$$\boldsymbol{\theta = \frac{T - T_{\infty}}{T_{s,max} - T_{\infty}}} \qquad \text{Equation 3-11}$$

where, $T$ is the temperature along the height of the channel, $T_{\infty}$ is the channel inlet temperature, and $T_{s,max}$ is the maximum surface temperature for all scenarios considered (i.e., $0.03 \leq e/D \leq 0.30$). The wall shear stress profile can inform on the near wall flow structure. A negative shear

stress is an indication of reversed flow, and a positive shear is an indication of reattached flow if it occurs after a region of negative shear (i.e., recirculation) or a clockwise rotating vortex if it occurs before the recirculation region. The presence of ribs induces turbulence in which should enhance momentum transfer from the free stream downstream of the rib elements, causing the flow to reattach for sufficient pitch lengths. The turbulence induced at smaller rib heights is not sufficient to incite flow reattachment for the specified relative pitch length of $p/e$ = 10. As such, the near wall flow for $e/D \leq 0.03$ is characterised by recirculation flow as inferred from the wall shear stress profiles (See Figure 3-13). The recirculation flow hinders the heat transfer between the heated plate and the fluid and is reflected in the relatively higher temperatures seen in Figure 3-14.

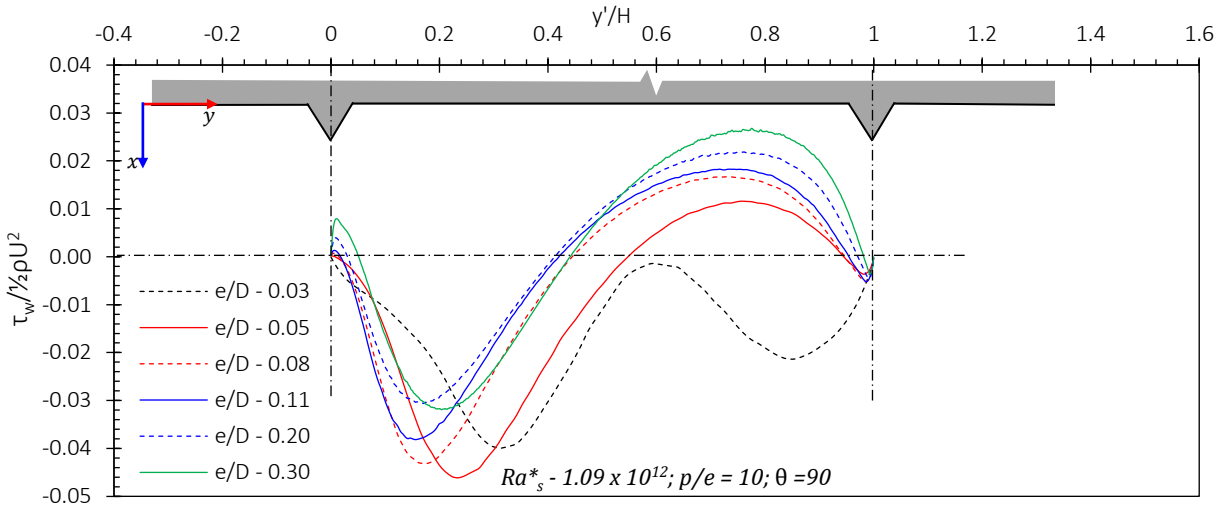


Figure 3-13: Comparison of the typical wall shear stress profiles for different relative roughness heights for $p/e$ = 7.5 and θ = 90

For $e/D$ = 0.05 the turbulence induced is sufficient to incite flow reattachment in the air channel for the specified relative pitch length (i.e., $p/e$ = 10). This is reflected in the wall shear stress profile (Figure 3-13). The wall shear stress profile turns positive after a certain pitch length and is suggestive of flow reattachment. Note that the wall shear stress profile is shown for the region where the fully developed temperature profile is reached (i.e., $y/H > 0.5$). Similarly, for $e/D > 0.05$, the induced turbulence in the BIPV channel is sufficient to incite flow reattachment for the specified pitch length such that the fully developed thermal field is reached sooner. The fully developed temperature profile is reached at $y/H$ values of 0.35, 0.25, 0.21, and 0.21 for $e/D$ values

of 0.08, 0.11, 0.20, and 0.30 respectively. The heat transfer enhancement diminished for *e/D* = 0.30 because the higher blockage ratio incites flow recirculation that spans a larger pitch length which is detrimental for effective heat transfer. The flow reattachment points for *e/D* values of 0.05, 0.08, 0.11, 0.20, and 0.30 are 0.534, 0.452, 0.424, 0.416, and 0.443 respectively. The optimum rib height is then the rib height that minimizes the reattachment length (i.e., *e/D* = 0.20).

The fluctuating temperature is because of the local increase in temperature or hot spots associated with transverse ribs (see Figure 3-10). The fluctuating temperature profile is consistent with published experimental data (Srinivasan et al., 2017). In this experimental study, a thermochromic liquid crystal technique was used to experimentally measure the heat transfer coefficients. The results showed regions of low heat transfer coefficients in the immediate upstream and downstream of flow elements and high heat transfer coefficients for the reattached flow.

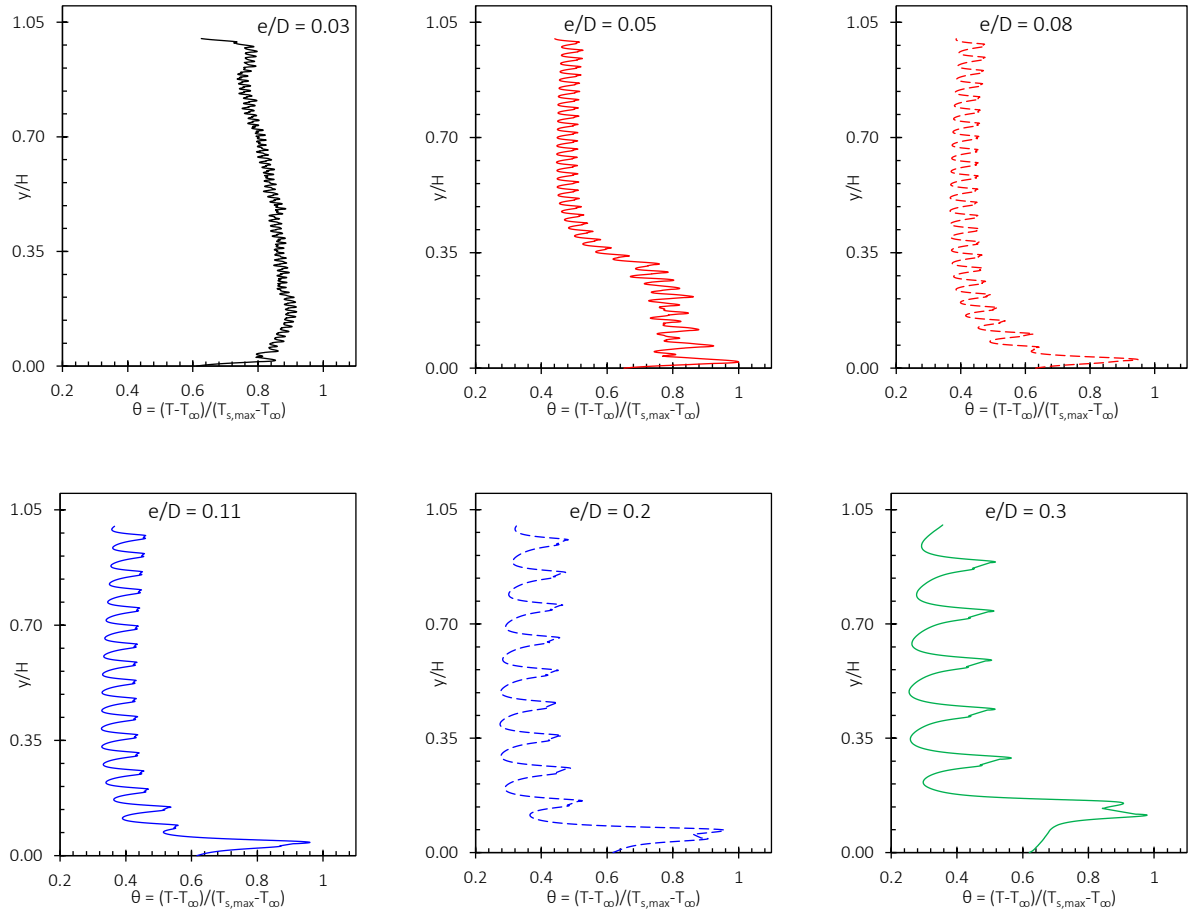


Figure 3-14 - The effect of varying the relative roughness height on the dimensionless temperature

The true optimal relative roughness height can be determined from the wall shear stress profiles shown in Figure 3-13 for the case $Ra_s^*$ - $1.09 \times 10^{12}$. This can be deduced by integrating the wall shear stress profiles in Figure 3-13. The true optimal relative roughness height occurs when the arithmetic integration of the wall shear stress profiles is zero. In other words, the length of the recirculation region is minimized. The true optimum relative toughness height has been estimated to be 0.16 as seen in Figure 3-15. At this point the shear force is zero.

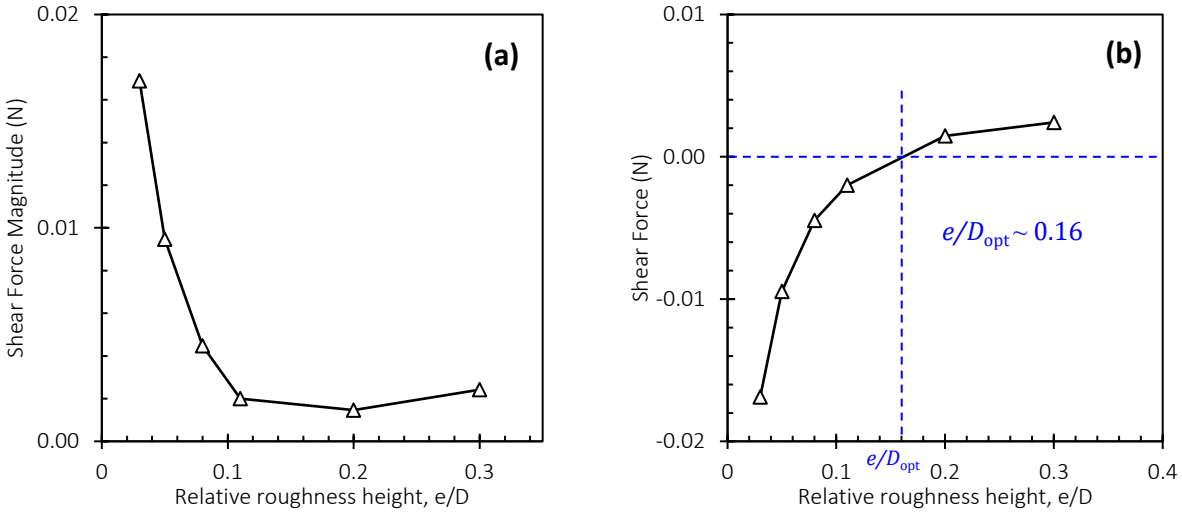


Figure 3-15: Variation of the (a) shear force magnitude and (b) shear force with relative roughness height

### 3.4.3 Effect of relative pitch ratio (*p/e*)

The effect of varying the relative pitch ratio; *p/e*, on the Nusselt number can be seen in Figure 3-16 for *e/D* = 0.20. As the relative roughness pitch is increased, the convective heat transfer coefficient increases up to an optimum value (i.e., *p/e* = 10) beyond which the heat transfer coefficient reduces for the range of Rayleigh numbers considered. The enhancement in heat transfer can be seen in Figure 3-16*b* for *e/D* = 0.20. The convective heat transfer coefficient is increased by a factor of up to 1.74, 1.63, 1.46 and 1.07 for $Ra_s^*$ values of $3.48 \times 10^{11}, 8.63 \times 10^{11}, 1.03 \times 10^{12}$, and $1.04 \times 10^{12}$ respectively. The optimum spacing of *p/e* = 10 can be explained by examining the wall shear stress profiles in Figure 3-17.

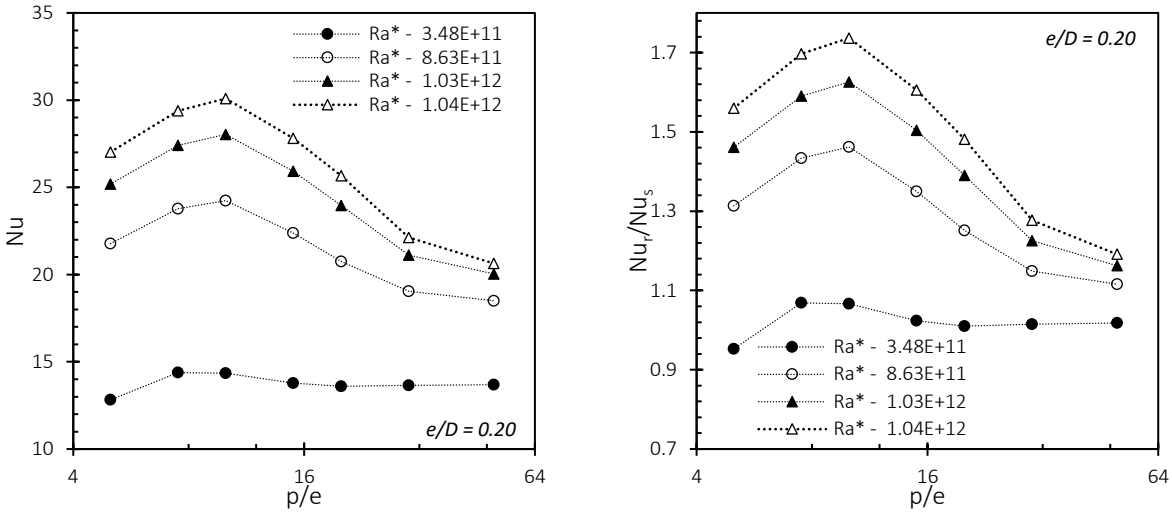


Figure 3-16: The effect of varying the relative pitch on the (a) Nusselt number and (b) Nusselt number ratio

Figure 3-17a plots the dimensionless wall shear stress for the different relative roughness pitch values considered for *e/D* = 0.20 and $Ra_s^* = 8.63 \times 10^{11}$. Flow reattachment occurs for all the relative pitch ratios considered. Figure 3-17a shows that the reattachment point is dependent on the relative pitch ratio. Increasing the relative pitch ratio causes the flow reattachment point to occur sooner. The reattachment points for *p/e* values of 5, 7.5, 10, 15, 20, 30, and 50 are 0.71, 0.50, 0.41, 0.34, 0.29, 0.21, and 0.12 respectively. Figure 3-17b has been derived by performing an arithmetic integration of the shear stress profiles in Figure 3-17a. As seen in Figure 3-17b, the relative roughness pitch that minimizes the shear force magnitude for the range of relative roughness pitch values considered is *p/e* = 10. The true point of minimum shear force occurs at *p/e* = 8.84 and is inferred from Figure 3-17c as the *p/e* value for which the shear force is zero.

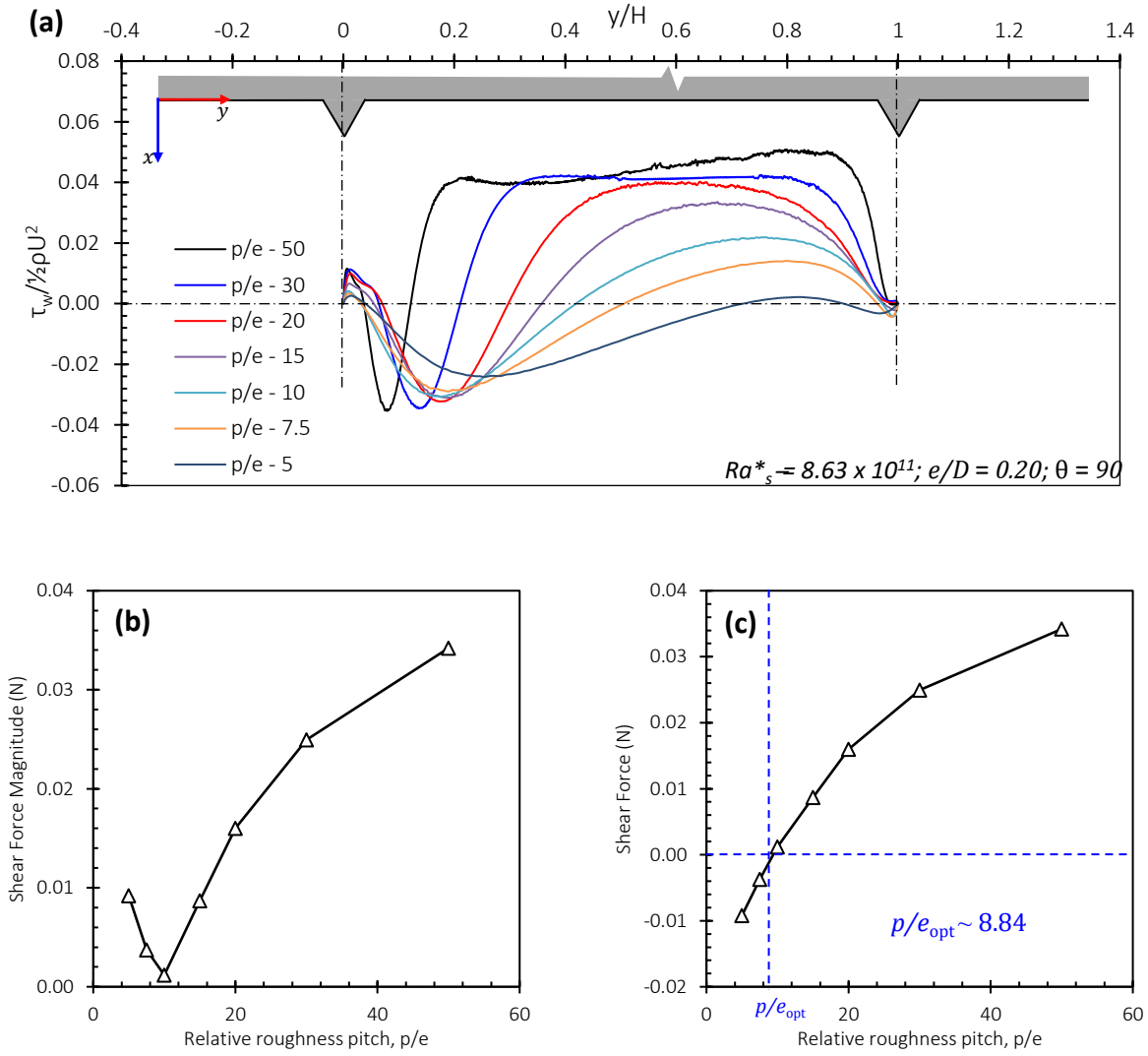


Figure 3-17: Effect of varying the relative roughness pitch on the (a) typical wall shear stress profiles, (b) shear force magnitude, and (c) shear force for $e/D$ = 0.20 and $p/e$ = 10

### 3.4.4 Effect of channel inclination angle

The effect of theta on the heat transfer coefficient can be seen in Figure 3-18*a* for $e/D$ = 0.20 and $p/e$ = 10. The heat transfer effectiveness decreases with higher inclination of the air channel. Using $q''$ = 400 $W/m^2$ as case study, the Nusselt number is 24.2, 19.6, 15.3, and 9.5 for theta values of 90, 45, 30, and 15 degrees respectively. This is expected as the buoyancy drive decreases with decrease in the inclination angle. Note that the enhancement in heat transfer shown in Figure 3-18*b* is similar for $\theta \geq 30$ degrees. Using $q''$ = 400 $W/m^2$ as case study, the heat transfer enhancement attributed to appending ribs in the air channel is 1.46, 1.44 and 1.37 for channel inclination angles of 90, 45 and

30 degrees respectively. For $\theta$ < 30 degrees, the heat transfer enhancement drops considerably. For the case with $q'' = 400\ W/m^2$, the heat transfer enhancement attributed to appending ribs in the air channel is 1.05 for $\theta$ = 15 degrees. Note that even for low heat flux availability of 100 $W/m^2$ appending ribs in the channel does not degrade the heat transfer performance of the air channel for $\theta$ > 30 degrees. The heat transfer enhancement is 1.07, 1.02, 0.99, and 0.84 for $\theta$ values of 90, 45, 30, and 15 respectively.

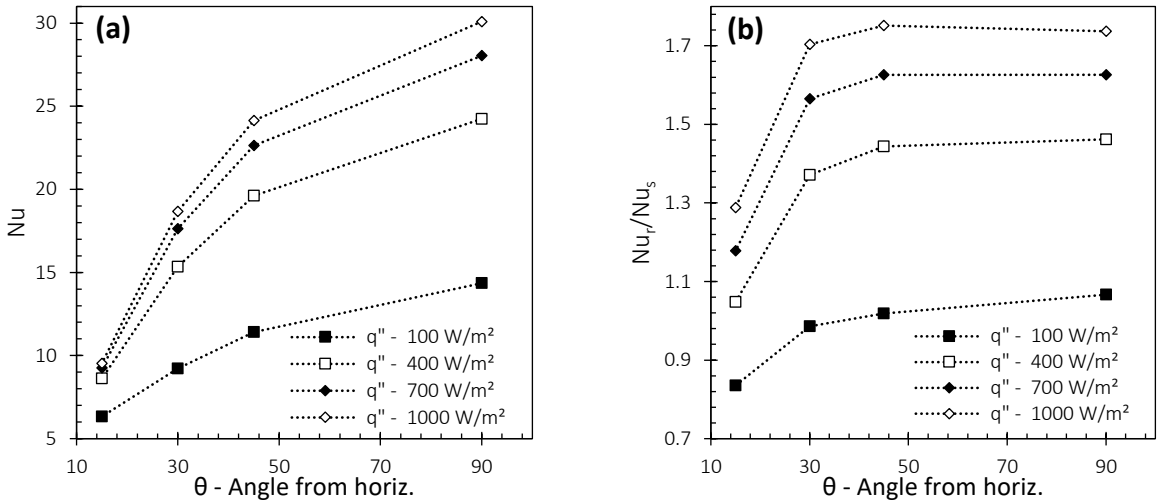


Figure 3-18 The effect of varying the channel inclination angle on the (a) Nusselt number and (b) Nusselt number ratio for a rib roughened channel

### 3.4.5 Development of correlation for Nusselt number and friction factor

In this section, Nusselt number is correlated with the relative roughness pitch ($p/e$), relative roughness height ($e/D$), channel inclination angle ($\theta$) and modified Rayleigh number using a Multivariate Polynomial Regression (Cecen, 2020). The correlation is given in Eq. 11.

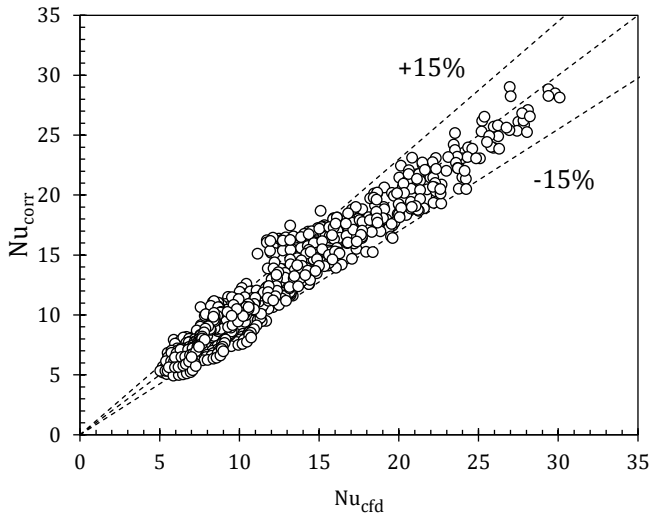


Figure 3-19: Comparison of predicted and simulated Nusselt number

$$\boldsymbol{Nu = 6.482 + 10.242(e/S) + 0.0168(p/e) - 0.0646(\theta - 90) + 2.16203 \times 10^{-10}[Ra_s^*(S/H)]} \qquad \text{Equation 3-12}$$

The accuracy of the developed correlation is checked with results of the computational analysis and as seen in Figure 3-19, the Nusselt number is predicted to with 15% error for more than 80% of the CFD simulated values.

## 3.5 CONCLUSION

The effect of varying rib geometry on the natural connective heat transfer coefficient in a BIPV/T channel was assessed using to CFD. A 2D numerical approach was adopted and validated with experimental data from literature. The parameters considered were the rib shape (i.e., square, triangle and semi-circle), relative rib height (i.e., $0.01 \leq e/D \leq 0.30$) and relative pitch ratio (i.e., $5 \leq p/e \leq 50$); where e is the rib height, D is the channel depth and p is rib spacing. In each instance, the heat flux is varied from 100 $W/m^2$ – 1000 $W/m^2$ and the channel inclination angle is varied from 15 – 90 degrees. The triangular rib section showed the most heat transfer enhancement. The enhanced mixing in the channel with the triangular rib was evident in the higher curvature of the velocity streamlines. As such, flow attachment was delayed and consequently, the boundary layer (i.e., the thermal resistive layer) was thinner. Further it is seen that the optimal roughness height that maximizes the convective heat transfer is 0.20 and the optimal rib spacing is $p/e = 10$ for the range of parameters considered. At the optimal spacing and roughness height, the shear

force magnitude is minimized. Also, the heat transfer enhancement is sustained for channel inclination angles up till 30 degrees. For $\theta < 30°$, the ribs are detrimental to the natural convective heat transfer especially at low heat flux. Nusselt number is correlated with *Ra*(S/H)*, *e/D*, *p/e* and theta to within 15% for more than 80% of the derived data.

## 3.6 REFERENCES


Abidi-Saad, A., Kadja, M., Popa, C., & Polidori, G. (2017). Effect of adiabatic square ribs on natural convection in an asymmetrically heated channel. Heat and Mass Transfer, 53(2), 743-752.

Abidi-Saad, A., Polidori, G., Kadja, M., Beaumont, F., Popa, C. V., & Korichi, A. (2016). Experimental investigation of natural convection in a vertical rib-roughened channel with asymmetric heating. Mechanics Research Communications, 76, 1-10.

Agathokleous, R. A., & Kalogirou, S. A. (2018). Part II: Thermal analysis of naturally ventilated BIPV system: Modeling and Simulation. Solar Energy, 169, 682-691.

Ahmet Cecen (2020). Multivariate Polynomial Regression (https://github.com/ahmetcecen/MultiPolyRegress-MatlabCentral), GitHub. Retrieved November 20, 2020.

Alzwayi, A. S., & Paul, M. C. (2013). Effect of width and temperature of a vertical parallel plate channel on the transition of the developing thermal boundary layer. International Journal of Heat and Mass Transfer, 63, 20-30.

Ambrosini, D., Paoletti, D., & Tanda, G. (2005). Measurement of free-convection heat transfer coefficients along a rib-roughened vertical surface. In 16th international symposium of transport phenomena.

Brinkworth, B. J., & Sandberg, M. (2006). Design procedure for cooling ducts to minimise efficiency loss due to temperature rise in PV arrays. Solar energy, 80(1), 89-103.

Brinkworth, B. J., Cross, B. M., Marshall, R. H., & Yang, H. (1997). Thermal regulation of photovoltaic cladding. Solar energy, 61(3), 169-178.

Cavazzuti, M., & Corticelli, M. A. (2008). Optimization of a buoyancy chimney with a heated ribbed wall. Heat and mass transfer, 44(4), 421-435.

Cuce, E., & Cuce, P. M. (2014). Tilt angle optimization and passive cooling of building-integrated photovoltaics (BIPVs) for better electrical performance. Arabian Journal for Science and Engineering, 39(11), 8199-8207.

Fedorov, A. G., & Viskanta, R. (1997). Turbulent natural convection heat transfer in an asymmetrically heated, vertical parallel-plate channel. International Journal of Heat and Mass Transfer, 40(16), 3849-3860.

Fossa, M., Ménézo, C., & Leonardi, E. (2008). Experimental natural convection on vertical surfaces for building integrated photovoltaic (BIPV) applications. Experimental thermal and fluid science, 32(4), 980-990.

Gan, G. (2009). Effect of air gap on the performance of building-integrated photovoltaics. Energy, 34(7), 913-921.

Hamed, T. A., Alshare, A., & El-Khalil, H. (2019). Passive cooling of building-integrated photovoltaics in desert conditions: Experiment and modeling. Energy, 170, 131-138.

Han, J., Lu, L., Yang, H., & Cheng, Y. (2019). Thermal regulation of PV façade integrated with thin-film solar cells through a naturally ventilated open air channel. Energy Procedia, 158, 1208-1214.

Kwak, C. E., & Song, T. H. (1998). Experimental and numerical study on natural convection from vertical plates with horizontal rectangular grooves. International journal of heat and mass transfer, 41(16), 2517-2528.

Lau, G. E., Sanvicente, E., Yeoh, G. H., Timchenko, V., Fossa, M., Ménézo, C., & Giroux-Julien, S. (2012). Modelling of natural convection in vertical and tilted photovoltaic applications. Energy and Buildings, 55, 810-822.

Lau, G. E., Yeoh, G. H., Timchenko, V., & Reizes, J. A. (2013). Large-eddy simulation of turbulent buoyancy-driven flow in a rectangular cavity. International journal of heat and fluid flow, 39, 28-41.

Sanvicente, E., Giroux-Julien, S., Ménézo, C., & Bouia, H. (2013). Transitional natural convection flow and heat transfer in an open channel. International Journal of Thermal Sciences, 63, 87-104.

Sarper, B., Saglam, M., & Aydin, O. (2018). Experimental and numerical investigation of natural convection in a discretely heated vertical channel: Effect of the blockage ratio of the heat sources. International Journal of Heat and Mass Transfer, 126, 894-910.

Shahrestani, M., Yao, R., Essah, E., Shao, L., Oliveira, A. C., Hepbasli, A., ... & Lechón, J. L. (2017). Experimental and numerical studies to assess the energy performance of naturally ventilated PV façade systems. Solar Energy, 147, 37-51.

Sinha, M. K., & Dash, S. K. (2014). Laminar natural convection heat transfer from an isothermal vertical ribbed plate. International Conference on Heat Transfer, Fluid Mechanics and Thermodynamics.

Srinivasan, S., Ekkad, S. V., & Tolpadi, A. (2018). Heat transfer measurements inside narrow channels with ribs and trenches. Heat Transfer Engineering, 39(9), 750-759.

Tanda, G. (1997). Natural convection heat transfer in vertical channels with and without transverse square ribs. International journal of heat and mass transfer, 40(9), 2173-2185.

TANDA, G. (2007). Free-convection heat transfer coefficients along a vertical surface with square protrusions. In Proceedings of the Vth Baltic Heat Transfer Conference, Saint Petersburg, Russia.

Tkachenko, O. A., Timchenko, V., Giroux-Julien, S., Ménézo, C., Yeoh, G. H., Reizes, J. A., ... & Fossa, M. (2016). Numerical and experimental investigation of unsteady natural convection in a non-uniformly heated vertical open-ended channel. International Journal of Thermal Sciences, 99, 9-25.

Tonui, J. K., & Tripanagnostopoulos, Y. (2008). Performance improvement of PV/T solar collectors with natural air flow operation. Solar energy, 82(1), 1-12.

Wu, T., & Lei, C. (2015). On numerical modelling of conjugate turbulent natural convection and radiation in a differentially heated cavity. International Journal of heat and Mass transfer, 91, 454-466.

Yilmaz, T., & Fraser, S. M. (2007). Turbulent natural convection in a vertical parallel-plate channel with asymmetric heating. International Journal of Heat and Mass Transfer, 50(13-14), 2612-2623.

Yilmaz, T., & Gilchrist, A. (2007). Temperature and velocity field characteristics of turbulent natural convection in a vertical parallel-plate channel with asymmetric heating. Heat and mass transfer, 43(7), 707.

# Chapter 4

# 4 BIPV/T with transverse rib roughened air channel - Parametric analysis of the effect of transverse roughness shape, roughness height (*e/D*), and roughness spacing (*p/e*) on the turbulent forced convection heat transfer

In Chapter 3, it was shown that the natural convection cooling can be an effective and cost-effective thermal management measure for building integrated photovoltaics (BIPVs). However, forced air cooling channels are more predictable and can easily be adapted with the building energy systems (i.e., HVAC) to offset some of the building heating loads. The effectiveness of forced air cooling as a thermal management strategy has been demonstrated (Athienitis et al., 2011; Chen et al., 2010; Corbin & Zhai, 2010; Dubey et al., 2009; Kamel & Fung, 2014; Pantic et al., 2010; Peng et al., 2013; Zogou & Stapountzis, 2011). However, the effectiveness of forced air cooling to improve the energy conversion efficiency of PV modules is limited by the development of boundary layer over the length of the air channel (Peng et al., 2013; Gaur et al., 2016). In the viscous sub-layer, which is the region of the boundary layer closest to the wall, the flow becomes laminar due to the drag of skin friction. This creates a stagnation in the region closest to the wall, which creates unfavorable condition for heat transfer (Patil et al., 2015; Kumar & Kim, 2015; Pandey & Bajpai, 2016).

For this reason, multiple inlets were introduced to disrupt the boundary layer growth and increase the heat transfer effectiveness (Yang & Athienitis 2014; Yang & Athienitis, 2015; Rounis et al., 2016). A more common heat transfer augmentation strategy especially in solar air heater (*SAH*) applications is the appending of transverse roughness at the back of the absorber plate. The roughness elements interrupt the development of the boundary layer which promotes turbulence in the near wall region thereby enhancing the heat transfer (Yadav & Bhagoria, 2014; Pandey & Bajpai, 2016; Poongavanam et al., 2018). Table 4-1 list the experimental research conducted for heat transfer augmentation of SAH with transverse ribs. The findings suggest an enhancement in heat transfer and an accompanying increase in the pumping penalty. It is important that the heat transfer augmentation does not increase the pumping penalty since the pumping power is a cubical function of the flow rate (Aharwal et al., 2014). The goal is then to maximize the heat transfer and minimize the pumping penalty (Bekele et al., 2014; Luo et al., 2016).

Further numerical studies on heat transfer augmentation with transverse ribs roughness elements is summarized in Table 4-2. In the development of roughness elements for SAH, conventional techniques such as experimental designs are often used which can be expensive and time consuming (Yadav & Bhagoria, 2014). There's also limitation on the extensiveness of the variables or parameters that can possibly be explored stemming from cost constraints. This has inspired the Computational fluid dynamics (CFD) approach in the design and optimization of roughened solar air heaters. In addition to the cost-effectiveness of the CFD approach, visualization of the flow structures in CFD can provide deeper insight into the optimization of geometric parameters and arrangement to enhance convective heat transfer and minimize system pressure loss since it provides spatial and temporal details on the flow structures.

The effectiveness of transverse roughness ribs is limited because of the problem inherent with transverse roughness elements. Vortices are trapped in the immediate upstream and downstream of transverse roughness elements which creates hot spots (Coleman et al., 2007). These hot spots can be detrimental to the electrical conversion efficiency of the PV module. An additional measure is to introduce refrigerant fluid flow within the transverse rib roughness elements with the aim to improve the overall thermal efficiency. Inherently, the roughness elements or refrigerant tubes are likely to protrude more into the boundary layer due to the typical roughness expected to be in the range of 8 – 19 mm (Bakar et al., 2014; Othman et al., 2016; Wang et al., 2016). This imposes different flow characteristics as dictated by the roughness Reynolds number, $e^+$. The roughness Reynolds number function is given Equation 4-1 (Karwa et al., 1999)

$$\boldsymbol{e^+ = \sqrt{f/2}\, Re(e/D)} \qquad \text{Equation 4-1}$$

where, $f$ is the friction factor, $Re$ is the Reynolds number, $e$ is the roughness height, and $D$ is the hydraulic diameter. The value of the roughness Reynolds number gives an indication of the flow paradigm. Karwa et al. (1999) highlighted the three different roughness paradigms or flow regions. The three regions are; the hydraulically smooth flow ($0 < e^+ \leq 5$); the region in which the friction factor are similar to what is encountered in smooth pipes in that the roughness elements lie within the laminar sublayer; transitionally rough flow ($5 < e^+ \leq 70$); the region in which the roughness elements are in the same scale as the laminar sublayer; and fully rough flow ($e^+ > 70$); the region in which the roughness elements extend beyond the laminar sublayer.

The literature review revealed that most of the research has been focused on flow in the hydraulically smooth and transitional rough flow (Table 4-1 and Table 4-2). However, the operational variability of the bi-fluid BIPV/T concept proposed for the thermal management of the PV panel imposes constraints on the limit to which the roughness elements can be scaled down to reduce the system pressure loss. As such, the flow patterns encountered will mostly be in the transitionally rough flow and the fully rough flow regions. This increases the necessity to optimize the roughness geometry to enhance the convective heat transfer and minimize the pressure loss.

Accordingly, the first objective of this study is to investigate the heat transfer and pressure loss characteristics of a high blockage ratio *BIPV/T* air channel with circular transverse roughness. The second objective is to numerically compare the heat transfer effectiveness of the square, circular, semi-circular, and triangular transverse roughness profile. The third objective is to develop a correlation for the heat transfer coefficient and friction factor as a function of the geometry and flow characteristics. The numerical study will be done using *CFD*. First, the CFD model will be validated with experimental data from literature (Skullong et al., 2015) for a similar transverse roughness geometry. Then, the impact of the roughness shape, roughness height and roughness pitch on the thermo-hydraulic performance is studied.

Table 4-1: Summary of Experimental research on transverse roughness applied on the absorber plate

| No. | Authors | Roughness profile | Range of parameters | Key findings |
|---|---|---|---|---|
| 1 | Bhagoria et al. (2002) | Transverse wedge ribs | $e/H$: 0.015 – 0.033<br>$p/e$: 5.67 – 12.12<br>$\varphi$: 8 - 15º<br>$W/H$: 5<br>$Re$: 3,000 – 18,000<br>$e^+$: 4 - 87 | • 2.4 and 5.3 times increase in $Nu$ and friction factor respectively.<br>• The best thermal performance occurred at $p/e$ = 7.57, $e/H$ =0.033 and $\varphi$ of 10º |
| 2 | Karwa et al. (1999) | Chamfered rectangular ribs | $e/D$: 0.014 – 0.032<br>$p/e$: 4.5 – 8.5<br>$W/H$: 4.8 – 12.0<br>$L/D$: 32, 66<br>$\varphi$: -15 - 18º<br>$Re$: 3,000 – 20,000<br>$e^+$: 5 - 60 | • Up to two- and three-times enhancement of the Stanton number and the friction factor respectively.<br>• $St/St_s$ decreased by 5% and $f/f_s$ increased by 20% with increase in $W/H$ from 4.5 to 8.5.<br>• Monotonous increase of $St$ and $f$ with $e/D$.<br>• $\varphi$ value of 15 ensured the best thermal performance. |
| 3 | Sharma et al. (2019) | Pentagonal ribs | $e/D$: 0.25<br>$p/e$: 6 - 12<br>$\alpha$: 0 - 20º<br>$Re$: 9400 – 58850<br>$e^+$: > 70 | • The best thermo-hydraulic performance was achieved for $\alpha$ = 5 and $p/e$ = 10 such that the use of pentagonal ribs over square ribs is justified for thermal performance enhancement. |
| 4 | Jaurker et al. (2006) | Rib and groove roughness | $e/D$: 0.0181 – 0.0363<br>$p/e$: 4.5 – 10<br>$g/p$: 0.3 – 0.7<br>$Re$: 3,000 – 21,000<br>$e^+$: 5 - 73 | • The maximum heat transfer augmentation occurred at $p/e$ = 6.0; $g/p$ = 0.4; and $e/D$ = 0.0363. |

| | | | | |
|---|---|---|---|---|
| 5 | Aharwal et al. (2014) | Wedge-shaped rib and groove roughness | $e/D$: 0.033<br>$p/e$: 8<br>$g/p$: 0.4 – 0.8<br>$\varphi$: 10 - 25º<br>$\alpha$: 60º (groove angle)<br>$Re$: 3,000 – 18,000<br>$e^+$: 10 - 62 | • The best thermal performance was observed for $\varphi$ = 15 and $g/p$ = 0.65 such that a $ThPP$ value of up to 2.16 was attained. |
| 6 | Skullong et al. (2015) | Square ribs | $e/D$: 0.22<br>$p/e$: 6.67<br>$Re$: 5,000 – 24,000<br>$e^+$: > 70 | • $ThPP$ <1 for $Re$ > 11,000 |

**Table 4-2: Summary of Literature on transverse roughness applied on the absorber plat using computational fluid dynamics approach**

| No. | Authors | Roughness profile | Range of parameters | Key findings |
|---|---|---|---|---|
| 1 | Thakur et al. (2017a) | Hyperbolic ribs | $e$: 0.5 – 2 mm<br>$e/D$: 0.0125 – 0.05<br>$p$: 10 – 20 mm<br>$Re$: 4,000 – 15,000<br>$e^+$: 10 - 150 | • The parametric analysis yielded an optimum rib height of 1 mm with pitch of 10 at $Re$ = 6,000 flow conditions. |
| 2 | Kumar et al. (2019) | Square ribs | $e/D$: 0.013 – 0.05<br>$p/e$: 5 - 13<br>$Re$: 3,900 – 17,900<br>$e^+$: 1 - 49 | • $ThPP$ of up to 1.97 for $p/e$ value of 10 and $e/D$ value of 0.05 at $Re$ of 17,900.<br>• Flow reattachment occurs just before the adjacent rib for the optimal $p/e$ to prevent reformation of the laminar sublayers. |
| 3 | Kumar et al. (2018) | Forward-facing chamfered ribs | $e/D$: 0.018 – 0.043<br>$p/e$: 5 - 13 | • Up to 2.88 and 3.52 enhancement of heat transfer and friction penalty. |

| | | | | |
|---|---|---|---|---|
| | | | $e'/e$: 0 – 1<br>$e/w$: 0.24 – 1.5<br>$Re$: 4,000 – 17,000<br>$e^+$: 8 - 65 | • Optimal configuration: $e'/e$ = 0.75, $e/w$ = 1.5 and $e/D$ = 0.043 |
| 4 | Yadav & Bhagoria (2013) | Transverse wire rib roughness element | $e/D$: 0.021 – 0.042<br>$p/e$: 7.14 – 35.71<br>$W/H$: 5<br>$Re$: 3,800 – 18,000<br>$e^+$: 7 - 81 | • the wire rib with $p/e$ = 10.71 and $e/D$ = 0.042 provided the better thermo-hydraulic performance at *Re* value of 18,000. |
| 5 | Yadav & Bhagoria, (2014a) | Triangular rib | $e/D$: 0.021 – 0.042<br>$p/e$: 7.14 – 35.71<br>$W/H$: 5<br>$Re$: 3,800 – 18,000<br>$e^+$: 7 - 79 | • Maximum $Nu_{enh}$ of 3.073 for $e/D$ value of 0.042 and $p/e$ of 7.14 at $Re$ of 15,00.<br>• Maximum $f_{pen}$ of 3.356 for $e/D$ value of 0.042 and $p/e$ of 7.14 at $Re$ of 3,800. |
| 6 | Yadav & Bhagoria, (2014b) | Semi-circular rib | $e/D$: 0.021 – 0.06<br>$p/e$: 14.29<br>$W/H$: 5<br>$Re$: 3,800 – 18,000<br>$e^+$: 7 - 79 | • $e/D$ value of 0.042 and $Re$ value of 15,000 provided the better $ThPP$. |
| 7 | Kumar et al. (2017) | Rectangular rib | $e/D$: 0.02 – 0.4<br>$p/e$: 5 - 15<br>$e/w$: 0.25 – 4.0<br>$Re$: 4,000 – 18,000<br>$e^+$: 10 - 76 | • The maximum $ThPP$ value is obtained at $Re$ = 15,000 for $p/e$, $e/D$ and $e/w$ values of 10, 0.04 and 4 respectively. |
| 8 | Chaube et al. (2006) | Rectangular rib<br>Chamfered rib<br>Semi-circular rib | $e$: 3 mm<br>$w$: 2, 3, 4, 5 mm<br>$\varphi$: 11, 13, and 15° | • For the operational conditions simulated, the rectangular rib of 3 × 5 mm gives the best performance over the range of $Re$ from 3,000 to 20,000. |

| | | | | |
|---|---|---|---|---|
| | | Circular rib | $e^+$: > 50 | |
| 9 | Gawande et al. (2016) | L shaped rib in solar air heater duct | $e/D$: 0.042<br>$p/e$: 7.14 – 17.86<br>$Re$: 3,800 – 18,000<br>$e^+$: 16 - 80 | • Max $Nu_{enh}$ and $f_{enh}$ for $p/e$ of 7.14 at $Re$ of 15,000 and 3,800 respectively.<br>• Max $ThPP$ of 1.9 for $p/e$ of 7.14, $e/D$ of 0.042 at $Re$ of 15,000. |

1

## 4.1 BIPV/T envelope system considered for the study

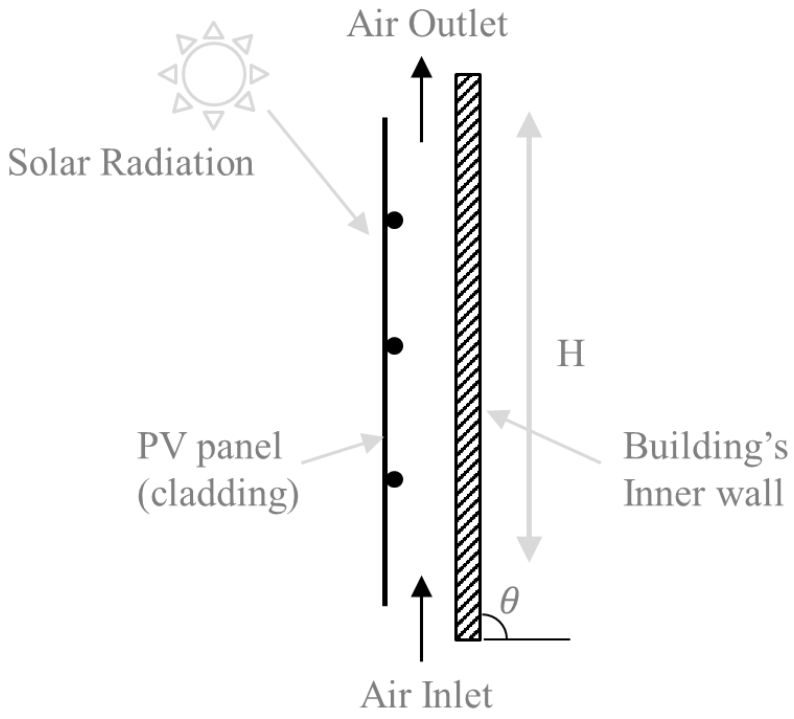


Figure 4-1: An illustration of BIPV/T with transverse rib roughness

Figure 4-1 shows a cross-section of the physical model of an air cooled BIPV/T with circular transverse ribs for heat transfer enhancement. The system consists of different eclosure layers and the outer wall (i.e., PV panel as a cladding substitute). The inner and outer wall assemblies are separated by an air channel for forced air flow which serves as capillary break to prevent moisture ingress from the outer wall to the inner wall. The system is decribed by the following geometrical parameters as seem in Figure 4-2 and Figure 4-3: the roughness height, *e*, which is the diameter of the circular ribs; the roughness pitch, *p*, which is the distance between successive ribs; and the channel height, *H*. The physical model of the BIPV with transverse rib roughness is numerically represented as a *SAH* channel roughened with transverse ribs (Figure 4-2). This simplification of the computational domain is valid since the BIPV/T air channel is a SAH channel with reduced surface temperature as part of the available solar is converted to electrical energy. In effect, the solar panel is an absorber plate. The absorber plate is not directly modelled in the solution domain since its thermal conductivity is three orders of magnitude higher than the

fluid (i.e., air). A fully developed flow condition is ensured by the 1 m entrance length. An exit length of 1 m is also provided to ensure settled flow at the outlet. The entrance and exit lengths satisfy the condition for fully developed flow (i.e., $x_{fd}/D \geq 10$ – Incropera et al., 2007). The other geometrical parameters of the computational domain are outlined in Table 4-3.

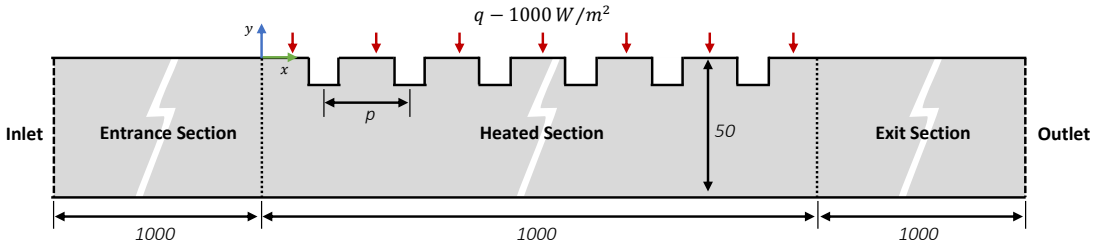


Figure 4-2: The computational domain and computational domain

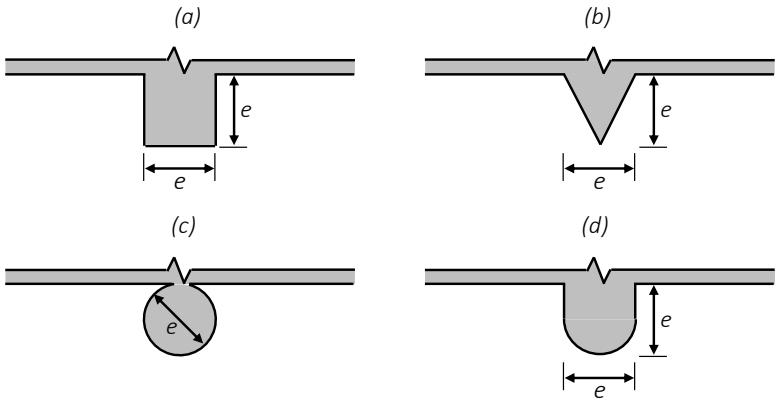


Figure 4-3: The roughness geometries considered in the study: (a) square (b) triangle (c) circle and (d) semi-circle

For heat transfer enhancement, the top surface of the heated section is roughened with transverse ribs. Four different roughness shapes are considered as depicted in Figure 4-2 and Figure 4-3; square, triangle, square and semi-circle. In all instances, e, is the height and width of the roughness element, and p is the pitch (i.e., the distance between consecutive roughness elements). The range of roughness heights considered (i.e., 1 – 10 mm) is such that the relative roughness height (*e/D*) is in the range of 0.01 to 0.10 respectively. The *e/D* range ensured that the circular roughness elements protrude extensively into the boundary layer for a fully rough flow regime. The roughness elements

are arrayed with relative pitch ratios (*p/e*) from 1.5 to 50. Reynolds number in the range of 5,000 to 19,000 were considered which is the typical operating range of *SAH* to ensure better thermo-hydraulic performance (Yadav & Bhagoria, 2014). Refer to Table 4-3 for the discrete values within the range of parameters investigated. A uniform heat flux of 1000 $W/m^2$ is considered on the flat top surface of the test section.

Table 4-3: Geometrical and operational parameters of the computational domain

| **Parameter** | **Symbol** | **Value** |
|---|---|---|
| Test section Length, mm | $L_{test}$ | 1000 |
| Entrance Length, mm | $L_{ent}$ | 1000 |
| Exit Length, mm | $L_{exit}$ | 1000 |
| Channel height, mm | $H$ | 50 |
| Hydraulic diameter, mm | $D$ | 100 |
| Rib Height, mm | $e$ | 1, 2, 3, 5, 7, 10 |
| Rib axial pitch, mm | $P$ | 5, 7.5, 12.5, 15, 17.5, 25, 50, 75, 100 |
| Reynolds number range | $Re$ | 5000, 7000, 9000, 11000, 13000, 15000, 17000, 19000 |
| Relative roughness height | $e/D$ | 0.01, 0.02, 0.03, 0.05, 0.07, 0.10 |
| Relative roughness pitch | $p/e$ | 1 - 50 |

## 4.2 Numerical Simulation setup

In this study, a two-dimensional (2D) model of the SAH duct roughened with transverse circular roughness elements is developed and simulated using CFD. Simcenter STAR-CCM+ version 13.06.012 has been employed to solve the steady state Reynolds averaged navier stokes and energy equation. The details of the numerical setup including the

governing equations, turbulence model, boundary conditions, and solution strategy are presented in the following sections.

### 4.2.1 Governing equations and turbulence model

The governing equations to solve the conjugate heat transfer problem are given in Equation 4-2 – Equation 4-4. The equations have been simplified with assumptions of fluid incompressibility and negligible radiation heat transfer.

Continuity equation:

$$\frac{\partial}{\partial x_i}(u_i) = 0 \qquad \text{Equation 4-2}$$

Momentum equation:

$$\frac{\partial}{\partial x_i}(\rho u_i u_j) = -\frac{\partial p}{\partial x_i} + \mu \frac{\partial}{\partial x_j}\left(\frac{\partial u_i}{\partial x_j} + \frac{\partial u_j}{\partial x_i}\right) - \frac{\partial}{\partial x_j}(\rho u_i' u_j') \qquad \text{Equation 4-3}$$

Energy equation:

$$\frac{\partial}{\partial x_j}(\rho u_j T) = \frac{\partial}{\partial x_j}\left[\left(\frac{\mu}{Pr} + \frac{\mu_t}{Pr_t}\right)\frac{\partial T}{\partial x_j}\right] \qquad \text{Equation 4-4}$$

where, $\mu$ is the dynamic viscosity, $\rho$ is the fluid density, $p$ is pressure, $Pr$ is the prandtl number, $Pr_t$ is the turbulent prendtl number and, $\mu_t$is the eddy viscosity. The standard k-epsilon approach is implemented for the RANS closure as they are good for that contain complex recirculation, with or without heat transfer (Simcenter Star CCM+ Documentation). The k-epsilon turbulence model has been demonstrated to accurately capture the turbulence charaacteristics for SAH roughened with transverse ribs (Yadav & Bhagoria, 2013; Thakur et al., 2017a; Kumar et al., 2018; Kumar et al., 2019). A correct representation of the flow in the near wall region determines successful prediction of wall-bounded turbulent flows (Yadav & Bhagoria, 2014). Hence, the enhanced wall treatment is used to resolve the near wall physics depicting a low reynolds number approach for y+

≤ 1. The transport equations for the turbulence kinetic energy and dissipation rate are given in Equation 4-5 and Equation 4-6 respectively.

$$\rho u_j \frac{\partial k}{\partial x_j} = P_k - \rho(\varepsilon - \varepsilon_0) + \frac{\partial}{\partial x_j}\left[\left(\mu + \frac{\mu_T}{\sigma_k}\right)\frac{\partial k}{\partial x_j}\right] \qquad \text{Equation 4-5}$$

$$\rho u_j \frac{\partial \varepsilon}{\partial x_j} = \frac{1}{T_e} C_{\varepsilon 1} P_\varepsilon - \rho C_{\varepsilon 2} f_2 \left(\frac{\varepsilon}{T_e} - \frac{\varepsilon_o}{T_o}\right) + \frac{\partial}{\partial x_j}\left[\left(\mu + \frac{\mu_T}{\sigma_k}\right)\frac{\partial k}{\partial x_j}\right] \qquad \text{Equation 4-6}$$

where, $P_k$ and $P_\varepsilon$ are production terms, $f_2$ is the damping function, $T_o$ is the specific time scale, and $k_0$ and $\varepsilon_0$ are the ambient turbulence values that counteract turbulence decay. The model coefficients are: $C_\mu$ = 0.09, $\sigma_k$ = 1, $\sigma_\varepsilon$ = 1.3, $C_{\varepsilon 2}$ = 1.92, $C_{\varepsilon 2}$ = 1.44.

### 4.2.2 Mesh Generation

The governing equations are solved by discretizing the computational domain into finite control volumes. The computational domain is discretized using polyhedral mesh. Four prism layers have been employed in the near wall region with a geometric stretching factor of 1.5. This is done to capture important details of the temperature gradient near the heated top surface. The size of the mesh in the computational domain has been globally scaled to a fraction of the characteristic length. The height of the channel is the characteristic length. The mesh is refined around the roughness elements to capture the complex flow structures due to flow separation and possible reattachment. Figure 4-4 illustrates the typical meshing scheme. In Figure 4-4, the global reference size is $\frac{1}{15}H$. The size of the mesh is $\frac{3}{40}(\frac{1}{15}H)$ closer to the roughness elements and the heated top wall. A growth rate of 1.05 allows for a smooth transition from the finer mesh to the relatively coarser mesh in the undisturbed entrance and exit lengths. The thickness of the prism layer is $\frac{1}{10}\left(\frac{1}{15}H\right)$, this ensured that the $y^+ \leq 0.23$. The meshing scheme yielded 231,320 grid cells.

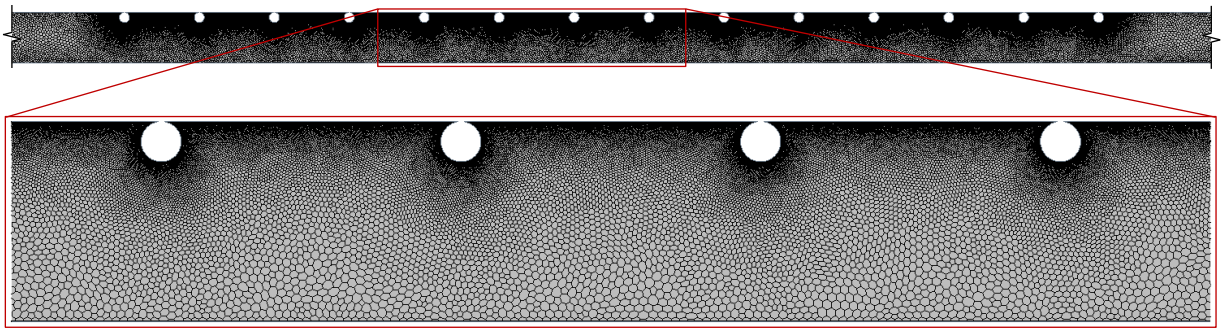

Figure 4-4: Typical mesh of the computational domain for circular rib, *e/D* = 0.1 and *p/e* = 7.5

The mesh is further refined such that the base size is $\frac{1}{30}H$ and $\frac{1}{40}H$; amounting to 283,943 and 397,198 cells respectively, and mesh independency study is performed. The mesh independency study is conducted for a typical solution domain with inflow at *Re* = 7,000, *e/D* = 0.2 and *p/e* = 6.67. The rate of change of Nusselt number and friction factor with further mesh refinement is monitored to assess mesh independency. Table 4-4 shows that with further refinement of the mesh beyond 172,916 grid cells, the change in both *Nu* and *f* is less than 1%. The Mesh with 231,320 cells is deemed enough to capture the flow characteristics.

Table 4-4: Summary of mesh independency study

| No. | Grid count | *Nu* | % Increase in *Nu* | *f* | % increase in *f* |
|---|---|---|---|---|---|
| 1 | 231,320 | 35.178 | - | 0.1225 | - |
| 2 | 283,943 | 35.162 | -0.04% | 0.1229 | 0.33% |
| 3 | 397,198 | 35.130 | -0.09% | 0.1227 | -0.24% |

### 4.2.3 Boundary conditions and solution strategy

An accurate specification of the boundary conditions is essential to obtain meaningful computational results. No-slip boundary condition is assigned to all the walls. All the walls are assumed adiabatic except the flat surfaces at the top of the test section. A uniform constant heat flux of 1000 $W/m^2$ is applied at the top of the test section. At the inlet, a constant velocity profile is imposed depending on the flow condition that is being simulated. The 1 m entrance length of the solution domain is enough to attain a fully developed velocity profile. Air at 300 K enters the solution domain. The properties of air

at 300 K is given in Table 4-5. The turbulence characteristics at the inlet is described by specifying the turbulence intensity. The turbulence intensity is estimated by the Equation 4-7 (Kumar et al., 2018).

$$\boldsymbol{I = 0.16(Re)^{-1/8}} \qquad \text{Equation 4-7}$$

where, *Re* is the Reynolds number. At the outlet, a pressure outlet boundary condition is assigned with gauge pressure of 0 Pa. The turbulence intensity at the outlet is specified like the inlet.

Table 4-5: Thermophysical properties of air

| Property | Unit | Air |
|---|---|---|
| Thermal conductivity, $k$ | *W/m/K* | 0.0263 |
| Density, $\rho$ | *kg/m$^3$* | 1.1614 |
| Specific heat, $C_p$ | *J/kg/K* | 1007 |
| Dynamic viscosity, $\mu$ | *N s/m$^2$* | 1.85 x 10$^{-5}$ |
| Prandtl number, $Pr$ | | 0.707 |

The conservation equations of mass, momentum and energy are solved simultaneously using a pseudo-time-marching approach. The pseudo-time-marching approach is implemented in the Coupled Flow Model. The Second-Order Upwind scheme is used to discretize the governing equations. The solution is converged for all residuals (i.e., continuity, velocity components and energy) less than $10^{-4}$.

### 4.2.4 Performance Indicators

The performance of the SAH system with transverse roughness ribs is quantified by the Nusselt number, friction factor and the thermo-hydraulic performance parameter. Nusselt number gives an indication of the heat transfer effectiveness (Equation 4-8).

$$\boldsymbol{Nu = \frac{h\,D}{k}} \qquad \text{Equation 4-8}$$

where, $D$ is the hydraulic diameter, $k$ is the thermal conductivity of air taken at the bulk fluid temperature (i.e., the average of the inlet and outlet temperature; $(T_{out} + T_{in})/2$) and $h$ is the average convective heat transfer coefficient.

The friction factor gives an indication of the pressure loss in the air channel (Equation 4-9).

$$\boldsymbol{f = \frac{\left(\Delta P / L\right)}{1/2\,\rho U^2} D} \qquad \text{Equation 4-9}$$

where, $\Delta P$ is the pressure drop from the inlet to the outlet, L is the length of the solution domain (i.e., 3 m), $D$ is the hydraulic diameter, $\rho$ is the density at the bulk fluid temperature, and $U$ is the inlet velocity derived from the Reynolds number (i.e., $Re = {\rho UD}/{\mu}$ ).

The thermo-hydraulic performance parameter ($ThPP$) gives an indication of the worthiness of a heat transfer augmentation approach in reference to a smooth channel (Equation 4-10) – (Yadav & Bhagoria, 2014).

$$\boldsymbol{ThPP = \left(Nu_r/Nu_s\right) \Big/ \left(f_r/f_s\right)^{1/3}} \qquad \text{Equation 4-10}$$

where, the subscripts; $r$ and $s$, indicate the Nusselt number and friction factor for the roughened channel and the smooth channel respectively. The thermal performance of the roughened duct is like a smooth channel if $ThPP$ =1. The system pressure loss is more significant than the heat transfer augmentation for $ThPP$ < 1. The heat transfer augmentation is more significant than the system pressure loss for $ThPP$ > 1. The Nusselt number and friction factor for the smooth channel is derived according to the Dittus-Boelter (Equation 4-11) and Blasius equation (Equation 4-12).

Dittus-Boelter equation (Incropera et al., 2007):

$$\boldsymbol{Nu = 0.0243 Re^{0.8} Pr^{0.4}} \qquad \text{Equation 4-11}$$

Blasius equation (Incropera et al., 2007):

$$f = 0.079Re^{-0.25}$$ Equation 4-12

The CFD model is validated in the next section (*Section 4.3*) and applied to study the heat transfer and pressure loss characteristics of SAH systems with different geometric roughness in Section 4.4.

## 4.3 CFD Validation and Verification

The numerical model is validated by comparison with experiment from literature for a *SAH* roughened with transverse square ribs. This experimental work has been chosen due to absence of well documented experimental work on *SAH* with circular roughness geometry especially for channels with high blockage ratios. *SAH*s with square transverse rib elements pose more complex flow structures than circular transverse ribs due to the higher-pressure gradients and higher streamline curvature. This is evidenced by higher turbulence intensities and kinetic energy for a square rib than circular rib (Chaube et al., 2006). Hence, an accurate representation of *SAH* with transverse square ribs is indicative of reliability of the model for a relatively simpler flow (i.e., *SAH* with transverse circular ribs). The numerical simulation setup is verified with similar CFD study of *SAH* with transverse circular ribs.

### 4.3.1 Experimental Validation

The experimental data for the SAH with transverse square rib roughness is derived from Skullong et al., (2015). The experimental setup consists of 440 *mm* by 300 *mm* by 30 *mm* air channel. The top wall of channel is roughened with square ribs with roughness height and pitch of 6 *mm* and 40 *mm* respectively. The uniform heat flux is applied on the roughened wall. The experimental setup is instrumented to measure the absorber plate temperature, inlet temperature, outlet temperature and pressure drop across the test section from which the Nusselt number (*Nu*) and friction factor (*f*) are derived. The uncertainty of the derived non-dimensional parameters is $\pm 6\%$ for Nusselt number and $\pm 8\%$ for friction factor. Please refer to the Skullong et al., (2015) for a more detailed description of the experimental setup.

#### 4.3.1.1 Experimental Validation Results

The accuracy of the CFD model is compared with the experimental data. Nusselt number and friction factor are the parameters of interest. Root mean square error (*RMSE*) analysis approach given in Equation 4-13 is adopted to quantify the numerical error (Chai & Draxler, 2014).

$$\boldsymbol{RMSE} = \sqrt{\frac{\mathbf{1}}{\boldsymbol{n}}\sum_{\boldsymbol{i=1}}^{\boldsymbol{n}}\left(\boldsymbol{y_{sim}} - \boldsymbol{y_{exp}}\right)^{\mathbf{2}}} \qquad \text{Equation 4-13}$$

where, $y_{exp}$ and $y_{sim}$ are the experimental data and numerical predictions respectively, and *n* is the number of data points. Figure 4-5 compares the numerical prediction of the average Nusselt number against experiment. There is a very good agreement between the numerical model prediction of the Nusselt number and the experimental data for the Reynolds number range considered. The *RMSE* for the numerical prediction of *Nu* is 1.138 for values from 35 to 85 over the Reynolds number range and the coefficient of variation of the *RMSE* is 2%. This is within the experimental error of ± 6% for the *Nu*. For a roughened duct, the thermally fully developed flow establishes in a short length of 2 – 3 hydraulic diameters (Karwa et al., 1999) and periodicity is attained. Hence, the accuracy of prediction of *Nu*. However, the friction loss is more complex and dependent on Reynolds number, entrance and exit lengths. In Figure 4-6, the friction loss in the roughened duct is accurately predicted between the *Re* range from 7,325 to 14,512. The friction factor is overpredicted and underpredicted at lower and higher Reynolds number respectively. The discrepancy may be attributed to the truncation of the secondary flow associated with flow in roughed ducts for a 2D approximation of a 3D phenomena. This is supported with experimental data in Karwa et al., (1999) for which the impact of duct aspect ratio on the frictional loss and heat transfer is investigated (Figure 4-6). It is seen that the frictional loss is higher for higher aspect ratio channels. The difference is more pronounced at lower Reynolds numbers. Similarly, the numerical prediction error for the frictional loss for *Re* < 7,325 is 14% compared to 11% for *Re* > 14,512. The *RMSE* for the numerical prediction of friction factor is 0.0108 for values in the range of 0.099 to 0.139 and the *CV(RMSE)* is 8% for the range of *Re* considered. Since the *CV(RMSE)* for the Nusselt number and friction factor is

within experimental error of the published data, the numerical model is considered sufficiently accurate for further computational analysis.

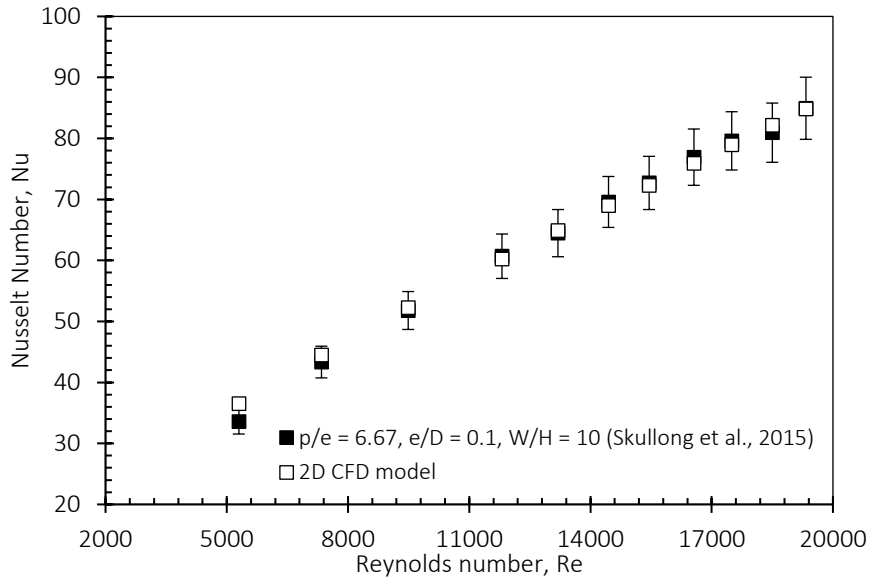


Figure 4-5: Comparison of the numerically derived Nusselt number with experimental data

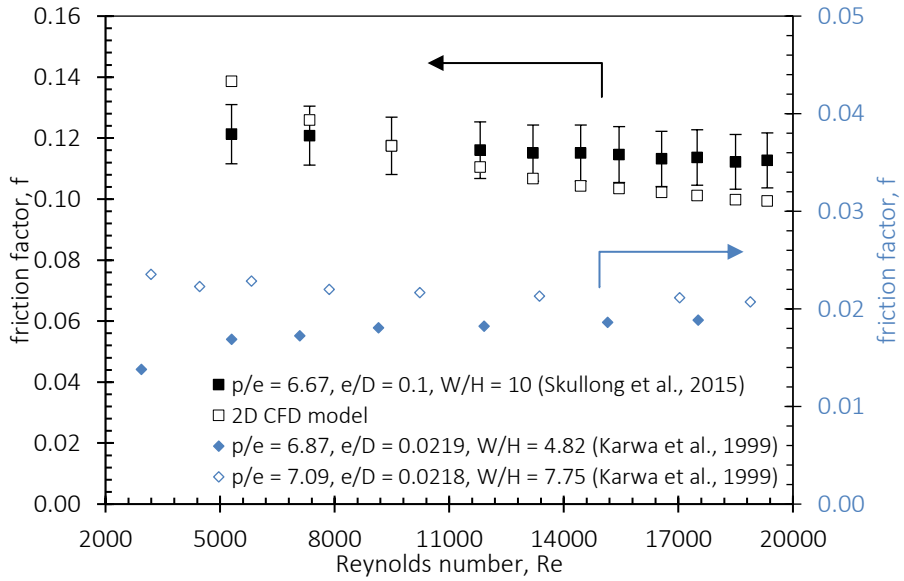


Figure 4-6: Comparison of the numerically derived friction factor with experimental data

### 4.3.2 Numerical Verification

The numerical simulation study is verified with CFD study by Yadav & Bhagoria (2013) for a *SAH* with transverse circular rib roughness. The air channel is 121 *mm* long, 100 *mm*

wide and 20 *mm* high. The top wall of the channel is roughened with circular ribs with roughness height and pitch of 1.4 *mm* and 10 *mm* respectively. The uniform heat flux is applied on the roughened bottom wall. Refer to the cited CFD study for more details on the numerical simulation setup.

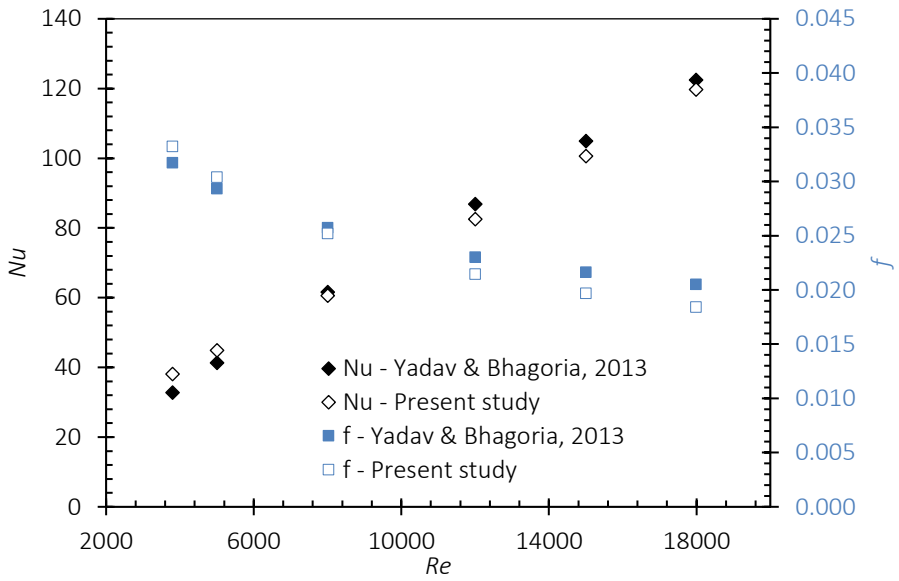


Figure 4-7: Verification of the Nusselt number and friction factor with published numerical study

The Nusselt number and friction factor from Yadav & Bhagoria (2013) and the present *CFD* study is compared in Figure 4-7. The Nusselt number compares well with the published *CFD* study. The *RMSE* for prediction of the Nusselt number is 3.804 for the Reynolds number range considered and the *CV(RMSE)* is 6.31%. The numerical error is attributed to the slight overprediction of Nusselt number for lower Reynolds number values (i.e., $Re < 8{,}000$) and underprediction of the convective heat transfer coefficient for higher Reynolds number values (i.e $Re > 8{,}000$). Similarly, the friction factor is overpredicted at lower Reynolds number values and underpredicted at higher Reynolds number values. The *RMSE* and *CV(RMSE)* for the prediction of the friction factor is 0.0015 and 6.07% respectively. Hence, the numerical model is considered sufficiently accurate for further computational analysis.

## 4.4 Results and Discussion

The results have been presented in two parts. In the first section, the results from the parametric analysis of the effect of roughness height (*e/D*) and roughness pitch (*p/e*) on the thermo-hydraulic performance of a BIPV/T air channel roughened with circular transverse rib. In the second section, the results from geometric optimization of the roughness geometry for the BIPV/T air channel is presented considering the roughness height (*e/D*), roughness pitch (*p/e*) and roughness shape.

### 4.4.1 Parametric analysis of the effect of roughness height (*e/D*) and roughness pitch (*p/e*) on the thermo-hydraulic performance of a BIPV/T air channel roughened with circular transverse rib

The results from the *CFD* based parametric analysis is presented in this section. First, the impact of the geometric parameters (i.e., *e/D* and *p/e*) on the flow structures is presented. The effect of *e/D, p/e* and *Re* on the convective heat transfer coefficient and friction factor is outlined. Then the overall thermo-hydraulic performance is assessed.

#### 4.4.1.1 Flow structure characterization: Near-wall flow

The impact of *p/e* and *e/D* on the flow structures in the roughened channel is quantitatively assessed by analyzing the velocity contours. Table 4-6 shows the three different flow structures identified for the range of relative roughness pitch considered. The flow structure nomenclature is consistent with work done by Awol et al., (2020) for an atmospheric layer flow in the built environment. As seen in Table 4-6, for $p/e < 3.5$, the vortex is trapped between consecutive roughness elements and the mean flow skims over the roughness elements. This is referred to as skimming flow. For $3.5 < p/e < 9.5$, there is interaction between vortices formed in the immediate downstream and upstream of the preceding and ensuing roughness elements, respectively. This is the wake interference flow regime. As the distance between consecutive roughness elements is increased (i.e., $p/e > 9.5$), the isolated roughness flow regime ensues and is characterized by no interaction between the vortices formed at the upstream and downstream of consecutive roughness elements.

Table 4-6: Description of flow regime based on the relative roughness pitch (*p/e*)

| Flow Regime | Description | Velocity Contour |
|---|---|---|
| *p/e* < 3.5 Skimming | *e/D* = 0.1, *p/e* = 2.5 | 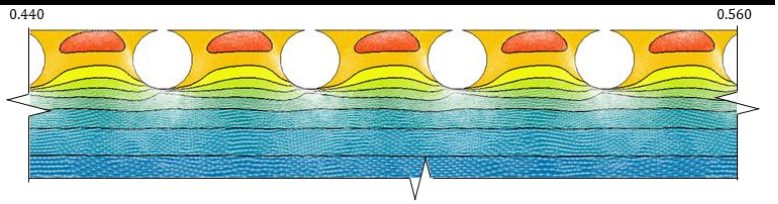  |
| | *e/D* = 0.02, *p/e* = 2.5 | 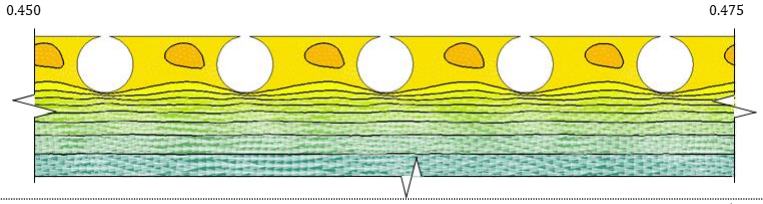  |
| 3.5 < *p/e* < 9.5 Wake interference | *e/D* = 0.1, *p/e* = 7.5 | 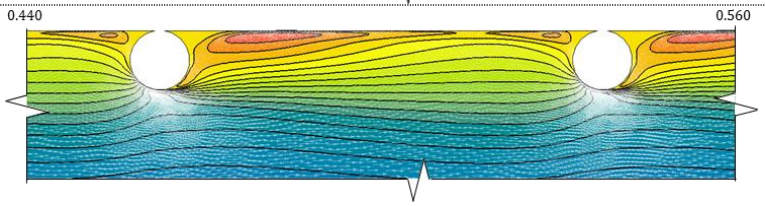  |
| | *e/D* = 0.02, *p/e* = 7.5 | 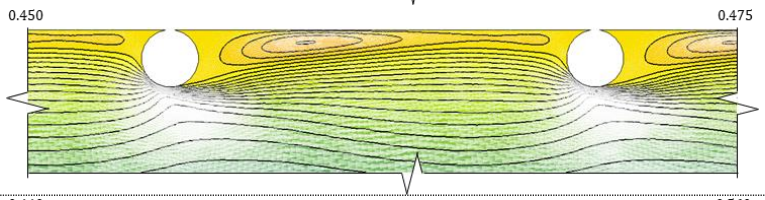  |
| *p/e* > 9.5 Isolated roughness | *e/D* = 0.1, *p/e* = 10 | 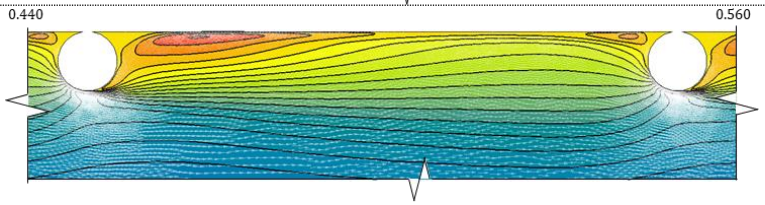  |
| | *e/D* = 0.02, *p/e* = 12.5 | 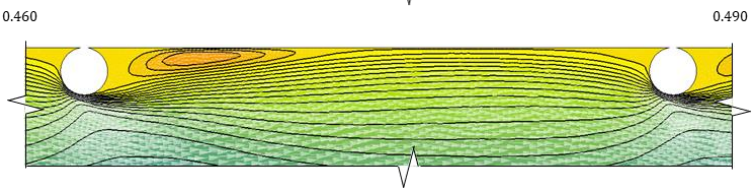  |
| | |   |

The upper and lower bounds of the wake interference flow regime which inherently determines the bounds for the isolated roughness flow regime and the skimming flow regime is determined by observing trends in the wall shear stress profile determined from the CFD simulation. Figure 4-8a shows the dimensionless wall shear stress between consecutive roughness elements for different rib spacings. The shear stress peak is highest and lowest for *p/e* values of 3.5 and 4.5 respectively which indicates that the strength of

the vortex diminishes as the spacing between the ribs are increased. The positive wall shear stress that occurs at the immediate upstream and downstream of the preceding and ensuing roughness elements indicate the presence of smaller magnitude trapped vortices. This is the reason for the hot spot problem inherent with transverse roughness elements. As the spacing is increased (i.e., $p/e > 3.5$), an inflection point in the wall shear stress profile is evident. This indicates the start of the wake interference flow regime.

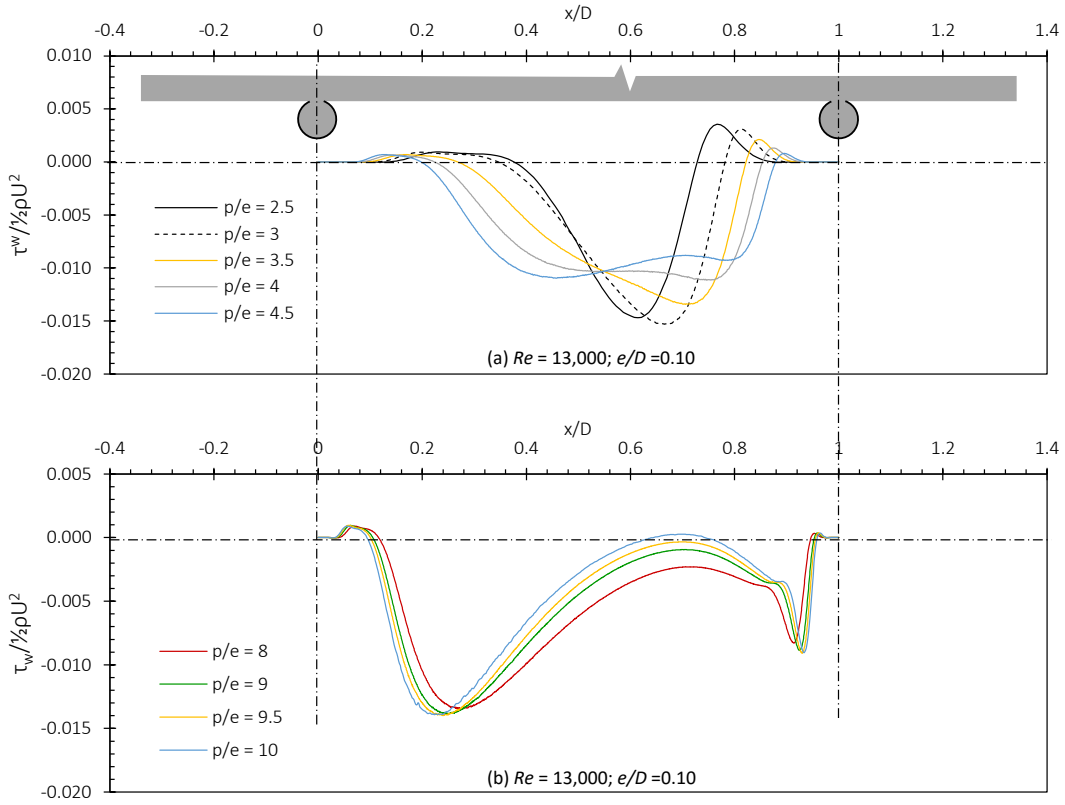


Figure 4-8: wall shear stress between consecutive ribs to determine the (a) lower-bound and (b) upper-bound, of the wake interference region ($Re$ = 13,000; $e/D$ = 0.10)

Similarly, the wall shear stress profile is plotted to determine the upper bound of the wake interference region (Figure 4-8b). The wall shear stress is plotted for $p/e$ values of 8, 9, 9.5 and 10. The upper bound of the wake interference flow regime is determined as the $p/e$ value for which the shear stress becomes positive at the inflection point. This indicates flow reattachment. As seen in Figure 4-8b, this occurs for $p/e > 9.5$. Beyond this value, the isolated flow roughness flow regime begins. Although, the wall shear stress profile is illustrated for $e/D$ value of 0.10, similar trend is noticed for the $e/D$ values considered and

is shown in Figure 4-9. The shear stress profiles are similar, and the flow regime is applicable for all relative roughness heights.

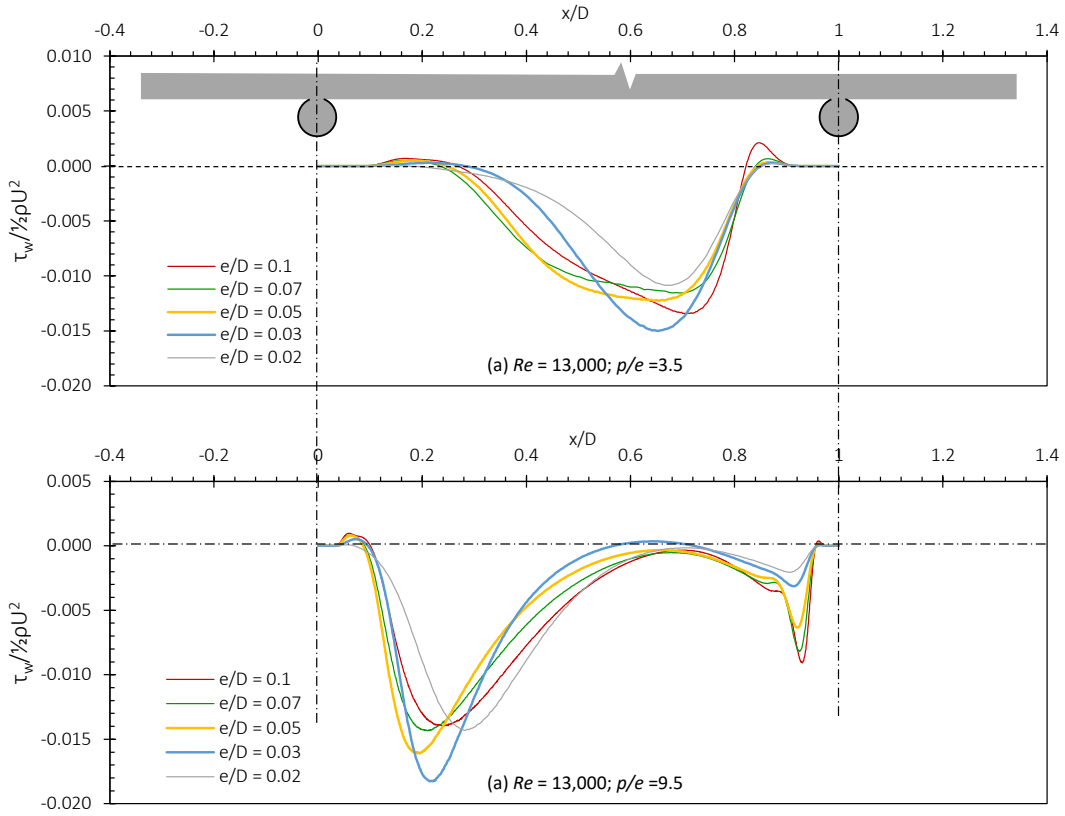


Figure 4-9: wall shear stress profiles showing similarity of flow for the different *e/D* values for the (a) lower-bound and (b) upper-bound of the wake interference region

### 4.4.1.2 Average Heat Transfer Characteristics

The impact of *e/D*, *P/e* and *Re* on heat transfer is presented in this section. Figure 4-10 shows the variation of *Nu* with Reynolds number for different *e/D* values and *p/e* value of 7.5 compared with a smooth channel. Nusselt number increases with increase in the Reynolds number. This is due to the thinning of the boundary layer; that acts to resist heat transfer, with increase in Reynolds number. The influence of the roughness elements on the heat transfer can also be seen. Up to 25%, 35%, 49%, 50%, 48% increase in Nusselt number for *e/D* values of 0.02, 0.03, 0.05, 0.07, and 0.10 are compared with the smooth channel. The protruding roughness elements cause flow separation creating a region of vortex flows between consecutive roughness elements. These vortices enhance flow

mixing due entrainment of the fluid (i.e., air) from the mean flow to the regions closer to the absorber plate. The stronger the turbulence, the stronger the strength of the vortices. Hence, the enhancement in heat transfer is more pronounced at higher Reynolds numbers. Using *e/D* value of 0.02 as case study, the enhancement in heat transfer at *Re* of 5,000 is 20% and increases up to 25% as the Reynolds number increases.

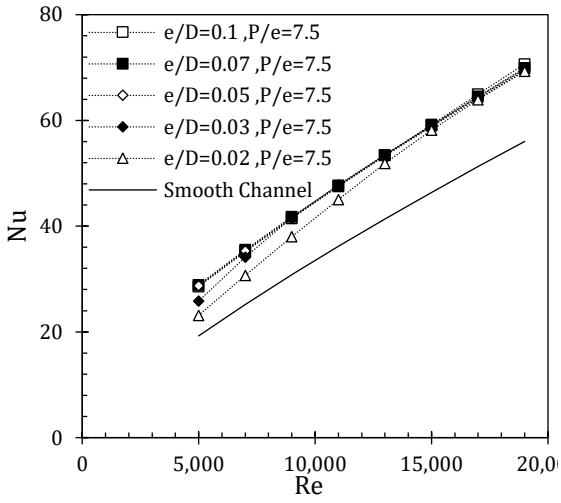


Figure 4-10: Variation of *Nu* with *Re* for different values of *e/D* and *p/e* = 7.5

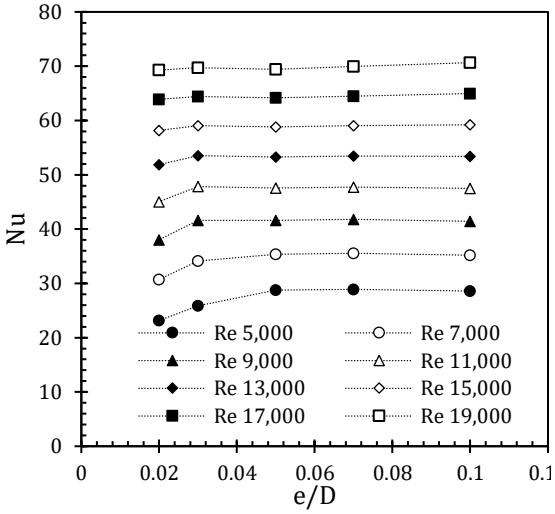


Figure 4-11: Variation of *Nu* with *e/D* for different *Re* values and *p/e* = 7.5

The effect of the relative roughness height on the convective heat transfer is explicitly shown in Figure 4-11 for similar pitch ratio of 7.5. The convective heat transfer increases initially with increase in the blockage ratio, but beyond *e/D* value of 0.03, the convective heat transfer is independent of the relative roughness ratio. This is contrary to what is typically reported in some literature which suggest that the convective heat transfer increases monotonously with increase in the relative roughness ratio (Karwa et al., 1999; Bhagoria et al., 2002; Kumar et al., 2019). This is true for lower blockage ratios; however, this may not be the case for higher blockage ratio flows. This is like findings in Skullong et al., (2015) in that the enhancement of heat transfer for the thin rib diminished as the blockage ratio increased. This is explained by a detailed look at the turbulence kinetic energy (*TKE*) profile for the range of roughness heights considered in this study (Figure 4-12). The dimensionless *TKE* profile is extracted for a line extending from the top of the channel to the bottom of the channel that is situated between consecutive roughness elements (i.e., half pitch length in the direction of the flow). The profiles are typical of the

developed flow regions in the test channel based on the assumption of periodicity after about 2 – 3 hydraulic diameters when the thermal boundary layer is fully developed (Gawande et al., 2016).

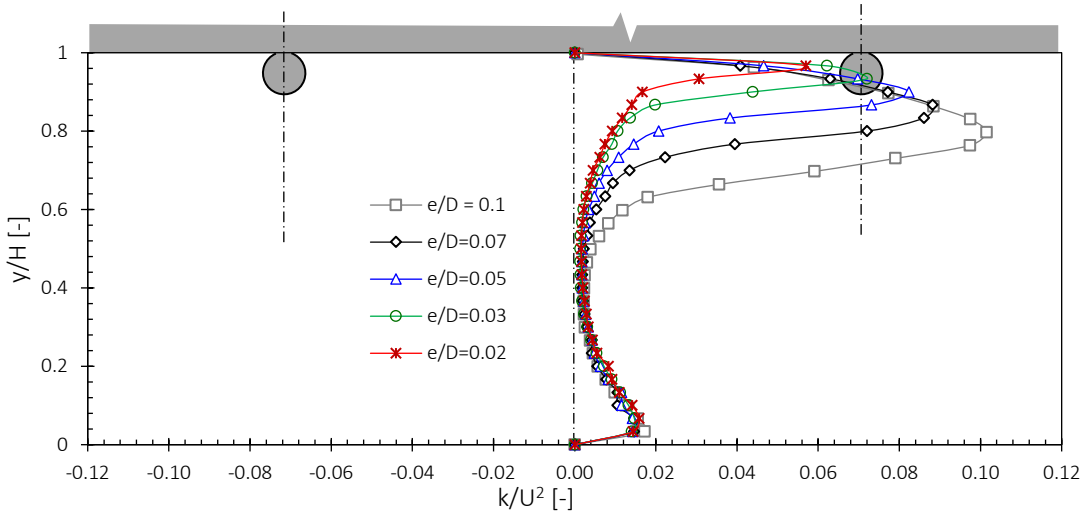


Figure 4-12: Variation of the TKE with height along the mid-plane between consecutive roughness elements for *Re* value of 17,000

As seen in Figure 4-12, the higher the blockage ratio, the higher the *TKE*. This is because of the flow acceleration due to the macroscopic narrowing of the flow channel for higher blockage ratios. Although the *TKE* is highest for the highest blockage ratio, this occurs at a considerable distance away from the absorber plate. A closer look shows that the turbulence intensity profiles are similar close to the plate. This is important because in this region, the increase in *TKE* directly translates to an increase in the heat transfer from the absorber plate to the fluid. Beyond this region, the increase in the turbulence kinetic energy may add more to the pressure loss of the system. This will be discussed in more detail in the Section 4.3.

In order to understand the impact of the relative roughness pitch on the heat transfer characteristics, the roughness Reynolds number for the range of geometric and flow parameters according to Eqn. (2). The flow classification based on the derived $e^+$ value is given in Equation 4-14 and Equation 4-15.

Fully rough flow:

$$\begin{cases} e/D > 0.05, & \forall\, Re \\ 0.05 \le e/D \le 0.03, & \forall\, Re \ge -400000(e/D) + 27000 \end{cases}$$ Equation 4-14

Transitionally rough flow:

$$\begin{cases} 0.05 \le e/D \le 0.03, & \forall\, Re \le -400000(e/D) + 27000 \\ e/D < 0.03, & \forall\, Re \end{cases}$$ Equation 4-15

As such, emphasis is placed on the *e/D* values of 0.07 to describe the fully rough flows and 0.02 for the transitionally rough flows. Figure 4-13a and Figure 4-13b show the effect of changing the relative roughness pitch on the heat transfer characteristics in the air channel. The maximum heat transfer occurs for *p/e* values of 14.29 and 12.5 for *e/D* of 0.07 and 0.02 respectively.

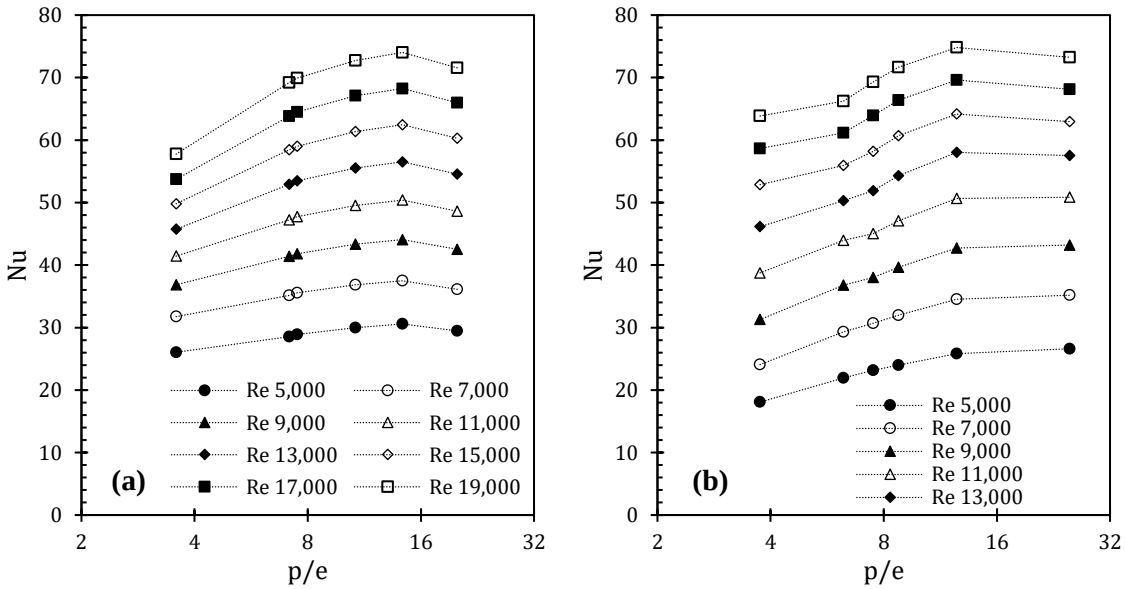


Figure 4-13: Variation of *Nu* with *p/e* for different values of *Re* under (a) fully rough flow (i.e., *e/D* = 0.07) and (b) transitionally rough flow (i.e., *e/D* = 0.02)

The optimal spacing for heat transfer enhancement suggests an isolated roughness flow regime for the transitionally and fully rough flow (refer to Table 4-6 for flow classification). This isolated roughness flow regime ensures that the ribs are sufficiently spaced apart to allow flow reattachment before the adjacent rib. This is because the maximum heat transfer coefficient occurs in the region of the reattachment point (Bhagoria

et al., 2002). At the optimal spacing (i.e., *p/e*), *Nu* is higher in for the transitionally rough flow compared to the fully rough flow. The slightly better heat transfer enhancement can be explained with the plot of the dimensionless wall shear stress after periodicity in the air channel has been reached (Figure 4-14). At about 0.4 pitch length the wall shear stress becomes positive which is indicative of an attached flow. The flow detaches at 0.8 pitch length because of the adverse pressure gradient created by the ensuing roughness element. The attachment and reattachment points are similar for the transitionally rough flow and the fully rough flow (i.e., *e/D* values of 0.02 and 0.07 respectively). However, there is dissimilarity between the profiles for *e/D* = 0.02 and *e/D* = 0.07. The wall shear stress is higher for *e/D* value of 0.02 in the immediate downstream of the preceding roughness element which may be indicative of a stronger vortex. The wall shear stress is higher for *e/D* value of 0.07 in the immediate upstream of the ensuing roughness element. The shear stress in the reattached flow region is similar for *e/D* values of 0.02 and 0.07 respectively. The overall contribution yields a slightly higher heat transfer coefficient for the transitionally rough flow regime than the fully rough flow regime.

The heat transfer enhancement caused by the roughness elements can be seen in Figure 4-15. The heat transfer enhancement is given by $Nu_r/Nu_s$ which is the ratio of the heat transfer coefficient of the roughened channel to the smooth channel. In the figure, for *e/D* = 0.07, the roughened duct showed slightly better heat transfer characteristics compared to a smooth channel. The maximum heat transfer enhancement is 1.6 for *p/e* value of 14.29 and *Re* value of 5,000 implying that the roughness elements are more efficient at lower flow rates. Similarly, the maximum heat transfer enhancement is 1.4 for *e/D* = 0.02 for *p/e* value of 14.29 and *Re* value of 5,000. For relative pitch ratios below four (4), there is heat transfer diminution. The fluid skims over the roughness elements inhibiting mixing between the mean flow and the secondary flow between the ribs.

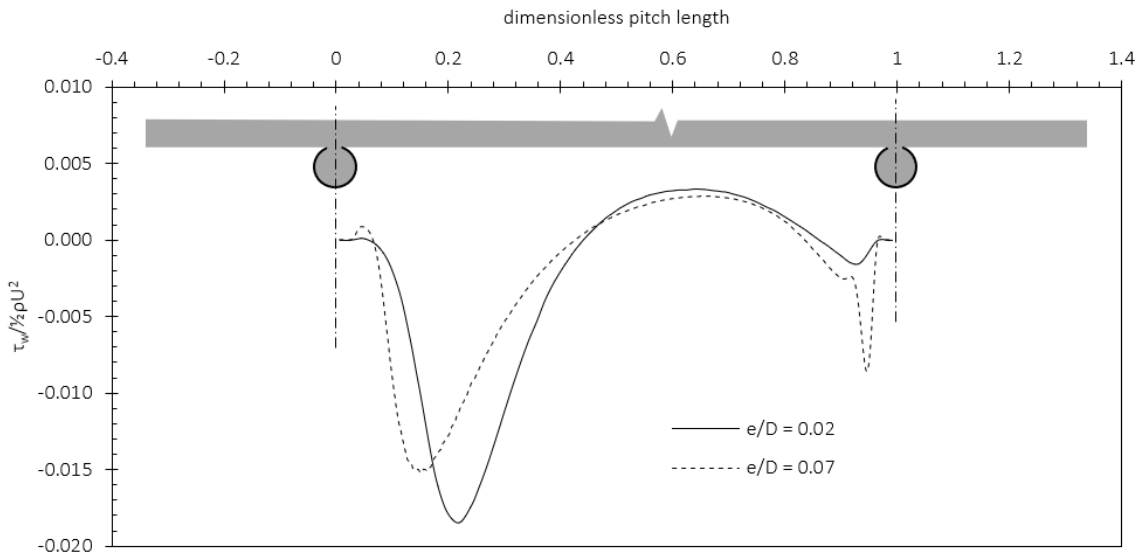


Figure 4-14: Typical wall shear stress distribution between consecutive roughness elements

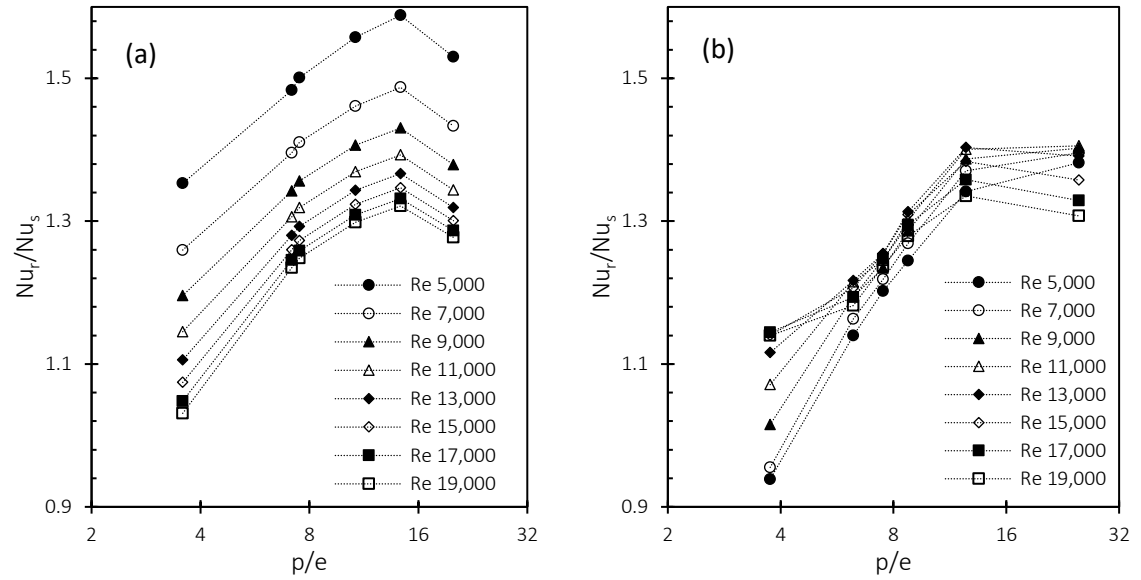


Figure 4-15: Variation of $Nu_s/Nu_r$ with $p/e$ for different values of $Re$ under (a) fully rough flow regime (i.e., $e/D$ = 0.07) and (b) transitionally rough flow regime (i.e., $e/D$ = 0.02)

### 4.4.1.3 Flow Friction Characteristics

Figure 4-16a shows the variation of the friction factor with Reynolds number. The friction factor reduces with increase in Reynolds number. The gradient of the curves in Figure 4-16a is relatively higher at lower Reynolds numbers than at higher Reynolds numbers. It is anticipated that the friction factor attains a constant value with further Reynolds number

Increase. This is due to the suppression of the viscous sub-layer with increase in the Reynolds number such that the energy loss associated with vortex formation and shedding attains a constant value and is not dependent on the viscous effects (Karwa et al., 1999; Yadav & Bhagoria, 2014). The friction factor increases with increase in *e/D* for the range of Reynolds numbers (Figure 4-16b). This is attributed to the reduction in the viscous sub-layer such that the form drag overrides the skin friction (Karwa et al., 1999). Intuitively, the form drag increases with *e/D*. This manifests as an increase in the turbulence kinetic energy as seen in Figure 4-12. This highlights the detriment of increasing *e/D* in bid to increase the heat transfer characteristics. As a rule of thumb, in order to minimize friction losses, the turbulence must be created in the laminar sub-layer (Yadav & Bhagoria, 2014).

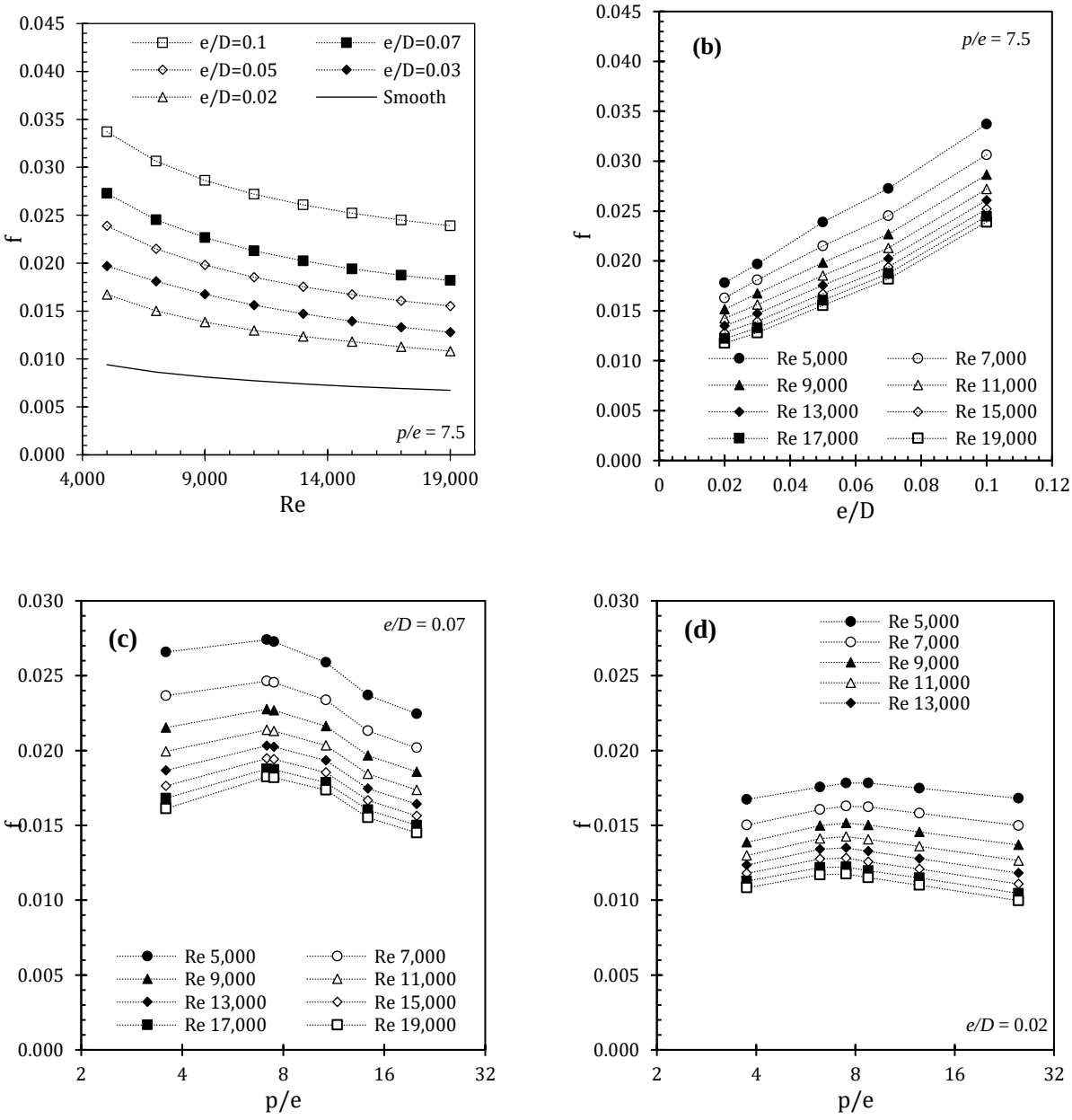


Figure 4-16: Variation of friction factor with (a) Reynolds number for different values of *e/D* (b) *e/D* for different Reynolds numbers (c) *p/e* for *e/D* = 0.07 (d) *p/e* for *e/D* = 0.02

The effect of the *p/e* can be seen in Figure 4-16c and Figure 4-16d for *e/D* values of 0.07 and 0.02 to indicate a fully rough flow and transitionally rough flow respectively. It can be observed that there is a relative roughness pitch that maximizes the friction factor. The maximum friction factor occurs at *p/e* value of 7.15 and 7.5 for *e/D* values of 0.07 and 0.02

respectively. In both cases, the optimum pitch ratios are suggestive of a wake interference flow (Table 4-6).

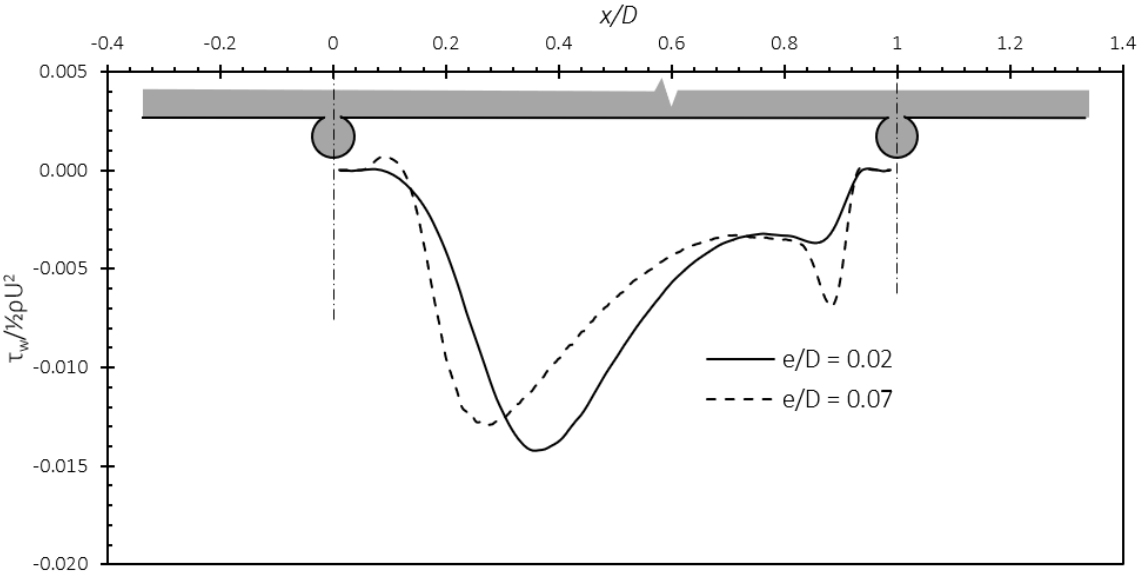


Figure 4-17:Typical wall shear stress distribution between consecutive roughness elements at max. friction

The wake interference flow is exasperated by the plot of the typical wall shear stress profile between consecutive roughness elements (Figure 4-17). The wall shear stress is negative throughout as expected with an inflection occurring at about 75% of the pitch length. There are three (3) noticeable peaks in the fully rough flow (i.e., $e/D$ = 0.07); one positive peak and two negative beaks, compared to the two (2) noticeable peaks for the transitionally rough flow ($e/D$ = 0.02). These peaks are indicative of the relative size of the trapped vortex in the immediate upstream of the contact point between the absorber plate and the roughness element. The energy of the recirculation flow is sustained by the momentum transfer with the undisturbed flow in the channel. As such, more energy is required to sustain the recirculation for the fully rough flow than in the transitionally rough flow. This loss of energy is reflected in the higher friction factor for the fully rough flow.

The friction factor penalty inherent with roughness elements can be seen in Figure 4-18. The friction factor penalty ($f_r/f_s$) is defined as the ratio of the friction factor of the roughened channel to the smooth channel under identical operating conditions. The maximum friction

factor penalty is 2.84 and 1.85 for *e/D* values of 0.07 and 0.02 respectively. This occurs a *p/e* values of 7.14 and 7.5 for *e/D* values of 0.07 and 0.02 respectively.

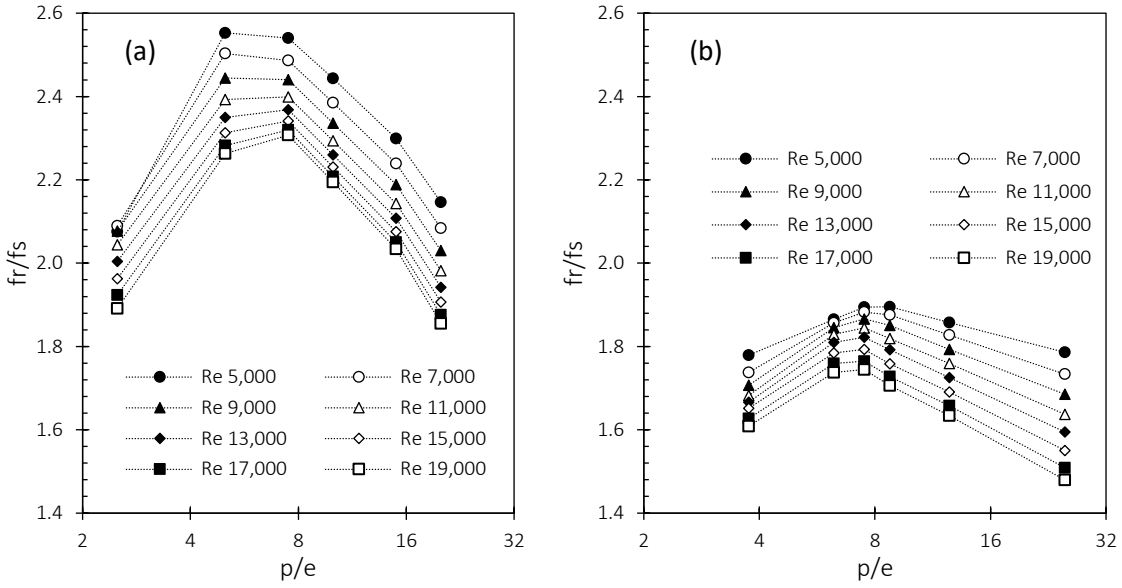


Figure 4-18: Variation of $f_r/f_s$ with *p/e* for different values of *Re* under (a) fully rough flow (i.e., *e/D* = 0.07) and (b) transitionally rough flow (i.e., *e/D* = 0.02)

### 4.4.1.4 Thermo-hydraulic Performance Parameter

The *p/e* value with the highest heat transfer enhancement did not coincide with the *p/e* with the highest friction factor penalty. Hence, both parameters are evaluated congruently to optimize the geometry such that the heat transfer enhancement is maximized, and the friction factor enhancement is minimized. This is achieved by considering the Thermo-hydraulic performance parameter (*ThPP*). Figure 4-19 shows the variation of the *ThPP* with Reynolds number for *e/D* values of 0.07 and 0.02. For the roughness height in the fully rough regime (i.e., *e/D* = 0.07), the friction penalty is significant, hence, the *ThPP* is mostly below one. The maximum *ThPP* for *e/D* of 0.07 occurs at *p/e* value of 14.29 and Reynolds number of 5,000. *ThPP* reduces significantly with increase of *Re*, and above *Re* value of 17,000 the friction factor penalty becomes more significant than the heat transfer enhancement. In the transitionally rough flow regime (i.e., *e/D* = 0.02), the friction penalty is more significant than the heat transfer enhancement for *p/e* values less than 6.25. The heat transfer enhancement is more significant than the friction factor penalty for $p/e \geq 6.25$.

The maximum *ThPP* for *e/D* = 0.02 occurs at *p/e* value of 25 and Reynolds number of 11,000. This signifies that the lower the blockage ratio, the higher the operational range of the solar air heater.

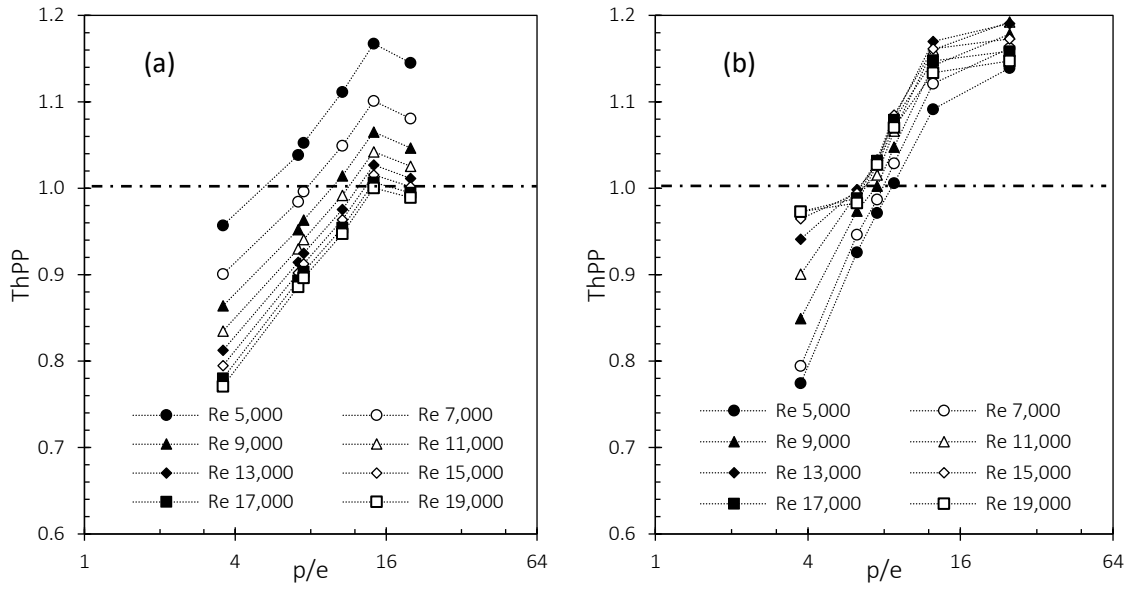


Figure 4-19: Variation of *ThPP* with *p/e* for different values of *Re* under (a) fully rough flow (i.e., *e/D* = 0.07) and (b) transitionally rough flow (i.e., *e/D* = 0.02)

Figure 4-20 compares the *ThPP* for the optimum *p/e* values for the range of relative roughness heights (*e/D*). In the fully rough flow regime (i.e., *e/D* values of 0.1 and 0.07), *ThPP* decreases with increase in Reynolds number because of the higher friction penalty. In the transitionally rough regime (*e/D* = 0.02), *ThPP* increases with Reynolds number. For the range of geometrical and operational parameters considered, the maximum *ThPP* occurs for *e/D*, *p/e* and *Re* values of 0.05, 20 and 5,000 respectively.

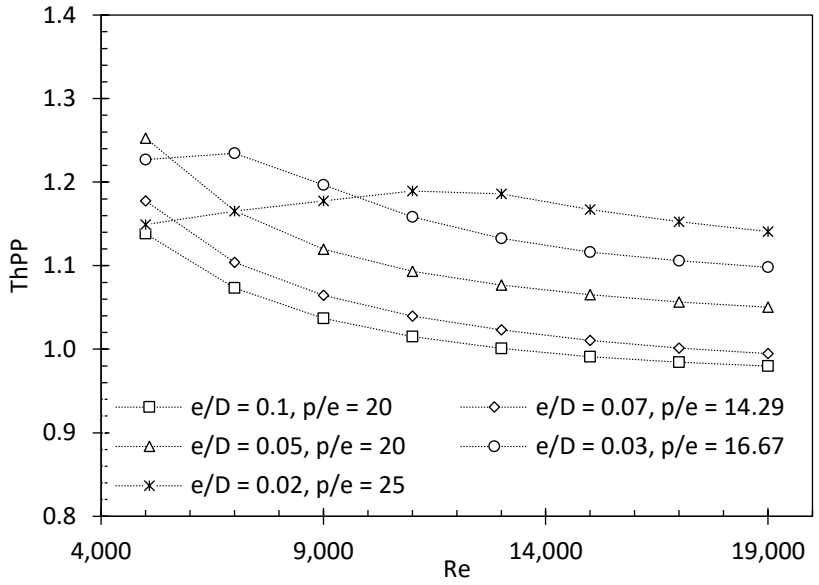


Figure 4-20: Variation of *ThPP* with Re for all values of *e/D* at their optimal p/e configuration

#### 4.4.1.5 Development of correlation for Nusselt number and friction factor for a circular transverse rib roughened channel

In this section, the *Nu* and *f* are correlated with the relative roughness pitch (*p/e*), relative roughness height (*e/D*) and Reynolds number. The correlation is developed by a stepwise regression analysis that involves first correlating the *Nu* with *Re*, then with *e/D* and finally with *p/e*. The functional relationship for *Nu* and *f* are given in Equation 4-16 and Equation 4-17.

$$\boldsymbol{Nu = \frac{0.0326\, Re^{0.7079}}{\exp\left\{0.1058\, ln\left(\frac{p}{e}\right)^2\right\}} \times \left(\frac{e}{D}\right)^{0.0435} \times ln\left(\frac{p}{e}\right)^{0.6199}} \qquad \text{Equation 4-16}$$

$$\boldsymbol{f = 4.682\, Re^{-0.338}\left(\frac{e}{D}\right)^{1.0413} \times \left(\frac{p}{e}\right)^{1.5825} \times exp\left\{0.0884 \ln\left(\frac{p}{e}\right)^3 - 0.6871 \ln\left(\frac{p}{e}\right)^2 + 0.1097\, \ln\left(\frac{e}{D}\right)^2\right\}} \qquad \text{Equation 4-17}$$

The accuracy of the developed correlation is checked with results of the computational analysis for the Nusselt number (Figure 4-21a) and friction factor (Figure 4-21b). The derived correlation predicts 92% and 96% of the CFD simulated values to within 10% error for the Nusselt number and friction factor respectively. Therefore, the derived correlations can be relied upon to predict the heat transfer coefficient for a solar air heater roughened with circular transverse roughness elements of various combinations of Reynolds number, *e/D* and *p/e*.

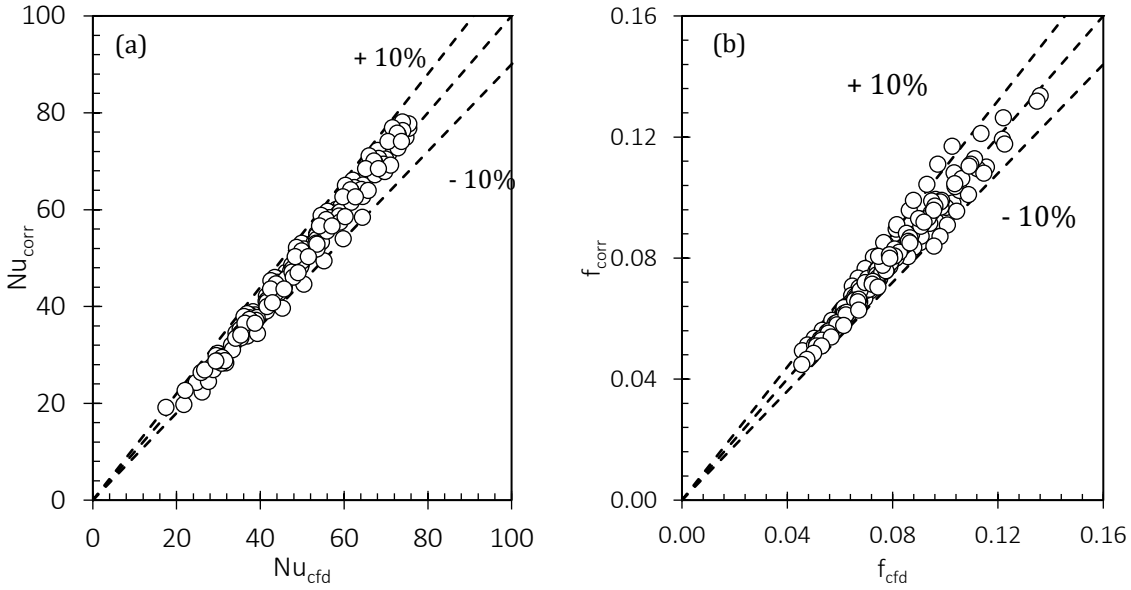


Figure 4-21: Comparison of predicted and simulated data for (a) Nusselt number and (b) friction factor

## 4.4.2 Geometric optimization of transverse rib in a building integrated photovoltaic and thermal system air channel with emphasis on roughness shape, height and spacing

The results from the computational analysis on the effect of transverse rib shape on the heat transfer and friction factor is presented.

### 4.4.2.1 Effect of shape of the transverse rib profile

The effect of changing the transverse roughness profile is examined in this section. Figure 4-22 compares the heat transfer in the channel roughened with transverse roughness elements of different shapes and a smooth channel. The comparison is done for *e/D* = 0.10

and *p/e* = 7.5. The heat transfer enhancement attributed to the presence of the transverse roughness elements for the shapes can be seen. Up to 48%, 76%, 74%, and 78% increase in *Nu* is seen for the circle, semi-circle, square and triangle respectively. The maximum heat transfer improvement is noticed at *Re* value of 5,000 for all the transverse roughness shapes considered. The triangular transverse roughness element yields the highest improvement in heat transfer. In fact, at *Re* = 19,000 the Nusselt number arranged in descending order is 96.7, 84.2, 83.1, and 70.7 for the triangular, semi-circular, square and circular shaped transverse roughness elements.

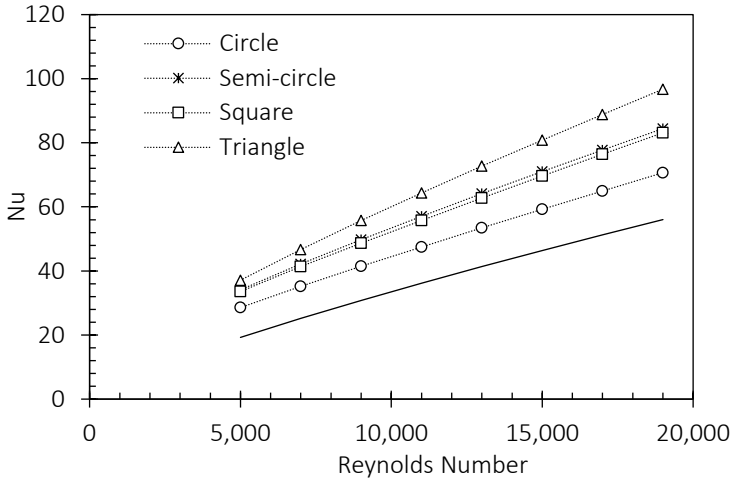


Figure 4-22: Effect of varying the transverse rib profile on the Nusselt number for *e/D* = 0.10 and *p/e* = 7.5

The better heat transfer enhancement for the triangular roughness element can be explained quantitatively with the aid of the velocity contour plot as shown in Table 4-7. The velocity contours for all four transverse rib roughness profiles show a wake interference flow in that the vortices formed in the immediate downstream and upstream of the preceding and ensuing rib interfere with each other (Section 4.4.1.1). More importantly, is the size of the trapped vortex in the immediate upstream of the first roughness element in the velocity contours. The size of the trapped vortex is largest for the circular rib and smallest for the triangular rib. The acute angle created by the bond between the circular rib and the bottom of the absorber plate increases the potential for the hot spot problem which is fostered by the trapped vortex and a consequent reduction in heat transfer. However, the obtuse angle

associated with the bond between the triangular rib and the absorber plates aids shedding of the trapped vortex and consequently enhancing the heat transfer.

Table 4-7: velocity contours for the different transverse rib roughness for *e/D* = 0.10 and *p/e* = 7.5

| Description | Velocity Contour |
|---|---|
| *Circle* | 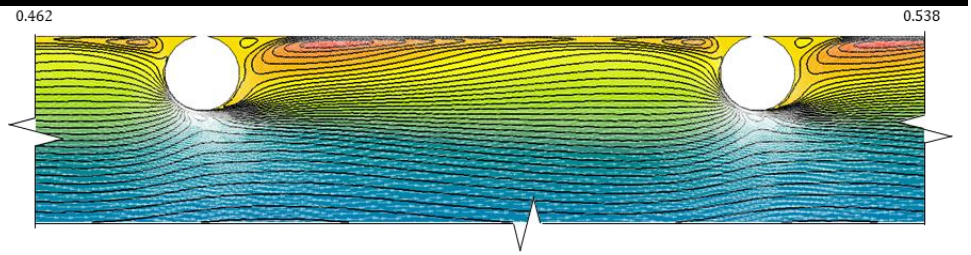 |
| *Square* | 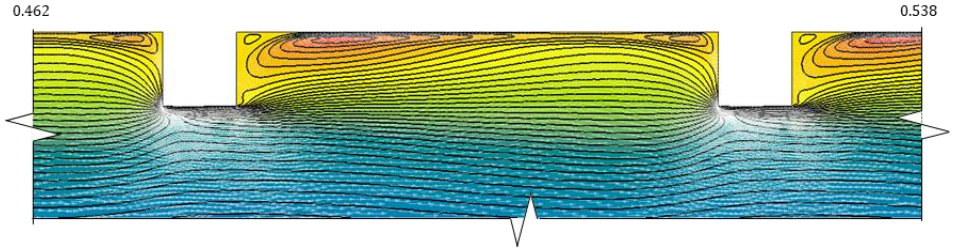 |
| *Semi-circle* | 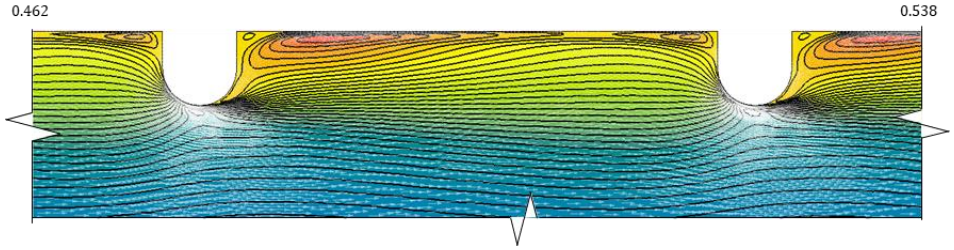 |
| *Triangle* | 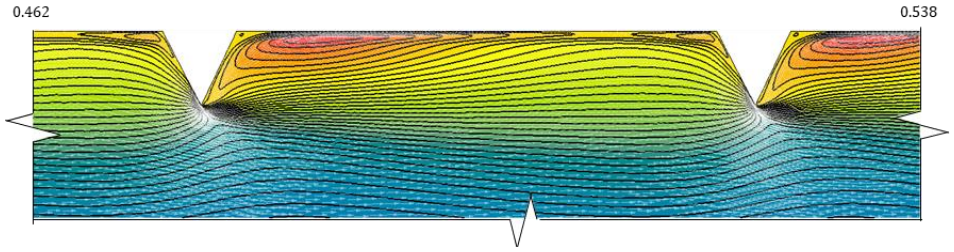 |



The better heat transfer enhancement of the triangular roughness element for heat transfer enhancement is further explained by the wall shear stress profile between consecutive ribs (Figure 4-23). The wall shear stress profile shows the highest negative peak (i.e., -0.016 for the triangular rib compared to -0.013 for the other roughness profiles) and is suggestive of a stronger vortex in the immediate downstream of the first rib which aids heat removal from the hot top surface. Also, the trapped vortex for the triangular rib is smaller as

evidenced by the shorter length of the positive shear stress below 10% of the pitch length between consecutive ribs. All these contribute to the better heat transfer performance of the triangular roughness element over the other shapes considered.

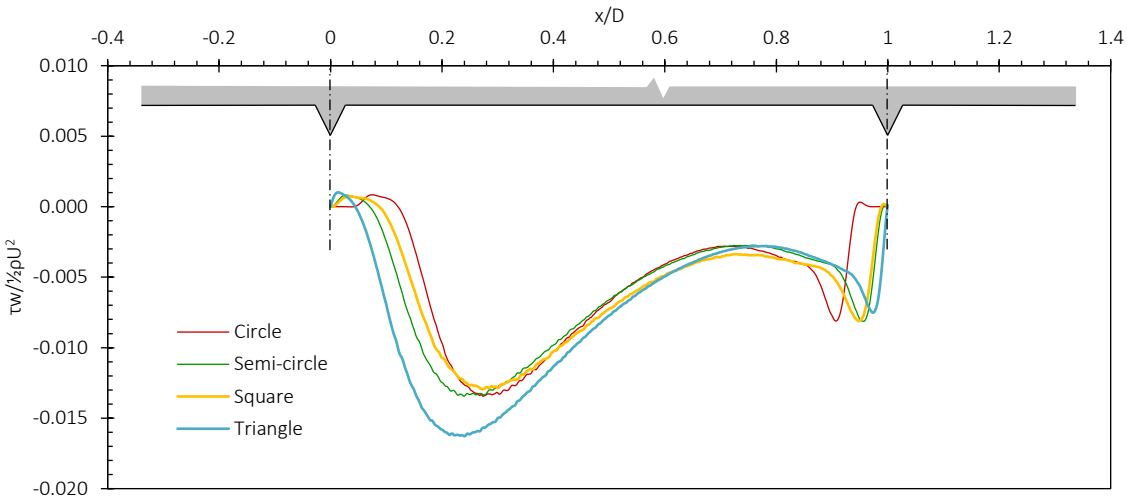


Figure 4-23: Comparison of the typical wall shear stress profiles for different transverse roughness profiles for $e/D$ = 0.10 and $p/e$ = 7.5

Further, the pressure loss penalty associated with the different transverse roughness rib profiles is examined. The impact of the roughness profile on the friction factor is two-fold. First, is the narrowing of the channel as the fluid transitions from the smooth entrance to the disturbed flow in the test section. This causes, the fluid to accelerate thereby increasing the turbulence in the test section. This is emphasized by the plot of the turbulence kinetic energy (*TKE*) in the regions close to the top surface of the test section (Table 4-8). As observed in Table 4-8, the channel with the triangle ribs shows the highest *TKE*. The channel with the circular rib and the semi-circular rib show similar turbulence characteristics.

Table 4-8: Turbulent kinetic energy contours for the different transverse rib roughness

| **Description** | **Turbulent kinetic energy** |
|---|---|
| *Circle* | 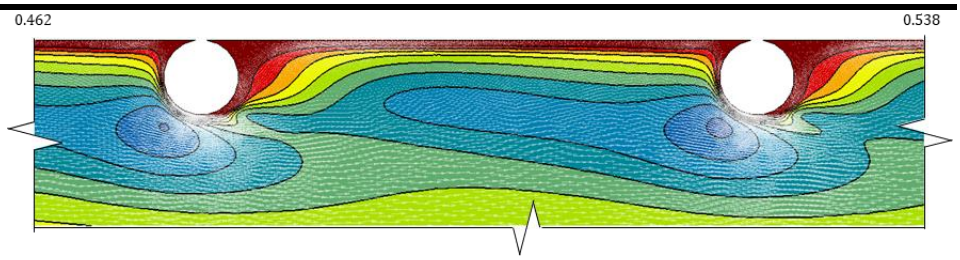  |

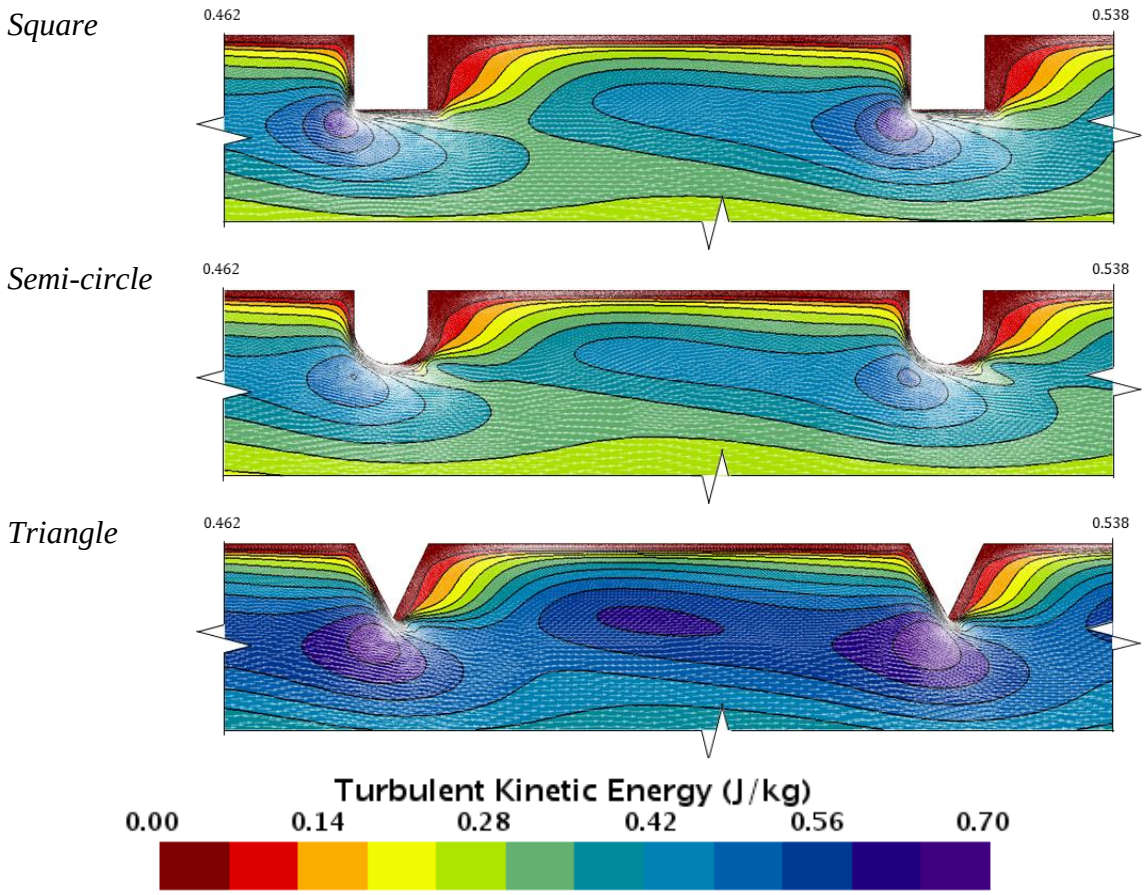


The other aspect of the shape of the ribs as it pertains to the increase in the friction factor is the momentum exchange between the secondary flow (i.e., vortices) and the mean flow (i.e., the undisturbed flow in the channel). This essentially contributes to the pressure loss. Hence, the higher the strength of the vortices, the higher the contribution to the pressure loss across the channel. The strength of the vortices formed between consecutive ribs is indicated by the area under the wall shear stress profile (Figure 4-23). The area under the curve is calculated using the Reimann sum in Eqn. 13 (Sealey, 2014).

$$\sum_{k=1}^{n} f(x_k)\Delta x \qquad \text{Equation 4-18}$$

where, $x_k$ is any x-value on the $i$-th subinterval, $\Delta x = (b-a)/n$. $a$ and $b$ are the left and right endpoints of the interval. The Reimann sum yields 0.00554 [-], 0.00618 [-], 0.00617 [-], and 0.00748 [-] for the circular, semi-circular, square, and triangular rib respectively. The vortex strength is strongest for the triangular rib while the vortex strength for the circle,

semi-circle and square rib are similar. The combination of the pressure loss due to the blockage effects and the loss due to momentum exchange that drives the recirculation yields a higher friction factor for the triangular rib and similar friction factor for other roughness profiles considered as seen in Figure 4-24.

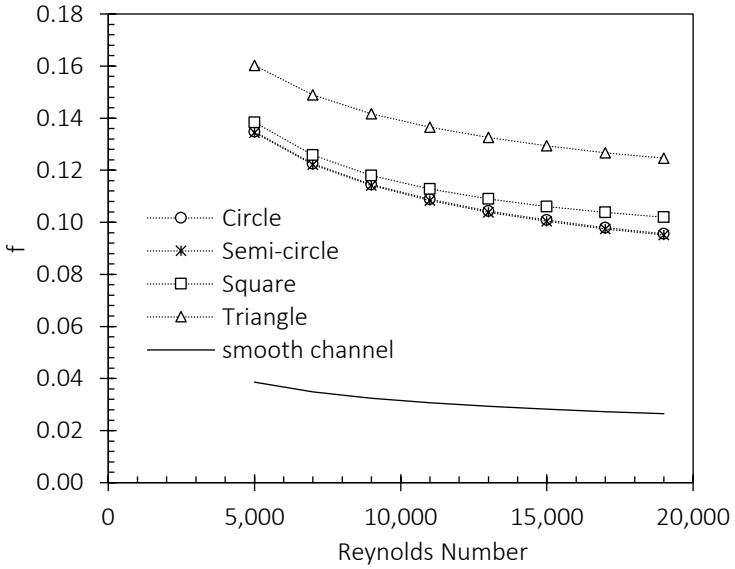


Figure 4-24: Effect of varying the transverse rib profile on the friction factor for *e/D* = 0.10 and *p/e* = 7.5

### 4.4.2.2 Effect of relative pitch ratio

The transverse roughness rib with the triangular shape showed the most significant thermo-hydraulic performance, hence, further parametric analysis is conducted to understand the impacts of the relative roughness pitch on Nusselt number and friction factor.

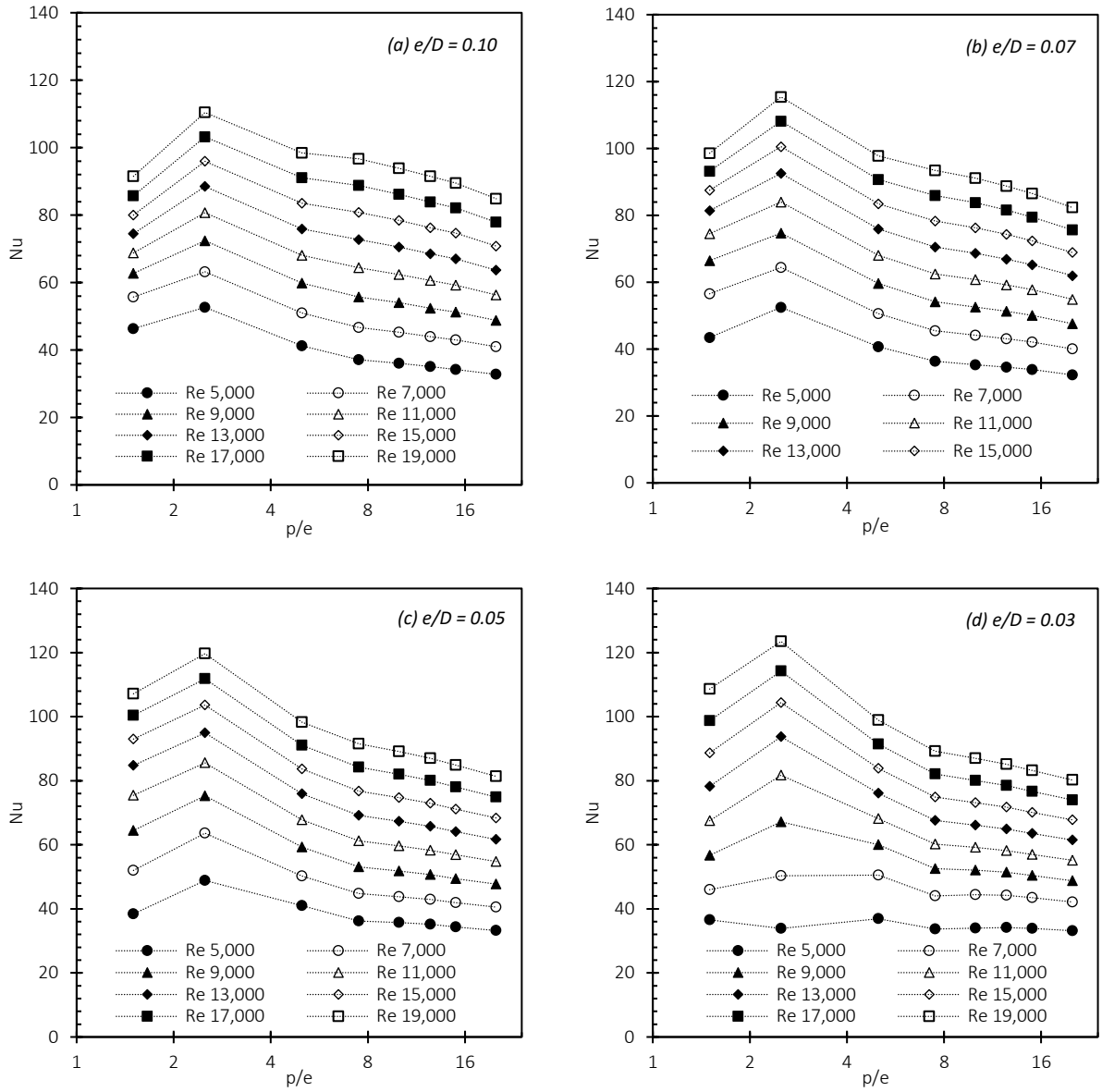


Figure 4-25: The effect of varying *p/e* on the Nusselt number for different relative roughness heights

Figure 4-25 shows the effect of varying the distance between roughness elements on the heat transfer. The Nusselt number increases with increase in Reynolds number as expected. It can be observed that at higher Reynolds numbers (i.e., *Re* > 13,000), the Nusselt number increases as *e/D* decreases which is especially noticeable at the curve apex. For instance, the Nusselt number for *e/D* values of 0.10, 0.07, 0.05 and 0.03 at the apex for *Re* = 19,000 is 110.411, 115.407, 119.647, and 123.457 respectively. However, for lower Reynolds numbers (i.e., *Re* < 13,000), Nusselt number increases with increase in *e/D*. For instance,

the Nusselt number for *e/D* values of 0.10, 0.07, 0.05 and 0.03 at the apex for Reynolds number of 5,000 is 52.663, 52.509, 48.852, and 33.923 respectively. This is the case because of the thinning the boundary layer with increase in Reynolds number. As explained in Section 4.4.1, the turbulence for higher *e/D* values is created at a considerable distance away from the absorber plate especially for higher Reynolds number flows, hence, the increase in turbulence kinetic energy for higher roughness heights does not necessarily translate to increase in heat transfer. Further, there is a consistent trend for all relative roughness heights (i.e., *e/D* values of 0.03, 0.05, 0.07 and 0.10). As *p/e* is increased, the heat transfer increases up till 2.5 beyond which the Nusselt number decreases with further increase in the relative pitch ratio. The optimum *p/e* value of 2.5 is suggestive of a skimming flow regime (See Section 4.4.1). In other words, irrespective of the relative roughness height value similar secondary flow structures are evident. The secondary vortex flow structures formed between consecutive ribs aids efficient heat exchange between the heat source (i.e., the absorber plate) and the heat sink (i.e., the heat transfer medium).

The heat transfer enhancement as a result of the roughness elements can be seen in Figure 4-26. The heat transfer enhancement is the ratio of the Nusselt number of the roughened channel to the ratio of the smooth channel at the same Reynolds number. The trend of the heat transfer enhancement curves also follows the trend of the Nusselt number curves as expected. Figure 4-26 shows that the heat transfer enhancement decreases with increase in Reynolds number. This is the case since transverse roughness elements increase the heat transfer by acting as turbulence generators which will be more beneficial at lower Reynolds number values. Also, noticeable is the spread of the curves for each relative roughness ratio value. At the apex, the heat transfer enhancement varies from 1.97 to 2.74, 2.06 to 2.72, 2.14 to 2.52, and 2.20 to 2.25 for *e/D* values of 0.10, 0.07, 0.05 and 0.03 respectively. The values that are not consistent with the trend in Figure 4-26d have been regarded as outliers and were ignored. However, it shows that the heat transfer enhancement is higher for smaller values of *e/D* at higher Reynolds number and vice versa. This is the case because the boundary layer is thicker for lower Reynolds numbers which requires taller roughness elements to effectively break the boundary layer and enhance heat transfer. The maximum heat transfer enhancement occurs at *p/e* value of 2.5 for the range of pitch ratios considered in this study which is coincident with the maximum heat transfer in Figure 4-25.

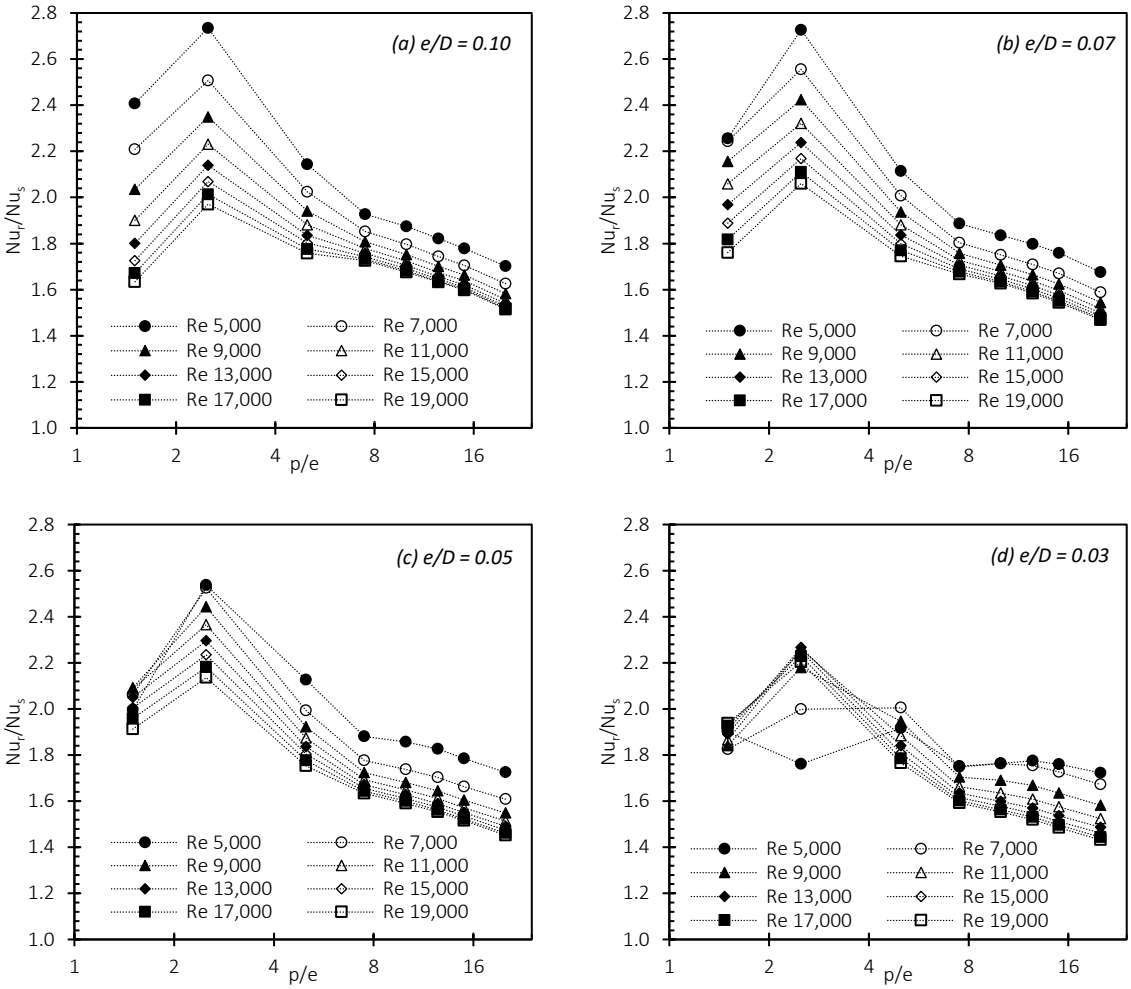


Figure 4-26: The effect of varying p/e on the heat transfer enhancement for different *e/D* values

Similarly, Figure 4-27 shows the variation of friction factor with relative pitch ratio. The friction factor increases with increase of the relative roughness height as expected due to protrusion of the roughness elements further into the boundary layer. For *Re* = 19,000 the friction factor is 0.16, 0.12, 0.10, and 0.08 for e/D values of 0.10, 0.07, 0.05 and 0.03 respectively at *p/e* value of 7.5. This trend of increase of friction factor with roughness height is consistent for all Reynolds numbers. The friction factor increases with increase in the relative pitch ratio, attains a maximum value and diminishes with further increase in the relative pitch ratio. The maximum friction factor occurs at *p/e* = 7.5 for *e/D* = 0.10 and 0.03 while the maximum friction factor occurs at *p/e* = 5 for *e/D* = 0.07 and 0.05. Recall that the friction factor was validated to within ± 8% of the experimental value, it can be said that the friction factor for *p/e* = 5 and 7.5 are similar.

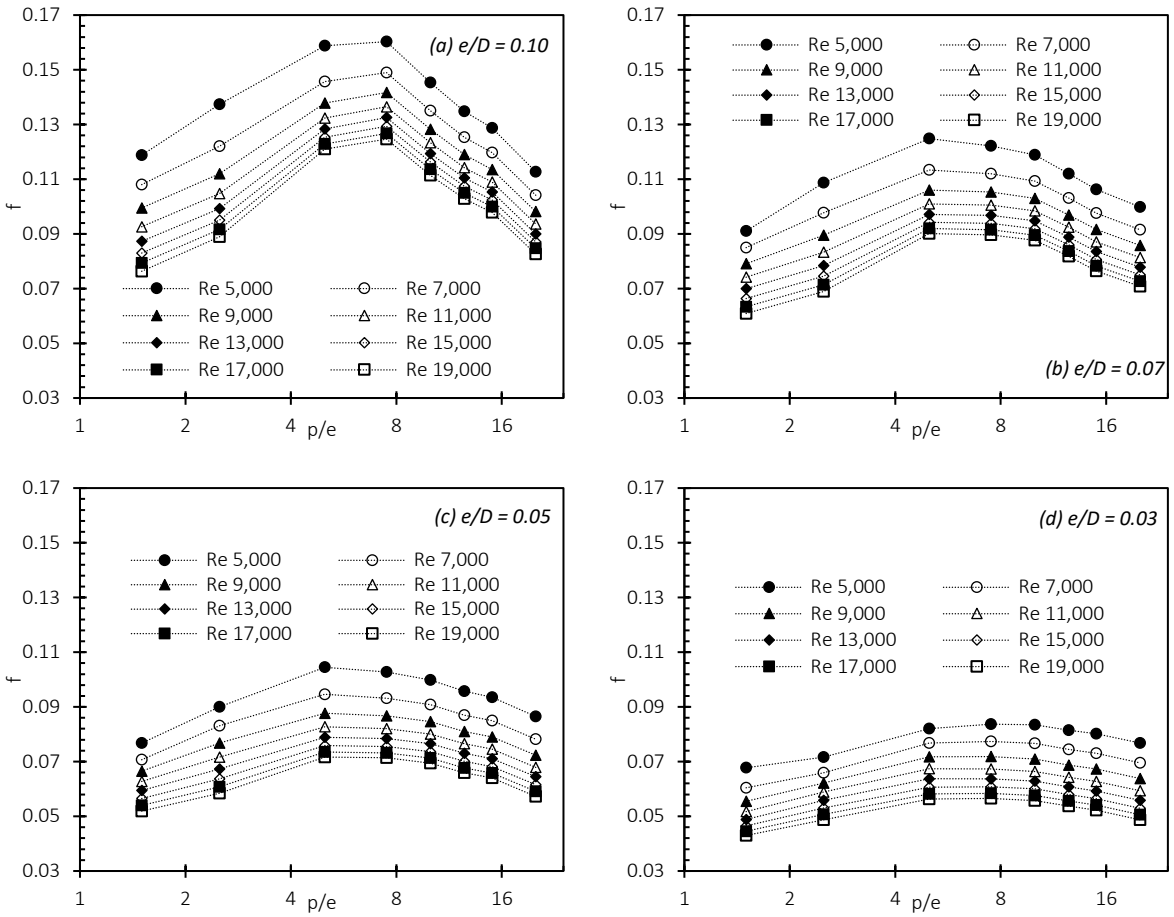


Figure 4-27: The effect of varying *p/e* on the friction factor for different relative roughness heights

To be certain about the optimal *p/e* that maximizes the friction factor, it is necessary to review the wall shear stress profiles (Figure 4-28). For all *e/D* values, as the relative pitch ratio is increased beyond 2.5, an inflection point ensues which is an indication of the onset of flow reattachment or the wake interference region. The inflection point is observed for *p/e* = 5. At the maximum friction factor the strength of the vortex is maximum and enhances mixing with the mean flow such that fluid is pulled to the vicinity of the absorber plate. This creates disturbances in the flow that increases pressure loss in the channel.

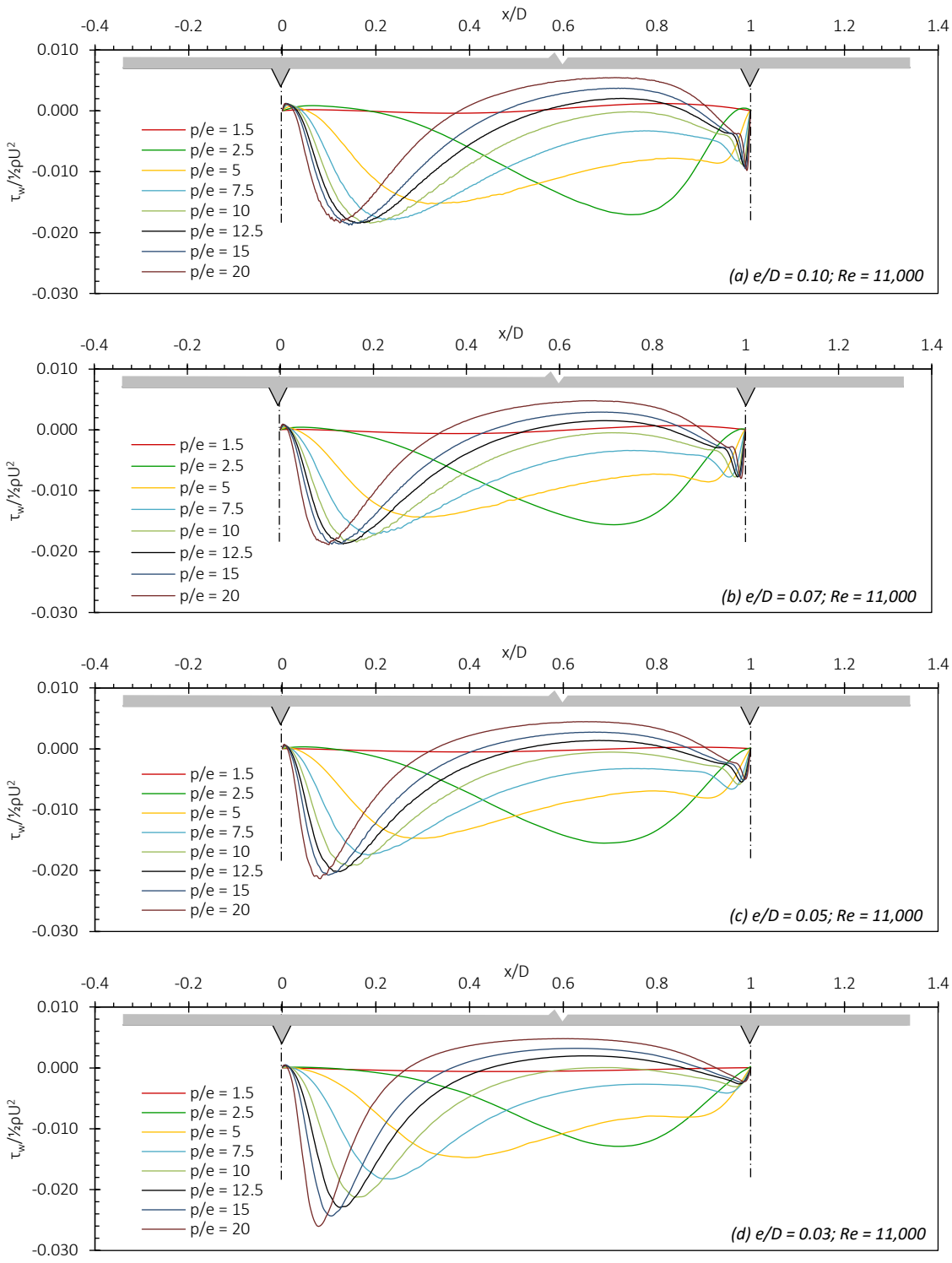


Figure 4-28: Dimensionless wall shear stress profiles for different *e/D* values and *Re* = 11,000

Figure 4-29 further emphasis the effect of increasing the relative pitch ratio on the friction factor. In Figure 4-29, the shear force has been computed for *e/D* values of 0.10, 0.07, 0.05

and 0.03 and plotted against the relative pitch ratio. Recall that the shear force is the area under the wall shear stress profile and is calculated using the Reiman sum. Figure 4-29 shows that the relative pitch ratio that maximizes the friction factor is $p/e$ = 5 since the shear force is maximized.

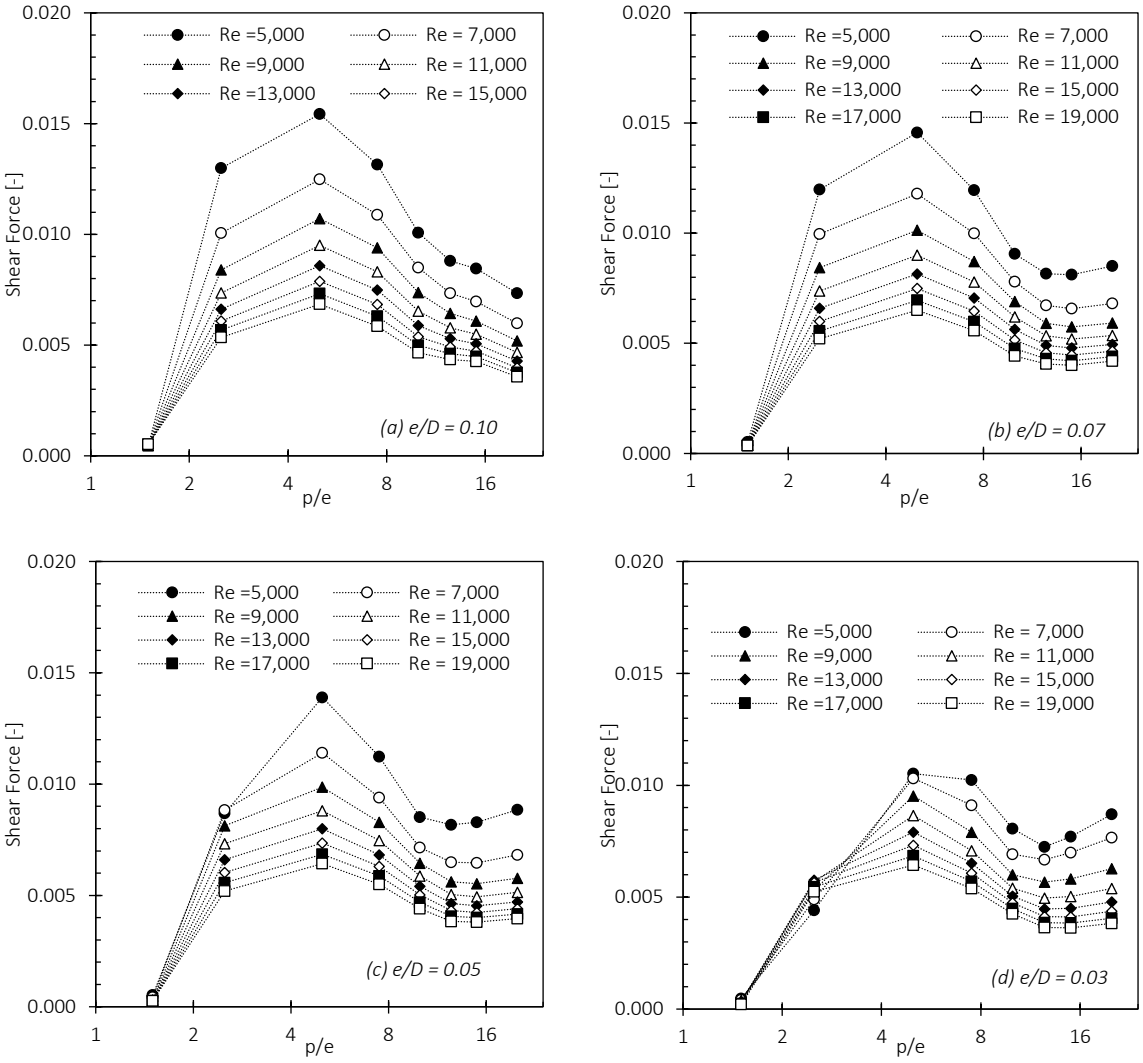


Figure 4-29: Dimensionless shear force profiles for different *e/D* values

Similarly, the friction penalty follows the same trend as the friction profile as seen in Figure 4-30. It can be observed that the maximum friction penalty occurs at $p/e$ = 5 which is supported by the detailed analysis of the shear force as seen in Figure 4-29. The spread in the figures with increase in *e/D* value can be seen and is attributed to the impact or effectiveness of the taller roughness heights even at lower Reynolds number flows.

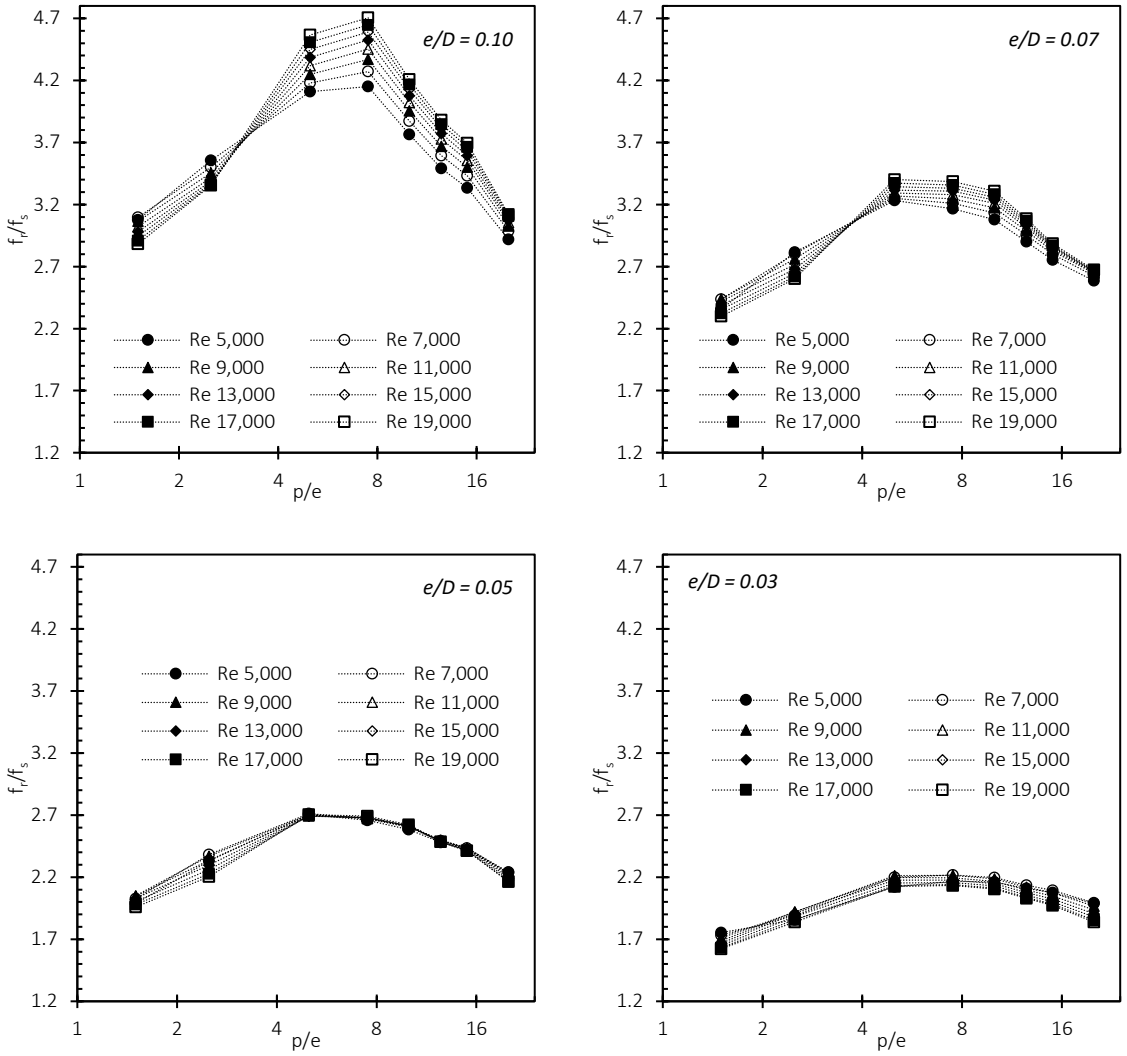


Figure 4-30: The effect of varying *p/e* on the friction penalty for different relative roughness heights

The effect of *p/e* on the thermo-hydraulic performance can be seen in Figure 4-31. Thermo-hydraulic performance parameter in analyzes the combi-effect on the heat transfer and friction factor since it is expected that the heat transfer enhancement should not yield significant increase in the friction penalty. The range of roughness heights, the thermo-hydraulic performance parameter is maximized for *p/e* = 2.5 and *Re* = 5,000. The maximum thermo-hydraulic performance parameter is 1.79, 1.93, 1.89 and 1.81 for *e/D* values of 0.10, 0.07, 0.05 and 0.03 respectively. It is worth noting that for all values of *p/e* and *e/D* in Figure 4-31. The Thermohydraulic performance parameter is greater than one.

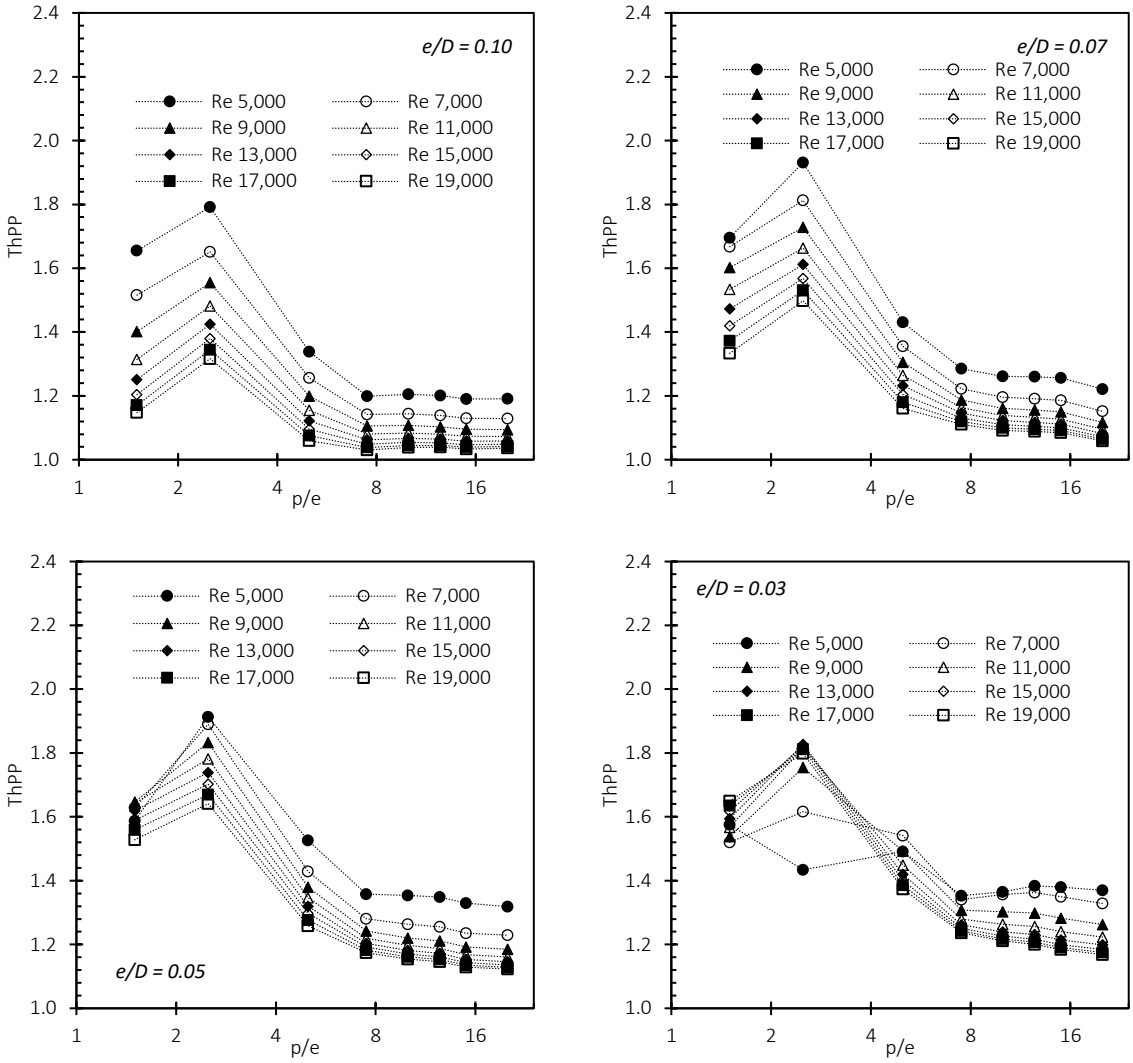


Figure 4-31: The effect of varying *p/e* on *ThPP* penalty for different relative roughness heights

### 4.4.2.3 Effect of relative roughness height

Figure 4-32 shows the effect of *e/D* on the convective heat transfer coefficient for different values of relative roughness pitch and Reynolds numbers. The relative roughness pitch values that are shown in Figure 4-32 are representative of the skimming flow regime (i.e., *p/e* = 2.5), wake interference regime (i.e., *p/e* values of 5 and 7.5) and the isolated flow roughness regime (i.e., *p/e* = 15). In the skimming flow regime, Nusselt number increases with increase in the relative roughness height up till 0.05 for $Re \leq 9{,}000$; beyond which Nusselt number is constant. For $Re > 9{,}000$; Nusselt number increases with increase in relative roughness heights up till 0.03 and a further increase causes a reduction in the

Nusselt number. As indicated in Section 4.4.1.2 as the height of the roughness is increased, the turbulence is created far from the surface of the absorber plate which does not translate to an increase in the heat transfer coefficient.

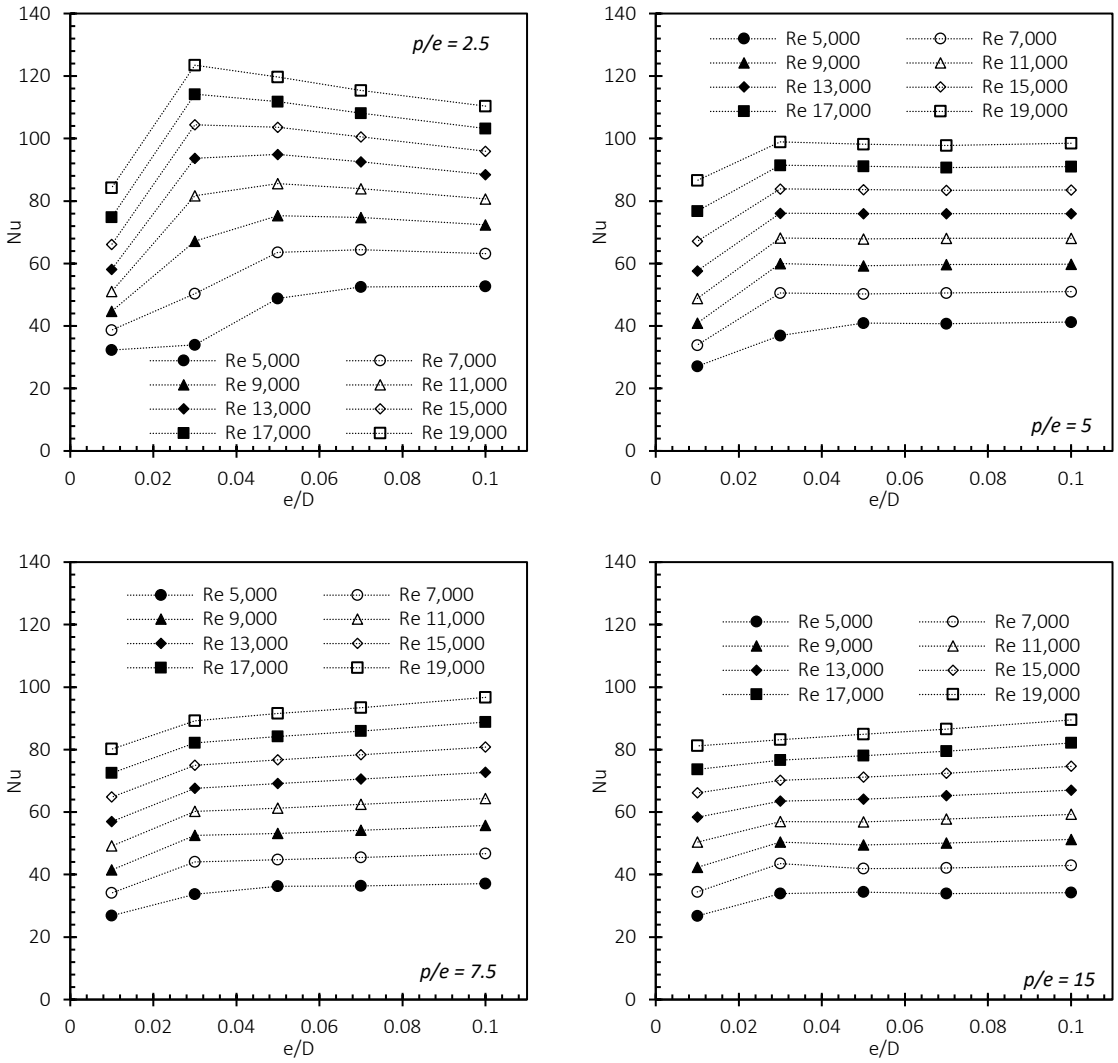


Figure 4-32: The effect of varying *e/D* on the Nusselt number for different relative pitch ratios

In the wake interference region (i.e., *p/e* = 5), Nusselt number is independent of an increase in the relative roughness height as evidenced by the flat profile for *e/D* > 0.03 for the range of Reynolds numbers considered in the study. As the relative roughness pitch is increased (i.e., *p/e* = 7.5), there seems to be a monotonous increase of the heat transfer coefficient with increase in the relative roughness height especially at higher Reynolds number flows. This is a similar trend for the isolated roughness flow regime (i.e., *p/e* = 15). This can be explained by referring to Figure 4-28. The wall shear stress profile indicates that with higher

roughness height, the reattachment point is delayed (i.e., the point where the wall shear stress is zero). This is because of the higher adverse pressure gradient. As such, the reattached flow length is higher for the lower roughness height. The boundary layer develops for the reattached flow length and acts to resist heat transfer. Since the reattached flow length is relatively smaller for the higher relative roughness heights, the resistance to the heat transfer is lower and hence the increase of the Nusselt number with relative roughness height.

The same trends noticed on the convective heat transfer by varying the relative roughness height can be seen in Figure 4-33. For the skimming flow regime, the maximum heat transfer enhancement of 2.73 occurs at the $Re$ = 5,000 flow condition and $e/D$ = 0.07. Further increase in the relative roughness height does not lead to significant increase in the heat transfer coefficient. Similarly, the maximum heat transfer enhancement is 2.13 for $p/e$ = 5. This occurs at the $Re$ = 5,000 flow condition and $e/D$ = 0.05. The maximum heat transfer enhancement also occurs at $e/D$ = 0.05 and $Re$ = 5,000 for $p/e$ = 7.5. However, the enhancement in heat transfer is 1.88. In the isolated roughness regime (i.e., $p/e$ = 15), the maximum heat transfer enhancement of 1.76 occurs at $Re$ = 5,000 and $e/D$ = 0.03.

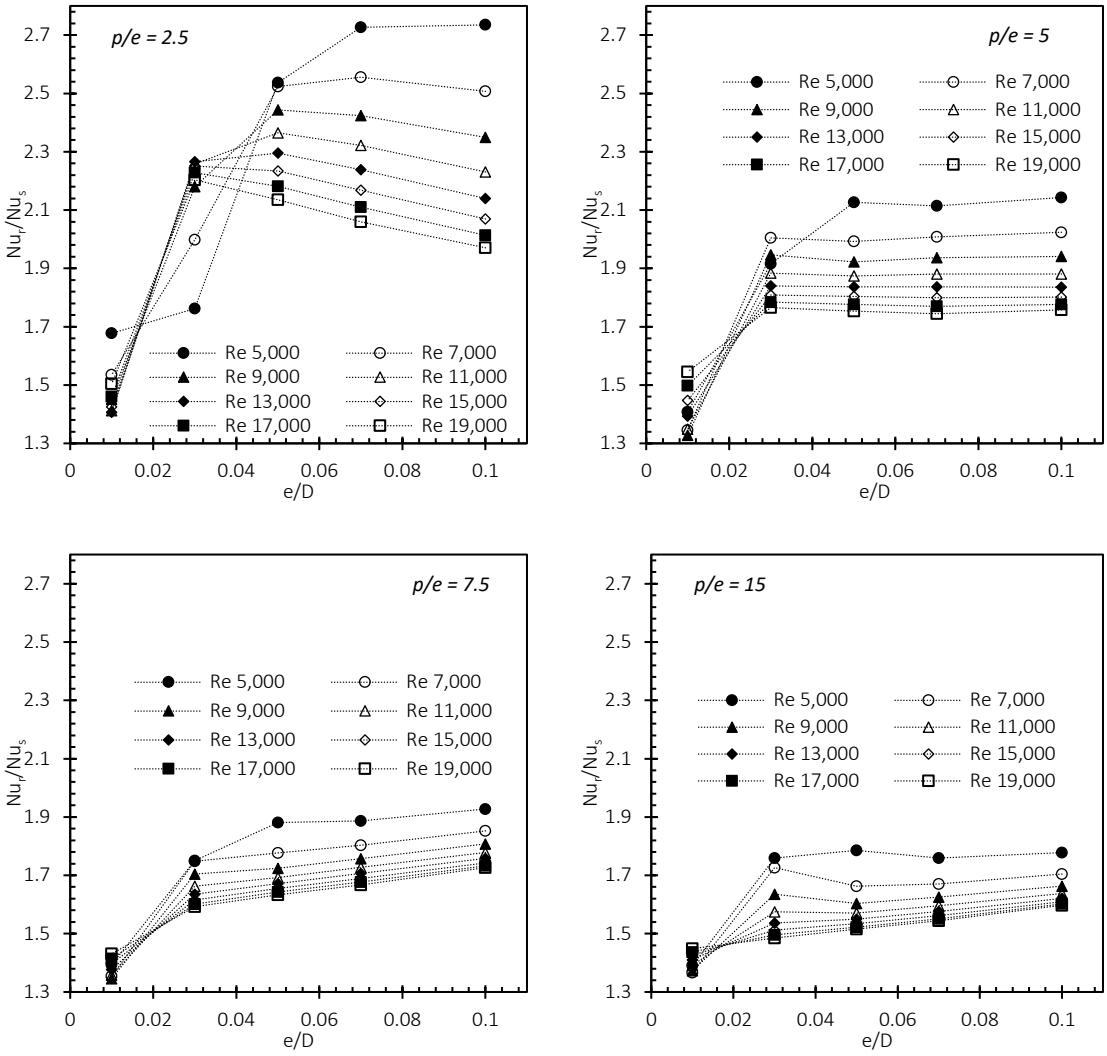


Figure 4-33: The effect of varying *e/D* on the heat transfer enhancement for different relative pitch ratios

The effect of the relative roughness height on the friction factor can be seen in Figure 4-34. As expected, the friction factor increases with increase in the relative roughness height due to increase in the turbulence kinetic energy for all values of *p/e*.

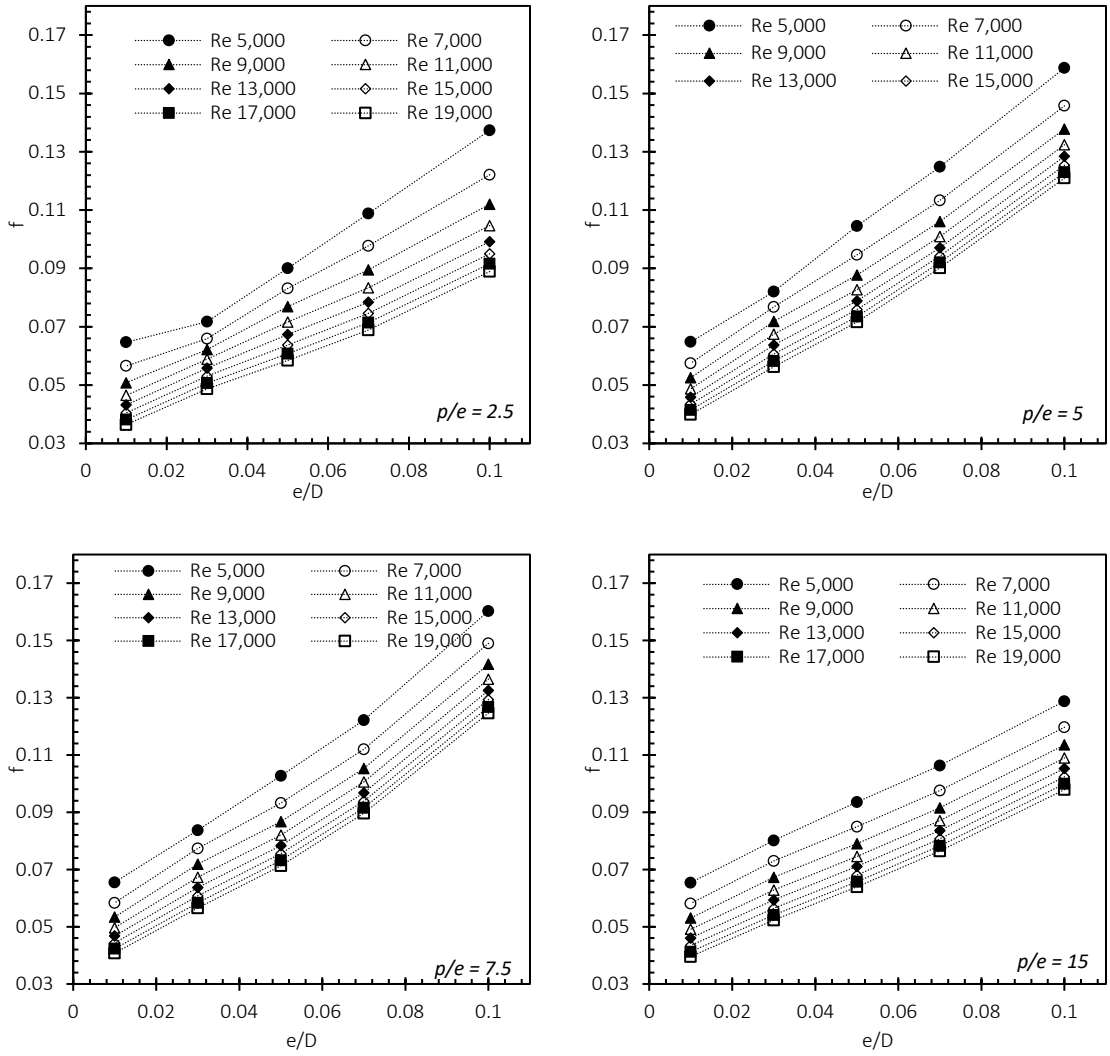


Figure 4-34: The effect of varying *e/D* on the friction factor for different relative pitch ratios

Figure 4-35 shows the effect of the relative roughness height on the friction penalty. The trend of the profiles for all relative roughness heights is like that of the friction factor. In that, the friction penalty increases with increase in the relative roughness height. The maximum friction penalty in the skimming flow regime is 3.65 and it occurs at *e/D* = 0.10 and *Re* = 5,000. The maximum friction penalty in the wake interference flow regime is 4.7 and occurs at *e/D* = 0.1 and *Re* = 5,000. The maximum friction penalty in the isolated roughness flow regime is 3.9 and occurs at *e/D* = 0.1 and *Re* = 5,000. In other words, the higher the relative roughness height, the higher the pressure loss in the channel. Notice the spread in the friction penalty profiles for all values of *p/e*. This alludes to the statement in Section 4.4.2.2 that the taller relative roughness heights enhance the turbulence intensity

in the air channel even at lower Reynolds number flows when the boundary layer thickness is thicker compared to the higher Reynolds number flows.

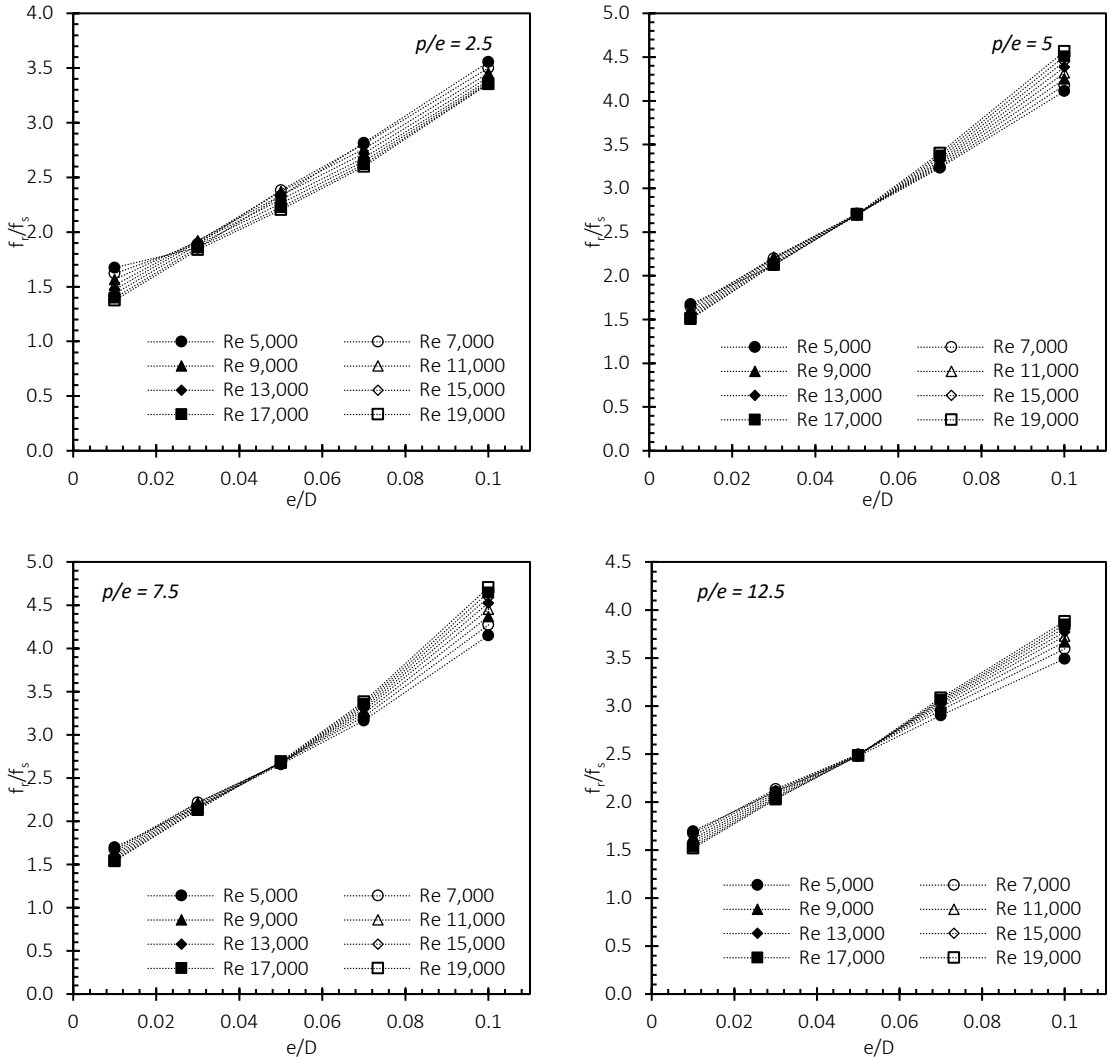


Figure 4-35: The effect of varying *e/D* on the friction factor penalty for different relative pitch ratios

The effect of varying the relative roughness height on the thermohydraulic performance parameter can be seen in Figure 4-36. For *p/e* = 2.5 the maximum thermohydraulic performance parameter is 1.93 and occurs at *e/D* = 0.07 and *Re* = 5,000. The maximum thermohydraulic performance parameter for *p/e* = 5 is 1.54 and occurs at *e/D* = 0.03 and *Re* = 7,000. The maximum thermohydraulic performance parameter for *p/e* = 7.5 is 1.36 and occurs at *e/D* = 0.05 and *Re* = 5,000. The maximum thermohydraulic performance parameter for *p/e* = 15 is 1.38 and occurs at *e/D* = 0.03 and *Re* = 5,000. The thermo-

hydraulic performance analysis shows that the configuration for the triangular roughness element that maximizes the heat transfer and minimizes the friction factor of the system is *p/e* = 2.5, *e/D* = 0.07 and *Re* = 5,000.

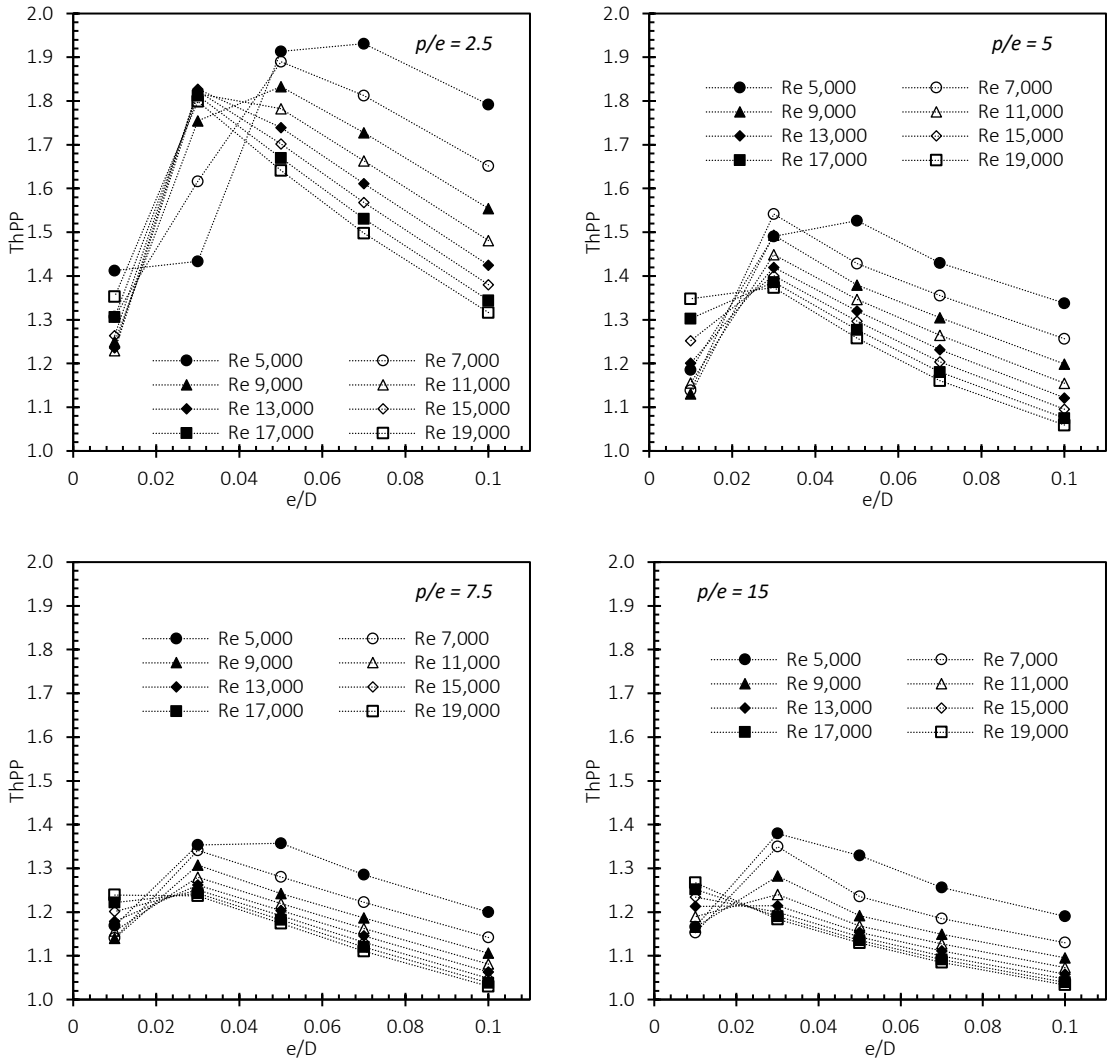


Figure 4-36: The effect of varying *e/D* on *ThPP* for different relative pitch ratios

### 4.4.2.4 Development of correlation for Nusselt number and friction factor

The dimensionless heat transfer coefficient and friction factor for the triangular roughness elements are correlated with the relative roughness pitch (*p/e*), relative roughness height (*e/D*) and Reynolds number according to the polynomial expressions given in Equation 4-19 and Equation 4-20 respectively.

$$Nu = Re^{0.7079}\left(\frac{p}{e}\right)^{-0.123}\left(-4.6596\left(\frac{e}{D}\right)^{2} + 0.7017\left(\frac{e}{D}\right) + 0.0895\right) \quad \text{Equation 4-19}$$

$$f = Re^{-0.299}e^{9.3271\left(\frac{e}{D}\right)}\left(-0.001625\left(\frac{p}{e}\right)^{2} + 0.034005\left(\frac{p}{e}\right) + 0.623332\right) \quad \text{Equation 4-20}$$

Figure 4-37 compares the prediction of the derived correlations and the computational data for the average Nusselt number and friction factor. The correlation is accurate to within ± 10% for the average Nusselt number and friction factor for more than 80% of the *CFD* generated data. The polynomial expressions in Equation 4-19 and Equation 4-20 are sufficiently accurate in predicting the Nusselt number and friction factor respectively.

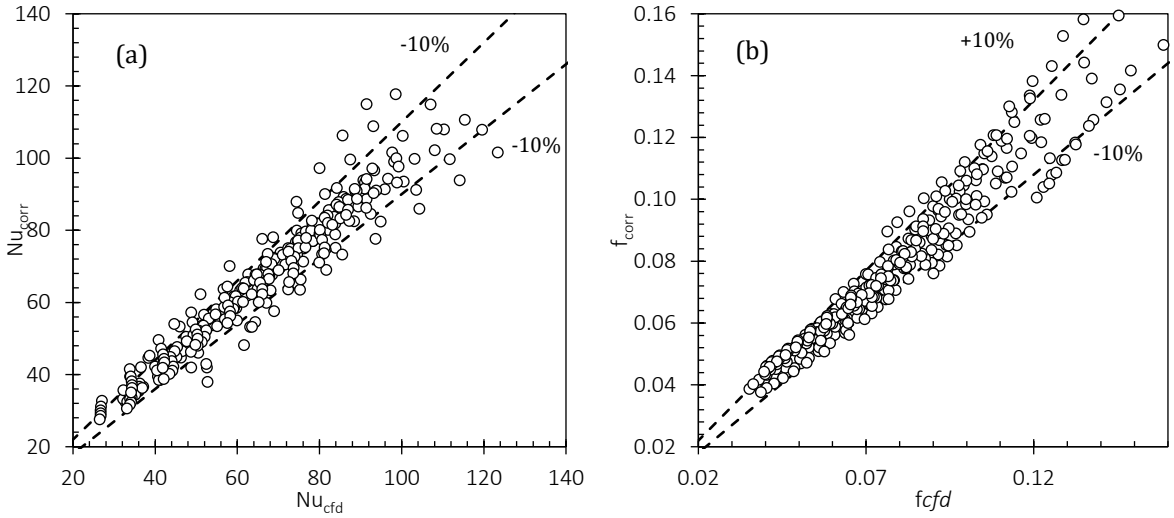


Figure 4-37: Comparison of predicted and simulated (a) Nusselt number and (b) friction factor

The Nusselt numbers for the square and semi-circle correlate linearly with the Nusselt number of the triangular rib for the same geometry and flow parameters. The Nusselt numbers for the air channel with square and semi-circular transverse rib can be estimated from Equation 4-21 and Equation 4-22 respectively. Refer to Section 4.4.1.5 for correlation estimating the Nusselt number and friction factor for the circular transverse rib.

$$\boldsymbol{Nu_{square} = 0.7669\, Nu_{triangle} + 7.03} \qquad \text{Equation 4-21}$$

$$\boldsymbol{Nu_{semi-circle} = 0.7943\, Nu_{triangle} + 5.9965} \qquad \text{Equation 4-22}$$

The accuracy of the derived correlation is checked with the CFD derived data and shown to be sufficiently accurate in Figure 4-38.

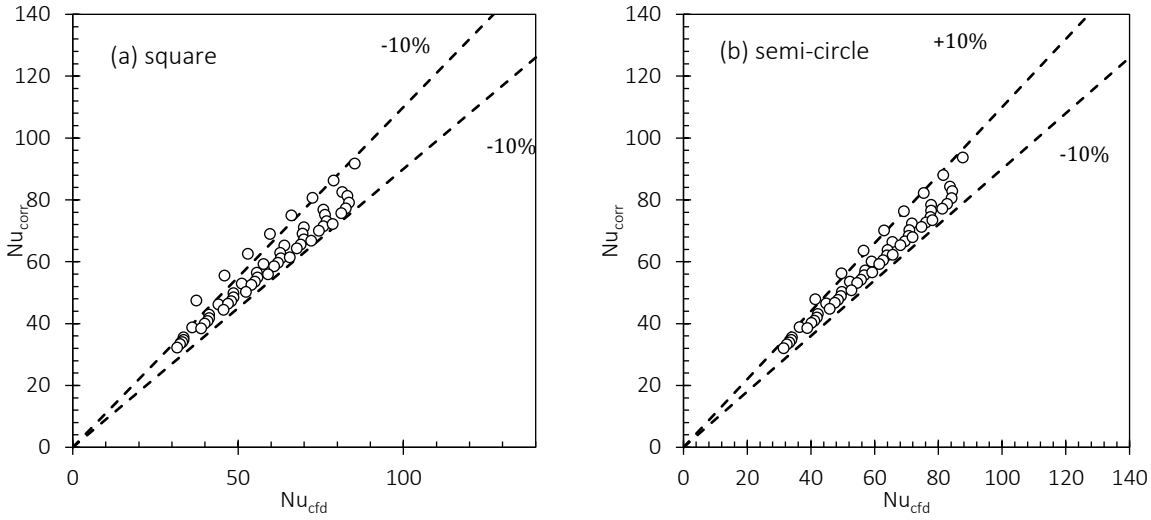


Figure 4-38: Comparison of predicted and simulated Nusselt number for (a) square and (b) semi-circular rib

Similarly, the friction factor for the square and semi-circle correlates linearly with the friction factor of the triangular rib for the same geometry and flow parameters. The friction factor for the air channel with square and semi-circular transverse rib can be estimated from Equation 4-23 and Equation 4-24 respectively.

$$\boldsymbol{f_{square} = 0.86613\, f_{triangle} - 0.0042564} \qquad \text{Equation 4-23}$$

$$\boldsymbol{f_{semi-circle} = 0.87523\, f_{triangle} - 0.0085587} \qquad \text{Equation 4-24}$$

The accuracy of the derived correlation is checked with the CFD derived data and shown to be sufficiently accurate in Figure 4-39.

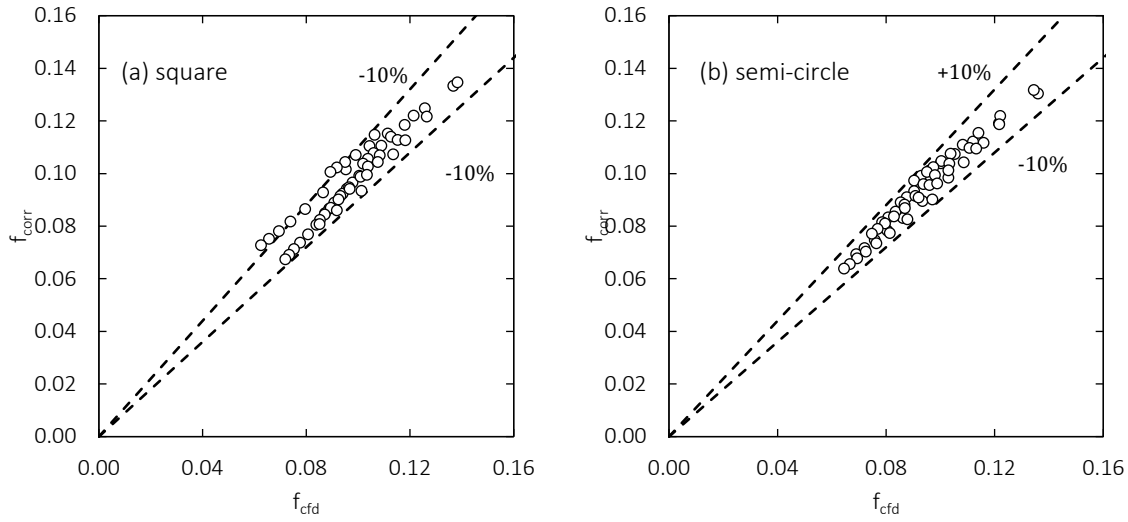


Figure 4-39: Comparison of predicted and simulated friction factor for (a) square and (b) semi-circular rib

## 4.5 Conclusion

The effect of shape, height, and pitch of a transverse roughness element in a Building integrated photovoltaic and thermal (*BIPV/T*) air channel has been numerically assessed. The shapes considered in this study are square, circle, semi-circle, and triangle. These shapes have been chosen because they are the most prevalent in literature on transverse ribs. The rib height is varied from 1 mm to 10 mm for a channel with hydraulic diameter of 100 mm. Inherently, the relative roughness height is varied from 0.01 to 0.10. The relative roughness pitch (i.e., the dimensionless distance between consecutive ribs) was considered in the range of 1.5 to 50 for all the roughness heights considered in the study.

The numerical analysis is conducted using computational fluid dynamics (*CFD*). The numerical accuracy of the *CFD* model is confirmed with experimental data from literature to within experimental tolerance before the parametric analysis is conducted. The following conclusions are deduced from the computational analysis:

- Using the transverse circular rib as case study, three distinct flow structures are present and identified as skimming flow regime for $p/e < 3.5$, wake interference flow for $3.5 < p/e < 9.5$ and isolated roughness flow for $p/e > 9.5$

- Similarly, two clear flow regimes were observed according to the Reynolds roughness number parameter, the fully rough flow regime ($e^+ > 70$) for $e/D > 0.05$ and the transitionally rough flow regime ($5 < e^+ \leq 70$) for $e/D < 0.03$.
- The thermo-hydraulic performance analysis showed that the transverse circular rib with $e/D = 0.05$ and $p/e = 20$ and a flow condition of $Re = 5{,}000$ are the optimal geometric and operational parameters for the range of parameters considered.
- The triangular roughness profile demonstrated the best heat transfer enhancement. This inherently meant that the friction factor was the most significant compared to the other roughness profiles. However, the triangular transverse rib showed an overall better thermo-hydraulic performance. The mechanism of heat transfer was attributed to the shedding of the trapped vortex in the immediate downstream and upstream of the roughness element due the obtuse angle formed at the bond between the transverse rib and the hot surface representative of the PV module. The circular profile provided the least heat transfer enhancement while the semi-circle and square profile are similar.
- Further parametric analysis on the triangular rib is conducted since it yielded the most heat transfer enhancement. From the range of relative pitch ratios considered $p/e = 2.5$ (i.e., skimming flow regime) yielded the best heat transfer enhancement. The mechanism of heat transfer enhancement suggests that the recirculation flow between consecutive ribs enhances heat exchange between the hot plate and the heat transfer medium. Also, $p/e = 5$ showed the highest friction penalty in that the turbulence generated by the vortical flows between consecutive roughness elements contributed more to the overall pressure loss in the channel. Overall, $p/e = 2.5$ provided the best thermo-hydraulic performance.
- The maximum thermo-hydraulic performance is obtained at $p/e = 2.5$, $e/D = 0.07$ and $Re = 5{,}000$. This is because at higher relative roughness heights, the roughness element protrudes more into the boundary layer especially for lower Reynolds number flows which enhances the turbulence and consequently, the heat transfer coefficient.
- A polynomial expression is derived for the Nusselt number and friction factor as a function of the relative roughness height ($e/D$), relative roughness pitch ($p/e$) and

Reynolds number (*Re*); and shown to be accurate to within ± 10% and ±12% respectively.

## 4.6 References


Aharwal, K. R., Pawar, C. B., & Chaube, A. (2014). Heat transfer and fluid flow analysis of artificially roughened ducts having rib and groove roughness. Heat and Mass Transfer, 50(6), 835-847.

Athienitis, A. K., Bambara, J., O'Neill, B., & Faille, J. (2011). A prototype photovoltaic/thermal system integrated with transpired collector. Solar Energy, 85(1), 139-153.

Awol, A., Bitsuamlak, G. T., & Tariku, F. (2020). Numerical estimation of the external convective heat transfer coefficient for buildings in an urban-like setting. Building and Environment, 169, 106557.

Bakar, M. N. A., Othman, M., Din, M. H., Manaf, N. A., & Jarimi, H. (2014). Design concept and mathematical model of a bi-fluid photovoltaic/thermal (PV/T) solar collector. Renewable energy, 67, 153-164.

Bekele, A., Mishra, M., & Dutta, S. (2014). Performance characteristics of solar air heater with surface mounted obstacles. Energy conversion and management, 85, 603-611.

Bhagoria, J. L., Saini, J. S., Solanki, S. C. (2002). Heat transfer coefficient and friction factor correlations for rectangular solar air heater duct having transverse wedge shaped rib roughness on the absorber plate. Renewable Energy, 25, 341-369.

Chai, T., & Draxler, R. R. (2014). Root mean square error (RMSE) or mean absolute error (MAE)?–Arguments against avoiding RMSE in the literature. Geoscientific model development, 7(3), 1247-1250.

Chaube, A., Sahoo, P. K., & Solanki, S. C. (2006). Analysis of heat transfer augmentation and flow characteristics due to rib roughness over absorber plate of a solar air heater. Renewable Energy, 31(3), 317-331.

Chen, Y., Athienitis, A. K., & Galal, K. (2010). Modeling, design and thermal performance of a BIPV/T system thermally coupled with a ventilated concrete slab in a low energy solar house: Part 1, BIPV/T system and house energy concept. Solar Energy, 84(11), 1892-1907.

Coleman, S. E., Nikora, V. I., McLean, S. R., & Schlicke, E. (2007). Spatially averaged turbulent flow over square ribs. Journal of engineering mechanics, 133(2), 194-204.

Corbin, C. D., & Zhai, Z. J. (2010). Experimental and numerical investigation on thermal and electrical performance of a building integrated photovoltaic–thermal collector system. Energy and Buildings, 42(1), 76-82.

Dubey, S., Sandhu, G. S., & Tiwari, G. N. (2009). Analytical expression for electrical efficiency of PV/T hybrid air collector. Applied Energy, 86(5), 697-705.

Gawande, V. B., Dhoble, A. S., Zodpe, D. B., & Chamoli, S. (2016). Experimental and CFD investigation of convection heat transfer in solar air heater with reverse L-shaped ribs. Solar Energy, 131, 275-295.

Incropera, F. P., Lavine, A. S., Bergman, T. L., & DeWitt, D. P. (2007). Fundamentals of heat and mass transfer. Wiley.

Jaurker, A. R., Saini, J. S., & Gandhi, B. K. (2006). Heat transfer and friction characteristics of rectangular solar air heater duct using rib-grooved artificial roughness. Solar energy, 80(8), 895-907.

Kamel, R. S., & Fung, A. S. (2014). Modeling, simulation and feasibility analysis of residential BIPV/T+ ASHP system in cold climate—Canada. Energy and Buildings, 82, 758-770.

Karwa, R., Solanki, S. C., & Saini, J. S. (1999). Heat transfer coefficient and friction factor correlations for the transitional flow regime in rib-roughened rectangular ducts. International Journal of Heat and Mass Transfer, 42(9), 1597-1615.

Kumar, A., & Kim, M. H. (2015). Effect of roughness width ratios in discrete multi V-rib with staggered rib roughness on overall thermal performance of solar air channel. Solar Energy, 119, 399-414.

Kumar, A., Kumar, R., Maithani, R., Chauhan, R., Sethi, M., Kumari, A., Kumar, S., & Kumar, S. (2017). Correlation development for Nusselt number and friction factor of a multiple type V-pattern dimpled obstacles solar air passage. Renewable Energy, 109, 461-479.

Kumar, R., Goel, V., & Kumar, A. (2018). Investigation of heat transfer augmentation and friction factor in triangular duct solar air heater due to forward facing chamfered rectangular ribs: A CFD based analysis. Renewable Energy, 115, 824-835.

Kumar, R., Kumar, A., & Goel, V. (2017). A parametric analysis of rectangular rib roughened triangular duct solar air heater using computational fluid dynamics. Solar Energy, 157, 1095-1107.

Kumar, R., Kumar, A., & Goel, V. (2019). Performance improvement and development of correlation for friction factor and heat transfer using computational fluid dynamics for ribbed triangular duct solar air heater. Renewable energy, 131, 788-799.

Kumar, V. (2019). Nusselt number and friction factor correlations of three sides concave dimple roughened solar air heater. Renewable energy, 135, 355-377.

Luo, L., Wen, F., Wang, L., Sundén, B., & Wang, S. (2016). Thermal enhancement by using grooves and ribs combined with delta-winglet vortex generator in a solar receiver heat exchanger. Applied energy, 183, 1317-1332.

Othman, M. Y., Hamid, S. A., Tabook, M. A. S., Sopian, K., Roslan, M. H., & Ibarahim, Z. (2016). Performance analysis of PV/T Combi with water and air heating system: An experimental study. Renewable Energy, 86, 716-722.

Pandey, N. K., & Bajpai, V. K. (2016). Experimental investigation of heat transfer augmentation using multiple arcs with gap on absorber plate of solar air heater. Solar Energy, 134, 314-326.

Pantic, S., Candanedo, L., & Athienitis, A. K. (2010). Modeling of energy performance of a house with three configurations of building-integrated photovoltaic/thermal systems. Energy and buildings, 42(10), 1779-1789.

Patil, A. K., Saini, J. S., & Kumar, K. (2015). Experimental Investigation of Enhanced Heat Transfer and Pressure Drop in a Solar Air Heater Duct with Discretized Broken V-Rib Roughness. Journal of Solar Energy Engineering, 137(2), 021013.

Peng, J., Lu, L., Yang, H., & Han, J. (2013). Investigation on the annual thermal performance of a photovoltaic wall mounted on a multi-layer façade. Applied energy, 112, 646-656.

Poongavanam, G. K., Panchabikesan, K., Leo, A. J. D., & Ramalingam, V. (2018). Experimental investigation on heat transfer augmentation of solar air heater using shot blasted V-corrugated absorber plate. Renewable energy, 127, 213-229.

Rounis, E. D., Athienitis, A. K., & Stathopoulos, T. (2016). Multiple-inlet Building Integrated Photovoltaic/Thermal system modelling under varying wind and temperature conditions. Solar Energy, 139, 157-170.

Sealey, V. (2014). A framework for characterizing student understanding of Riemann sums and definite integrals. The Journal of Mathematical Behavior, 33, 230-245.

Sharma, N., Tariq, A., & Mishra, M. (2019). Experimental investigation of heat transfer enhancement in rectangular duct with pentagonal ribs. Heat Transfer Engineering, 40(1-2), 147-165.

Skullong, S., Thianpong, C., & Promvonge, P. (2015). Effects of rib size and arrangement on forced convective heat transfer in a solar air heater channel. Heat and Mass Transfer, 51(10), 1475-1485.

STAR CCM+ Users Manual. http://www.cd-adapco.com/products/star-ccm/documentation

Thakur, D. S., Khan, M. K., & Pathak, M. (2017). Performance evaluation of solar air heater with novel hyperbolic rib geometry. Renewable energy, 105, 786-797.

Wang, Z., Qiu, F., Yang, W., Zhao, X., & Mei, S. (2016). Experimental investigation of the thermal and electrical performance of the heat pipe BIPV/T system with metal wires. Applied energy, 170, 314-323.

Yadav, A. S., & Bhagoria, J. L. (2013). A CFD (computational fluid dynamics) based heat transfer and fluid flow analysis of a solar air heater provided with circular transverse wire rib roughness on the absorber plate. Energy, 55, 1127-1142.

Yadav, A. S., & Bhagoria, J. L. (2014). A CFD based thermo-hydraulic performance analysis of an artificially roughened solar air heater having equilateral triangular sectioned rib roughness on the absorber plate. International Journal of Heat and Mass Transfer, 70, 1016-1039.

Yadav, A. S., & Bhagoria, J. L. (2014). A numerical investigation of turbulent flows through an artificially roughened solar air heater. Numerical Heat Transfer, Part A: Applications, 65(7), 679-698.

Yang, T., & Athienitis, A. K. (2014). A study of design options for a building integrated photovoltaic/thermal (BIPV/T) system with glazed air collector and multiple inlets. Solar Energy, 104, 82-92.

Yang, T., & Athienitis, A. K. (2015). Experimental investigation of a two-inlet air-based building integrated photovoltaic/thermal (BIPV/T) system. Applied energy, 159, 70-79.

Zogou, O., & Stapountzis, H. (2011). Energy analysis of an improved concept of integrated PV panels in an office building in central Greece. Applied Energy, 88(3), 853-866.

# Chapter 5

# 5 A novel BIPV/T façade concept with coupled air and refrigerant heat extraction system – Validation of the coupled air and refrigerant flow CFD model

In Chapter 4, the heat transfer augmentation associated with a BIPV/T forced air channel roughened with transverse ribs was investigated. The influence of the roughness height, roughness shape and roughness shape were studied. Although, the transverse rib geometry was optimized, the hot spot problem associated with of the transverse rib roughness was still observed. An alternative cooling strategy is to institute a secondary flow in the transverse tube roughness elements to eliminate the hot spot phenomenon. The secondary fluid proposed herein is a refrigerant such that the BIPV/T façade as the evaporator for a heat pump cycle as seen in Figure 5-1.

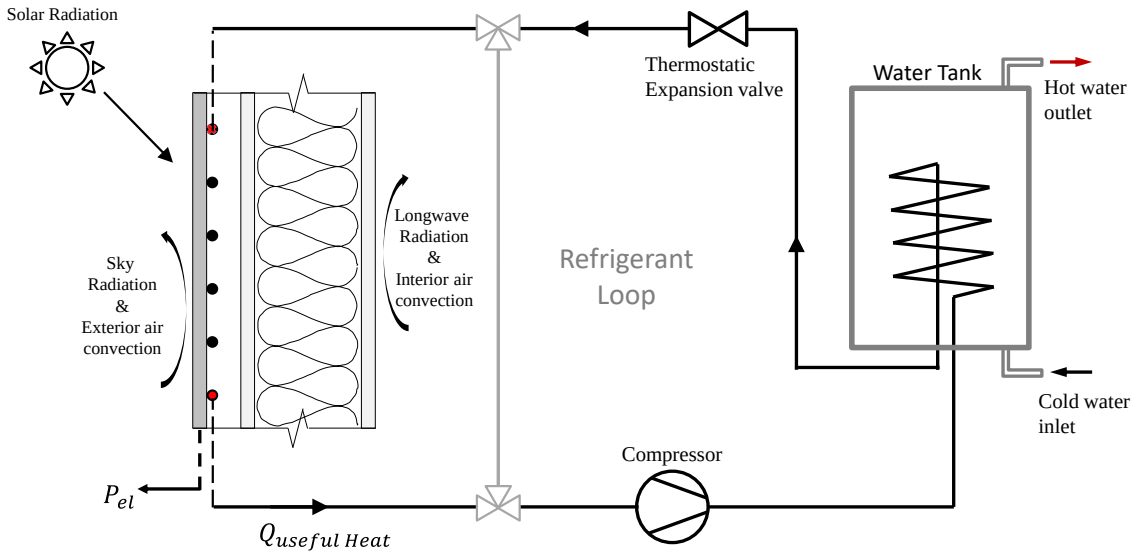


Figure 5-1: Schematic of a BIPV/T facade coupled with heat pump technology for domestic hot water heating

The BIPV/T wall assembly in Figure 5-1 consists of a PV cladding and the insulated inner wall. Refrigerant tubes are installed behind the PV cladding such that the BIPV/T wall assembly acts as a PV/T evaporator. At the same time, the surface temperature of the PV cladding is regulated since it is well known that the PV electrical efficiency is temperature

dependent. An airflow path separates the PV cladding from the insulated inner wall. The airflow in the cavity is mechanically controlled based on the building operation to enhance the operational feasibility of the BIPV/T and Heat pump concept (See Figure 5-2). In Mode 1, the airflow pattern is like an outdoor air curtain façade for a cooling mode building operation (i.e., peak summer operation). In Mode 2, a Trombe wall air flow pattern is simulated for the heating mode building operation (i.e., peak winter operation). In Mode 3, an exhaust air flow pattern is simulated for the building operation with no heating or cooling. In effect, the BIPV/T façade operates as a PV/T evaporator and an air source heat pump. Below an outdoor temperature of 5°C, the system is shut off. This multi-functionality has the potential to improve the cost effectiveness of the BIPV/T façade.

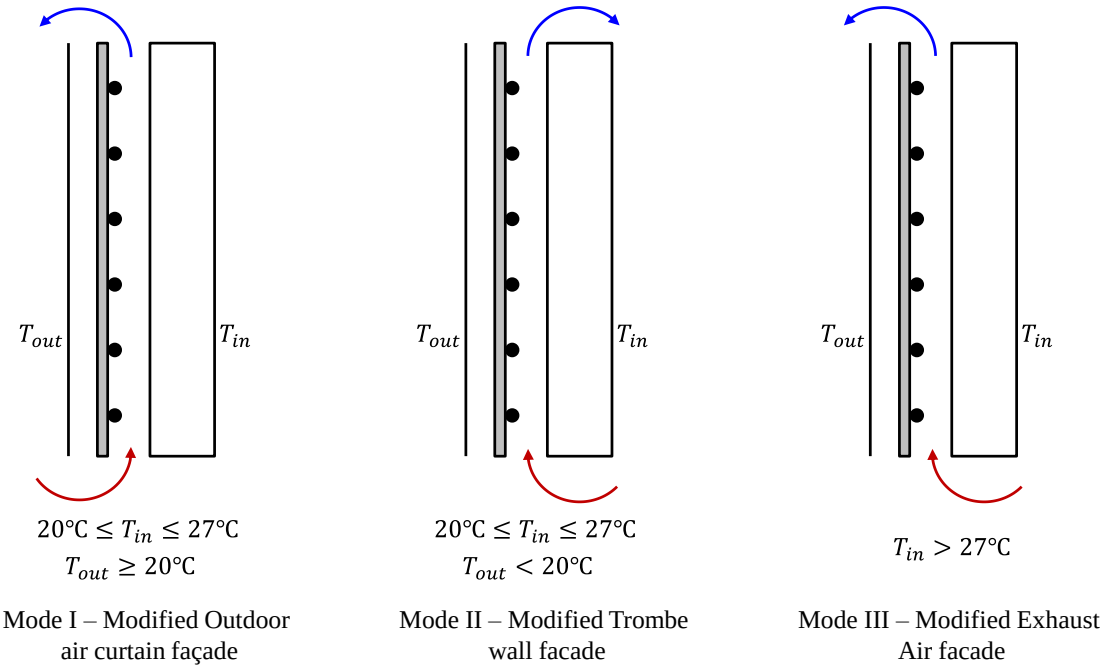


Figure 5-2 - Illustration of BIPV/T facade ventilation schemes

In essence, the BIPV/T concept proposed is an airflow enhanced PV/T evaporator. The enhancement provided by instituting airflow behind the cladding can be quantified by both experimental and numerical techniques. The decision on the approach taken to quantify the useful heat gain of the BIPV/T façade evaporator must be based on sound understanding of multiphase flow boiling heat transfer coupled with airflow heat transfer and flow

dynamics. A condensed literature review on saturated flow boiling is presented in the next section.

## 5.1 Literature Review

The refrigerant flow involves change of phase from liquid to gas due to the heat gain from the available solar radiation and ambient temperature. Figure 5-3 shows the flow regimes during evaporation (De Schepper et al., 2009).

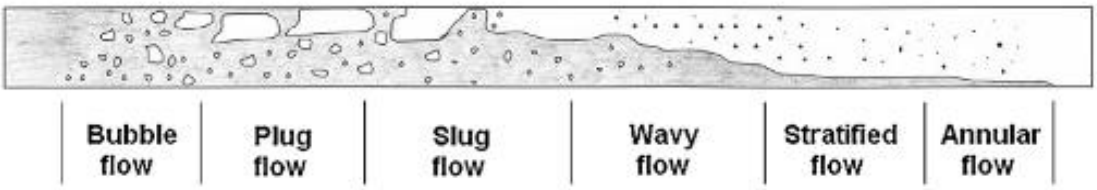


Figure 5-3: Flow regimes during saturated flow boiling (De Schepper et al., 2009)

As seen in Figure 5-3, the two-phase flow is characterized by six (6) flow regimes. These include the bubble flow, plug flow, slug flow, wavy flow, stratified flow, and annular flow regime. The two-phase flow regimes do not always occur in the sequence shown in Figure 5-3 since they are dependent on the density and viscosity of both phases, the heat flux on the tube wall, and the liquid and vapor velocity (De Schepper et al., 2009). That said, the flow regimes during evaporation can be characterised as the dispersed bubbles (i.e., Bubble flow), stratified flow (i.e., Slug flow) and dispersed sprays (i.e., Annular flow). In the dispersed bubble flow, the gas phase is dispersed in the liquid. In the stratified flow regime, the gas and the liquid remain separated by a large-scale interface and in the dispersed sprays, the liquid is dispersed in the gas.

Generally, the inception of boiling is characterized by the bubble flow regime. As the vapor mass fraction increases, the bubbles grow and coalesce to form vapor slugs (Incropera et al., 2007). The slug flow regime is followed by an annular flow regime. The annular flow regime is characterized by the formation of liquid films on the interior tube walls and vapor flow at the core of the tube. The fluid is superheated when the liquid films and the dispersed sprays are completely evaporated.

It is clear from Figure 5-3 that both liquid and gaseous phases can occur in any cross-section of the saturated flow boiling region. The mean vapor mass fraction (i.e., $\bar{X}$) is then defined according to Equation 5-1 (Incropera et al., 2007)

$$\bar{\boldsymbol{X}} \equiv \frac{\int_{A_c} \boldsymbol{\rho u(r,x) X dA_c}}{\dot{\boldsymbol{m}}} \qquad \text{Equation 5-1}$$

Further, the local heat transfer coefficient varies significantly along the tube in the saturated flow boiling region. Hence, predicting the local heat transfer coefficient is a complex exercise. While experiments can give us a more accurate representation of the saturated flow boiling heat transfer, experiments do not inform on the detailed heat transfer and flow characteristics due to limitations on sensor technology. Hence, only the bulk flow characteristics can be derived. Knowing that the heat transfer coefficients in two-phase flows are fluid dependent, the cost-effectiveness of conducting experiments is low. Yu et al., (1999) derived heat transfer coefficient correlations for flow boiling in smooth horizontal tubes based on experiment of some pure refrigerants. Similar experimental study was conducted by Tibirica & Ribatski (2010) for R134a and R245fa in a 2.3 *mm* refrigerant tube. The experimental data was compared with some flow boiling predictive methods from literature. The heat transfer prediction methods yielded errors in the range of 18.7% to 81.8%. Kaew-on & Wongwises, (2009) experimentally investigated the heat transfer coefficient and pressure drop of R410A in a multiport mini-channel.

CFD is a useful tool to understand the heat transfer and flow characteristics of each of the flow regimes in saturated flow boiling. The impact of vapor quality, heat flux, mass flux, channel diameter, bubble frequency, and saturation temperature on the saturated flow boiling heat transfer performance of a slug flow within a horizontal, circular microchannel was investigated using CFD (Magnini & Thome, 2016). It is shown that the heat transfer is enhanced by smaller channels and large bubble frequency. Increasing the saturation temperature reduces the heat transfer coefficient. Magnini et al. (2013) employed detailed CFD to derive a new multiple bubble heat transfer model to predict the local variation of the heat transfer coefficient for a slug flow. Ferrari et al. (2018) compared the flow features and heat transfer of slug flows in a square and circular channel cross-sections using CFD.

The effect of inlet mass flux, wall heat flux and inlet vapor quality on the heat transfer coefficients and flow patterns in the annular flow boiling regime in a single rectangular microchannel using CFD (Luo et al., 2020). Liu et al. (2017) presented a numerical study on transition from slug flow to annular flow in a micro-channel with a diameter of 0.4 mm.

The detailed analysis of the flow regimes reveals two types of heat transfer regimes that are associated with saturated inlet conditions (See Figure 5-4). In the Nucleate boiling dominant heat transfer, the bubbly and slug flow regimes span a significant fraction of the channel length while the annular flow regime convers a significant portion of the tube length in the convective boiling dominant heat transfer (Kim & Mudawar, 2013). The heat transfer coefficient for the nucleate boiling dominant heat transfer is relatively more stable than the convective boiling dominant heat transfer regime. The convective boiling dominant heat transfer is characteristic of high heat flux flows while the Nucleate boiling dominant heat transfer is more prevalent in low heat flux flows.

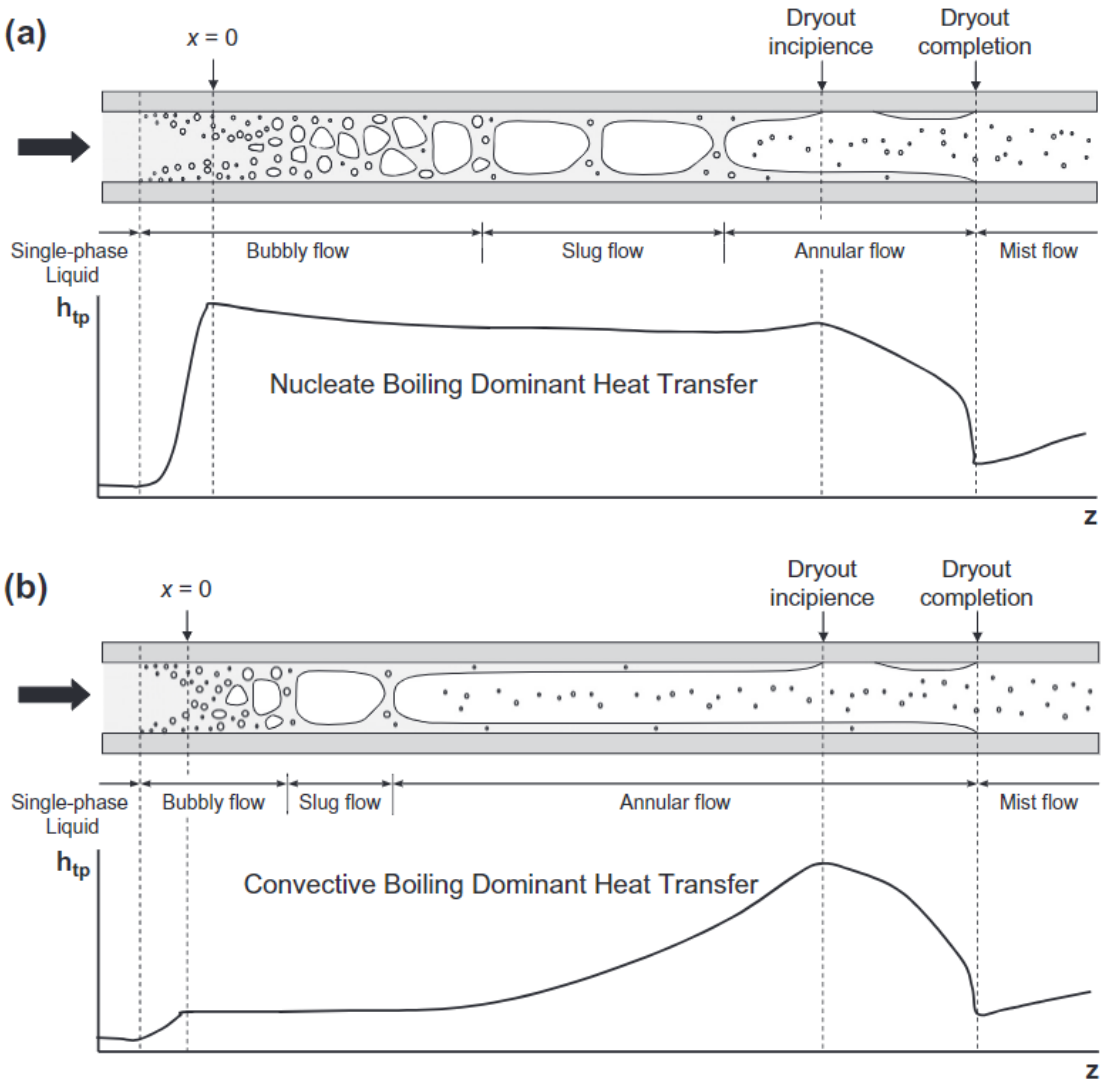


Figure 5-4: Schematic of the (a) Nucleate boiling and (b) Convective boiling dominant heat transfer regime (Kim & Mudawar, 2013)

Knowing that the two-phase heat transfer coefficient for low heat flows is relatively constant during saturated flow boiling, lower order numerical methods are often employed. This is the premise for the adoption of the CFD assisted numerical methods especially in heat exchanger simulations. The two-phase is predicted using one-dimensional mathematical methods that employ thermodynamics first laws, while the airflow is simulated using CFD. A finite volume heat exchanger (HX) model was coupled with 2D CFD simulations of airflow to optimize an A-type heat exchanger concept (Tancabel et al., 2021). Shojaeefard et al., (2017) coupled CFD for 3D airflow analysis and 1D finite

element model to solve the two-phase flow to model heat exchanger flow mal distribution. Lee et al., (2018) also employed this hybrid coupled CFD approach to investigate the effect of HX geometry and airflow rate on the airflow distribution and heat exchanger performance. A distributed model was applied to simulate the refrigerant flow and heat transfer and 3D CFD to simulate the air side flow and heat transfer performance via porous media approach (Ma et al., 2020). Other studies that employed this hybrid CFD approach are Paz et al. (2019), You et al., (2018), Singh et al., (2008; 2011), and Yashar et al., (2014). These hybrid CFD approaches are facilitated by generalized approaches based on experimental data for determining the heat transfer coefficients in two-phase flows (Fang et al., 2017 and Kim & Mudawar, 2013).

In HX applications, the hybrid CFD approach is used since the performance is highly dependent on the airflow distribution. However, for a BIPV/T application with coupled airflow and refrigerant heat extraction system, the performance is dependent on the airflow distribution, the pressure distribution in the refrigerant tube and the temperature distribution on the surface of the PV panel. This is important because of the implication of the accuracy of predicting the electrical efficiency and thermal efficiency (or useful heat gain) of the BIPV/T façade evaporator. Hence, a fully coupled CFD approach is implemented to study the heat transfer and flow characteristics of the BIPV/T façade concept.

## 5.2 CFD Validation

The numerical simulation is conducted using computational fluid dynamics (CFD) and validated using experimental data in Literature (Ji et al., 2009; Skullong et al., 2015). A decoupled approach is taken to validate the CFD model. In the decoupled approach, it is assumed that the BIPV/T façade evaporator is equivalent to superimposing a solar air heater with a transverse rib roughened channel for heat transfer augmentation and a PV/T evaporator as seen in Figure 5-5. In other words, the airflow and refrigerant flow are validated separately. The coupling of the air side and refrigerant-side (i.e., the BIPV/T façade evaporator in Figure **5-5**) is inherently handled by the governing equations.

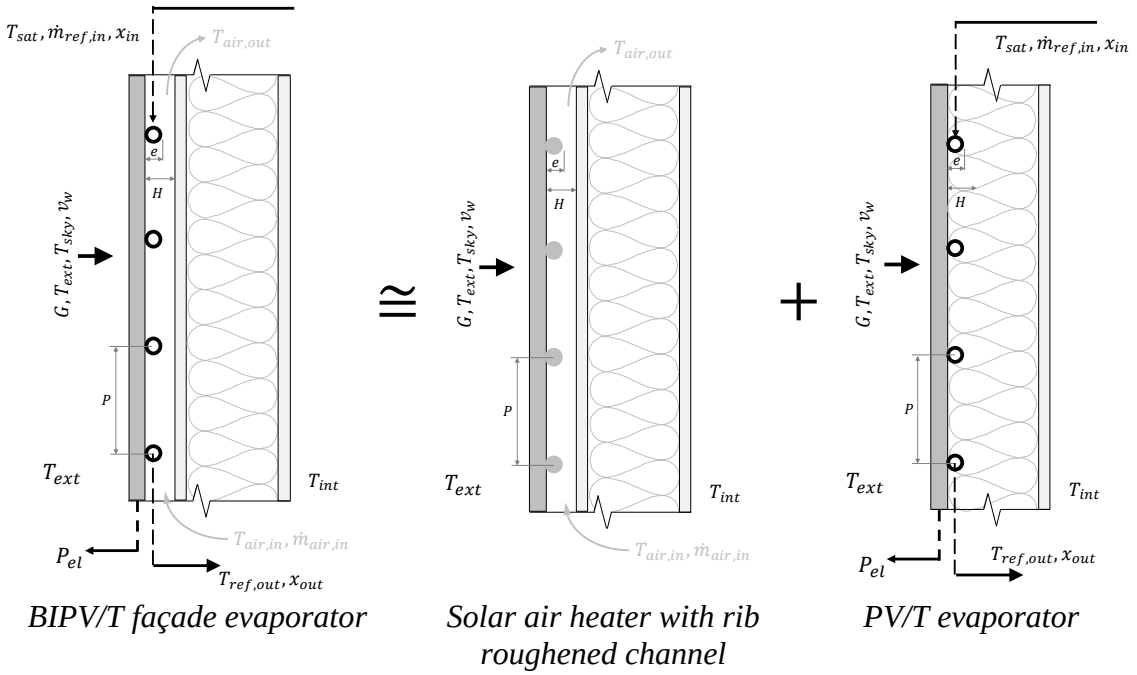


Figure 5-5 - Illustration of the decoupled validation approach

The air flow is validated using published experimental data from Skullong et al., (2015) in the heat transfer effectiveness of a SAH channel roughened with square was assessed. The derived dimensionless convective heat transfer coefficient (i.e., Nusselt number) and dimensionless pressure loss (i.e., friction factor) were compared with the experiment. To ensure numerical accuracy, the CFD model is numerically verified with CFD study by Yadav & Bhagoria (2013) for a SAH with transverse circular rib roughness. Similarly, the refrigerant side is validated with experiment on PV assisted heat pump (Ji et al., 2009). Please refer to Skullong et al., (2015) and Yadav & Bhagoria (2013) for a more detailed description of the experimental setup. The Air-side validation is presented in Section 5.2.2 and the refrigerant-side validation is presented in Section 5.2.1.

### 5.2.1 Refrigerant-Side Validation

This heat transfer and flow problem is solved by implementing the Steady Reynolds Averaged Navier-Stokes and Energy equations (See Section 5.2.1.2) for steady flow justification). The multiphase flow is typically modelled using the Volume of Fluid (VOF) method (Luo et al., 2020; Jatau & Bello-Ochende, 2021; Sarkar, 2021; Yue et al., 2018). The VOF method tracks the fluid-fluid interface which is especially important for

understanding the flow regime evolution in the two-phase flow. However, it was shown that the flow regime does not significantly affect the two-phase heat transfer coefficient for the current applications, hence, the additional modelling complexity associated with the VOF method is not desired. The multiphase flow is modeled using the Two-phase thermodynamic equilibrium model (a multiphase mixture Eulerian approach). The Two-phase thermodynamic equilibrium model assumes the liquid and gaseous phases exist as a homogeneous single-phase system. The phase distribution (i.e., Volume fraction) is derived from the static enthalpy distribution (Equation 5-2) under the assumption of thermodynamic equilibrium (Siemens, 2018).

$$\boldsymbol{Y = max\left[0, min\left(1, \frac{h_m - h_{ls}}{h_{vs} - h_{ls}}\right)\right]} \qquad \text{Equation 5-2}$$

where, $h_{ls}$ and $h_{vs}$ are the liquid and vapour enthalpy at saturation temperature and $h_m$ is the mixture enthalpy. Then the vapour volume fraction is given in Equation 5-3.

$$\boldsymbol{\alpha_v = \frac{Y}{Y + (1 - Y)\frac{\rho_{vs}}{\rho_{ls}}}} \qquad \text{Equation 5-3}$$

where, $\rho_{vs}$ and $\rho_{ls}$ are the vapour and liquid densities at saturation temperature. Turbulence is modeled using the shear stress transport k-omega turbulence model. The numerical model is validated with published experimental data (Ji et al., 2009). The details of the numerical setup are outlined in the following sections.

#### 5.2.1.1 Computational Domain

The computational domain consists of the PV module, the thermal collector, and the refrigerant fluid as seen in Figure 5-6.

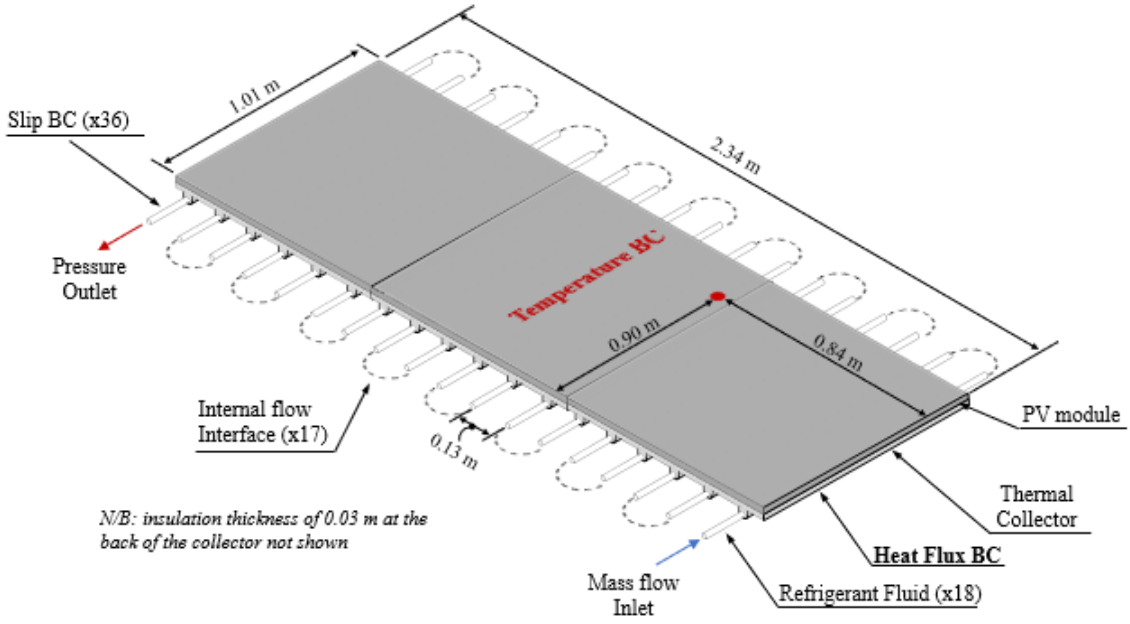


Figure 5-6 - Numerical representation of the PV evaporator and Boundary conditions

The insulation behind the thermal collector is accounted for by a thermal resistive value that will be discussed further in the Boundary conditions. The PV modules is represented by a 0.5 mm thick continuous plate. The thermal collector is represented by a 1.5*mm* thick aluminum plate with 7 mm semi-circular ribs spaced evenly at 130*mm* pitch lengths. Each semi-circular rib has 6 mm concentric hollow cylinders which contains the respective fluid segments. A contact resistance of 0.042 $m^2$-*K/W* is applied at the interface between the PV module and the thermal collector. The PV module is modelled as an aluminum plate. The optical properties of the solar cells are derived from published data in Ji et al., (2009). The fluid elements are simulated as 18 consecutive fluid segments that extend beyond the thermal collector by 0.4*m* on both sides. This was done to enhance meshing efficiency. An internal interface has been created between consecutive fluid elements.

### 5.2.1.2 Mesh Generation

The computational domain is discretized with extruded quadrilateral mesh as shown in Figure 5-7. This ensured that the interfaces between the sub-components of the computational domain was effectively captured. Ten prism layer meshes are employed to capture the near wall viscous dominated flow in the fluid domain such that the $y^+ \leq 1$. Four

perpendicular extruded meshes were employed across the PV module to effectively capture the temperature variation (Figure 5-7).

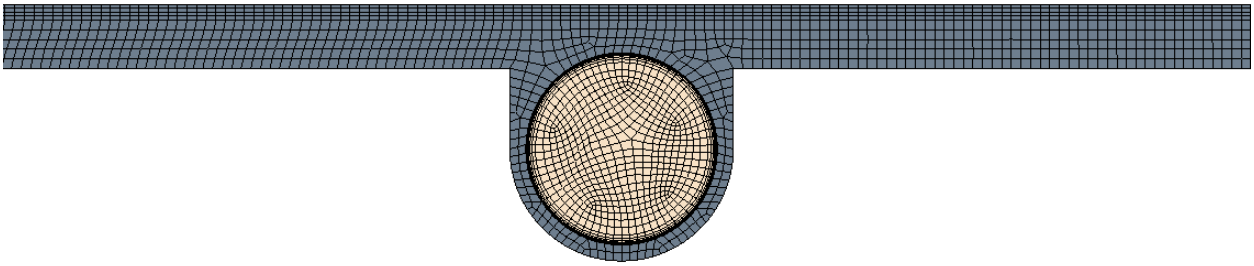

Figure 5-7 - Typical mesh of each fluid segment

Grid convergence or sensitivity was assessed by evaluating the number of longitudinal volume extrusions required for accurate prediction of the collector pressure drop and the outlet vapor quality. The coarse mesh, normal mesh and fine mesh had 2, 12 and 30 longitudinal volume extrusions respectively. This amounted to 151,148, 516,888 and 1,175,136 grid cells for the coarse, normal and fine mesh respectively. The mesh independency study is carried out for the peak outdoor conditions for the outdoor conditions given in Figure 5-8. The peak solar radiation intensity is 838 $W/m^2$ and it occurs at noon. The outdoor air temperature and PV surface temperature that corresponds with the peak solar is 12.4℃ and 34.6℃ respectively.

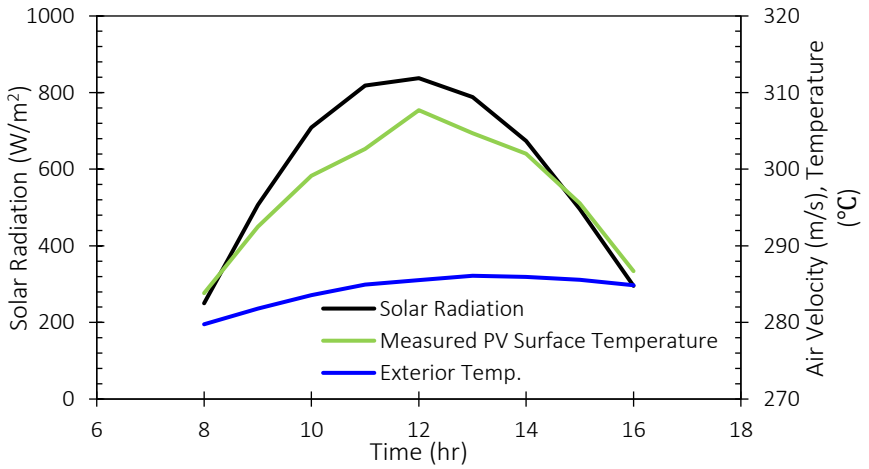


Figure 5-8: Exterior climate parameters and the measured PV surface temperature

Before the mesh sensitivity study is carried out, the unsteadiness in the flow is assessed for the peak outdoor conditions. The initial conditions for the simulations are specified from experimental data for the time step before. Note that the outdoor conditions were taken hourly as this time scale is consistent with typical building applications. Hence, the goal was to assess the variation of the collector surface temperature and the pressure drop in the channel at peak conditions. The simulation is carried out using a 5 min time step. Note that the unsteadiness in the flow is assessed by assuming a step function for the PV surface temperature. In other words, the PV surface temperature is constant for the hour being simulated. Figure 5-9 shows the variation of the collector temperature and pressure drop with time under peak conditions for the studied day. For an hourly weather data, the collector surface temperature varies from 289.4 K to 289.5K. This is a change of 0.022% within the time step. Also, the pressure drop increases from 95.7 MPa to 99.2 MPa. This corresponds to 3.55% increase in the time step for the peak solar hour being considered. In fact after 15 min, steady state conditions can be assumed.

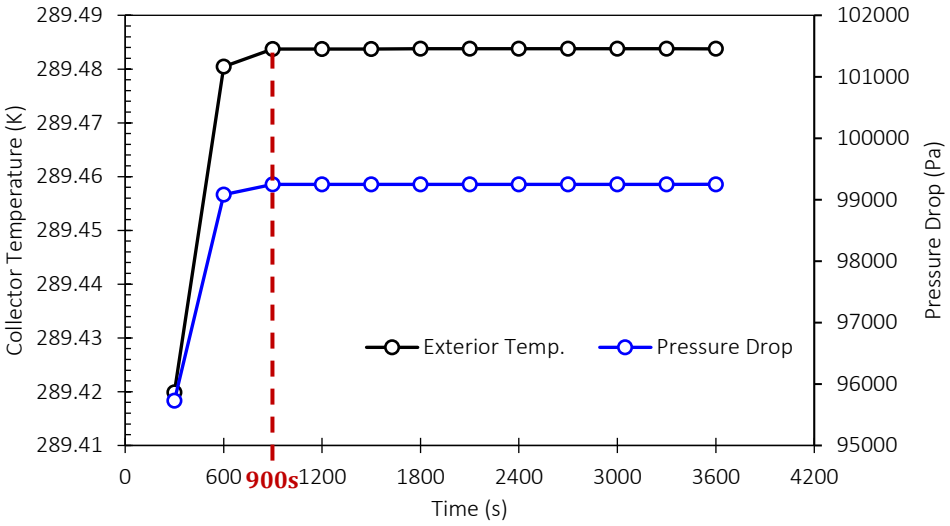


Figure 5-9: Variation of the collector temperature and pressure drop within a time step under peak outdoor air conditions

Since the collector temperature and pressure drop did not vary considerably within the peak solar hour. A steady state simulation approach is used for the mesh sensitivity study. The grid sensitivity study is also carried out under peak solar conditions. The outlet quality and the pressure drop are the parameters of interest. Table 5-1 shows that with further

refinement of the mesh beyond 516,888 grid cells, there is no improvement in the prediction accuracy of the numerical model. Hence, the normal mesh is deemed sufficiently accurate.

Table 5-1: Summary of mesh independency study

| | Grid count | *Outlet Quality, x* | % Increase in *x* | *Pressure drop, Δp* | % increase in *Δp* |
|---|---|---|---|---|---|
| Coarse | 151,148 | 0.561 | - | 9420.5 | - |
| Normal | 516,888 | 0.561 | 0.02% | 9561.1 | 1.49% |
| Fine | 1,175,136 | 0.561 | 0.02% | 9499.4 | 0.65% |

### 5.2.1.3 Boundary Conditions

A temperature boundary condition is applied on the top surface of the PV module and a uniform heat flux boundary condition on the bottom surface of the thermal collector. All the other walls are assumed adiabatic. The heat flux boundary condition specified at the bottom surface of the thermal collector is given in Equation 5-4.

$$\boldsymbol{Q = \frac{(T_{ext} - T_s)}{R_{th}}} \qquad \text{Equation 5-4}$$

Where, $T_{ext}$ is the outdoor air temperature (i.e., 285.6 *K*), $T_s$ is the collector surface temperature which is intrinsically calculated and $R_{th}$ is the thermal resistance between the back of the collector and the ambient (Equation 5-5).

$$\boldsymbol{R_{th} = {1}/{h_{ext}} + {t_{ins}}/{k_{ins}}} \qquad \text{Equation 5-5}$$

Where, $t_{ins}$ is the insulation thickness (i.e., 0.03 m), $k_{ins}$ is the thermal conductivity of the insulation material (i.e., 0.036 *W/m-K*), and $h_{ext}$ is the combined exterior convection and radiation heat transfer coefficient which is given in Equation 5-6 (Ji et al., 2009).

$$\boldsymbol{h_{ext} = 3.0\, V_{10} + 2.8} \qquad \text{Equation 5-6}$$

where, $V_{10}$ is the measured wind speed at 10 m above ground. The temperature BC is consistent with the experimentally measured data (See Figure 5-10). This is due to the lack

of availability of specific climate data. A mass flux is specified at the inlet as specified from the experiment (see Figure 5-10). The fluid domain was extended 0.4 m as seen in Figure 5-6 to attain a fully developed flow at the inlet and to minimize back flow at the outlet. No-slip boundary condition is assigned to all the walls except the extended fluid lengths to limit the impact on the collector pressure loss. The R22 refrigerant enters the domain at saturation temperature and pressure. The hourly variation of the saturation pressure is given in Figure 5-10. The properties of R22 at saturation are derived from NIST Chemistry WebBook (Linstrom & Mallard, 2001). The state properties are determined from a volume weighted mixture summation for the dynamic viscosity and thermal conductivity and mass-weighted mixture summation for the specific heat.

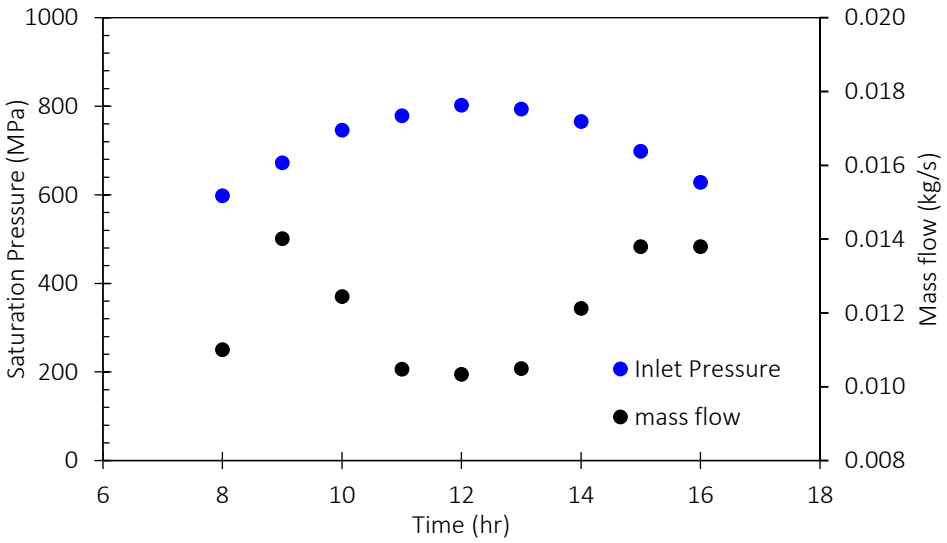


Figure 5-10: Variation of the Inlet saturation pressure and mass flow rate with time

The turbulence characteristics at the inlet is described by specifying the turbulence intensity. The turbulence intensity is estimated by the Equation 5-7. At the outlet, a pressure outlet boundary condition is assigned with gauge pressure of 0 Pa.

$$\boldsymbol{I = 0.16(Re)^{-1/8}} \qquad \text{Equation 5-7}$$

The conservation equations of mass and momentum are solved using the Segregated Flow Model while the energy equation is solved using the Segregated Enthalpy Model. The Second-Order Upwind scheme is used to discretize the governing equations. The solution

is converged for all residuals (i.e., continuity, velocity components and energy) less than $10^{-6}$.

#### 5.2.1.4 Performance Indicators

The accuracy of the CFD model is assessed by comparing the thermal output, the thermal efficiency, the pressure drop along the tube length, and collector efficiency. The thermal output is given in Equation 5-8.

$$\boldsymbol{Q_u = \dot{m}_{ref}(h_{out} - h_{in})} \qquad \text{Equation 5-8}$$

where, $\dot{m}_{ref}$ is the refrigerant flow rate from Reynolds number $\left(Re = {\dot{m}D}/{\mu A}\right)$, $h_{in}$ is the inlet enthalpy and, $h_{out}$ is the outlet enthalpy. The thermal efficiency is given in Equation 5-9.

$$\boldsymbol{\eta_{th} = {Q_u}/{G(\tau\beta)_{pv}A_c}} \qquad \text{Equation 5-9}$$

where, $G$ is solar radiation, $A_c$ is collector area, and $(\tau\beta)_{pv}$ is the effective absorptivity of the PV cells. The electrical efficiency is given in Equation 5-10 (Lai & Hokoi, 2015).

$$\boldsymbol{\eta_{el} = \eta_{ref}\left[1 - \beta_{ref}\left(T_c - T_{ref}\right)\right]} \qquad \text{Equation 5-10}$$

where, $\eta_{ref}$ is the electrical efficiency at reference temperature ($T_{ref}$), $\beta_{ref}$ is the temperature coefficient and, $T_c$ is the cell temperature. The electrical output of the PV cells is given in Equation 5-11,

$$\boldsymbol{Q_{elec} = G\tau_{eva}\eta_{el}} \qquad \text{Equation 5-11}$$

where, $\tau_{eva}$ is the transmissivity of EVA.

### 5.2.1.5 Validation Results

The numerical error was quantified with the root mean square error (RMSE) and the normalized root mean square error (NRMSE) given in Equation 5-12 and Equation 5-13 (Chai & Draxler, 2014).

$$\boldsymbol{RMSE} = \sqrt{\frac{\mathbf{1}}{\boldsymbol{n}}\sum_{\boldsymbol{i=1}}^{\boldsymbol{n}}\left(\boldsymbol{y_{sim}} - \boldsymbol{y_{exp}}\right)^{\mathbf{2}}} \qquad \text{Equation 5-12}$$

$$\boldsymbol{NRMSE} = \frac{\boldsymbol{RMSE}}{\bar{\boldsymbol{y}}} \qquad \text{Equation 5-13}$$

Figure 5-11 compares the CFD prediction of the hourly variation of collector temperature with the experimental setup. As seen in Figure 5-11, there is good agreement between the numerical prediction and the experimental data. The maximum deviation of the numerical predicted collector temperature is 1.20% and it occurs at 4pm for the day being considered. This may be due to the uncertainty in specification of the contact resistance between the PV cells and the absorber plate. Also, heat loss from the bottom surface may be underestimated in the CFD model due to the uncertainty in specifying the wind speed. However, the RMSE and NRMSE for the CFD prediction of the collector surface temperature is 2.10 K and 0.74% respectively.

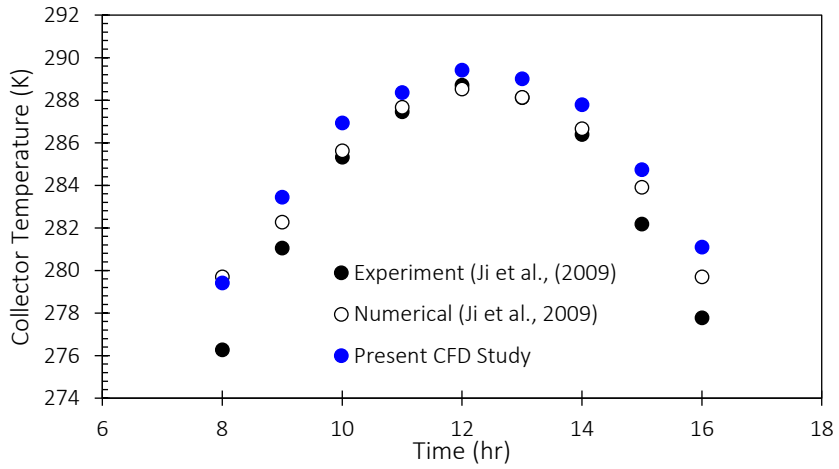


Figure 5-11: Comparison of the Numerical prediction of the collector temperature with experiment

Figure 5-12 compares the CFD prediction of the hourly variation of the heat gain with the experimental data. As seen in Figure 5-12, there is good agreement between the numerical prediction and the experimental data. The maximum deviation of the numerical deviation of the numerical data and the experimental data is 19.7% and it occurs at 3 pm for the experimental period. However, the *RMSE* and *NRMSE* for the CFD prediction of the PV evaporator heat gain for the day is 151.4W and 7.81% respectively.

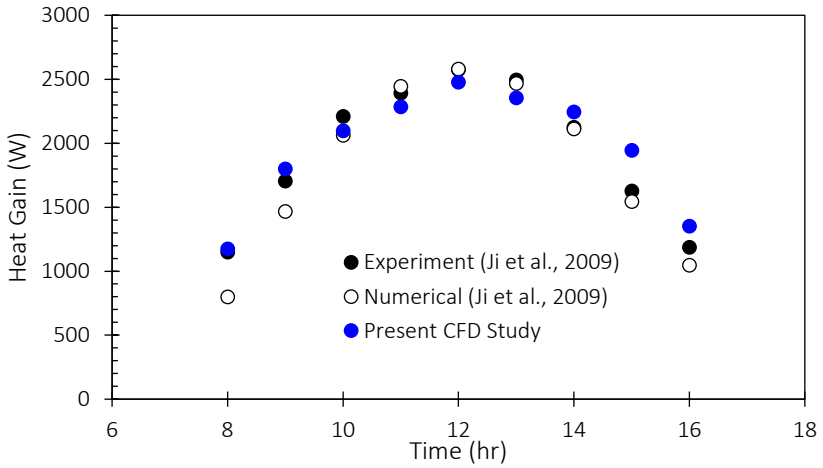


Figure 5-12: Comparison of the Numerical prediction of the hourly variation of the useful heat gain with experiment

Figure 5-13 compares the CFD prediction of the PV evaporator pressure loss with the experimental data. The good agreement between the CFD prediction of the evaporator pressure loss and experimental data can be seen in Figure 5-13. The *RMSE* and *NRMSE* for the CFD prediction of the PV evaporator pressure loss is 5.22 kPa and 5.53% respectively.

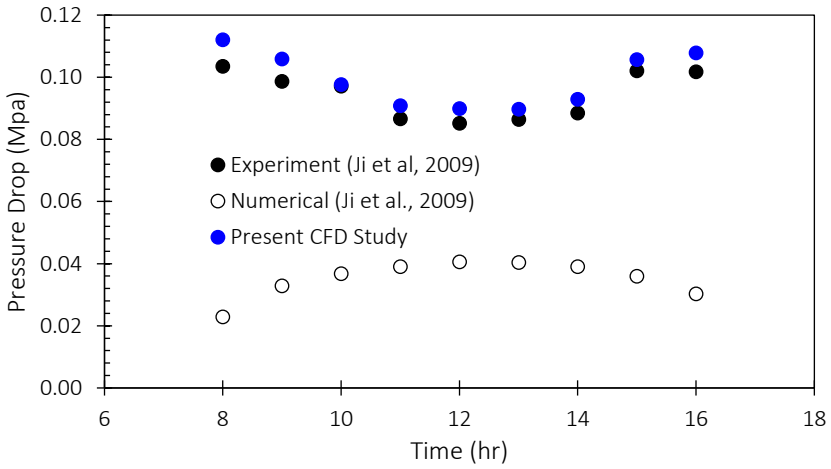


Figure 5-13: Comparison of the numerical prediction of the hourly prediction of the pressure drop with experimental data

The accuracy demonstrated in the present CFD study is better than similar numerical studies in literature. A similar study conducted to verify the accuracy of a dynamic mathematical PV/T model to predict the heat gain and pressure loss is also shown in Figure 5-11, Figure 5-12, and Figure 5-13 respectively. The mathematical model is composed of the heat balance equations of the PV module, the 2D heat conduction equation of the thermal collector and the conservation equations of the refrigerant flow. The equations of the mathematical model are discretized with the implicit finite difference method and solved by implementing a numerical simulation program written in C++ language. The distributed mathematical model predicts the collector temperature and heat gain with a reasonable degree of accuracy. The NRMSE for the numerical prediction of the collector temperature and PV evaporator heat gain is 0.53% and 8.6% respectively. However, NRMSE for prediction of the pressure drop is 61.4%. The error is significantly higher than what is achieved in the CFD model. Hence, the CFD model is sufficiently capture the thermohydraulic characteristics of the PV evaporator.

### 5.2.2 Air-Side Validation

The flow in the air channel is characterized by separated flow caused by the pseudo roughness elements and heat transfer. This conjugate heat transfer problem is solved by implementing the steady Reynolds Averaged Navier-Stokes and Energy equations.

Turbulence is modeled using the shear stress transport (SST) k-omega turbulence model. The governing equations have been simplified by assuming fluid incompressibility and negligible radiation heat transfer. The numerical setup for validation of the CFD model is detailed in the following section.

#### 5.2.2.1 Computational Domain

The computational domain is shown in Figure 5-14. The computational domain consists of the Aluminum absorber plate and air channel. The absorber plate is a 440 mm x 300 mm x 6 mm plate 6mm square roughness elements appended on the bottom surface of the plate. The square roughness elements are spaced 40 mm apart. Uniform heat flux is applied at the top of the absorber plate. The thermal properties of absorber plate is outlined in

Table 5-3. The air channel consists of the 600 mm entrance section, the 440 mm test section and the 300 mm exit section. The entrance section ensures a fully developed flow prior to the test section and the exit section ensures a settled flow at the air channel exit. The air channel depth is 30 mm and the channel width is 300 mm.

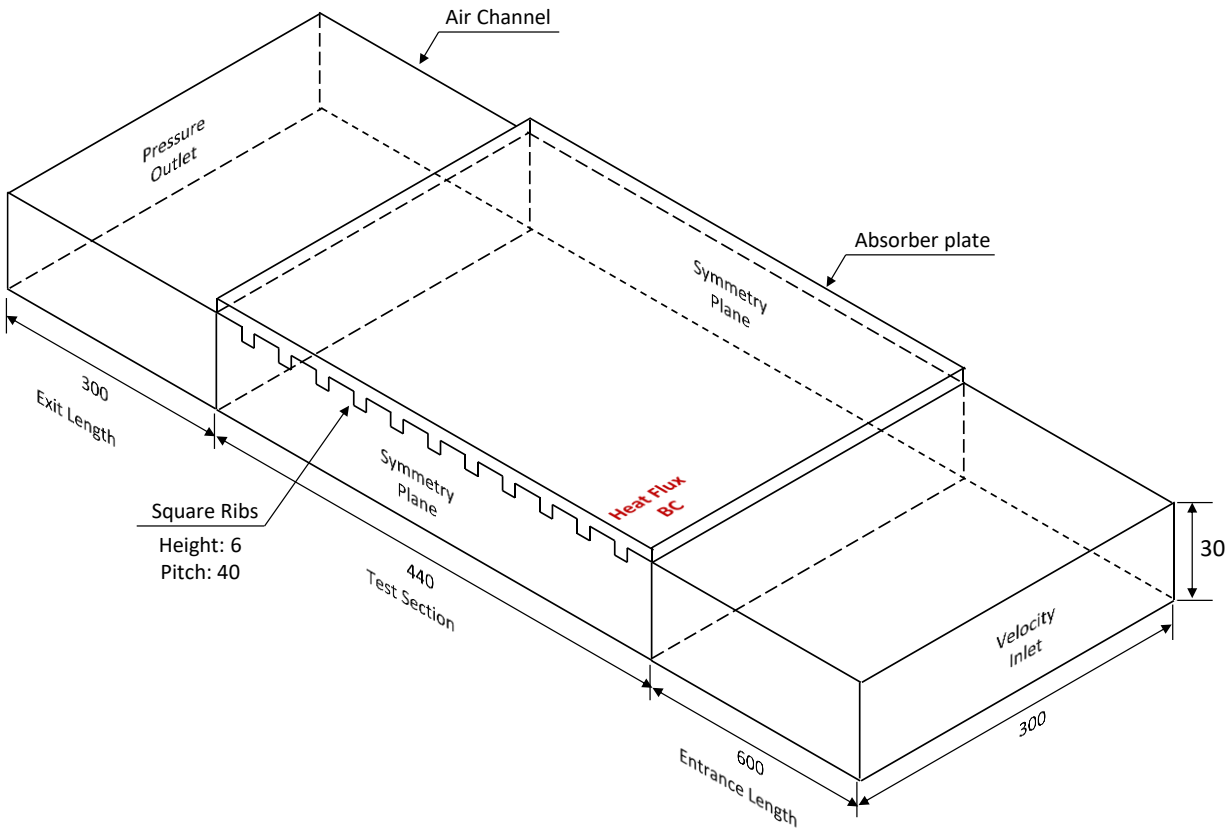


Figure 5-14: 3D Computational Domain and Boundary Conditions

### 5.2.2.2 Mesh Generation

The computational domain is discretized using extruded quadrilateral mesh with a typical size of $\frac{1}{25}H$, where H is the channel height (i.e., 30 *mm*). The mesh is refined around the roughness elements by a factor of 10 to capture the complex flow structures due to flow separation and possible reattachment. A mesh growth rate of 1.05 ensured a smooth transition from the finer mesh to the relatively coarse mesh in the undisturbed flow region. To capture the near wall temperature gradient, four prism layers have been employed. The total thickness of the prism layer is $\frac{1}{10}\left(\frac{1}{15}H\right)$ and a stretching factor of 1.5 ensured that the $y^+ \leq 1$. The 2D quadrilateral is extruded to form 10 equidistant volumetric meshes perpendicular to the flow. The meshing scheme yielded 1,491,250 grid cells (Figure 5-15).

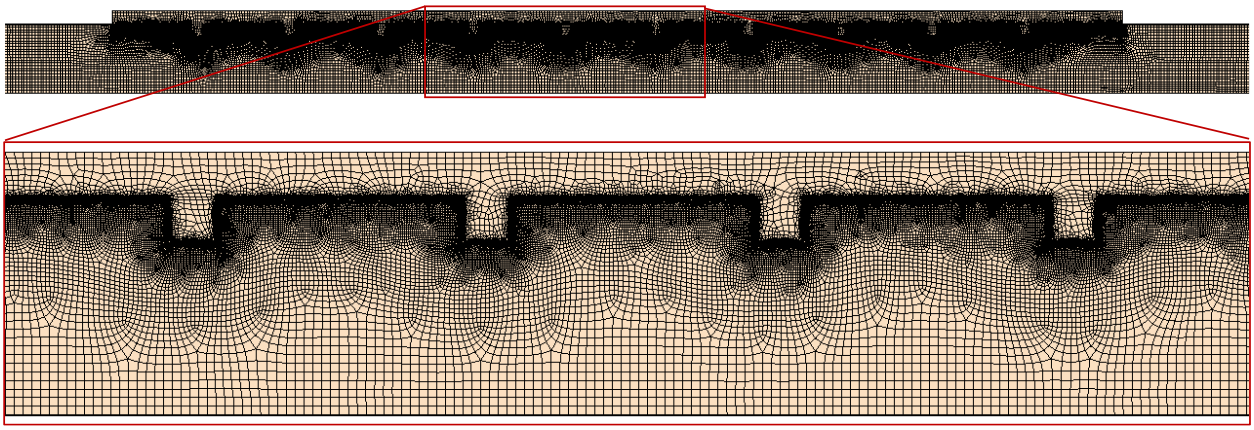

Figure 5-15 - Typical mesh cross-section

The mesh is further refined to 2,236,875 and 2,982,500 cells and a mesh sensitivity is carried. The mesh independency study is conducted for an inflow of *Re* – 7,342. The impact of the mesh refinement on the prediction of Nusselt number and friction factor is summarized in Table 5-2. Further refinement beyond 1,491,250 yielded negligible improvement in the numerical accuracy of the CFD model. Hence, the mesh with 1,491,250 cells is sufficiently accurate to simulate the flow characteristics.

Table 5-2: Summary of mesh independency study

| No. | Grid count | *Nu* | % Increase in *Nu* | *f* | % increase in *f* |
|---|---|---|---|---|---|
| 1 | 1,491,250 | 62.057 | - | 0.107 | - |
| 2 | 2,236,875 | 62.380 | 0.52% | 0.107 | 0.59% |
| 3 | 2,982,500 | 62.699 | 0.51% | 0.107 | 0.29% |

### 5.2.2.3 Boundary Conditions and Solution Strategy

A uniform heat flux of 1000 $W/m^2$ is applied on the top surface of the absorber plate. All the other walls of the computational domain are adiabatic. No-slip boundary condition is applied to all the walls in the air channel. Air at 300 *K* enters the computational domain ( Table 5-3). A constant velocity inflow profile is specified at the inlet depending on the flow condition. A pressure boundary is specified at the outlet with gauge pressure of 0 *Pa*. The inflow and outflow turbulence intensity were estimated according to Equation 5-7 (Kumar et al., 2018).

Table 5-3: Thermophysical properties of Aluminum and air

| Property | Unit | Aluminum | Air |
|---|---|---|---|
| Thermal conductivity, $k$ | W/m/K | 237 | 0.0263 |
| Density, $\rho$ | kg/m$^3$ | 2702 | 1.1614 |
| Specific heat, $C_p$ | J/kg/K | 903 | 1007 |
| Dynamic viscosity, $\mu$ | N s/m$^2$ | - | 1.85 x 10$^{-5}$ |
| Prandtl number, $Pr$ | | - | 0.707 |

The conservation equations of mass, momentum and energy are solved sequentially by implementing the segregated solver. The Second-Order Upwind scheme is used to discretize the governing equations. The SIMPLE (semi-implicit method for pressure linked equations) algorithm is implemented for the pressure-velocity coupling. The solution is converged for all residuals (i.e., continuity, velocity components and energy) less than $10^{-6}$.

#### 5.2.2.4 Performance Indicators

The heat transfer effectiveness and hydraulic performance of the SAH system with transverse roughness ribs is quantified by the Nusselt number and friction factor respectively. The Nusselt number is given in Equation 5-14.

$$\boldsymbol{Nu = \frac{h\,D}{k}} \qquad \text{Equation 5-14}$$

The fluid properties of air are taken at the bulk fluid temperature (i.e., the average of the inlet and outlet temperature;$(T_{out} + T_{in})/2$. The friction factor gives an indication of the pressure loss in the air channel (Equation 5-15).

$$\boldsymbol{f = \frac{\left(\Delta P/L\right)}{1/2\,\rho U^2} D} \qquad \text{Equation 5-15}$$

where, $\Delta P$ is the pressure drop from the inlet to the outlet, L is the length of the solution domain (i.e., 3 m), $D$ is the hydraulic diameter, $\rho$ is the density at the bulk fluid temperature, and $U$ is the inlet velocity derived from the Reynolds number (i.e., $Re = \rho UD/\mu$ ).

### 5.2.2.5 Validation Results

The numerical error was quantified with the root mean square error (*RMSE*) and the normalized root mean square error (*NRMSE*). Figure 5-16 compares the numerical prediction of the average Nusselt number and friction factor against experiment. There is a very good agreement between the numerical model prediction of the Nusselt number and the experimental data for the Reynolds number range considered. The *RMSE* and NRMSE for the numerical prediction of the Nusselt number is 2.92 and 4.65% respectively. This is within the experimental error of ± 6% for the Nusselt number. Similarly, The *RMSE* and NRMSE for the numerical prediction of the friction factor is 0.00714 and 6.16% respectively. This is within the experimental error of ± 8% for the friction factor. Since the *NRMSE* for the Nusselt number and friction factor is within experimental error of the published data, the numerical model is considered sufficiently accurate for further computational analysis.

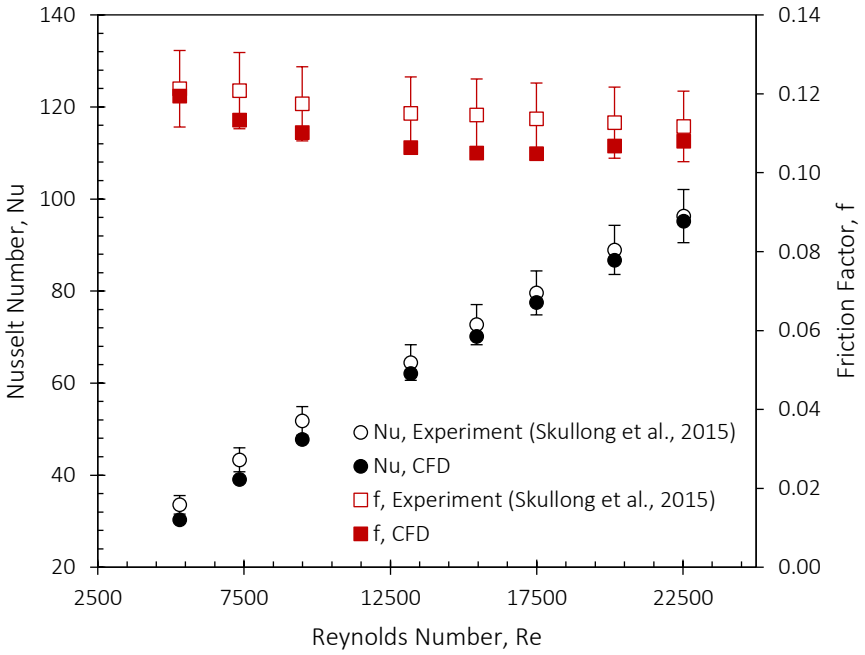


Figure 5-16: Comparison of the Numerical prediction of the Nusselt number and friction factor with published experimental data

## 5.3 Coupling of the Refrigerant-side and air-side CFD model

The air-side and refrigerant side were validated and coupled as shown in Figure 5-17 and a preliminary analysis is conducted on the heat transfer and flow characteristics of the BIPV/T cooled with air and refrigerant flow. The boundary conditions are similar to Figure 5-6 with some modifications.

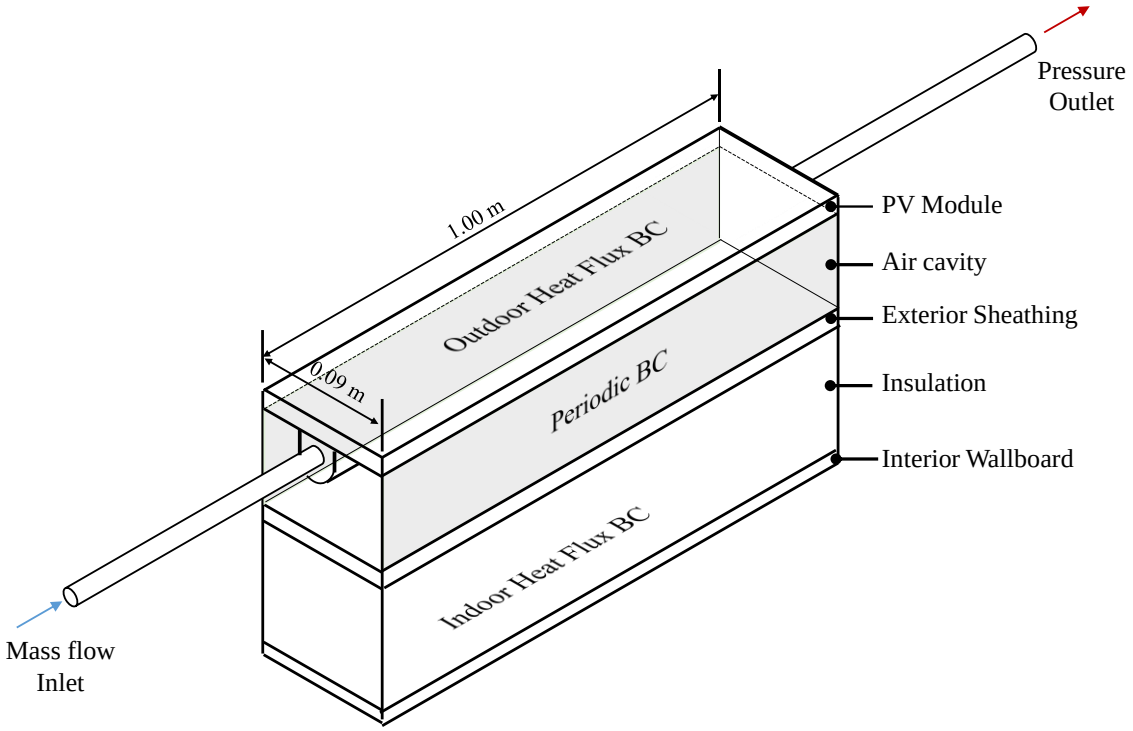


Figure 5-17: 3D computational domain of the BIPV/T facade evaporator concept

An indoor heat flux boundary condition is specified at the bottom of the computational domain. The indoor heat flux boundary is given in Equation 5-16.

$$\boldsymbol{Q}_{\boldsymbol{indoor}} = \boldsymbol{h}_{\boldsymbol{int}}(\boldsymbol{T}_{\boldsymbol{s}} - \boldsymbol{T}_{\boldsymbol{int}}) \qquad \text{Equation 5-16}$$

where, $T_s$ is the surface temperature, $T_{int}$ is the indoor air temperature (i.e., 20°C) and $h_{int}$ is the combined convection and radiation heat transfer coefficient which is given as 8.29 $W/m^2K$ for the vertical oriented surface (AHSRAE HOF, 2017). The Outdoor heat flux boundary condition specified on the PV module is given in Equation 5-17.

$$\boldsymbol{Q}_{\boldsymbol{total}} = \mathbf{PF}\left(\boldsymbol{Q}_{\boldsymbol{rad}} + \boldsymbol{Q}_{\boldsymbol{conv}} + \boldsymbol{Q}_{\boldsymbol{sky}} + \boldsymbol{Q}_{\boldsymbol{elec}}\right) \qquad \text{Equation 5-17}$$

where, $Q_{rad}$ is the measured solar radiation intensity on the PV evaporator, $Q_{conv,ext}$ is convective heat loss or gain due to wind, $Q_{sky}$ is the sky radiation, $Q_{elec}$ is the electricity output from the PV cells, and *PF* is the packing factor (i.e., 85%). The convective heat transfer in given in Equation 5-18.

$$\boldsymbol{Q_{conv,ext} = h_{ext}(T_s - T_{ext})} \qquad \text{Equation 5-18}$$

where, $T_s$ is the PV surface temperature. The sky radiation is given in Equation 5-19 (Nghana et al., 2021):

$$\boldsymbol{Q_{sky} = \varepsilon_s \sigma \left(T_s^4 - T_{sky}^4\right)} \qquad \text{Equation 5-19}$$

where, $\varepsilon_s$ is the surface emissivity (i.e., 0.85 for the PV cells), $\sigma$ is the Stefan Boltzmann constant (5.67 x $10^{-8}$ W/$m^2$/$K^4$), and $T_{sky}$ is the sky temperature. The sky temperature is estimated according to Equation 5-20.

$$\boldsymbol{T_{sky} = 0.0552 T_{ext}^{\,1.5}} \qquad \text{Equation 5-20}$$

The electrical output of the PV cells is given in Equation 5-21 and the solar radiation on the PV evaporator is given in Equation 5-22.

$$\boldsymbol{Q_{elec} = G \tau_{eva} \eta_{el}} \qquad \text{Equation 5-21}$$

where, $G$ is the solar radiation (i.e., 840 *W/$m^2$*) $\tau_{eva}$ is the transmissivity (i.e., 0.89 derived for the peak solar condition), the temperature dependent electrical efficiency (i.e., $\eta_{el}$) is given in Equation 5-10.

$$\boldsymbol{Q_{rad} = G(\tau\beta)_{pv}} \qquad \text{Equation 5-22}$$

where, $(\tau\beta)_{pv}$ is the effective absorptivity of the PV cells given in Equation 5-23 (Ji et al., 2009).

$$\boldsymbol{(\tau\beta)_{pv} = \frac{\tau_{eva}\beta_{pv}}{1 - (1 - \beta_{pv}) \cdot r}} \qquad \text{Equation 5-23}$$

where, $\beta_{pv}$ is the absorptivity of the PV cell. The transmissivity (i.e., $\tau_{eva}$) and reflectivity; $r$, are derived according to Equation 5-24 and Equation 5-25 respectively (Ji et al., 2009).

$$\boldsymbol{\tau_{eva} = \frac{1 - r}{1 + r}} \qquad \text{Equation 5-24}$$

$$\boldsymbol{r = \frac{sin^2\,(\theta_1 - \theta_2)}{sin^2\,(\theta_1 + \theta_2)} + \frac{tan^2\,(\theta_1 - \theta_2)}{tan^2\,(\theta_1 + \theta_2)}} \qquad \text{Equation 5-25}$$

where, $\theta_1$ and $\theta_2$ are the incidence and refraction angle of the solar beam. The solar incidence angle is calculated according to Equation 5-26 (AHSRAE HOF, 2017).

$$\begin{aligned}\boldsymbol{\cos(\theta_1) = \sin(L)\sin(\delta)\cos(\beta)} \\ \boldsymbol{- \cos(L)\sin(\delta)\sin(\beta)\cos(Z_s)} \\ \boldsymbol{+ \cos(L)\cos(\delta)\cos(h)\cos(\beta)} \\ \boldsymbol{+ \sin(L)\cos(\delta)\cos(h)\sin(\beta)\cos(Z_s)} \\ \boldsymbol{+ \cos(\delta)\sin(h)\sin(\beta)\sin(Z_s)}\end{aligned} \qquad \text{Equation 5-26}$$

where, $L$ is the location latitude, $\beta$ is the surface tilt angle from the horizontal, $Z_s$ is the surface azimuth angle. The hour angle and declination angle are given in Equation 5-27 and Equation 5-28 respectively (AHSRAE HOF, 2017).

$$\boldsymbol{h = 15° \times (LST - 12)} \qquad \text{Equation 5-27}$$

$$\boldsymbol{\delta = 23.45\frac{\pi}{180}\sin\left[2\pi\left(\frac{284 + n}{36.25}\right)\right]} \qquad \text{Equation 5-28}$$

where, $LST$ is the corrected local solar time and $n$ is the day number. The refraction angle of the solar beam is calculated according to Equation 5-29 (Rivera-Ortega et al., 2019).

$$\boldsymbol{n_1 \sin\theta_1 = n_2 \sin\theta_2} \qquad \text{Equation 5-29}$$

where, $n_1$ and $n_2$ are the refractive index of air and glass respectively. For the flow in the refrigerant tube, A mass flux of 9.28 *kg/m$^2$-s* is specified at the inlet. A periodic boundary condition is specified at inlet and outlet of the air domain based on the assumption of a fully developed airflow. The other parameters are similar as specified in Section 5.2.1.

### 5.3.1 Preliminary Results

The results from the preliminary analysis is presented in this section. The heat transfer and flow structure in the refrigerant tube and air cavity is presented and the impacts on the overall heat transfer performance of the BIPV/T collector is highlighted. The outdoor climate for the preliminary analysis is specified as: Solar Radiation of 441 $W/m^2$, outdoor temperature of 14.4°C, and wind speed of 3.9 $m/s$. The saturation temperature is equivalent to the outdoor air temperature.

#### 5.3.1.1 Flow visualization of the saturated flow boiling

Figure 5-18 shows the mass fraction of vapor along the refrigerant tube length.

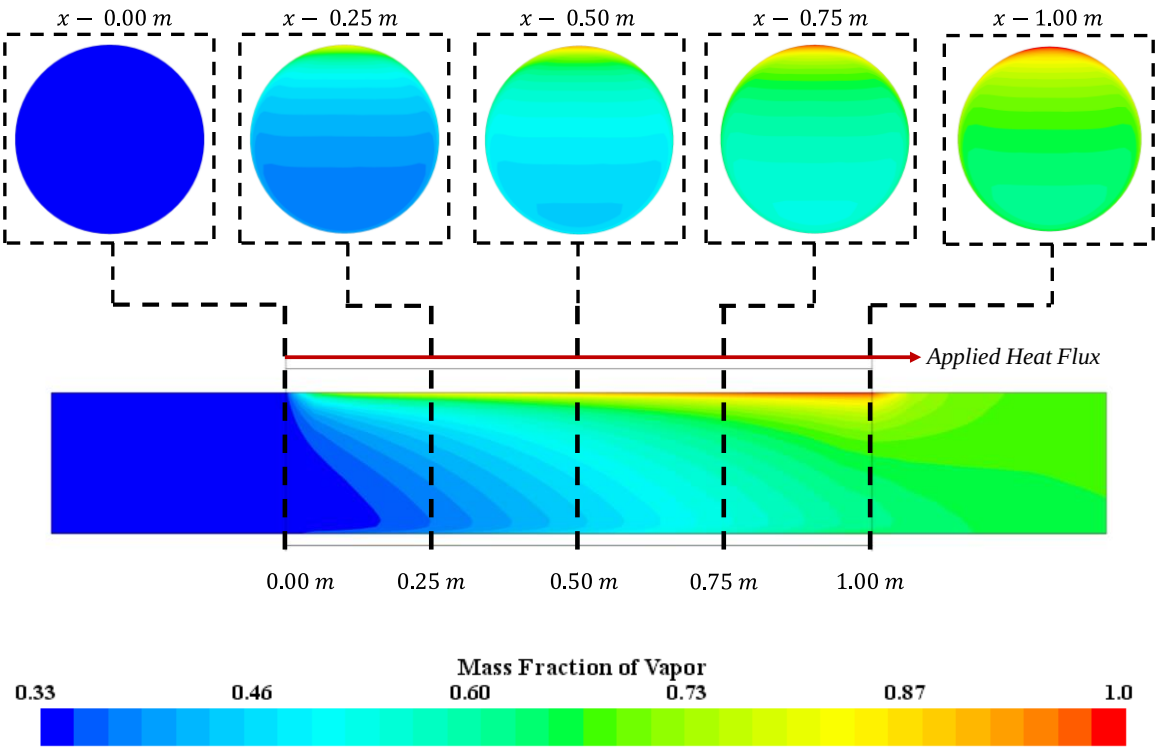


Figure 5-18: Variation of the mass fraction along the tube length

The vapor fraction increases along the tube length due to the excess heat extracted from the PV panel and the airflow in the cavity. The mean vapor mass fraction or quality increases from 0.33 at the inlet to 0.67 at the outlet. The asymmetric heating associated with BIPV/T façade concept can also be seen. Using the mass fraction at x – 1.00 m as case study. The mass fraction varies from 0.61 at the bottom of the tube adjacent to the airflow

stream to 1.00 at the top of the tube adjacent to the PV module. The asymmetric heating complicates the heat transfer coefficient evolution in the tube. It can be expected that the heat transfer coefficient will vary significantly along the tube length.

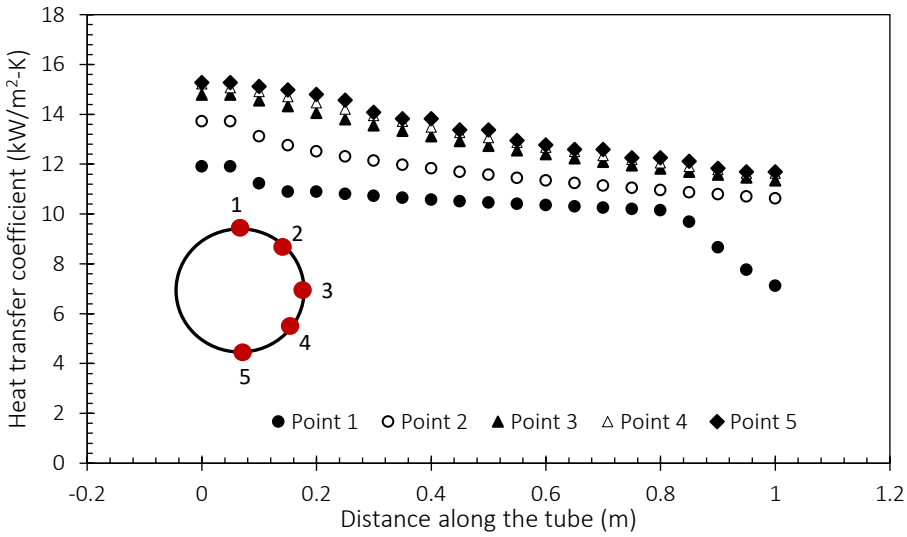


Figure 5-19: Variation of the local heat transfer coefficient along the tube length at different locations on the circumference

Figure 5-19 shows the axial variation of the heat transfer coefficient at different points on the tube cross-section. The local heat transfer coefficient is given in Equation 5-30 (Siemens, 2018)

$$\boldsymbol{h_{loc}} = \frac{\boldsymbol{\rho_f(y_c) C_{p,f}(y_c) u^*}}{\boldsymbol{T^+\left(y^+(y_c)\right)}} \qquad \text{Equation 5-30}$$

where, $\rho_f$ is the fluid density, $C_{p,f}$ is the fluid specific heat capacity, $u^*$ is the reference velocity, $T^+$ is the dimensionless temperature, and $y^+$ is the dimensionless wall distance respectively. The local heat transfer formulation implies that the higher the vapour mass fraction in the region closer to the wall, the lower the heat transfer coefficient. This is reflected in the Figure 5-19, the top of the tube adjacent the PV module has a higher enthalpy as seen in Figure 5-18, hence the local heat transfer coefficient is consistently lower over the tube length. Similarly, the vapor mass fraction is lower at the bottom of the tube compared and hence the heat transfer fraction is the highest for all the probed location.

The average heat transfer coefficient for point 1, point 2, point 3, point 4, and point 5 are 10.3 $kW/m^2$-$K$, 11.8 $kW/m^2$-$K$, 12.9 $kW/m^2$-$K$, 13.2 $kW/m^2$-$K$, and 13.4 $kW/m^2$-$K$ respectively. This is a 30.5% increase in the average heat transfer coefficient for the locations considered from point 1 to 5. The local heat transfer coefficient also increase by 113.7%. Figure 5-19 also shows that the heat transfer coefficient in the two-phase flow follows the nucleate boiling heat transfer regime as expected (See Figure 5-3).

#### 5.3.1.2 Airflow visualization

The near wall flow structure has been comprehensively discussed in Chapter 4. However, for completeness a brief discussion is presented heat to highlight the advantage of the BIPV/T façade cooled with air and refrigerant over the air cooled BIPV/T façade. Figure 5-20a shows the velocity contour of the airflow in the air channel. Typical of airflow in roughened channels is the formation of vortices in the immediate downstream and upstream of the roughness elements (i.e., tube element). Also, since the strength of the vortices is maintained by the momentum exchange with the mean flow, the bulk mean flow in the channel is distorted as seen in Figure 5-20. A consequence of the near-wall vortex flows is the development is hot spots especially in air cooled BIPV/T roughened channels. The temperature contour in Figure 5-20b shows that this hot spot problem characteristic of roughened channel flow (See Figure **3-11**) has been alleviated by introducing a secondary fluid (i.e., refrigerant) in the roughness elements. The ensures that the surface temperature of the PV module is more stable.

(a) Velocity Contour

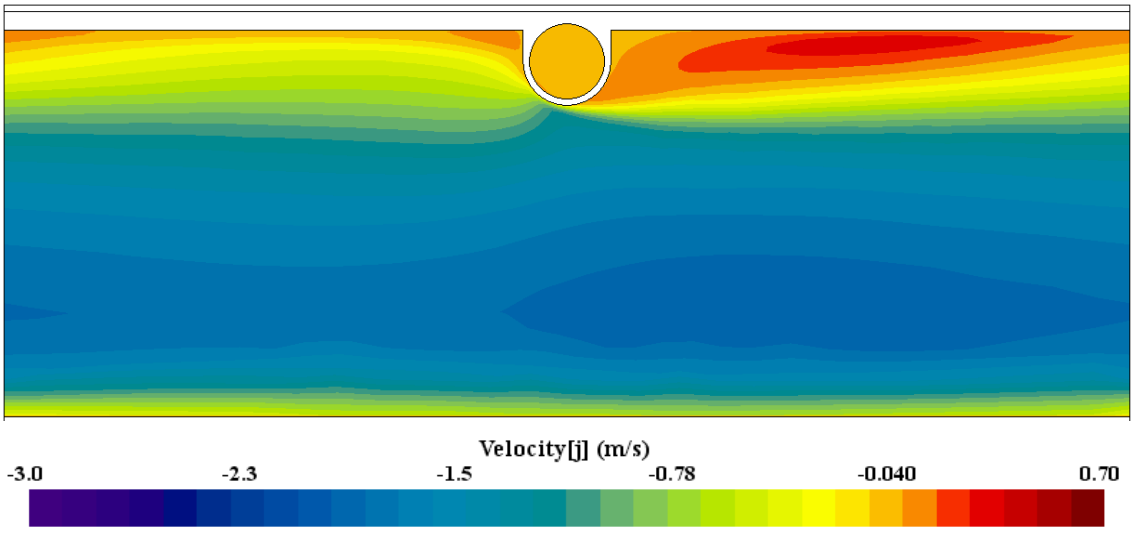


(b) Temperature Contour

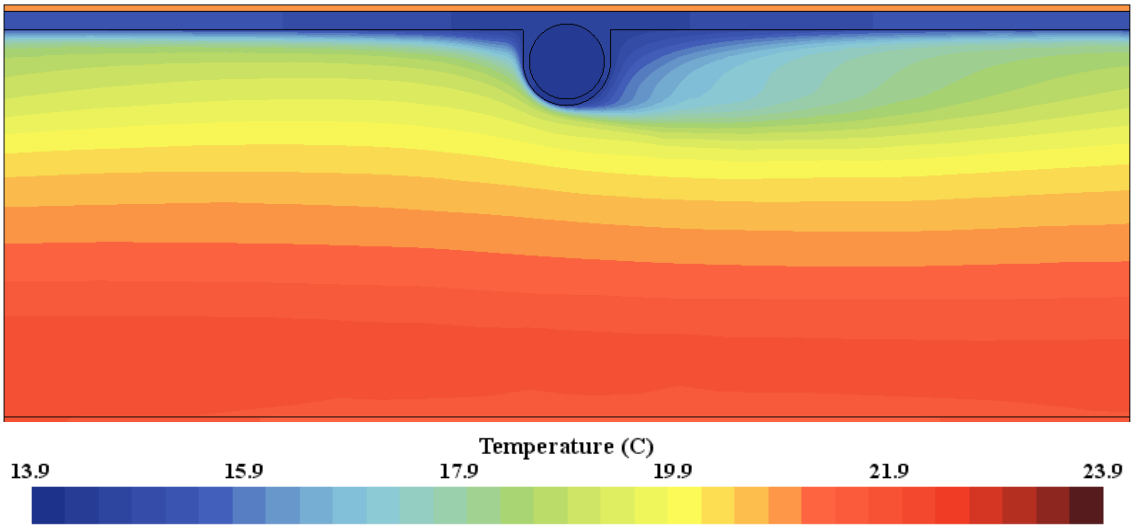


Figure 5-20: Cross section of the (a) velocity contour and (b) temperature contour for the BIPV/T facade evaporator

## 5.4 Conclusion

In this chapter, a BIPV/T façade concept coupled with heat pump technology was proposed. By coupling with heat pump the low-grade thermal energy extracted for the waste of the PV cells can be upgraded for domestic use. The useful heat extracted by the BIPV/T façade evaporator concept is enhanced by airflow in the cavity behind the cladding. The airflow is controlled to ensure that the inlet air in the cavity is always at least

within building comfort conditions. In the BIPV/T façade coupled with heat pump, the PV surface temperature is thermally regulated by both airflow and refrigerant flow. A fully coupled CFD approach was proposed to quantify the heat extracted from the PV module as well as to accurately capture the heat exchange between the airflow stream and the refrigerant flow stream. The main objective of this chapter was to validate the CFD model of the BIPV/T façade concept. Due to limited availability of experimental data to validate the CFD model, a decoupled approach is used. In the decoupled approach, the air flow and refrigerant flow are validated separately with experiment available in literature. The premise for adoption of the decoupled validation approach was the proposed BIPV/T façade concept superimposes the functionalities of the solar air heater and the PV/T evaporator. The refrigerant side is validated to within 5.5% of the experimental data with the highest errors associated with predicting the pressure drop along the refrigerant tube. The airside is validated within 6.16% of the experimental data. The air-side and refrigerant side were then coupled, and the flow visualization is discussed. It was seen that the heat transfer coefficient along the refrigerant tube is consistent with the nucleate boiling heat transfer regime. Also, the effect of the asymmetrical heating of the refrigerant is manifest in a variation of the local heat transfer coefficient by up to 113.7%. Further, the coupled airflow and refrigerant flow ensures that the hot spot problem associated with the BIPV/T air systems roughened with transverse ribs is eliminated.

## 5.5 References

ASHRAE. (2017). 2017 ASHRAE Handbook: Fundamentals. ASHRAE.

Chai, T., & Draxler, R. R. (2014). Root mean square error (RMSE) or mean absolute error (MAE)?–Arguments against avoiding RMSE in the literature. Geoscientific model development, 7(3), 1247-1250.

De Schepper, S. C., Heynderickx, G. J., & Marin, G. B. (2009). Modeling the evaporation of a hydrocarbon feedstock in the convection section of a steam cracker. Computers & Chemical Engineering, 33(1), 122-132.

Fang, X., Wu, Q., & Yuan, Y. (2017). A general correlation for saturated flow boiling heat transfer in channels of various sizes and flow directions. International journal of heat and mass transfer, 107, 972-981.

Ferrari, A., Magnini, M., & Thome, J. R. (2018). Numerical analysis of slug flow boiling in square microchannels. International Journal of Heat and Mass Transfer, 123, 928-944.

Incropera, F. P., Lavine, A. S., Bergman, T. L., & DeWitt, D. P. (2007). Fundamentals of heat and mass transfer. Wiley.

Jatau, T., & Bello-Ochende, T. (2021). Heat transfer and flow pattern map development of R134A in a U-bend tube for flow boiling evaporation. International Communications in Heat and Mass Transfer, 128, 105629.

Ji, J., He, H., Chow, T., Pei, G., He, W., & Liu, K. (2009). Distributed dynamic modeling and experimental study of PV evaporator in a PV/T solar-assisted heat pump. International Journal of Heat and Mass Transfer, 52(5-6), 1365-1373.

Kaew-On, J., & Wongwises, S. (2009). Experimental investigation of evaporation heat transfer coefficient and pressure drop of R-410A in a multiport mini-channel. International Journal of Refrigeration, 32(1), 124-137.

Kim, S. M., & Mudawar, I. (2013). Universal approach to predicting saturated flow boiling heat transfer in mini/micro-channels–Part II. Two-phase heat transfer coefficient. International Journal of Heat and Mass Transfer, 64, 1239-1256.

Kumar, R., Goel, V., & Kumar, A. (2018). Investigation of heat transfer augmentation and friction factor in triangular duct solar air heater due to forward facing chamfered rectangular ribs: A CFD based analysis. Renewable Energy, 115, 824-835.

Lai, C. M., & Hokoi, S. (2015). Solar façades: A review. Building and Environment, 91, 152-165.

Lee, M. S., Li, Z., Ling, J., & Aute, V. (2018). A CFD assisted segmented control volume based heat exchanger model for simulation of air-to-refrigerant heat exchanger with air flow mal-distribution. Applied Thermal Engineering, 131, 230-243.

Linstrom, P. J., & Mallard, W. G. (2001). The NIST Chemistry WebBook: A chemical data resource on the internet. Journal of Chemical & Engineering Data, 46(5), 1059-1063.

Liu, Q., Wang, W., & Palm, B. (2017). A numerical study of the transition from slug to annular flow in micro-channel convective boiling. Applied Thermal Engineering, 112, 73-81.

Luo, Y., Li, W., Zhou, K., Sheng, K., Shao, S., Zhang, Z., ... & Minkowycz, W. J. (2020). Three-dimensional numerical simulation of saturated annular flow boiling in a narrow rectangular microchannel. International Journal of Heat and Mass Transfer, 149, 119246.

Ma, X., Zhang, Q., Wang, J., & Yu, Y. (2020). A coupled CFD approach for performance prediction of fin-and-tube condenser. Numerical Heat Transfer, Part A: Applications, 78(6), 215-230.

Magnini, M., & Thome, J. R. (2016). A CFD study of the parameters influencing heat transfer in microchannel slug flow boiling. International Journal of Thermal Sciences, 110, 119-136.

Magnini, M., Pulvirenti, B., & Thome, J. R. (2013). Numerical investigation of the influence of leading and sequential bubbles on slug flow boiling within a microchannel. International Journal of Thermal Sciences, 71, 36-52.

Paz, C., Suárez, E., Porteiro, J., & Díaz, A. (2019). New methodology for CFD simulations of compact evaporators used in automotive ORC systems. International Journal of Thermal Sciences, 143, 14-26.

Sarkar, S. (2021). Computational Fluid Dynamics (CFD) Modeling of Two Phase Refrigerant Flow in Evaporator Refrigerant Distribution System.

Shojaeefard, M. H., Zare, J., & Nourbakhsh, S. D. (2017). Developing a hybrid procedure of one dimensional finite element method and CFD simulation for modeling refrigerant flow mal-distribution in parallel flow condenser. International Journal of Refrigeration, 73, 39-53.

Siemens, P. (2018). Simcenter STAR-CCM+ User Guide V13. 04. Siemens PLM.

Singh, V., Abdelaziz, O., Aute, V., & Radermacher, R. (2011). Simulation of air-to-refrigerant fin-and-tube heat exchanger with CFD-based air propagation. International journal of refrigeration, 34(8), 1883-1897.

Singh, V., Aute, V., & Radermacher, R. (2008). Numerical approach for modeling air-to-refrigerant fin-and-tube heat exchanger with tube-to-tube heat transfer. International Journal of Refrigeration, 31(8), 1414-1425.

Skullong, S., Thianpong, C., & Promvonge, P. (2015). Effects of rib size and arrangement on forced convective heat transfer in a solar air heater channel. Heat and Mass Transfer, 51(10), 1475-1485.

STAR CCM+ Users Manual. http://www.cd-adapco.com/products/star-ccm/documentation.

Tancabel, J., Aute, V., Ling, J., & Radermacher, R. (2021). Design Optimization of A-Type Heat Exchangers based on High Performance, Non-Round Tubes.

Tibiriçá, C. B., & Ribatski, G. (2010). Flow boiling heat transfer of R134a and R245fa in a 2.3 mm tube. International Journal of Heat and Mass Transfer, 53(11-12), 2459-2468.

Yadav, A. S., & Bhagoria, J. L. (2013). A CFD (computational fluid dynamics) based heat transfer and fluid flow analysis of a solar air heater provided with circular transverse wire rib roughness on the absorber plate. Energy, 55, 1127-1142.

Yashar, D. A., Domanski, P. A., & Cho, H. (2014). An experimental and computational study of approach air distribution for slanted and A-shaped finned-tube heat exchangers. HVAC&R Research, 20(5), 498-507.

You, Y., Wu, Z., Liu, H., Zhang, A., Zeng, X., & Shen, X. (2018). A flexible hybrid CFD model for refrigerant mal-distribution among minichannels in parallel flow condensers. International Journal of Refrigeration, 91, 80-88.

Yu, J., Momoki, S., & Koyama, S. (1999). Experimental study of surface effect on flow boiling heat transfer in horizontal smooth tubes. International journal of heat and mass transfer, 42(10), 1909-1918.

Yue, C., Zhang, Q., Zhai, Z., & Ling, L. (2018). CFD simulation on the heat transfer and flow characteristics of a microchannel separate heat pipe under different filling ratios. Applied Thermal Engineering, 139, 25-34.

# Chapter 6

# 6 BIPV/T façade concept with coupled air and refrigerant heat extraction system – Parametric analysis on the impact of the geometry and flow variables on the overall thermal efficiency

In chapter 5, a BIPV/T façade with coupled air and refrigerant heat extraction system was proposed and the principle of operation was outlined. The BIPV/T façade concept was proposed as the evaporator for a heat pump cycle (See Figure 5-1), where the extracted heat is used for domestic heating purposes. Coupling BIPV/T systems and heat pumps could present interesting possibilities (Anderson et al. 2009). Using heat pump, lower grade heat energy can be upgraded to an appropriate temperature for heating purposes (Xu et al., 2009). The co-generation of electricity and hot water using BIPV/T and heat pump coupling have the best cost performance (Ji et al., 2009; Delisle & Kummert, 2016).

The review of literature has demonstrated the effectiveness of the photovoltaic integrated solar assisted heat pump (PV-SAHP) system. The main advantage of the direct PV evaporator is the high temperature evaporation that improves the coefficient of performance (Ji et al., 2008). Note that the coefficient of performance is the ratio of the condenser output to the compressor input. The annual performance of a PV-SAHP system was compared with a direct-exchange solar assisted heat pump (DX-SAHP) system (Chow et al., 2010). The PV-SAHP achieved higher coefficient of performance (COP) values than the DX-SAHP. Also, the cooling of the PV by the refrigerant in the heat pump loop ensured that 6% of the PV electrical efficiency was recovered. It was also shown that the electrical energy generated was sufficient to meet the compressor needs, hence, the PV-SAHP system could function off grid. The self-sufficiency of the PV-SAHP was also demonstrated in Kielang et al. (2009).

COP values of up to 8.4 was achieved for a PV-SAHP system (Ji et al., 2008a). By varying the condenser inlet temperature, a COP of up to 11.4 was achieved for the PV-SAHP (Ji et al., 2008b). The sensitivity of the COP of the PV-SAHP system to the evaporation temperature was also demonstrated in Daghigh et al. (2011). The effect of glazing cover

on the PV evaporator of a PV-SAHP was investigated in Pei et al. (2008). The evaporation pressure and temperature were higher with the glazing cover since more heat is conserved. Consequently, the compressor power input was reduced by 23%. By the modifying the tube cross-section, the COP of the PV-SAHP and the collector thermal efficiency were improved by 7% and 6% respectively (Xu et al., 2009). Zhao et al. (2011) also reported improved thermal efficiencies for a roof integrated PV evaporator compared to conventional PV/T modules.

While the effectiveness of the PV-SAHP has been demonstrated in literature, most of the research implemented the PV-SAHP in a PV/T stand-alone collector concept. As such, research on the BIPV/T-SAHP concept is scarce. Also, the published literature was mostly focused on whole system performance. However, the performance of the BIPV/T-SAHP system is hinged mainly on the heat removal effectiveness of the BIPV/T façade evaporator. In this study, a parametric analysis is conducted to numerically investigate the impact of certain geometry and flow parameters on the thermos-hydraulic efficiency of the BIPV/T façade evaporator concept. The numerical simulation is conducted using computational fluid dynamics (CFD) that has been validated in Chapter 5.The parameters considered in this study are the tube shape, relative tube pitch, relative tube height, saturation temperature, and flow ratio. Each parameter will be studied under the two operational conditions identified earlier for peak solar conditions (i.e., solar radiation of 800 $W/m^2$, outdoor temperature of 20℃ and wind speed of 1 $m/s$) and off-peak solar conditions (i.e., outdoor temperature of 5℃ and wind speed of 1 $m/s$).

## 6.1 Computational evaluation of the BIPV/T façade with air and refrigerant heat extraction system

The BIPV/T façade features two fluid streams for heat extraction. Two-phase flow boiling occurs in the refrigerant stream due to the available excess heat from the PV module and the heat exchange with the roughened air channel. The problem is solved using steady RANS and the energy equations. The two-phase flow boiling is modeled using a multiphase mixture Eulerian approach - the Two-phase thermodynamic equilibrium model. The radiation exchange in the air channel is modeled using the Discrete Ordinate method

(DOM). Turbulence is modeled using the shear stress transport (SST) k-omega turbulence model.

## 6.2 Numerical Simulation Setup

The details of the numerical setup for the parametric analysis is detailed in the following section.

### 6.2.1 Computational Domain

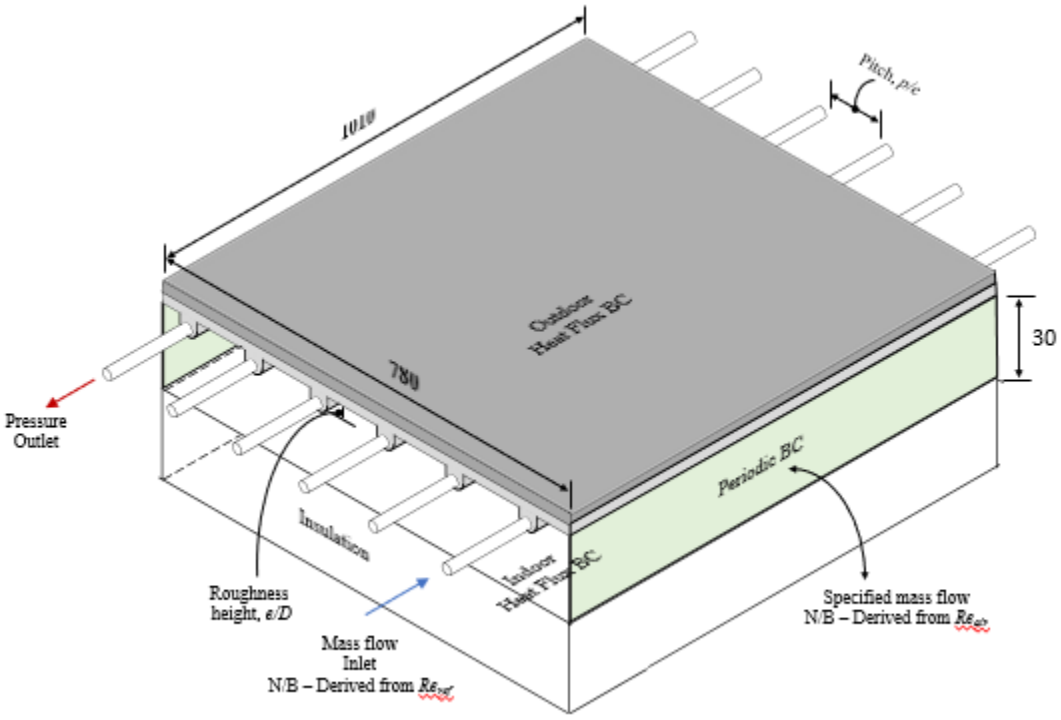


Figure 6-1 – Typical representation of the BIPV/T facade evaporator concept

Figure 6-1 shows the typical computational domain adopted for the numerical simulation. The computational domain consists of the 0.5 mm thick PV cells, the 1.5 mm thick absorber plate and the 6 mm diameter tube segments appended behind the absorber plate as shown in Figure 6-1. The fluid segments represent the serpentine tubing for thermal regulation of the PV cells. An internal interface is created between the inlet and outlet of consecutive fluid segments to ensure flow continuity. The A contact resistance of 0.042 $m^2$-$K/W$ is applied at the interface between the PV module and the thermal collector. The thermal

absorber is modelled as an aluminum plate. The thermal and optical properties of the solar cells are derived from Ji et al., (2009).

For additional thermal regulation of the PV cells and enhancement of thermal energy extraction, an airflow path is instituted beneath the collector plate. The width of the air channel is 1.01m and the depth of the air channel (i.e., *H*) is varied based on the simulation case. The air channel consists of the 780 mm heated section. Insulation of 0.03 m is provided at the bottom of the air channel in the heated section. The material properties of inner wall layers are shown in Table 6-1.

Table 6-1: Material properties of the components of the BIPV/T wall assembly[a]

| Material | $\rho$ | $\lambda$ | $c_p$ |
|---|---|---|---|
| Aluminum | 2702 | 237 | 903 |
| Batt Insulation | 12 | 0.043 | 800 |
| Air[b] | - | - | - |

[a]material properties adopted from ASHRAE Handbook of fundamentals, 2017

[b]temerature dependent air properties

Key geometric and flow parameters identified in Figure 6-1 were varied in the sensitivity study. The variables considered in this chapter are tube shape, relative tube pitch (*p/e*), relative tube height (*e/D*), and flow ratio ($Re_{ref}/Re_{air}$). The variables considered are summarized in Table 6-2. The impact of the variables listed in Table 6-2 on the wall heat flux will be investigated for peak solar (i.e., solar radiation of $800\ W/m^2$, outdoor temperature of 20°C and wind speed of 1 *m/s*) and off-peak solar conditions (i.e., outdoor temperature of 5°C and wind speed of 1 *m/s*).

Table 6-2 - Variables considered in the numerical study

| Parameter | Symbol | Iterations |
|---|---|---|
| Geometry | | Circle, square, triangle |
| Relative tube pitch | $p/e$ | 2.5 - 20 |
| Relative tube height | $e/D$ | 0.01 – 0.20 |
| Flow ratio | $Re_{ref}/Re_{air}$ | 0.13 – 75.6 |

### 6.2.2 Boundary Conditions

The detailed specifications of the indoor and outdoor heat flux boundary conditions are given in Section 5.3. However, the outdoor boundary condition is simplified by assuming that the solar incidence angle is perpendicular to the surface of the PV module. The boundary conditions for the refrigerant side and air side are consistent with Section 5.3. the inlet air temperature is specified as 20℃ for the periodic boundary condition in the air channel.

### 6.2.3 Mesh Generation

The computational domain is discretized using extruded 2D quadrilateral mesh. The mesh size was chosen to ensure a minimum of four (4) elements in the direction of heat flow for the solid components. In the air domain, the mesh is refined in upstream and downstream of the tube elements to capture the vortex flow structures associated with flow separation and reattachment. Taking this into account the mesh size varied from 0.3 mm for the absorber plate to 5 mm for the insulation material. A smooth transition from the relatively fine mesh to the coarse mesh was ensured by specifying a mesh growth rate of 1.1. To capture the near wall temperature gradient, four prism layers have been employed such that the $y^+ \leq 1$. The 2D quadrilateral is extruded to form 12 equidistant volumetric meshes perpendicular to the airflow direction. The meshing scheme yielded 1,496,372 grid cells (Figure 6-2).

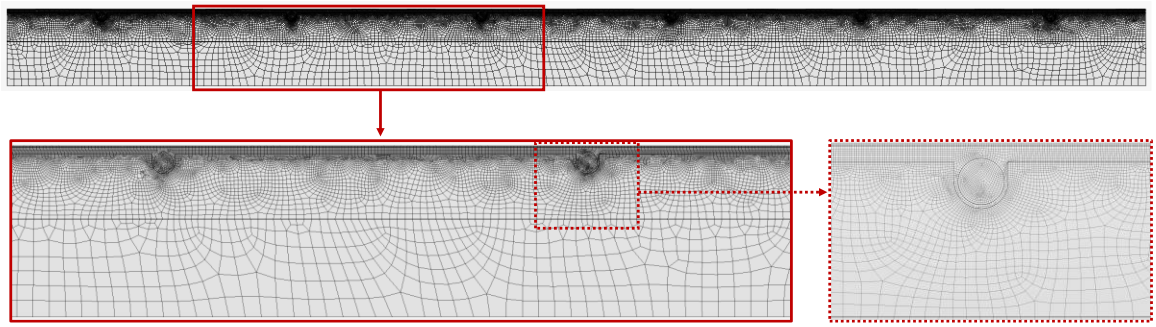

Figure 6-2 - Typical mesh cross-section

Grid independency study is carried out with a coarser and finer mesh of 308,942 and 2,446,316 cells respectively. The mesh independency study is conducted by assuming a PV surface temperature of 35°C and an inflow condition of *Re* – 5,000. The heat gain and the combined pressure loss in the refrigerant tube and air channel is calculated to assess mesh sensitivity. As seen in Table 6-3, further refinement beyond 308,942 yielded negligible improvement in the numerical accuracy of the CFD model. Hence, the mesh with 308,942 cells is sufficiently accurate to simulate the flow characteristics.

Table 6-3: Summary of mesh independency study

| | Grid count | *Heat Gain (kW)* | % Increase | *Pressure drop, Δp* | | | |
|---|---|---|---|---|---|---|---|
| | | | | *Air-side* | % Increase | *Refrigerant-side* | % increase |
| Coarse | 308,942 | 0.721 | | 7.14 | | 4,358 | |
| Normal | 1,496,372 | 0.721 | 0.0341% | 7.14 | 0.0003% | 4,354 | -0.090% |
| Fine | 2,446,316 | 0.721 | 0.0086% | 7.14 | -0.0001% | 4,343 | -0.260% |

## 6.2.4 Performance Indicators

The variables are assessed based on the thermal efficiency, electrical efficiency and overall thermal efficiency for the peak solar condition and the modified thermal efficiency for the off-peak solar condition. The thermal efficiency is given in Equation 6-1 (Layek, 2010).

$$\eta_{th} = \left(Q_u - \frac{P_{m,ref}}{C_1}\right) \Big/ GA_c \qquad \text{Equation 6-1}$$

where, $G$ is solar radiation, $A_c$ is collector area, $P_{m,ref}$ is the compressor mechanical power, $C_1$ is the conversion factor from mechanical power to thermal, and $Q_u$ is the useful heat gain given in Equation 6-2.

$$\boldsymbol{Q_u = \dot{m}_{ref}(h_{out} - h_{in})} \qquad \text{Equation 6-2}$$

where, $\dot{m}_{ref}$ is the refrigerant flow rate from Reynolds number $\left(Re = {\dot{m}D}/{\mu A}\right)$, $h_{in}$ is the inlet enthalpy and, $h_{out}$ is the outlet enthalpy. The mechanical power is given in Equation 6-3 (Layek, 2010).

$$\boldsymbol{P_{m,ref} = \frac{\dot{m}_{ref}\Delta P_{ref}}{\rho}} \qquad \text{Equation 6-3}$$

where, $\Delta P$ is the pressure loss and $\rho$ is the outlet fluid density. The electrical efficiency is given in Equation 6-4 (Lai & Hokoi, 2015).

$$\boldsymbol{\eta_{el} = \eta_{ref}\left[1 - \beta_{ref}\left(T_c - T_{ref}\right)\right]} \qquad \text{Equation 6-4}$$

where, $\eta_{ref}$ is the electrical efficiency at reference temperature ($T_{ref}$), $\beta_{ref}$ is the temperature coefficient and, $T_c$ is the cell temperature. The overall thermal efficiency is given in Equation 6-5, where 0.38 is the thermal power plant efficiency (Ji et al., 2009).

$$\boldsymbol{\eta_{o,th} = \eta_{th} + \frac{\eta_{el}}{0.38}} \qquad \text{Equation 6-5}$$

The modified thermal efficiency for the evaluation of the variables in Table 6-2 during off-peak solar conditions is given in Equation 6-6.

$$\boldsymbol{\eta_{th} = \left(Q_u - \frac{P_{m,\,tot}}{C_1}\right) \Big/ \dot{m}_{air}\left(T_{air,\,out} - T_{air,\,in}\right)} \qquad \text{Equation 6-6}$$

where, $\dot{m}_{air}$ is air mass flow rate, $T_{air,\,in}$ is the inlet air temperature at 20°C, $T_{air,\,out}$ is the outlet air temperature. The total mechanical power, $P_{m,\,tot}$, is sum of the power required to drive the airflow and the refrigerant (i.e., $P_{m,\,tot} = P_{m,\,air} + P_{m,\,ref}$). $P_{m,air}$ is the fan mechanical power given in Equation 6-7 (Layek, 2010).

$$P_{m,\,air} = \frac{\dot{m}_{air}\Delta P_{air}}{\rho_{air}} \qquad \text{Equation 6-7}$$

where, $\Delta P$ is the air pressure loss and $\rho$ is the outlet air density. The friction factor is given in Equation 6-8.

$$f = \frac{\Delta P_{air} D_h}{{}^{1}/_{2}\,\rho u_m{}^{2}} \qquad \text{Equation 6-8}$$

where, $D_h$ is the hydraulic diameter, $u_m$ is the fluid velocity. The sensible heat fraction (*S.H.F*) is given in Equation 6-9.

$$S.H.F = {}^{Q_{u,off-peak}}\Big/_{GA_c} \qquad \text{Equation 6-9}$$

were, *G* is 800 $W/m^2$. The sensible heat fraction is the ratio of the off-peak useful heat gain to the peak solar available. The *S.H.F* gives an indication of the practicality of running the heat pump under off-peak solar conditions.

## 6.3 Results and Discussion

The results from the parametric analysis are presented in this section.

### 6.3.1 Effect of relative flow ratio, $Re_{ref}/Re_{air}$

The relative flow ratio was varied from 0.1 – 1.2. The air flow Reynolds number ($Re_{air}$) was fixed at 5,000 for the simulated cases. To maintain the similarity between the scenarios, the dimensionless pitch ratio (*p/e*) and tube height (*e/D*) were 5.0 and 0.10 respectively. The saturation temperature is 20°C. Figure 6-3a shows the effect of varying the flow ratio on the thermal efficiency for the peak case study. The thermal efficiency for the flow ratios of 0.17, 0.29, 0.40, 0.58, 0.86, and 1.15 are 29.7%, 36.5%, 39.5%, 39.5%, 39.3%, and 39.2% respectively. This means that the thermal efficiency is maximized for $Re_{ref}/Re_{air} \geq 0.4$. Figure 6-3b also shows that the maximum electrical efficiency is electrical efficiency is 14.9% and occurs for $Re_{ref}/Re_{air} \geq 0.4$.

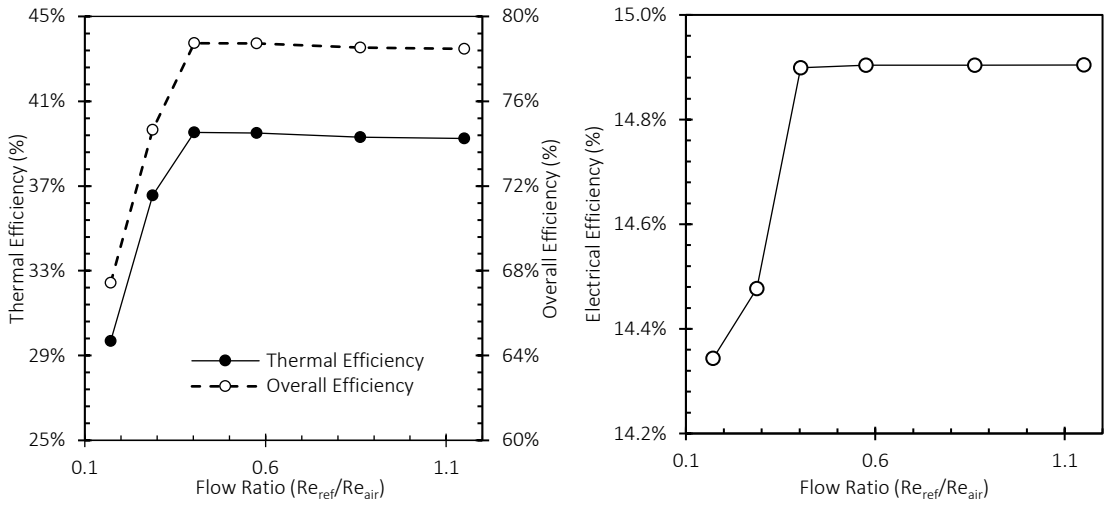


Figure 6-3 - The effect of varying the flow ratio on the (a) thermal, and (b) electrical efficiency for the peak-solar case study

The contour plots of the surface temperatures for the range of flow ratios considered in Figure 6-4 reveals that for $Re_{ref}/Re_{air} \geq 0.4$, the surface temperature is more uniform and constant at 305.2 *K*. Higher surface temperatures occur for flow ratios less than 0.4. For instance, the surface temperature varies by 8.07℃ and 6.17℃ for flow ratios of 0.17 and 0.29 respectively. As such, surface temperatures of up to 313.27 *K* and 311.37 *K* occur for flow ratios of 0.17 and 0.29 respectively. This may suggest that the refrigerant may be fully evaporated for $Re_{ref}/Re_{air} \leq 0.4$ and the heat transfer for a large section of the tube length occurs in the sensible heat region.

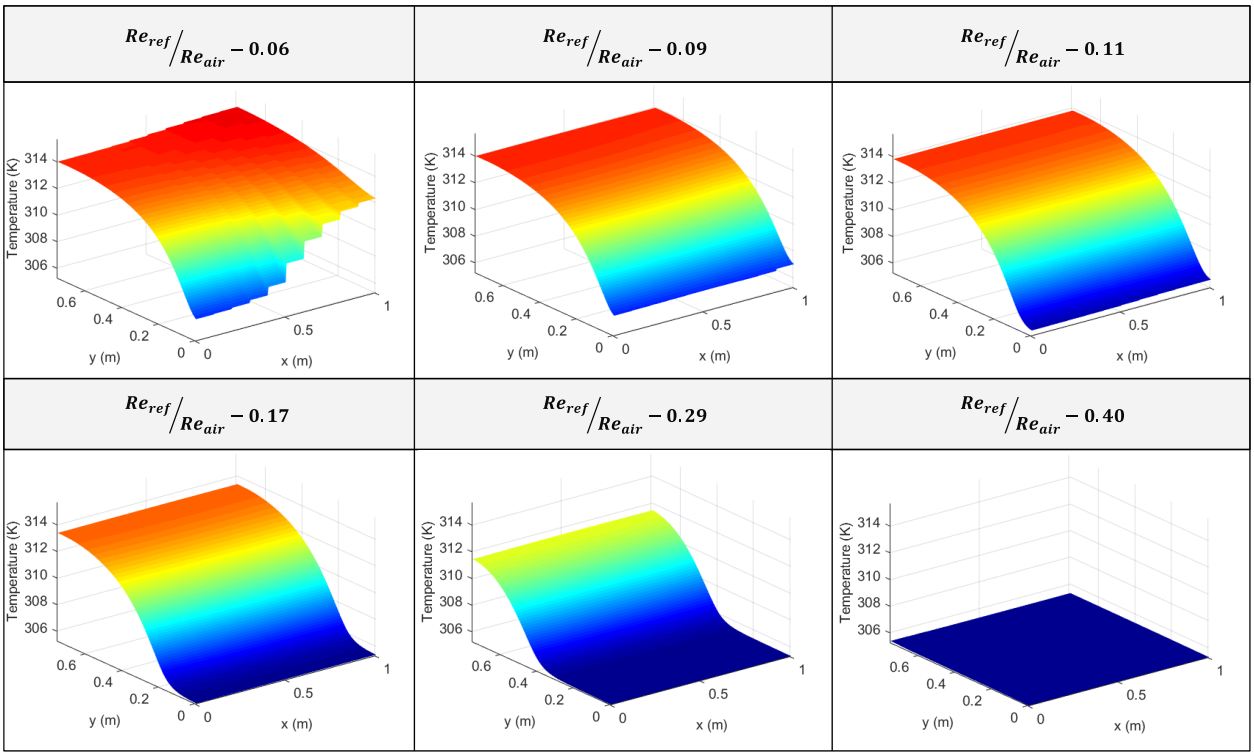


Figure 6-4 - The effect of varying the flow ratio on the PV surface temperature

This is confirmed in Figure 6-5, the refrigerant is completely evaporated at *s/L* values of 0.31, 0.63, and 1.00 for flow ratios of 0.17, 0.28, and 0.40 respectively. For $Re_{ref}/Re_{air} > 0.4$, the heat transfer occurs within the latent heat region for the full tube length. Since latent heat transfer is more desirable in this collector configuration, the thermal efficiency is maximized for $Re_{ref}/Re_{air} \geq 0.40$. Consequently, the overall efficiency is maximized for $Re_{ref}/Re_{air} \geq 0.40$.

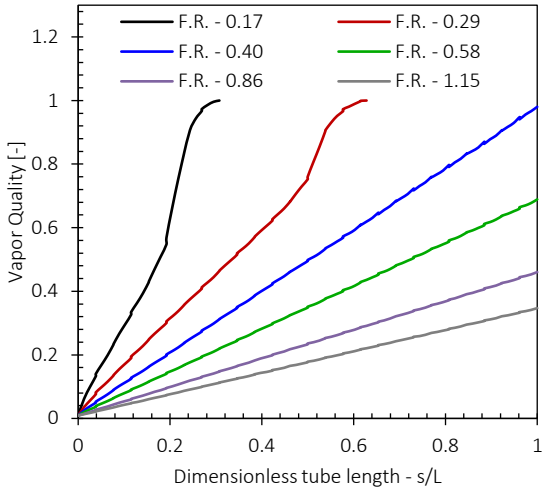


Figure 6-5 - The effect of varying the relative flow ratio (F.R.) on the point of complete evaporation

For the off-peak case study, the flow ratio is varied from 0.5 – 75.6. The air flow Reynolds number ($Re_{air}$) was fixed at 20,000 for the simulated cases. The saturation temperature is 5°C. Figure 6-6*a* shows the effect of varying the flow ratio on the thermal efficiency and the sensible heat fraction. The thermal efficiency for the off-peak case study is maximized for $Re_{ref}/Re_{air}$ = 1.0. This corresponds to a thermal efficiency of 77.8% as seen in Figure 6-6a. Figure 6-6b shows that for $Re_{ref}/Re_{air} \geq 1$, the system pressure loss significantly increases which results in a decrease in the thermal efficiency. In fact, the thermal efficiency is only 11.5% for the flow ratio of 11.34. for $Re_{ref}/Re_{air} \geq 11.34$, the system cannot recover heat from the air flow as evidenced by the negative thermal efficiency (see Figure 6-6a). The sensible heat fraction shown in Figure 6-6a indicates that the recovered heat at the optimal flow ratio is equivalent to 42.3% of the heat available during peak outdoor conditions (i.e., Solar radiation of 800 $W/m^2$ and outdoor air temperature of 20°C) considered in this study.

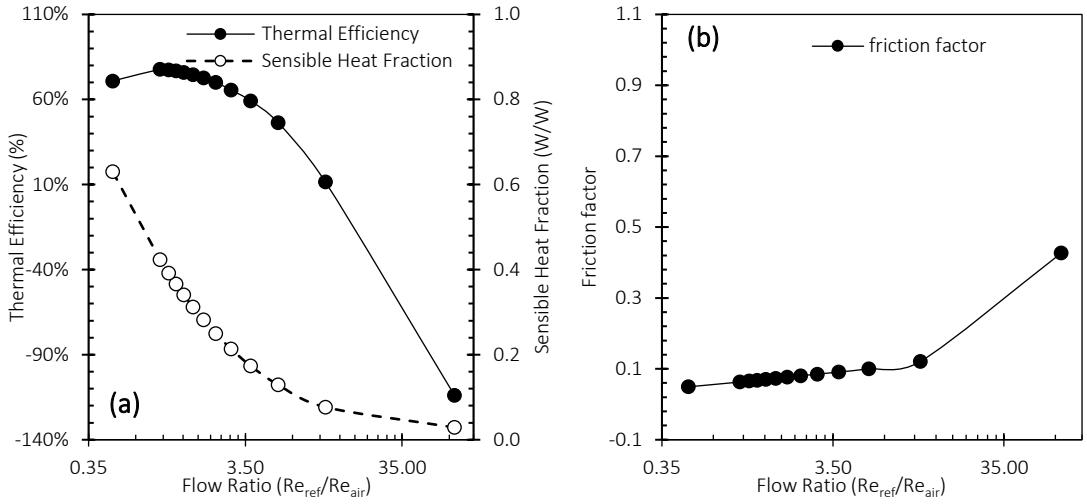


Figure 6-6 - Effect of varying the flow ratio on the (a) thermal efficiency and (b) friction factor for the off-peak case study

### 6.3.2 Effect of relative tube height, *e/D*

The dimensionless tube height (*e/D*) was varied from 0.01 to 0.20 to assess its effects on the electrical and thermal efficiency for the peak solar case study. The other parameters are *p/e* = 5.0, flow ratio of 1.0 ($Re_{ref}$ = 20,000), and saturation temperature of 20°C. Figure 6-7a shows the effect of changing the relative roughness height on the thermal efficiency. Figure 6-7a shows that the thermal efficiency is independent of the dimensionless tube height for $e/D \leq 0.10$. The thermal efficiency for *e/D* values of 0.01, 0.03, 0.05, 0.07, and 0.10 are 46.6%, 46.5%, 46.4%, 46.0%, and 44.5% respectively. For $e/D > 0.10$, the pumping power increases significantly as reflected in the reduction of the thermal efficiency. The thermal efficiency is 7.8% for *e/D* value of 0.20. Figure 6-7b shows the effect of varying the dimensionless tube height on the electrical efficiency. The electrical efficiency for *e/D* values of 0.01, 0.03, 0.05, 0.07, 0.10, and 0.20 is 14.9% as seen in Figure 6-7b. The electrical efficiency is insensitive to changing the dimensionless tube height (*e/D*). As such, the overall efficiency evolution with *e/D* follows the same trend as the thermal efficiency. The overall efficiency varies from 83.5% to 85.5% as the dimensionless tube height is reduced from 0.10 to 0.03. As seen in Figure *6-7a*, the overall efficiency is 46.7% for *e/D* = 0.20. The overall efficiency is optimized for *e/D* = 0.10 during the peak solar case study.

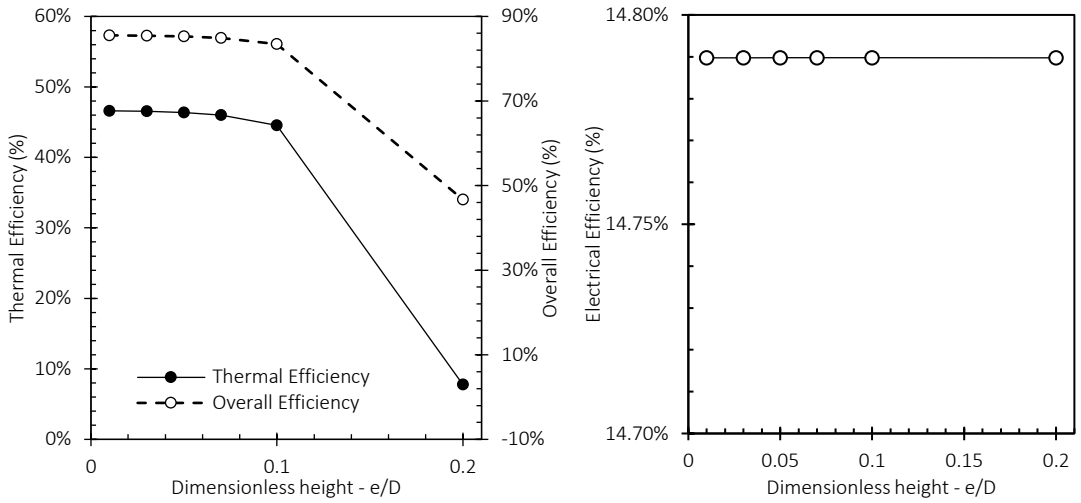


Figure 6-7 - The effect of varying the dimensionless tube height (e/D) on the (a) thermal efficiency and (b) electrical efficiency

For the off-peak case study, the geometry and flow constraints were similar as in the peak solar case study except for the saturation temperature that is 5°C. Figure 6-8a shows the effect of varying the dimensionless tube height on the thermal efficiency and the sensible heat fraction for the off-peak case study. The thermal efficiency increases from 51.8% for $e/D$ = 0.03 to a maximum of 83.7% for $e/D$ = 0.10 and decreases to 66.9% for $e/D$ = 0.20. The transverse tube act as turbulators that enhance the heat transfer between the airflow and refrigerant flow. As such, the thermal efficiency initially increases with increase in the dimensionless tube height for $e/D \leq 0.10$. The pressure loss associated with the blockage of the flow passage becomes significant for $e/D > 0.10$. This is seen in the growth of the friction factor from 0.31 for $e/D$ = 0.10 to 3.23 for $e/D$ = 0.20 (Figure 6-8b). This leads to a decrease in the thermal efficiency for $e/D > 0.10$. The sensible heat fraction shown in Figure 6-8a indicates that the recovered heat at the optimal dimensionless tube height is equivalent to 57.0% of the heat available during peak outdoor conditions considered in this study.

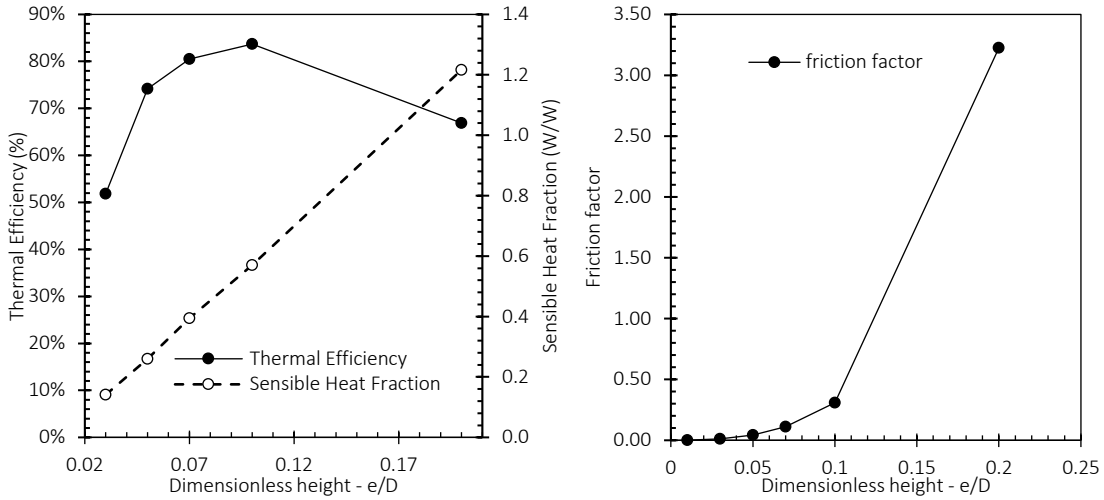


Figure 6-8 - Effect of varying the dimensionless tube height (*e/D*) on the (a) thermal efficiency and (b) friction factor for the off-peak case study

### 6.3.3 Effect of relative tube pitch, p/e

The relative roughness pitch was varied from 2.5 to 20 to assess its effects on the electrical and thermal efficiency for the peak solar case study. The other parameters are *e/D* = 0.10, flow ratio of 1.0 ($Re_{ref}$ = 20,000), and saturation temperature of 20℃. The tube spacing is important to ensure a more uniform surface temperature on the collector. However, if the tubing is spaced too close, the collector may become too cold which may be detrimental for the system thermal efficiency. Figure 6-9a shows the effect of changing the dimensionless tube pitch (*p/e*) on the thermal efficiency. The thermal efficiency for *p/e* values of 2.5, 5.0, 7.5, 10.0, 12.5, 15.0, and 20.0 are 45.7%, 44.9%, 44.4%, 44.2%, 44.1%, 44.0%, and 43.8% respectively. The thermal efficiencies are similar for the range of dimensionless pitch (*p/e*) values considered in the study. Hence, the thermal efficiency is independent of *p/e*. Also, Figure 6-9b shows that the electrical efficiency is independent of *p/e*. The electrical efficiency varies between 14.8% to 14.7% as *p/e* is increased from 2.5 to 20. This implies that the surface temperature is uniform for all the *p/e* values considered. The uniform surface temperature for the higher *p/e* values is facilitated by the airflow in the channel. Consequently, the overall efficiency is similar for the range *p/e* values considered (Figure 6-9*a*).

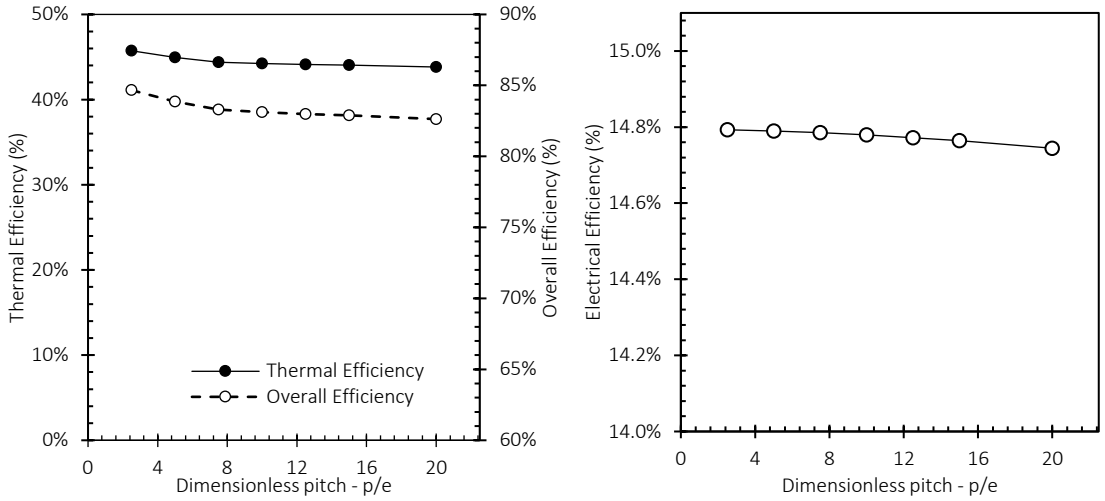


Figure 6-9 - The effect of varying the dimensionless tube pitch (p/e) on the (a) thermal efficiency and (b) electrical efficiency

For the off-peak case study, relative roughness pitch was varied from 2.5 to 20. Similar geometric and flow constraints as in the peak solar case study were imposed except the saturation temperature that is 5°C. Figure 6-10a shows the effect of varying the dimensionless tube pitch on the thermal efficiency and the sensible heat fraction for the off-peak case study. The thermal efficiency for *p/e* values of 2.5, 5.0, 7.5, 10.0, 12.5, 15.0, and 20.0 are 85.0%, 85.7%, 83.5%, 82.4%, 81.7%, 80.8%, and 78.6% respectively. The thermal efficiency is maximized for $p/e \leq 5.0$. The pressure loss associated with the flow blockage is maximized for $p/e = 7.5$ as seen in Figure 6-10b. The transverse tube elements in the flow path incite flow recirculation in the immediate upstream and downstream of the tube elements. The near-wall recirculation flow pattern is dependent on the dimensionless pitch ratio (*p/e*). The recirculation flow is sustained by momentum exchange with the mean flow. This induces disturbances in the mean flow that is maximized at $p/e = 7.5$. The sensible heat fraction shown in Figure 6-10a indicates that the recovered heat at the optimal dimensionless tube pitch (i.e., $p/e = 5.0$) is equivalent to 50.0% of the heat available during peak outdoor conditions considered in this study.

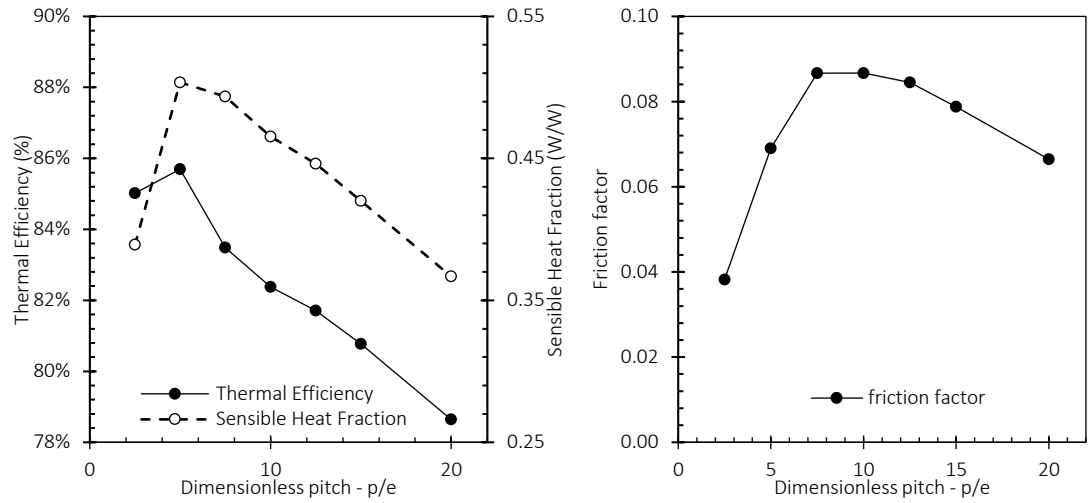


Figure 6-10 - Effect of varying the dimensionless tube pitch (*p/e*) on the (a) thermal efficiency and (b) friction factor for the off-peak case study

### 6.3.4 Effect of tube shape

The cross-sectional tube shape was varied as shown in Figure 6-11. A circular, rectangular, and triangular tube shape were considered as they indicate the most common variations in literature.

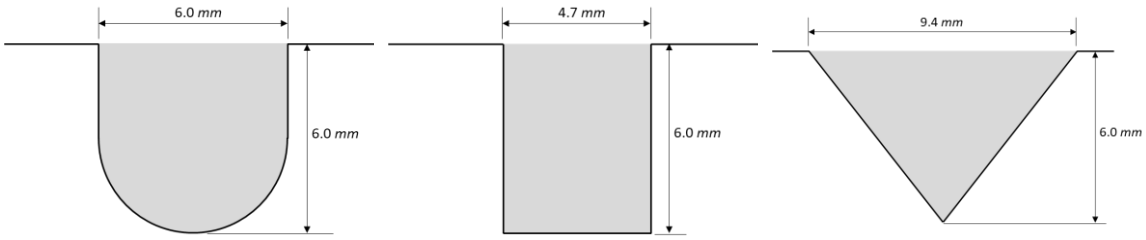


Figure 6-11 - Cross-section of the tube shapes considered for the peak and off-peak case study

Similarity between the tube shape alternatives was ensured by setting the other geometric and flow parameters as: *p/e* = 21.7, *e/D* = 0.1, flow ratio of 1.0 ($Re_{ref}$ = 20,000), and saturation temperature of 20°C. The cross-sectional area for the respective tube shapes were identical to ensure similar volume flow rates. Figure 6-12 shows the impact of the tube shape on the thermal efficiency and electrical efficiency for the peak solar case study. The cross-sectional shape has negligible impact on the electrical and thermal efficiency.

The similarity between all the cross-sectional shapes is attributed to the air flow in the channel which is in thermal equilibrium with the refrigerant in the tubes.

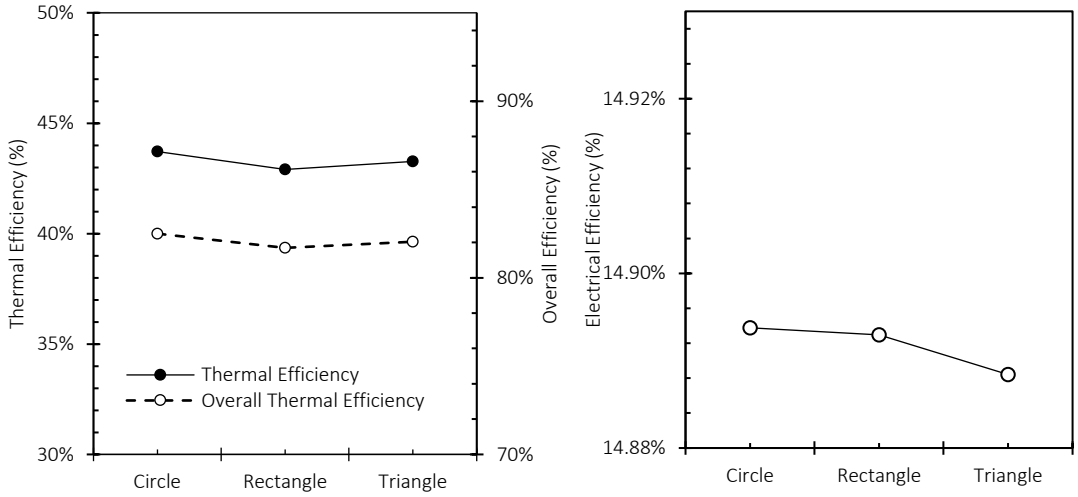


Figure 6-12 - The effect of varying the cross-sectional tube shape on the (a) thermal efficiency, and (b) electrical efficiency

For the off-peak case study, similar geometric and flow constraints as in the peak solar case study were imposed except the saturation temperature that is 5°C. Figure 6-13a shows the effect of varying the tube cross-section on the thermal efficiency and the sensible heat fraction for the off-peak case study. The thermal efficiency for the circle, rectangle and triangle cross-section are 77.8%, 83.8% and 76.9% respectively. The thermal efficiency is maximized for the rectangular cross-section. The sensible heat fraction for the circle, rectangle and triangle cross-section are 34.8%, 43.1% and 38.3% respectively. Figure 6-13b shows that the pressure loss associated with the rectangular cross-section is more significant than the circular and triangular cross-section. The better thermal performance associated with the rectangular cross-section is attributed to the reduced surface are for heat loss to the colder outdoor air. In Figure 6-11, for a unit depth, the exposed are for heat loss is 6.0 $mm^2$, 4.7 $mm^2$ and 9.4 $mm^2$ for the circular, rectangular and triangular cross-section.

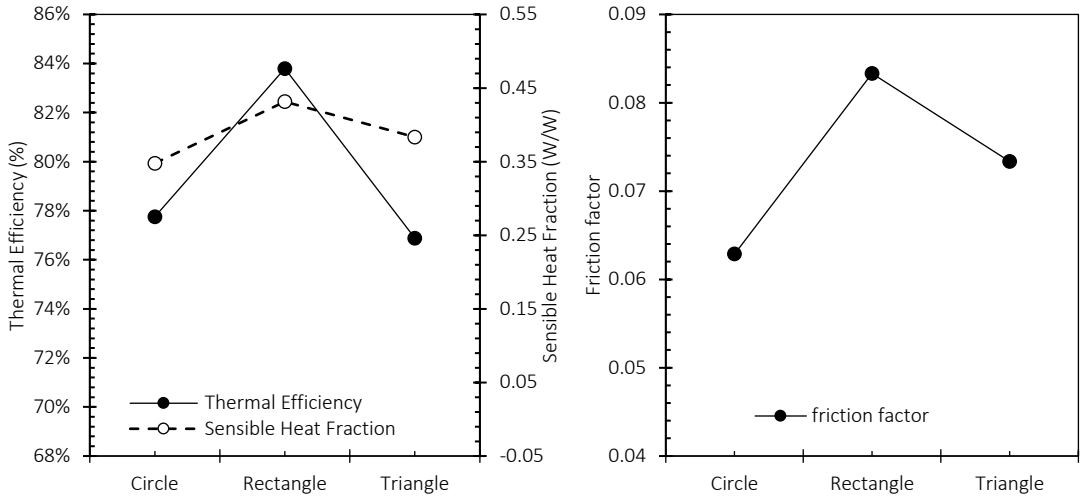


Figure 6-13 - Effect of varying the dimensionless tube pitch (p/e) on the (a) thermal efficiency and (b) friction factor for the off-peak case study

## 6.4 Conclusion

A building integrated photovoltaic solar assisted heat pump (BIPV-SAHP) concept was presented. The performance of the BIPV-SAHP concept was enhanced by incorporating a ventilation scheme that utilized the building exhaust air to drive the heat pump especially for relatively low outdoor air conditions (i.e., outdoor temperatures < 20°C). In effect, the BIPV served multiple functions including, alternative cladding system, on-site electrical energy generation, PV evaporator, and air source heat pump when the solar radiation may be low to drive the heat pump. The multifunctionality is anticipated to improve the cost effectiveness of the PV integration with buildings. Knowing that the performance of the BIPV-SAHP is based on the integration efficiency of the BIPV wall assembly, a numerical model of the BIPV wall assembly was developed in CFD.

The CFD model was validated with published experimental data in literature. A decoupled approach was taken that involved validating the airflow and refrigerant flow separately. The decoupled air-side and refrigerant side were coupled in the CFD environment, and a parametric analysis is conducted to investigate the effects of key geometric and flow parameters on the overall efficiency of the BIPV evaporator design. The variables considered were the relative flow ratio ($Re_{ref}/Re_{air}$), dimensionless tube height ($e/D$), dimensionless tube spacing ($p/e$), and tube cross-sectional shape. The variables are

evaluated for the peak solar condition (i.e., Solar radiation of 800 $W/m^2$ and outdoor air temperature of 20℃) and an off-peak outdoor condition (i.e., outdoor air temperature of 5℃). For the peak solar condition, the overall efficiency is maximized for $Re_{ref}/Re_{air} \geq 0.40$ and $e/D \leq 0.10$ for all values of $p/e$ and tube shapes (i.e., circle, square, and triangle). For the off-peak case study, the overall efficiency is maximized for $Re_{ref}/Re_{air} = 1.0$, $e/D = 0.10$, $p/e = 5.0$, and a square tube cross-section.

## 6.5 References

Anderson, T. N., Duke, M., Morrison, G. L., & Carson, J. K. (2009). Performance of a building integrated photovoltaic/thermal (BIPVT) solar collector. Solar Energy, 83(4), 445-455.

ASHRAE. (2017). 2017 ASHRAE Handbook: Fundamentals. ASHRAE.

Chow, T. T., Fong, K. F., Pei, G., Ji, J., & He, M. (2010). Potential use of photovoltaic-integrated solar heat pump system in Hong Kong. Applied Thermal Engineering, 30(8-9), 1066-1072.

Daghigh, R., Ruslan, M. H., & Sopian, K. (2011). Advances in liquid based photovoltaic/thermal (PV/T) collectors. Renewable and Sustainable Energy Reviews, 15(8), 4156-4170.

Delisle, V., & Kummert, M. (2016). Cost-benefit analysis of integrating BIPV-T air systems into energy-efficient homes. Solar Energy, 136, 385-400.

Ji, J., He, H., Chow, T., Pei, G., He, W., & Liu, K. (2009). Distributed dynamic modeling and experimental study of PV evaporator in a PV/T solar-assisted heat pump. International Journal of Heat and Mass Transfer, 52(5-6), 1365-1373.

Ji, J., Liu, K., Chow, T. T., Pei, G., He, W., & He, H. (2008). Performance analysis of a photovoltaic heat pump. Applied Energy, 85(8), 680-693.

Ji, J., Pei, G., Chow, T. T., Liu, K., He, H., Lu, J., & Han, C. (2008). Experimental study of photovoltaic solar assisted heat pump system. Solar energy, 82(1), 43-52.

Keliang, L., Jie, J., Tin-tai, C., Gang, P., Hanfeng, H., Aiguo, J., & Jichun, Y. (2009). Performance study of a photovoltaic solar assisted heat pump with variable-frequency compressor–a case study in Tibet. Renewable Energy, 34(12), 2680-2687.

Lai, C. M., & Hokoi, S. (2015). Solar façades: A review. Building and Environment, 91, 152-165.

Layek, A. (2010). Optimal thermo-hydraulic performance of solar air heater having chamfered rib-groove roughness on absorber plate. International Journal of Energy and Environment, 1(4), 683-696.

Pei, G., Ji, J., Chow, T. T., He, H., Liu, K., & Yi, H. (2008). Performance of the photovoltaic solar-assisted heat pump system with and without glass cover in winter: a comparative analysis. Proceedings of the Institution of Mechanical Engineers, Part A: Journal of Power and Energy, 222(2), 179-187.

Xu, G., Deng, S., Zhang, X., Yang, L., & Zhang, Y. (2009). Simulation of a photovoltaic/thermal heat pump system having a modified collector/evaporator. Solar Energy, 83(11), 1967-1976.

Zhao, X., Zhang, X., Riffat, S. B., & Su, Y. (2011). Theoretical study of the performance of a novel PV/e roof module for heat pump operation. Energy conversion and Management, 52(1), 603-614.

# Chapter 7

# 7 Energy Performance of BIPV/T Façade system Coupled with Heat Pump Technology for Domestic Hot Water

In chapter 6, a sensitivity study on the impact of key geometric and flow parameters on the thermal performance of the BIPV/T façade system with air and refrigerant heat extraction was assessed. This was done to maximize the heat extraction from the airflow enhanced BIPV/T façade evaporator concept. In this chapter the optimized BIPV/T façade coupled with heat pump technology is utilized for domestic hot water heating and the potential energy savings is quantified. The potential of the photovoltaic assisted heat pump (PV-HP) system has been demonstrated in literature. The main advantage of the PV evaporator is the high temperature evaporation. This means that the PV evaporator is more thermally efficient than conventional PV/T modules (Zhao et al., 2011). Consequently, the compressor input is reduced. Pei et al., (2008) showed that the compressor power input is reduced by 23% for PV/T evaporator with glazing. The reduced compressor electrical input improves the potential of the PV/T evaporator as a self-sufficient system in that the electrical energy generated was sufficient to meet the compressor needs (Chow et al., 2010 and Kielang et al., 2009). The reduced compressor input reflects in an increase in the coefficient of performance (COP). Ji et al., (2008) and Zhao et al. (2011) demonstrated that it is possible to achieve COP values of 8.0 or higher with a PV/T assisted heat pump. Further increase in the COP was facilitated by modifying the refrigerant tube shape of the PV/T evaporator for a more efficient heat transfer. This improved the COP by 7% compared to the conventional sheet and tube PV/T evaporator concept (Xu et al., 2009).

Another benefit of the high temperature evaporation is the increase in the overall thermal energy yield. Chow et al. (2010) demonstrated that the annual heat gain of the PV-HP is 25% higher than the DX-SAHP. The heat extracted from the PV/T evaporator enhances the electrical efficiency of the PV cells by about 6% compared with a stand-alone PV system. while the high temperature evaporation of the PV-HP is beneficial, some authors have demonstrated the efficacy of the PV/T solar assisted heat pump system (PV/T-SAHP). Manzolini et al. (2016) showed that the produced was sufficient to supply about 50% of the heat load. Similarly, Bai et al. (2012) demonstrated that the indirect water-based PV/T

solar-assisted heat pump system installed in a sports facility in Hong Kong was sufficient to offset 65% and 90% of the hot water load during winter and summer respectively.

While the effectiveness of the PV assisted heat pump has been demonstrated in literature, most of the research implemented the PV-HP in a PV/T stand-alone collector concept. As such, research on the BIPV/T assisted heat pump concept is limited. In this study, the energy associated with BIPV/T façade coupled with heat pump for DHW is investigated with emphasis on the impact of orientation and climate. The methodology employed for the energy analysis is discussed in the next section.

## 7.1 Methodology

The annual water heating energy savings associated with incorporating the BIPV/T façade coupled with heat pump technology was assessed by implementing the methodology illustrated in Figure 7-1. The simulation methodology involved four (4) distinct phases: weather analysis, detailed CFD simulation, regression analysis and Building energy simulation (BES).

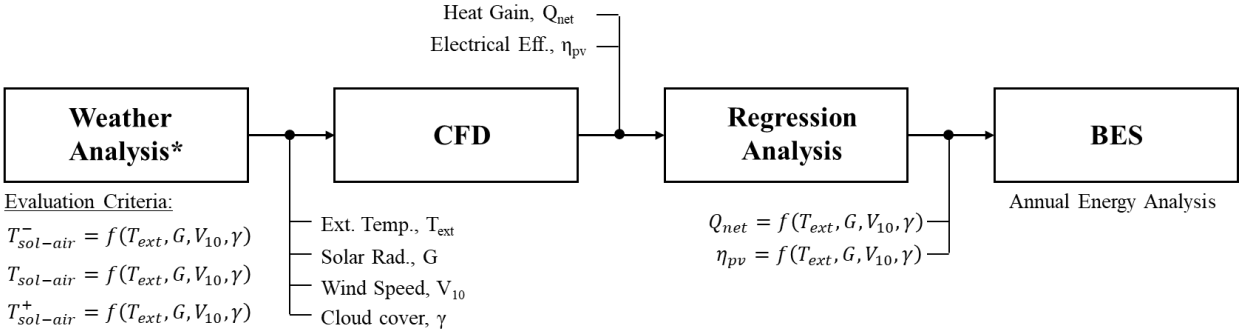


Figure 7-1 - Illustration of simulation methodology

The objective of the weather analysis is to determine representative days for each month of the year. The representative days are characteristic of maximum, minimum and average solar availability for each month of the year. The measure of solar radiation availability is evaluated using the hourly Sol-air temperature especially for periods with global solar radiation higher than 150 $W/m^2$ (i.e., the threshold for operation of the BIPV/T system). The result of the weather analysis is 36 representative days for the 12 months of the year (i.e., 3 days for each month). The outdoor conditions determined from the weather analysis

served as boundary conditions for the detailed CFD simulation from which the useful heat gain and the electrical efficiency are determined. The multi-variable polynomial regression analysis carried out to correlate the heat gain and electrical efficiency with the outdoor conditions. Once the accuracy of the correlation has been verified, the correlation is implemented in the BES platform to dynamically predict the additional thermal and electrical energy afforded by implementing the BIPV/T façade coupled with heat pump technology for domestic hot water and the associated energy savings. The details of the weather analysis, detailed CFD simulation, regression analysis, and Building energy simulation are outlined in Section 7.2, Section 7.3, Section 7.4, and Section 7.5 respectively.

## 7.2 Weather Data Analysis

The weather data for Vancouver, BC has been analyzed as case study; however, it should be noted that the correlations that will be determined in Section 7.4 may be applied accurately to other climates within the constraints of the derived correlations. Please refer to Section 7.4 for more detail. That said, the EnergyPlus weather file (i.e., .epw) for Vancouver, BC was analyzed to determine the typical outdoor conditions for each month in the year. The representative days in each month are determined by considering the Sol-air temperature given in Equation 7-1.

$$\boldsymbol{T_{sol-air} = T_o + \frac{(\alpha \cdot G - Q_{sky})}{h_{comb,ext}}} \qquad \text{Equation 7-1}$$

where, $T_o$ is the outdoor air temperature, $G$ is the global solar radiation, $\alpha$ is the solar radiation absorptivity (i.e., $\tau\beta$), $Q_{sky}$ is the sky radiation given in Section 5.3 (note that the surface temperature is replaced by the outdoor temperature), and $h_{comb,ext}$ is the combined heat transfer coefficient for radiation and convection given in Equation 7-2.

$$\boldsymbol{h_{comb,ext} = h_{conv,ext} + h_{rad,ext}} \qquad \text{Equation 7-2}$$

Where, $h_{conv,ext}$ is the exterior convective heat transfer coefficient given in Equation 7-3 (Nghana et al., 2020) and $h_{rad,ext}$ is the radiation heat transfer coefficient given in Equation 7-4 (Siemens, 2018).

$$\boldsymbol{h_{conv,ext} = 3.8\,V_{10} + 7.4} \qquad \text{Equation 7-3}$$

$$\boldsymbol{h_{rad,ext} = \sigma\varepsilon\left[\left(T_{sky}{}^{2} + T_{o}{}^{2}\right)\left(T_{sky} + T_{o}\right)\right]} \qquad \text{Equation 7-4}$$

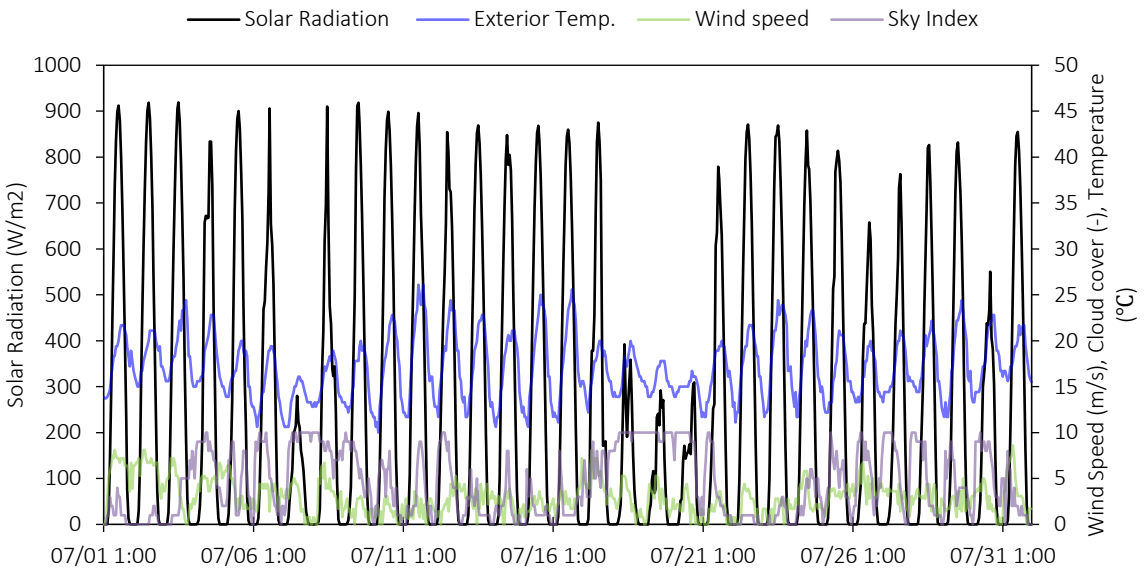


Figure 7-2 - TMY3 weather data in Vancouver, BC for the month of July

The monthly weather data analysis is illustrated for the month of July. Figure 7-2 shows the outdoor temperature, Solar radiation, wind speed and cloud cover for the month July. As seen in Figure 7-2, the outdoor conditions are elevated with peak outdoor air conditions of up to 25℃ on July 11$^{th}$, and peak solar radiation of up to 919 $W/m^2$ on July 3$^{rd}$. Characteristic of summer conditions is the low wind speeds and clear sky conditions as evident in Figure 7-2. Given the relevant outdoor information, the hourly sol-air temperature is computed for the hours during which the solar radiation is higher than 150 $W/m^2$ using Equation 7-1. The daily average Sol-air temperature is computed from the hourly Sol-air temperature. Figure 7-3 shows the daily Sol-air temperature computed for the month of July.

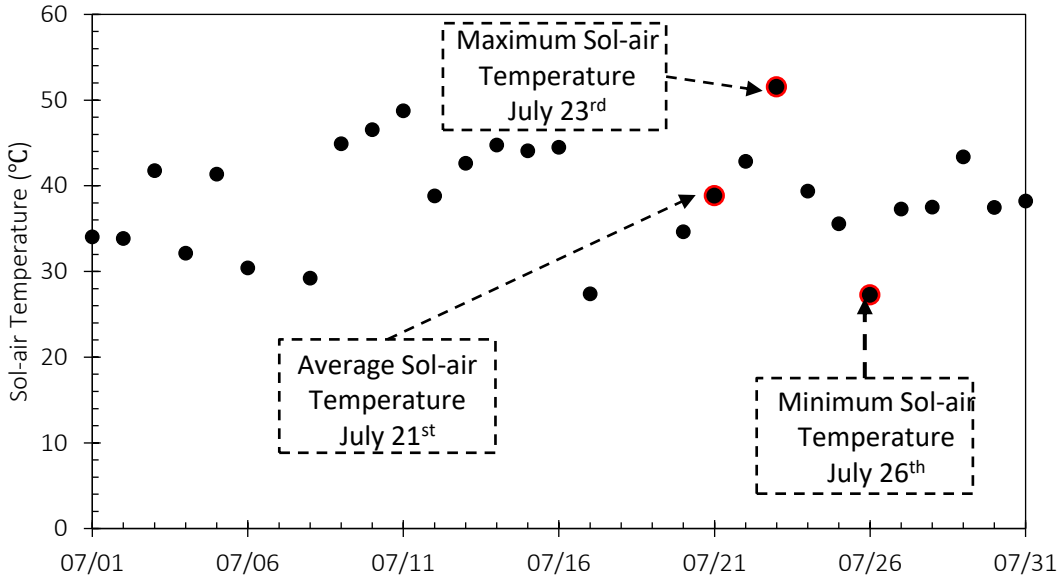


Figure 7-3 - Daily Sol-air temperature computed for July with the three representative days for maximum, minimum and average solar conditions highlighted

Figure 7-3 shows that the maximum, average and minimum Sol-air temperature are 51.5°C, 38.8°C, and 27.3°C and occur on July 23rd, July 21st, and July 26th respectively. Note that the minimum sol-air temperature is for conditions when the global solar radiation is higher than or equal to 150 W/m$^2$ to satisfy the minimum requirements for efficient operation of Solar cells. The same procedure has been applied for all the months of the year and summarized in Table 7-1.

Table 7-1 - Representative days for Solar minimum, average and maximum based on derived Sol-air temperature

| Month | Min. | Avg. | Max. |
|---|---|---|---|
| January | 01/09 | 01/29 | 01/15 |
| February | 02/24 | 02/10 | 02/25 |
| March | 03/05 | 03/31 | 03/26 |
| April | 04/23 | 04/27 | 04/29 |
| May | 05/15 | 05/26 | 05/07 |
| June | 06/13 | 06/29 | 06/28 |
| July | 07/26 | 07/21 | 07/23 |
| August | 08/18 | 08/28 | 08/09 |
| September | 09/24 | 09/15 | 09/13 |
| October | 10/22 | 10/23 | 10/04 |
| November | 11/20 | 11/14 | 11/09 |
| December | 12/06 | 12/10 | 12/07 |

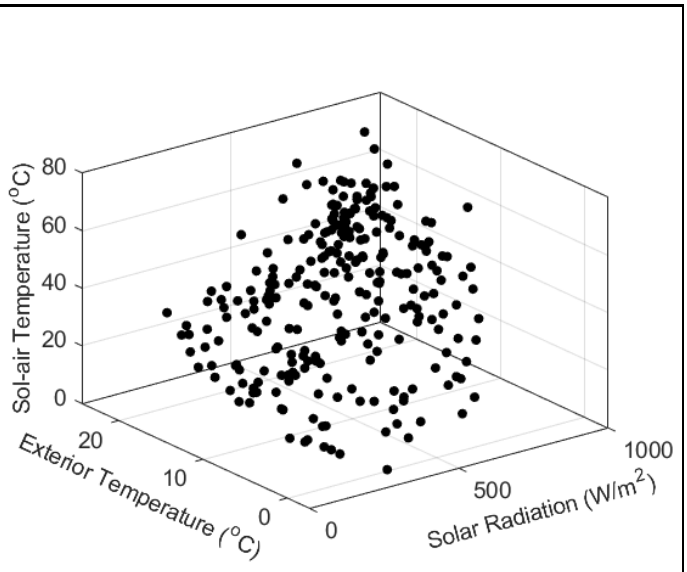


## 7.3 Determination of the thermo-electric BIPV/T façade parameters

Upon determination of the representative days for each month of the year, the useful heat gain and electrical efficiency associated with implementing the BIPV/T façade are determined numerically using CFD. The CFD model and boundary conditions have been validated extensively and reported in Chapter 5 and Chapter 6. However, the computation domain is briefly described. Figure 7-4 shows the computational domain adopted for the numerical simulation. The computational domain consists of the 0.5 mm thick PV cells mounted on the 1.5 mm thick aluminum absorber plate with 6 mm diameter fluid segments appended behind the absorber plate as. The fluid segments represent the serpentine tubing to facilitate meshing efficiency. An internal interface is created between the inlet and outlet of consecutive fluid segments to ensure flow continuity. The length of the air channel is 0.78 m, width of the air channel is 1.01m, and the depth of the air channel is 30 mm. The inner insulated wall consists of the sheathing materials (i.e., plywood), insulation material and interior board (i.e., gypsum). The material properties of the inner wall layers were derived from ASHRAE HOF (2017).

The BIPV/T façade system is decribed by the following geometrical parameters: the roughness height, *e*, which is the diameter of the circular ribs; the roughness pitch, *p*, which is the distance between successive ribs; and the channel height, *H*. The dimensionless roughness height and pitch are then derived as *e/D* and *p/e* respectively. *D* is the hydraulic diameter of the air channel. The dimensionless roughness height and pitch were specified as 0.10 and 15 respectively to ensure optimal performance for peak solar conditions (See Section 6.4). Similarly, the flow rate in the air cavity is derived for Re = 5000 as this maximized the thermohydraulic performance for forced airflow (See Section 4.5). The Refrigerant flow rate is then derived such that the flow ratio (i.e., $Re_{ref}/Re_{air}$) is always greater than or equal to 0.40. The tube shape did not significantly impact the performance for the couple flow, so a circular fluid geometry is assumed (See See Section 6.4).

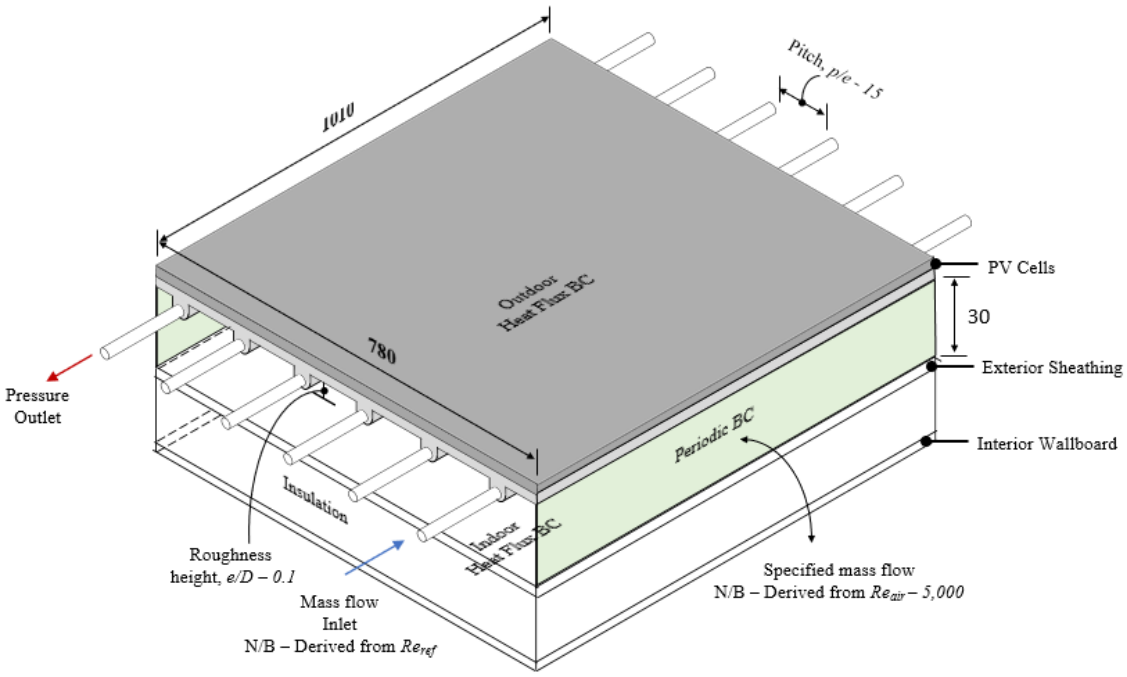


Figure 7-4 - Numerical representation of the BIPV/T facade evaporator concept

### 7.3.1 Derived Quantities

Once the CFD simulation had been conducted based on the numerical simulation setup specified in in Chapter 5 and Chapter 6, the performance of the BIPV/T façade concept was analyzed from a component scale (PV/T), system scale (PV/T-HP) and building envelope scale (BIPV/T-HP). In the component scale, the primary concern is maximizing

the useful heat gain and the electrical output. In the system scale, the other components of the BIPV/T façade driven heat pump technology are considered like the compressor electrical input, etc. In the system scale, the emphasis is on maximizing the heat added to the water storage tank on the condenser side of the heat pump loop.

#### 7.3.1.1 Component scale derived quantities

The BIPV/T façade is assessed based on the useful heat gain and the electrical efficiency. the useful heat gain given in Equation 7-5.

$$\boldsymbol{Q_u = \dot{m}_{ref}(h_{out} - h_{in})} \qquad \text{Equation 7-5}$$

where, $\dot{m}_{ref}$ is the refrigerant flow rate from Reynolds number $\left(Re = {\dot{m}D}/{\mu A}\right)$, $h_{in}$ is the inlet enthalpy and, $h_{out}$ is the outlet enthalpy. The thermal efficiency is then derived as shown in Equation 7-6 (Layek, 2010).

$$\boldsymbol{\eta_{th} = \left(Q_u - \frac{\Delta P_{air}\dot{m}_{air}}{C_1\rho_{air}} - \frac{\Delta P_{ref}\dot{m}_{ref}}{C_1\rho_{ref}}\right)\Big/ GA_c} \qquad \text{Equation 7-6}$$

where, $A_c$ is collector area, ${\Delta P_{air}\dot{m}_{air}}/{C_1\rho_{air}}$ and ${\Delta P_{ref}\dot{m}_{ref}}/{C_1\rho_{ref}}$ are the power required to drive the airflow and the refrigerant flow respectively. $C_1$ is the conversion factor from mechanical power to thermal. The electrical efficiency is given in Equation 6-4. Further, the heat transfer effectiveness and hydraulic performance of the air flow path is quantified by the Nusselt number and friction factor respectively. The Nusselt number is given in Equation 7-7 (Incorpera et al., 2007) and friction factor is given in Equation 7-8 (Incorpera et al., 2007).

$$\boldsymbol{Nu = \frac{h\,D}{k}} \qquad \text{Equation 7-7}$$

$$\boldsymbol{f = \frac{\Delta P_{air} D}{{}^1/_2\,\rho u_m{}^2}} \qquad \text{Equation 7-8}$$

where, $D$ is the hydraulic diameter, $u_m$ is the fluid velocity, $\rho$ is the fluid density, $h$ is the CFD derived convective heat transfer coefficient and $k$ is the thermal conductivity. The fluid properties of air are taken at the bulk fluid temperature (i.e., $T_{out} + T_{in}/2$).

#### 7.3.1.2 System scale derived quantities

The system scale derived quantities required additional manipulation of the thermo-electric and hydraulic parameters from the CFD model (i.e., Useful heat gain and electrical efficiency). From the CFD derived output variables, the total heat gain and the total Net heat gain are derived. The total heat gain is derived by considering the modular construction in Figure 7-5. As seen in Figure 7-5, the wall assembly consists of *n*, layers of one fluid element simulated such that the total modular height and width are 2.40 m and 1.00 m respectively.

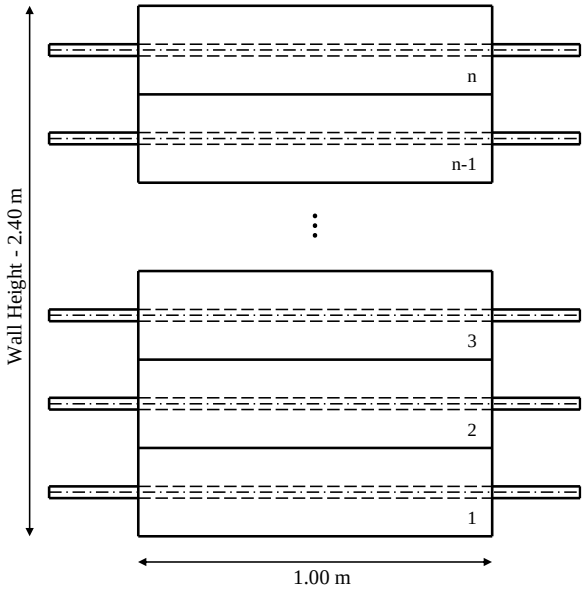


Figure 7-5 - Illustration of BIPV/T wall module

The total heat gain is given in Equation 7-9

$$\boldsymbol{Q_{total} = \sum_{i=1}^{n} Q_i} \qquad \text{Equation 7-9}$$

Where, $Q_i$ is the derived heat gain from the CFD model for a single fluid element. Inherently, a linear relationship between the heat gain and collector area has been assumed.

However, the pressure drop in the refrigerant tube is not linear; hence, incorporating a similar approach as given in Equation 7-9 will lead to underestimation of the pressure drop in the tube. The frictional pressure drop is estimated according to Equation 7-10 (Muller-Steinhagen & Heck, 1986).

$$\left(\frac{dp}{dL}\right)_{f,tp} = \dot{x}(1-\dot{x})^{1/3}[A + 2(B-A)] + B\dot{x}^3 \qquad \text{Equation 7-10}$$

where, $\dot{x}$ is the flow quality, $dp$ is the pressure drop, and $dL$ is the tube length. The other variables in Equation 7-10 are given in Equation 7-11 - Equation 7-12.

$$\left(\frac{dp}{dL}\right)_{f,l} = f_l \frac{\dot{m}^2}{2\rho_l d} = A \qquad \text{Equation 7-11}$$

$$\left(\frac{dp}{dL}\right)_{f,g} = f_g \frac{\dot{m}^2}{2\rho_g d} = B \qquad \text{Equation 7-12}$$

where, $\dot{m}$ is the flow rate, $d$ is the hydraulic diameter, $\rho$ is the fluid density and $f$ is the friction factor given in Equation 7-13 and Equation 7-14 for liquid and gases respectively.

$$f_i = \frac{0.3164}{Re_i^{1/4}} \;\therefore i = l, g \qquad \text{Equation 7-13}$$

And

$$Re_i = \frac{\dot{m}d}{\vartheta_i} \;\therefore i = l, g \qquad \text{Equation 7-14}$$

In Equation 7-14, $\vartheta$ is the dynamic viscosity of the fluid. The accuracy of Equation 7-10 has been verified in Figure 7-6.

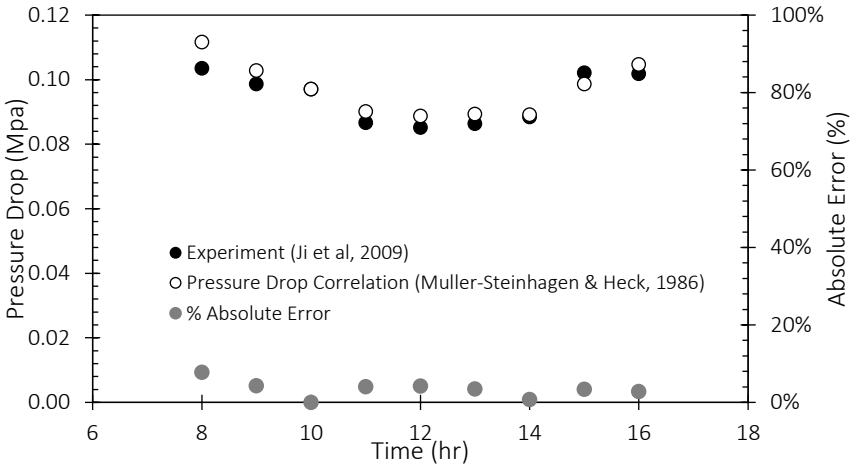


Figure 7-6 - Experimental validation of pressure drop correlation

Figure 7-6 shows that the pressure drop is accurately predicted when compared with experimental data published in Ji et al., (2009). The maximum absolute error is 7.81% and occurs at 8:00 am for the day in study. The RMSE and NRMSE for the prediction of the pressure drop are 3919.1 Pa and 4.16% respectively. Note that the correlation predicts the friction pressure drop only citing negligible impacts of the acceleration and static pressure drop. The frictional pressure drop in the air channel is also estimated according to Equation 7-15

$$\boldsymbol{f = \frac{2\,\Delta P}{L\rho U^2} D} \qquad \text{Equation 7-15}$$

where, $f$ is the friction factor, $L$ is the channel length, $\Delta P$ is the pressure drop, $U$ is the flow velocity, $D$ is the hydraulic diameter, and $\rho$ is the density of the fluid. The friction factor is estimated from Equation 7-16 and Equation 7-17 (See Chapter 4.4.2.4).

$$\boldsymbol{f_{triangle} = Re^{-0.299} e^{9.3271\left(\frac{e}{D}\right)} \left( -0.001625 \left(\frac{p}{e}\right)^2 + 0.034005 \left(\frac{p}{e}\right) + 0.623332 \right)} \qquad \text{Equation 7-16}$$

$$\boldsymbol{f_{semi-circle} = 0.87523\, f_{triangle} - 0.0085587} \qquad \text{Equation 7-17}$$

where, *e/D* is the dimensionless roughness height, and *p/e* is the dimensionless roughness pitch. A contribution to the net heat gain of the BIPV façade coupled with heat pump is the compressor input. The compressor input was derived by considering the first laws of thermo dynamics and assuming an ideal heat pump cycle. Figure 7-7 illustrates the heat pump cycle on a T-s (i.e., Temperature and entropy) diagram. In Figure 7-7, $P_1$ and $P_2$ are the evaporation and condensing pressure respectively. This also sets the condensing and evaporating temperature since phase change typically occurs over a constant temperature and pressure.

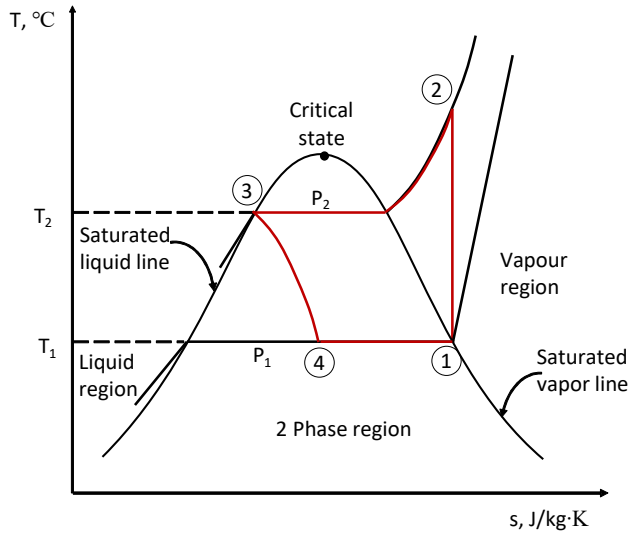


Figure 7-7 - Heat pump cycle represented on a T-s diagram

As seen in Figure 7-7, the refrigerant is evaporated from (4) to (1), compressed from (1) to (2) for a higher pressure, condensed from (2) to (3) for a saturated fluid and throttled from (3) to (4) at constant enthalpy. The compressor input (i.e., process (1) to (2)) is given in Equation 7-18.

$$\boldsymbol{W_{in,comp} = \dot{m}_{comp}(h_2 - h_1)} \qquad \text{Equation 7-18}$$

where, $h_1$ and $h_2$ are the outlet and inlet enthalpies of the compressor, $\dot{m}_{comp}$ is the flow rate at the compressor inlet. The outlet enthalpy of the compressor is fixed by specifying a condensing temperature of 60°C. Ideally, the compressor flow rate is the same as the condenser and compressor flow rate especially at peak solar conditions when the refrigerant is completely evaporated. However, at off-peak conditions, the refrigerant is not

completely evaporated; hence, the refrigerant is passed through an accumulator to remove the liquid phase in the two-phase mixture such that the refrigerant is fully evaporated at the inlet of the compressor. The pressure is maintained within the accumulator. Figure 7-8 shows the accumulator with input and output states; (1) and (2) respectively.

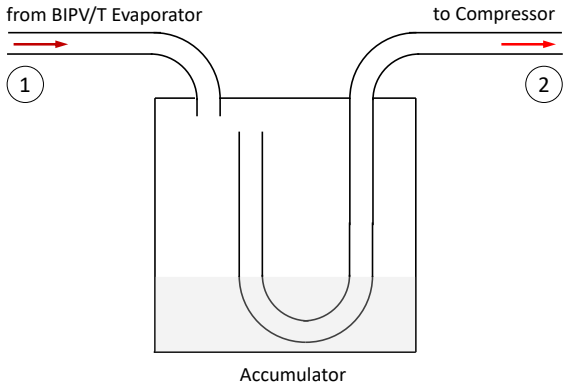


Figure 7-8 - Illustration of accumulator

By applying Bernoulli to the inlet and outlet states of the accumulator, the velocity at the outlet (i.e., state (2)) is given in Equation 7-19.

$$\boldsymbol{\rho_1 {V_1}^2 = \rho_2 {V_2}^2} \qquad \text{Equation 7-19}$$

where, $\rho_1$ and $V_1$ are the inlet density and velocity; and $\rho_2$ and $V_2$ are the outlet density and velocity respectively. The compressor mass flow rate is then derived according to Equation 7-20.

$$\boldsymbol{\dot{m}_{comp} = \rho_2 V_2 A_2} \qquad \text{Equation 7-20}$$

where, $\rho_2$ is the density of the saturated gas, $A_2$ if the area of the tube (assumed to be the same as used in the CFD model) and $V_2$ is the flow velocity. With the known heat gain (Equation 7-9), pressure drop in the refrigerant tube and air channel, and the compressor input. The net heat gain is then derived according to Equation 7-21.

$$\boldsymbol{Q_{net} = Q_{total} - W_{in,comp} - \left(\frac{\Delta P_{air}\dot{m}_{air}}{\rho_{air}} + \frac{\Delta P_{ref}\dot{m}_{ref}}{\rho_{ref}}\right)/0.18} \qquad \text{Equation 7-21}$$

Where, 0.18 is the constant of conversion from electrical energy to thermal energy (Layek, 2010).

#### 7.3.1.3 Building Envelope Scale derived quantities

In the building scale, the impact of the BIPV/T façade concept on the heat flux through the wall assembly is accounted for. This is estimated from the comparing the dynamic performance the airflow enhanced BIPV/T evaporator with the typical rainscreen assembly with the same boundary conditions.

##### 7.3.1.3.1 Dynamic Performance of The Airflow Enhanced BIPV/T Evaporator

The dynamic performance of the airflow enhanced BIPV/T façade evaporator is investigated for a typical summer day in Vancouver, BC. The solar radiation, wind speed, and outdoor air temperature are given in Figure 7-9. The typical sunny day is characterized by Solar radiation of 800 $W/m^2$, an average outdoor air temperature of 24.2℃, and Wind speeds of up to 1.27 *m/s*.

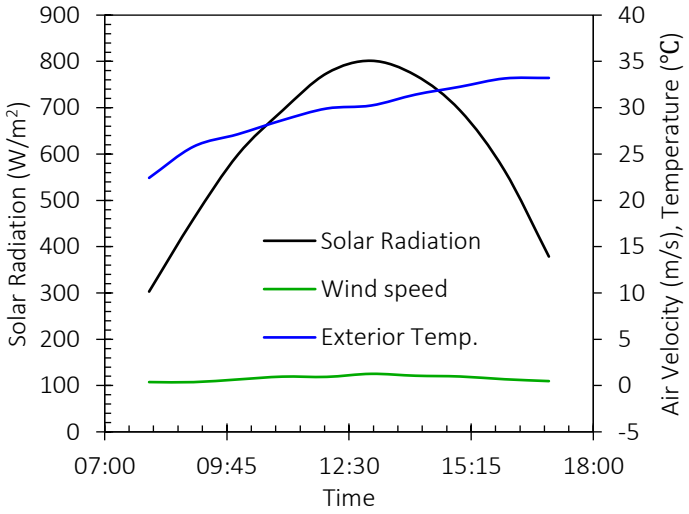


Figure 7-9 - Outdoor conditions for a typical summer day in Vancouver, BC

Figure 7-10a compares the cladding temperature for the typical rainscreen wall assembly and the BIPV/T façade. The boundary conditions are consistent with Section 2.2.1.2. The cladding temperature fluctuates between 13.7℃ – 55.2℃ for the typical rainscreen wall

assembly and 11.4℃ - 38.6℃ for the BIPV/T façade. The peak cladding temperature is reduced by 16.6℃ for the BIPV/T façade. The reduction in the peak temperature is attributed to the thermal regulation of the PV cell temperature because of the refrigerant flow behind the BIPV cladding (i.e., PV cells). Recall that the refrigerant fluid evaporates at a temperature close to the outdoor air. This high temperature evaporation reduces the compressor electrical input. Consequently, the coefficient of performance may be improved. This suggests that the cladding temperature should be similar to the outdoor temperature, especially for a BIPV/T façade with an optimized flow rate to ensure the refrigerant fluid is within the two-phase region for a significant portion of the façade area. However, as seen in Figure 7-10a, the cladding temperature peaks at a temperature higher than the outdoor temperature due to the solar availability and the contact resistance between the PV cells and the collector. Temperature differences of up to 28.1℃ was experienced as seen in Figure 7-10a. The airflow behind the BIPV/T cladding also contributes to the reduced cladding temperature since the air is assumed to be introduced into the air cavity at outdoor air temperature. Further, the electrical conversion of the BIPV/T façade contributes to the net heat balance on the façade therefore reducing the temperature of the surface of the cladding.

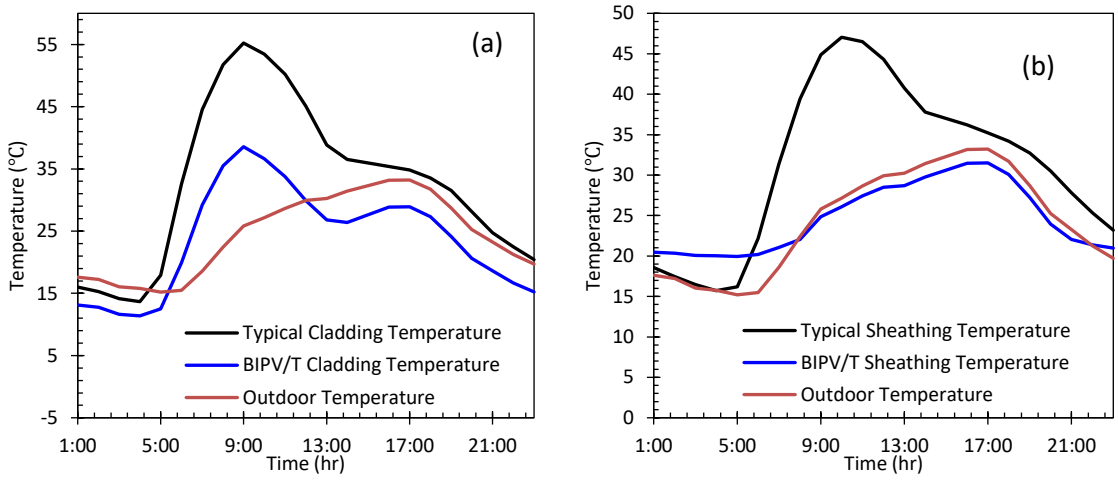

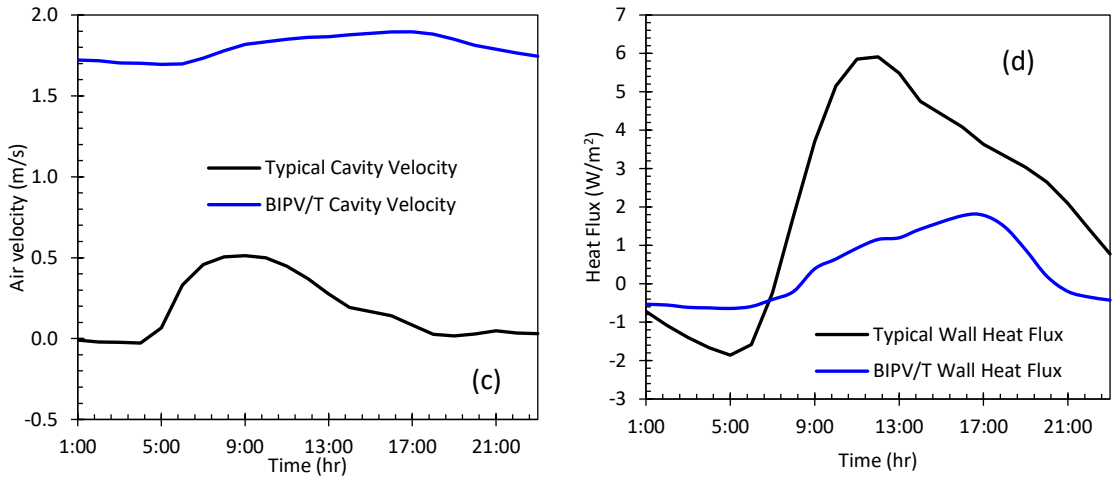


Figure 7-10 – Comparison of the (a) cladding surface temperature, (b) sheathing temperature, (c) mid-cavity air velocity, and (d) wall heat flux for the BIPV/T façade and a typical rainscreen wall assembly

Figure 7-10b and Figure 7-10c compare the sheathing temperature and air velocity for the typical rainscreen assembly and the BIPV/T wall assembly. The sheathing temperature is influenced mainly by the long wave radiation exchange with the cladding and the convective heat gain or heat loss due to the airflow in the cavity. Although the cladding temperature is relatively higher than the sheathing temperature during the morning hours of the day (consistent with an east facing façade), the sheathing temperature follows closely the outdoor air temperature. This insinuates that the sheathing temperature is mostly influenced by the airflow for the BIPV/T façade wall assembly. Figure 7-10c compares the cavity airflow the BIPV/T wall assembly and the typical rainscreen wall assembly. The induced air velocity in the rainscreen cavity fluctuates between -0.028 *m/s* and 0.512 *m/s* for the typical rainscreen wall assembly while the forced airflow in the BIPV/T wall assembly fluctuates between 1.69 *m/s* and 1.90 *m/s*. This corresponds to a constant Reynolds number of 5,000 for the typical day in study. The maximum sheathing temperature is 47.0°C and 31.5°C for the typical rainscreen wall assembly and BIPV/T wall assembly respectively. The peak sheathing temperature occurs at 10:00 am and 5:00 pm for the typical rainscreen wall assembly and BIPV/T wall assembly respectively. Notice that between 1am and 6am, the sheathing temperature for the BIPV/T wall assembly is higher than the typical rainscreen wall assembly. This is because of the implemented

control strategy that ensures that the air at the inlet of the cavity is always higher or equal to the indoor air temperature.

The consequence of the reduced sheathing temperature is a reduction in the heat flow for the BIPV wall assembly (See Figure 7-10d). The peak heat flux for the typical rainscreen and BIPV/T wall assembly are 5.91 $W/m^2$ and 1.79 $W/m^2$ respectively. This is a 69.7% reduction in the peak wall heat gain. For the whole day in study, the heat gain is calculated to be 53.9 $W/m^2$ and 11.9 $W/m^2$ for the rainscreen wall assembly and the BIPV/T façade assembly respectively. The heat gain is reduced by 77.9% for the BIPV/T wall assembly.

#### 7.3.1.3.2 Summary

The reduction of heat gain with the BIPV/T wall assembly compared to the rainscreen wall assembly was demonstrated for the typical summer day considered in the study. it is also evident in Figure 7-10b that the sheathing temperature is similar to the outdoor air temperature for outdoor conditions higher than 20℃. For outdoor conditions lower than 20℃, the sheathing temperature is constant at 20℃ when the BIPV/T façade is in operation. Hence, the heat flux difference with respect to the reference rainscreen wall is given in Equation 7-22.

$$\boldsymbol{dQ_{wall} = abs\left(Q_{ref,rainscreen} - Q_{BIPV/T}\right)} \qquad \text{Equation 7-22}$$

where, $Q_{ref,rainscreen}$ and $Q_{BIPV/T}$ are the heat fluxes for the reference rainscreen wall assembly and the BIPV/T wall assembly respectively. The wall heat fluxes are derived using the 1D heat conduction equation given in Equation 7-23

$$\boldsymbol{Q = \frac{T_{int} - T_s}{R_{th}}} \qquad \text{Equation 7-23}$$

where, $T_{int}$ is the indoor air temperature and $T_s$ is the wall surface temperature (i.e., cladding surface for the rainscreen wall assembly assumed as the sheathing temperature and the actual sheathing surface temperature for the BIPV/T wall assembly). the thermal resistance of the wall assembly is given in Equation 7-24

$$R_{th} = {}^{1}/_{h_{int}} + \sum {}^{t_i}/_{k_i} \qquad \text{Equation 7-24}$$

where, $h_{int}$ is the interior heat transfer coefficient, $t_i$ is the thermal conductivity of the inner wall assembly layers and $k_i$ is the thermal conductivity of the wall assembly layers. Knowing the heat flux difference, the combined heat gain is given in Equation 7-25.

$$Q_{combined} = Q_{total} + dQ_{wall} - W_{in,comp} - \left(\frac{\Delta P_{air}\dot{m}_{air}}{\rho_{air}} + \frac{\Delta P_{ref}\dot{m}_{ref}}{\rho_{ref}}\right)/0.18 \qquad \text{Equation 7-25}$$

### 7.3.2 Discussion of Results

The thermo-electric quantities derived for the typical summer day (See Section 7.3.1.3.1) is investigated by comparing with the typical PV/T-evaporator concept. The evaporator heat gain and electrical output and overall COP are the parameters of interest. Figure 7-11a and Figure 7-11b compare the electrical output and the electrical efficiency of the BIPV/T heat pump and the PV/T enhanced heat pump. In both cases, the electrical output is maximized at 8:00 am while the electrical efficiency is maximized at 6:00 am. The highest electrical output coincides with the peak solar radiation as aspect. However, the electrical efficiency is strong function of the available solar radiation and the PV cells temperature. The highest electrical efficiency is 12.8% and it coincides with the lowest outdoor air temperature (Figure 7-10). Since the wall orientation being considered is south-east, the electrical output and efficiency diminish after 12:00 pm. That said, the additional airflow showed negligible impact on the electrical efficiency. This is attributed to the high outdoor air for the typical summer day being simulated relative to the reference outdoor air temperature. This significantly reduces the cooling potential of the airflow in the channel. The modified outdoor airflow scheme was assumed for the simulation. The modified Trombe wall airflow scheme may have been a better approach since the indoor air is mostly lower than the reference temperature for which the electrical efficiency is specified (i.e., 25°C).

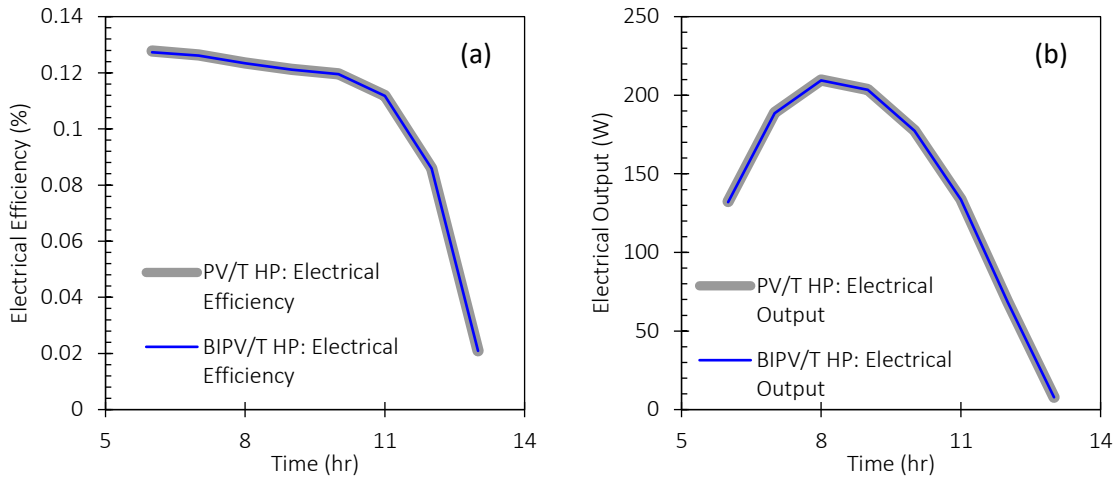


Figure 7-11 - comparison of the (a) electrical efficiency and (b) electrical output for the PV/T and BIPV/T heat pump system

Figure 7-12a and Figure 7-12b compare the heat gain and thermal efficiency for the PV/T and BIPV/T façade driven heat pump respectively. Figure 7-12a shows that the airflow enhances the heat gain of the evaporator. The heat gain is enhanced by up to 61.7% and it occurs at 7:00 am. For the typical sunny day considered, the heat gain is increased by 28.4% on average. The higher heat gain for the BIPV/T façade coupled heat pump translates to a higher thermal efficiency as seen in Figure 7-12b. The maximum thermal efficiency for the PV/T and BIPV/T heat pump is 56.4% and 94.4% respectively. This is a 67.3% increase of the thermal efficiency. For the typical summer day, the thermal efficiency the average daily thermal efficiency is 49.5% and 70.4% for the PV/T and BIPV/T coupled heat pump evaporator.

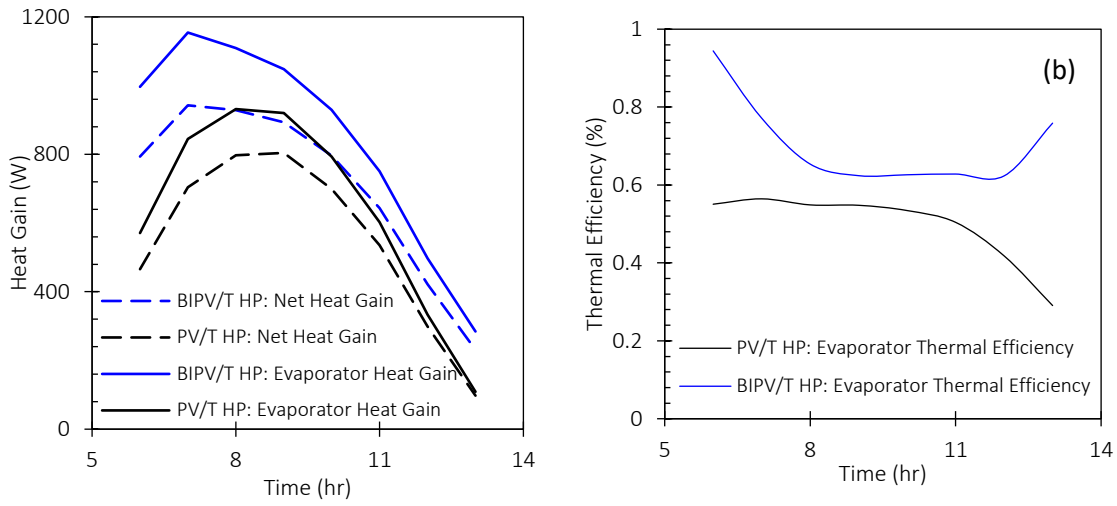


Figure 7-12 - Comparison of the evaporator (a) heat gain and (b) thermal efficiency for the PV/T and BIPV/T heat pump system

Figure 7-12a also shows the net heat gain for the BIPV/T façade system. The net heat gain is derived by considering the BIPV/T façade driven heat pump system (See section 4.1.3.2). As stated earlier, for a BIPV/T façade coupled with heat pump for water heating, the net heat gain in Figure 7-12b is the thermal energy delivered to the water storage tank barring pipe losses and other operational losses that are not accounted for in this study. The net heat gain is calculated for the representative days determined in Section 7.2. Figure 7-13 shows the net heat gain and the electrical efficiency as a function of the available solar radiation and outdoor air temperature for all the data points generated by considering representative days for each month of the year.

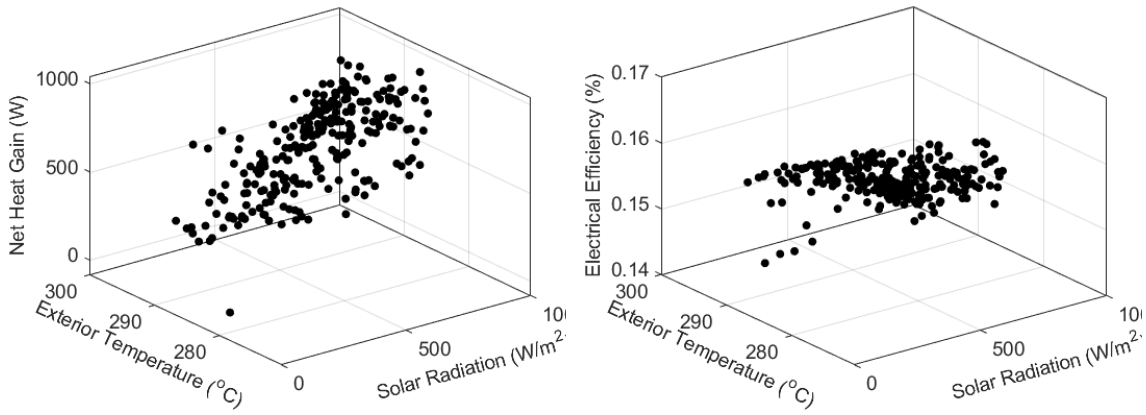

Figure 7-13 - 3D scatter plot of (a) Net heat gain and (b) electrical efficiency for the representative days

## 7.4 Development of correlation for net heat gain and electrical efficiency

The net heat gain (i.e., $Q_{net}$) and electrical efficiency are correlated with the outdoor conditions in this section. The aim is to derive a function that accurately predicts the net heat gain and electrical efficiency given the solar radiation, outdoor temperature, wind speed, and cloud cover. Thus, we are presented with curve fitting problem with two (2) dependent variables and four (4) independent variables. For simplicity, the two dependent variables (i.e., net heat gain and electrical efficiency) are fitted separately. For each dependent variable, a multi-variable polynomial regression analysis is performed (Ahmet Cecen, 2021). Let the dependent and independent variables be defined as follows:

$Y_1$ Net heat gain (W)

$Y_2$ Electrical efficiency (%)

$X_1$ Solar radiation (W/m$^2$)

$X_2$ Outdoor temperature (K)

$X_3$ Wind speed (m/s)

$X_4$ Cloud cover (-)

The polynomial expression for the net heat gain and electrical efficiency are given in Equation 7-26 and Equation 7-27 respectively.

$$\begin{aligned} \boldsymbol{Q_{net}} = &\boldsymbol{-325.4X_4 + 76.8X_3 - 5.23X_3X_4 + 111.3X_2 + 2.24X_2X_4} \\ &\boldsymbol{- 0.306X_2X_3 + 1.44X_1 - 0.230X_1X_4 - 0.046X_1X_3} \\ &\boldsymbol{- 0.00104X_1X_2 - 13642.4 - 0.000239{X_1}^2} \\ &\boldsymbol{- 0.22{X_2}^2 + 1.20{X_3}^2 - 153.4{X_4}^2} \end{aligned} \qquad \text{Equation 7-26}$$

$$\eta_{pv} = -0.00158X_4 + 0.00484X_3 - 0.0000599X_3X_4 + 0.00453X_2 - 0.0000246X_2X_4 - 0.0000171X_2X_3 - 0.000178X_1 + 0.00000677X_1X_4 + 0.0000012X_1X_3 + 0.000000582X_1X_2 - 0.343 - 0.00000000827{X_1}^2 - 0.00000965{X_2}^2 - 0.0000229{X_3}^2 + 0.0050554{X_4}^2$$ Equation 7-27

The goodness-of-fit for the derived polynomial expressions in Equation 7-26 and Equation 7-27 is checked by considering the R-squared value. The $R^2$ value for Equation 7-26 and Equation 7-27 is 0.8691 and 0.9497 respectively. The polynomial expression is validated using the Leave one out cross validation technique (Ahmet Cecen, 2021). Figure 7-14*a* and Figure 7-14*b* show the goodness of fit scatter plot for the net heat gain and electrical efficiency respectively.

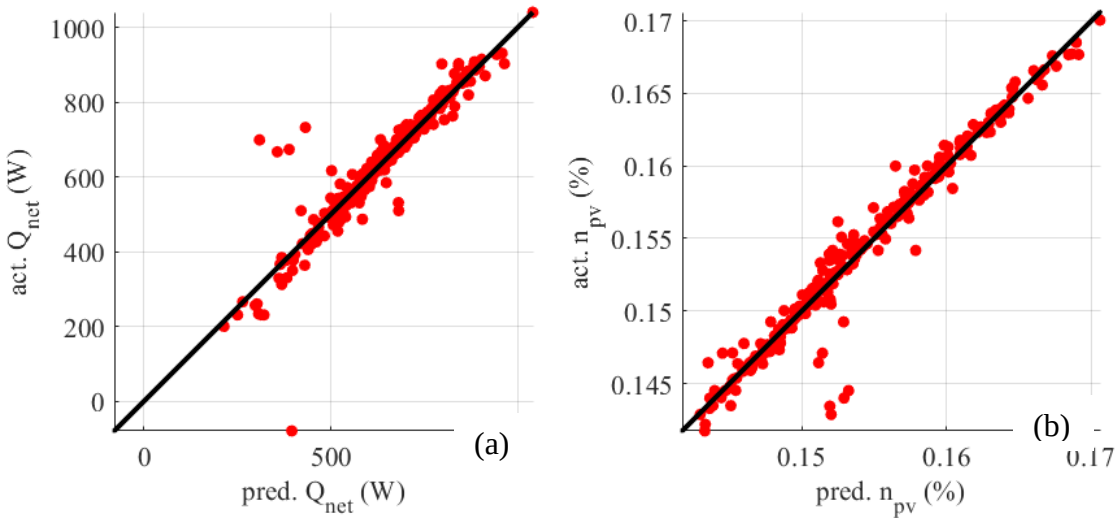


Figure 7-14 – Goodness of fit scatter plot showing the predictive accuracy of the multivariable polynomial expression for the (a) net heat gain and (b) electrical efficiency

To aid easier implementation of the polynomial expression in the building energy simulation platform, a subset selection is carried out with the aim to reduce the independent variables without sacrificing accuracy (Eksioglu et al., 2005). Given the number of dependent and independent variables, there are 24 possible combinations of variables that should be considered in the subset selection analysis. However, $X_1$ and $X_2$ are key variables in the solar thermal applications. Hence, the objective of the subset selection reduces to investigation of the influence of $X_3$ and $X_4$ on the predictive accuracy of the polynomial expressions in Equation 7-26 and Equation 7-27. This reduces the possible combinations of variables to eight (8) as seen in Table 7-2. Table 7-2 summarizes the $R^2$ values for the possible combinations of the independent variables in Equation 7-26 and Equation 7-27.

Table 7-2 – Summary of subset selection for a limited combination of outdoor parameters

| Regressors in model | $R^2$-value | Regressors in model | $R^2$-value |
|---|---|---|---|
| $Y_1 = f(X_1, X_2, X_3, X_4)$ | 0.8691 | $Y_2 = f(X_1, X_2, X_3, X_4)$ | 0.9497 |
| $Y_1 = f(X_1, X_2, X_3)$ | 0.8571 | $Y_2 = f(X_1, X_2, X_3)$ | 0.9452 |
| $Y_1 = f(X_1, X_2, X_4)$ | 0.7197 | $Y_2 = f(X_1, X_2, X_4)$ | 0.9209 |
| $Y_1 = f(X_1, X_2)$ | 0.7142 | $Y_2 = f(X_1, X_2)$ | 0.9172 |

As seen in Table 7-2, the electrical efficiency can be accurately predicted by considering just the solar radiation and outdoor temperature as independent variables. This simplifies Equation 7-27 to Equation 7-29. Also, the net heat gain can be accurately predicted by considering the solar radiation, outdoor temperature, and the wind speed. The simplified polynomial expressions for net heat gain is given in Equation 7-28. Similarly, Equation 7-28 and Equation 7-29 are validated using Leave one out cross validation technique (Ahmet Cecen, 2021).

$$\begin{aligned} \boldsymbol{Q_{net}} = \mathbf{103.4}\boldsymbol{X_3} + \mathbf{171.3}\boldsymbol{X_2} - \mathbf{0.385}\boldsymbol{X_2X_3} + \mathbf{0.0830}\boldsymbol{X_1} \\ - \mathbf{0.0482}\boldsymbol{X_1X_3} + \mathbf{0.00337}\boldsymbol{X_1X_2} - \mathbf{21813.6} \\ - \mathbf{0.000243}\boldsymbol{X_1}^{\mathbf{2}} - \mathbf{0.329}\boldsymbol{X_2}^{\mathbf{2}} + \mathbf{0.858}\boldsymbol{X_3}^{\mathbf{2}} \end{aligned} \qquad \text{Equation 7-28}$$

$$\begin{aligned} \boldsymbol{\eta_{pv}} = \mathbf{0.00291}\boldsymbol{X_2} - \mathbf{0.000105}\boldsymbol{X_1} + \mathbf{0.000000355}\boldsymbol{X_1X_2} - \mathbf{0.123} \\ - \mathbf{0.0000000923}\boldsymbol{X_1}^{\mathbf{2}} - \mathbf{0.0000067}\boldsymbol{X_2}^{\mathbf{2}} \end{aligned} \qquad \text{Equation 7-29}$$

The goodness of fit scatter plot for the net heat gain and the electrical efficiency is shown in Figure 7-15a and Figure 7-15b.

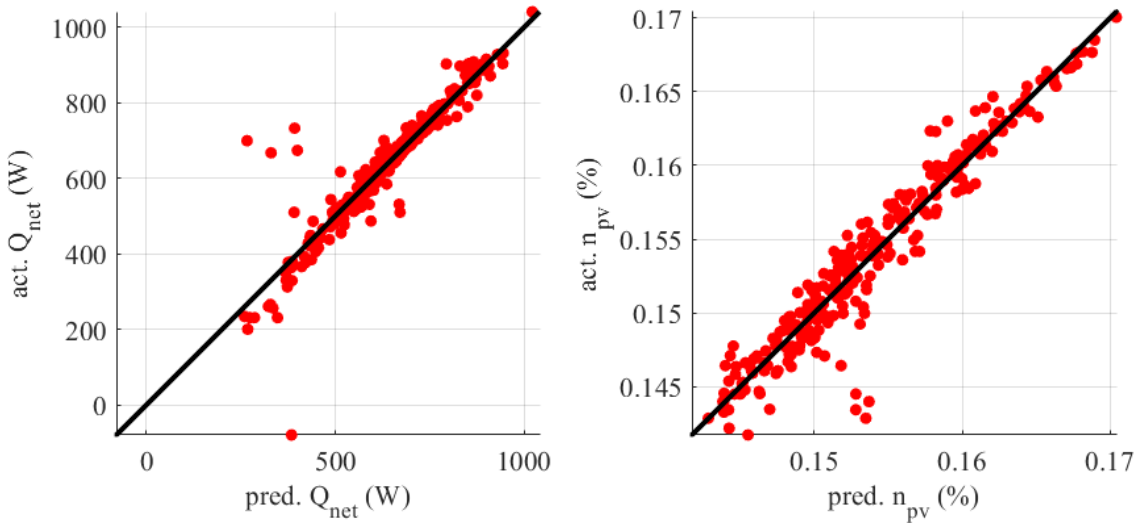


Figure 7-15 - Goodness of fit scatter plot showing the predictive accuracy of the simplified multivariable polynomial expressions for the (a) net heat gain and (b) electrical efficiency

The polynomial expressions were derived for a mild climate like Vancouver, BC. Hence, the accuracy of the model is assessed for a more extreme climate like Kamloops, BC. Figure 7-16*a* and Figure 7-16*b* compare the net heat gain and electrical efficiency predicted by the polynomial expression in Equation 7-28 and Equation 7-29 against the detailed CFD simulation for the hottest day in Kamloops derived from the EnergyPlus weather data (i.e., July 30$^{th}$).

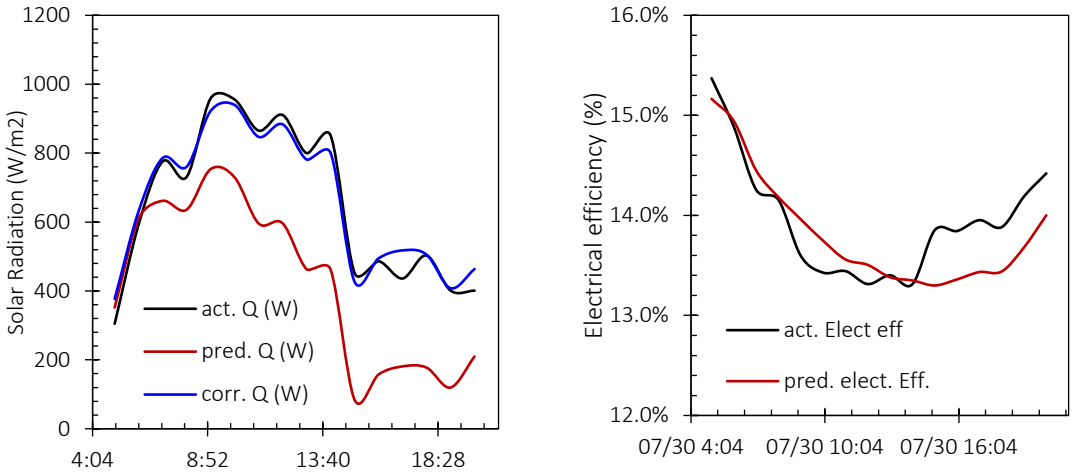


Figure 7-16 – Comparison of the predictive accuracy of the simplified multivariable polynomial expressions for the (a) net heat gain and (b) electrical efficiency against CFD for the hottest day in Kamloops, BC

Figure 7-16 shows that the electrical efficiency predicted by Equation 7-29 can be extrapolated for other climates with warmer outdoor conditions. The *RMSE* and *NRMSE* for predicting the electrical efficiency is 0.00337 and 2.41% respectively. However, the error in predicting the heat gain for warmer climates is significant. For the day in study, the *RMSE* and the *NRMSE* for predicting the net heat gain are 301.7 *W* and 49.3% respectively. The accuracy of Equation 7-28 is enhanced by adding a correction term as highlighted in Equation 7-30.

$$\begin{aligned} \boldsymbol{Q_{net}} = \; & \boldsymbol{103.4X_3 + 171.3X_2 - 0.385X_2X_3 + 0.083X_1} \\ & \boldsymbol{- 0.0482X_1X_3 + 0.00337X_1X_2 - 21813.6} \\ & \boldsymbol{- 0.000243{X_1}^2 - 0.329{X_2}^2 + 0.858{X_3}^2} \\ & \boldsymbol{+ (24.5(X_2 - 294.15) + 22.8)} \end{aligned}$$

Equation 7-30

The correction term is derived by correlating the errors in Figure 7-16 with the temperature difference for the hottest day and the threshold temperature (i.e., 21°C). The temperature correction is only applied when the outdoor air temperature is higher than 21°C. The correction term improves the accuracy as seen in Figure 7-16a. The *RMSE* and *NRMSE* are 69.7 W and 10.7% respectively. Further validation of the effectiveness of the temperature correction to enhance the predictive accuracy of the net heat gain is seen when other

warmer days is seen in Figure 7-17a and Figure 7-17b for May 12th and Aug 9th respectively.

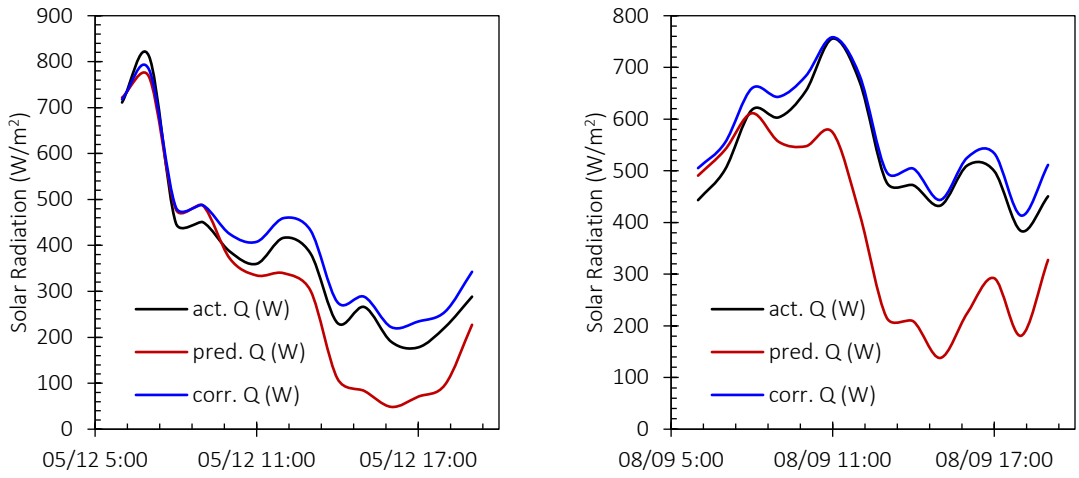


Figure 7-17 - Further validation of the temperature correction to enhance the prediction accuracy of multivariable polynomial expressions for the (a) net heat gain and (b) electrical efficiency on May 12th and August 9th in Kamloops, BC

## 7.5 BES Implementation of BIPV/T façade coupled with heat pump for DHW

Upon deriving the correlations for the net heat gain and the electrical efficiency, the correlations are programmed into the Building Energy Simulation (BES) platform. This is done to quantify the energy savings associated with the BIPV/T façade coupled with heat pump for domestic water heating (DHW). The energy savings will be quantified by considering different façade orientations and different climate. EnergyPlus is the preferred BES software because of its flexibility of simulating customized systems (Nghana & Tariku, 2016). The energy simulation is first benchmarked before implementing the BIPV/T façade coupled heat pump for DHW in the energy simulation platform.

### 7.5.1 Benchmarking of Numerical Simulation setup in EnergyPlus

The EnergyPlus simulation is benchmarked by comparing with ANSI/ASHRAE Standard 140 Case 600 low mass building (Figure 7-18).

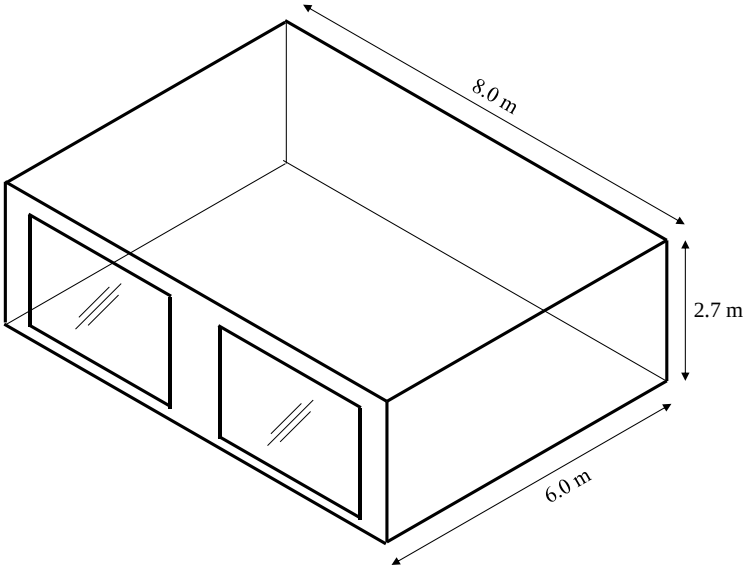


Figure 7-18 - Test building (ANSI/ASHRAE Standard 140 Case 600)

The test building is 8 *m* wide, 6 *m* long and 2.7 *m* high with windows oriented in the south direction. The windows are air filled double glazed insulated glazing units (IGUs). The wall, roof and floor construction is given in Table 7-3. The total internal load is 200 W (60% radiative and 40% convective). The building infiltration is 0.5 ACH. The soil temperature is 10°C continuous. The indoor air temperature is maintained between 20°C and 27°C by a 100% convective air system. The mechanical system is 100% efficient with no loses. The mechanical system is simulated in EnergyPlus using the Ideal Loads Air System. The building is simulated under Denver, Colorado weather conditions.

Table 7-3 – Summary of the Building envelope attributes

| Material | Thermal Conductivity (*W/m-K*) | Thickness (*m*) | Density (*kg/m³*) | Specific Heat (*J/kg-K*) |
|---|---|---|---|---|
| Wall Construction | | | | |
| Plasterboard | 0.160 | 0.012 | 950 | 840 |
| Fiberglass Quilt | 0.040 | 0.066 | 12 | 840 |
| Wood Siding | 0.140 | 0.009 | 530 | 900 |
| Roof Construction | | | | |
| Plasterboard | 0.160 | 0.010 | 950 | 840 |
| Fiberglass Quilt | 0.040 | 0.1118 | 12 | 840 |
| Roof Deck | 0.140 | 0.019 | 530 | 900 |
| Floor Construction | | | | |
| Timber Flooring | 0.140 | 0.025 | 650 | 1200 |
| Insulation | 0.04 | 1.003 | - | - |

The results from benchmarking the EnergyPlus model is summarized in Table 7-4. The heating and cooling energy consumption is compared with published results (BESTEST, 2004). As seen in Table 7-4, the heating and cooling energy derived from the EnergyPlus simulation is within the range of the Published results. The maximum deviation from the BESTEST average published data is 13% for the prediction of the Annual heating. In general, the derived Energyplus cooling energy is more consistent with published data.

Table 7-4 - Summary of the benchmarking results

| Description | BESTEST* Minimum | BESTEST* Maximum | BESTEST* Average | Present Simulation | % Diff |
|---|---|---|---|---|---|
| Annual Heating (*MWh*) | 4.296 | 5.709 | 5.046 | 4.383 | -13.1% |
| Peak Heating (*kW*) | 3.437 | 4.354 | 3.952 | 3.736 | -5.5% |
| Annual Cooling (*MWh*) | 6.137 | 8.448 | 7.053 | 7.460 | 5.8% |
| Peak Cooling (*kW*) | 5.965 | 7.188 | 6.535 | 6.690 | 2.4% |

### 7.5.2 Electric Water heater

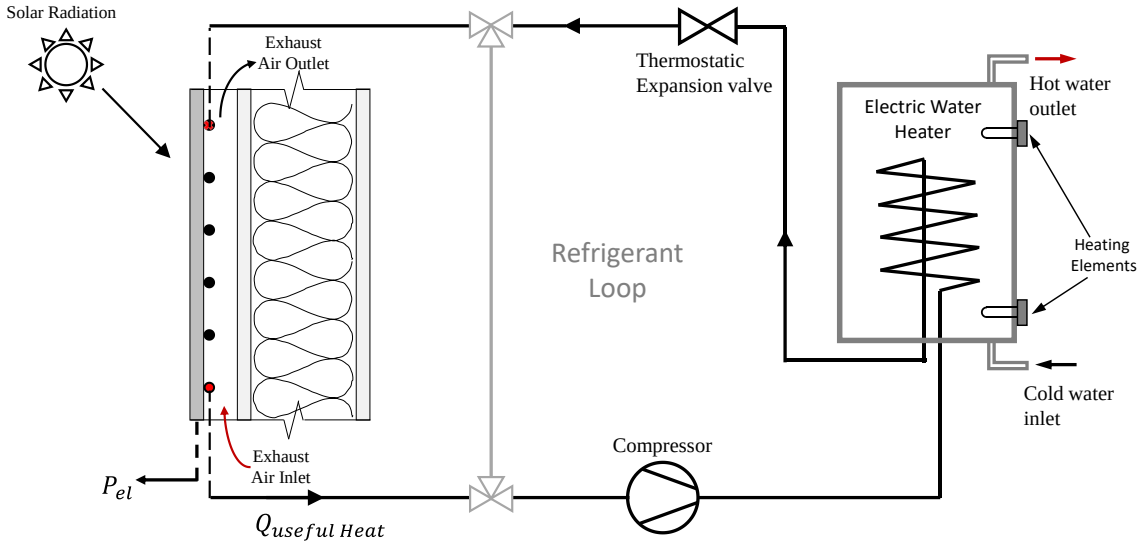


Figure 7-19 -Schematic of the electric water heater with auxiliary heating provided by the BIPV/T façade evaporator

Figure 7-19 illustrates the electric water heater. The electric heater is rated for a maximum heating capacity of 5000 W. The tank volume is 0.3785 m3 and the heater thermal efficiency is 95%. The water storage tank is located within the validated zone. Heat loss or gain of the water tank is accounted for by specifying a loss coefficient of 2.0 *W/K*. The additional heating afforded by the BIPV/T façade coupled with Heat pump is illustrated in Figure 7-19. The additional heating provided by the BIPV/T assisted heat pump system should offset some of the heating required by the electric water heater which will reflect in annual energy savings. The BIPV/T façade concept for water heating is implemented in EnergyPlus by writing a simple EnergyPlus Runtime Language (Erl) program to

dynamically override the zone temperature where the water tank is located such that the equivalent conduction heat flux between the water in the tank and the ambient is equivalent to the overall thermal energy extracted from the BIPV/T façade. The overall thermal energy is calculated for each time step according to Equation 7-31.

$$\boldsymbol{Q_{overall} = Q_{net} + dQ_{wall} + {\tau_{eva}\eta_{pv}G_{surf}A_{mod.}}/{0.38}} \qquad \text{Equation 7-31}$$

where, $Q_{net}$ and $\eta_{pv}$ are derived from Equation 7-29 and Equation 7-30 respectively, $A_{mod.}$ is the module area shown in Figure 7-5, $G_{surf}$ is the solar radiation on the surface and $\tau_{eva}$ is calculated according to Equation 5-24 for each surface orientation. Given the overall thermal energy in Equation 7-31 and the loss coefficient of the water tank, the equivalent zone temperature can be calculated by rearranging Equation 7-32.

$$\boldsymbol{Q_{overall} = k_{loss}(T_{zone,eq} - T_{tank\,water})} \qquad \text{Equation 7-32}$$

In other words, when the BIPV/T façade coupled with heat pump is in operation, the water heater tank is assumed to be in a pseudo zone with temperature equivalent to $T_{zone,eq}$. Alternatively, the water tank is in the actual zone boundary shown in Figure 7-19.

### 7.5.3 Verification of the Erl Implementation

As mentioned earlier the BIPV/T façade driven heat pump is implemented via the Energy Management System (EMS) in EnergyPlus. The Erl program implements mainly Equation 7-29, Equation 7-30, Equation 7-31, and Equation 7-32. The Erl programming references key "sensor" variables to get time varying data regarding the surface incident solar radiation, solar incident angle, wind speed, outdoor temperature, zone temperature, outside surface temperature, and tank temperature. The "actuator" variable is also defined to control the water zone temperature according to Equation 7-32. An important aspect of the EMS programming is specifying the EMS calling point for the Erl override. The EMS calling point is specified just before the zone load predictions for each time step of in EnergyPlus terms, "BeginTimestepBeforePredictor."

To ensure proper predictor capacity of the EMS program, the results are verified by comparing the EnergyPlus simulated output with the expected output. Figure 7-20

compares the EMS program output against the expected output. The comparison of the predicted and expected output was done for the Vancouver, BC climate.

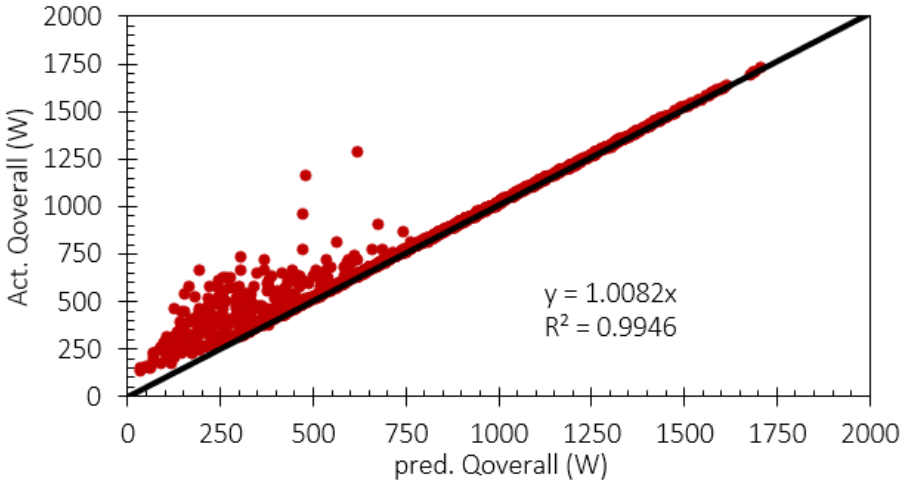


Figure 7-20 - Comparison of the predicted and expected overall heat gain

As seen in Figure 7-20, the predicted overall heat gain is consistent with the expected heat gain with some discrepancies. The overall heat gain is underpredicted in some instances. The discrepancy is attributed to the time step disparity the EnergyPlus derived overall heat gain and the expected value. The expected overall heat gain is derived by assuming the time step begins on the hour which may not be the case in the EnergyPlus Simulation. The EnergyPlus derived values are interpolated values. Upon inspection of the data, the error mostly occur at the initial timestep when the BIPV/T façade is assumed to be in operation. This therefore means, expected heat gain is the maximum possible value attainable; hence, while errors are expected, the values predicted by the Erl program should be less than expected which is reflected in Figure 7-20. That said, the $R^2$ value for the predicted overall heat gain is 0.9946. The NRMSE is 8.71% for the whole year simulation presented in Figure 7-20.

## 7.6 Parametric Analysis Results and Discussion

With the BIPV/T façade implemented in the BES platform, the impact of the integration of the BIPV/T façade is investigated and the energy savings is quantified. Also, the energy

savings associated with BIPV/T façade driven heat pump water heater is quantified for different climates across Canada.

### 7.6.1 Impact of Wall Orientation

Three wall orientations (i.e., East, West, and South) and the roof were investigated. Vancouver, BC climate is considered in the analysis. Vancouver has a solar production potential of 1007 *kWh/yr* (Urban, 2021). This is slightly lower than the average national solar production potential of 1133 *kWh/kW/yr* (Urban, 2021). Vancouver was chosen for consistency. The impact of wall orientation and roof was investigated by considering the daily hot water usage shown in Figure 7-21. As seen in Figure 7-21, the water consumption increases in the morning up to about 10 *L/hr* at 8:00 am, drops to a low of about 2 *L/hr* at 1pm and increases to about 9 *L/hr* at 6:00 pm. As expected, there is no water consumption from midnight to 6:00 am. This is typical of a residential building (Fuentes et al., 2018).

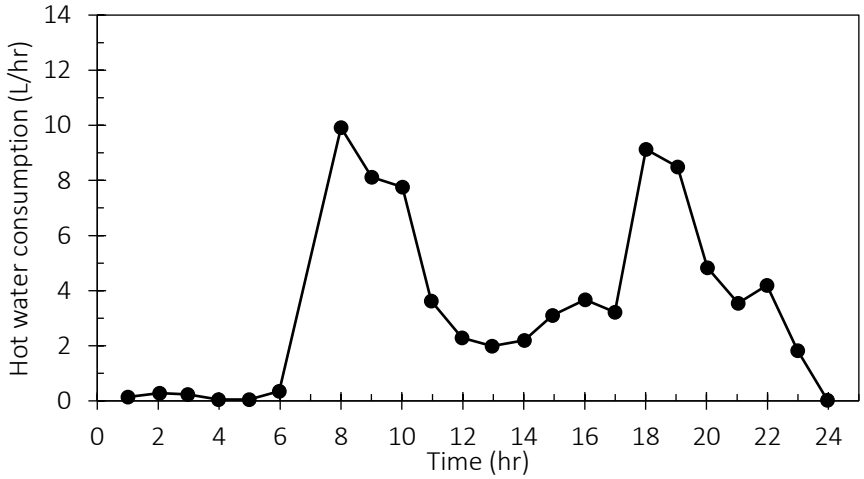


Figure 7-21 - Typical daily water consumption profile

Figure 7-22 shows the impact of integrating the BIPV/T façade evaporator on the water heating energy consumption for the different wall orientations considered and the roof. The Baseline model excludes the additional heating provided by the BIPV/T façade evaporator. The annual water heating energy is 33.3 *MWh*, 19.9 *MWh*, 22.6 *MWh*, 25.5 *MWh*, and 24.6 *MWh* for the Base model, and BIPV/T façade evaporator mounted on the roof, south wall, west wall, and east wall respectively. This shows that the auxiliary heating provided by the BIPV/T façade driven heat pump is effective in reducing the annual hot water heating

energy by 40.1%, 32.0%, 24.1%, and 26.0% for the BIPV/T façade evaporator mounted on the roof, south wall, west wall, and east wall respectively. The BIPV/T façade evaporator was sized by considering the average daily electricity usage for residential dwellings (Luyties & Luyties, n.d.). This was equivalent to having fifteen (15) BIPV/T façade evaporator modules (i.e., 36 $m^2$ of facade coverage).

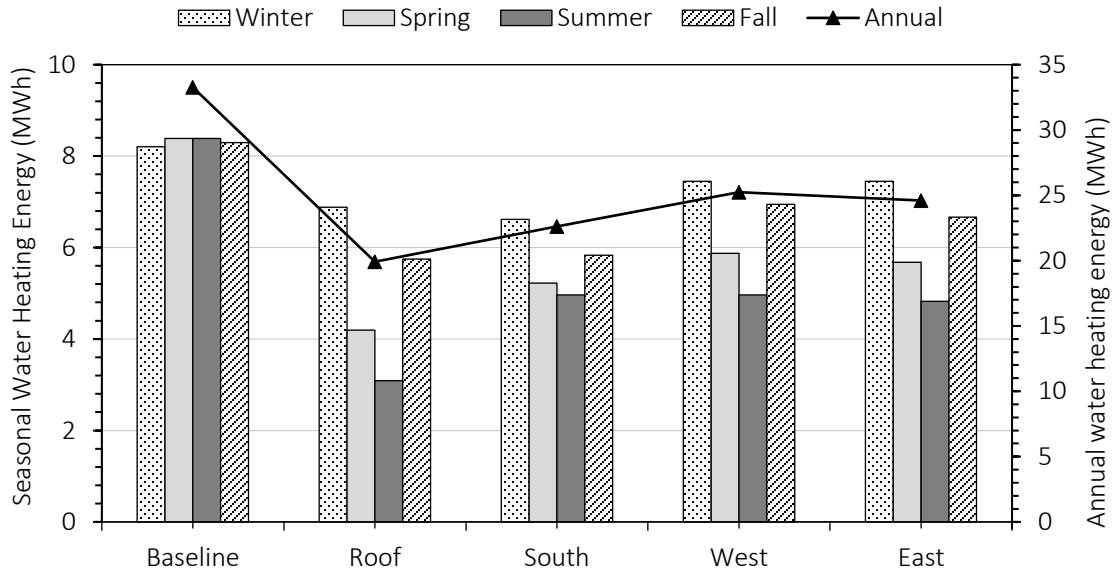


Figure 7-22 - Effect of varying the location of the BIPV/T facade evaporator on the water heating energy consumption

The energy savings for the Roof is the highest; however, the energy savings for the South oriented BIPV/T façade is comparable. The similarity in energy savings is attributed to the airflow behind the BIPV/T cladding. The East oriented BIPV/T façade shows slightly higher savings than the West oriented BIPV/T façade since the solar availability for the east facing wall coincides with low relatively lower outdoor air temperature. As such, the electrical output may be higher and hence a higher overall thermal energy. Energy savings for the roof integrated BIPV/T façade is 14.2% higher than the West oriented BIPV/T façade and 9.92% higher than the East oriented BIPV/T façade. This means that in an urban settlement where the roof to wall area ratio is relatively low, the BIPV/T façade can be integrated on the wall area without significant loss of overall thermal performance.

Further, the seasonal water heating energy consumption is shown in Figure 7-22. As seen, for all the orientations considered, the water heating energy is lowest during summer and highest during winter. Using the roof integrated BIPV/T façade evaporator as case study, the seasonal water heating energy consumption for winter, spring, summer, and fall are 6.89 *MWh*, 4.19 *MWh*, 3.09 *MWh*, and 5.75 *MWh* respectively. The relatively higher water heating energy savings is attributed to the higher solar potential during summer. In fact, the BIPV/T façade driven heat pump is in service for 1121 hours during summer and only 254 hours during winter. Also, during winter, the south wall showed the most energy savings for water heating of 19.3%. The winter water heating energy savings for the roof, west and east mounted BIPV/T façade are 16.1%, 9.19% and 9.19% respectively. Also, the water heating energy savings during summer was calculated to be 63.2%, 40.8%, 40.8%, and 42.5% for the roof, south, west, and east facing BIPV/T façade evaporator. The water heating energy savings during fall was calculated to be 30.7%, 29.7%, 16.3%, and 19.7% for the roof, south, west, and east facing BIPV/T façade evaporator. Finally, the water heating energy savings during spring was calculated to be 50.0%, 37.7%, 29.9%, and 32.3% for the roof, south, west, and east facing BIPV/T façade evaporator.

### 7.6.2 Impact of Climate

In this section, the potential of BIPV/T façade driven heat pump is investigated for additional cities in Canada. The additional cities investigated are Toronto, Montreal, Calgary, Ottawa, Regina, and Winnipeg. It was shown in the previous section that the BIPV/T evaporator façade mounted on the south oriented wall showed the highest potential for water heating energy savings; hence, only the south wall integrated BIPV/T is investigated in this section.

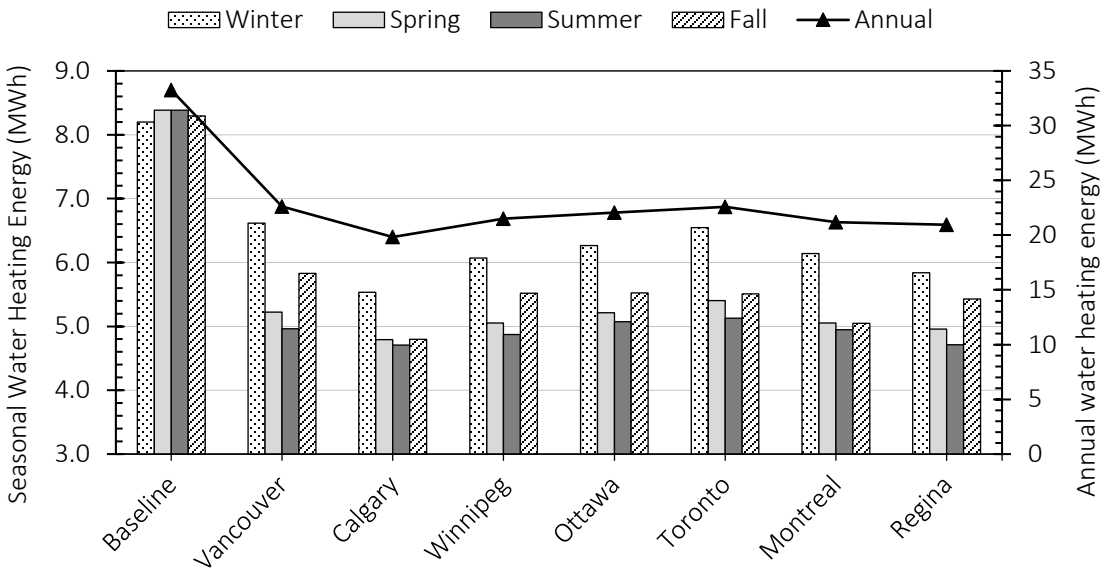


Figure 7-23 -Comparison of the Annual and Seasonal water heating energy consumption for the different cities in Canada

Figure 7-23 compares the annual and seasonal water heating energy for the cities being earlier listed and Figure 7-24 compares the annual and seasonal water heater energy savings for the cities considered in the study. The annual water heating energy consumption for Vancouver, Calgary, Winnipeg, Ottawa, Toronto, Montreal, and Regina is 22.6 *MWh*, 19.8 *MWh*, 21.5 *MWh*, 22.1 *MWh*, 22.6 *MWh*, 21.2 *MWh*, and 20.9 *MWh* respectively. The annual water heating energy consumption is 33.3 *MWh* for the reference case (i.e., electric heater without auxiliary heating simulated under Vancouver climate). In all cities, the water heating energy consumption is reduced by implementing the BIPV/T façade concept. The reduction in annual water heating energy consumption is 32.0%, 40.4%, 35.3%, 33.7%, 32.1%, 36.3%, and 37.1% for Vancouver, Calgary, Winnipeg, Ottawa, Toronto, Montreal, and Regina respectively.

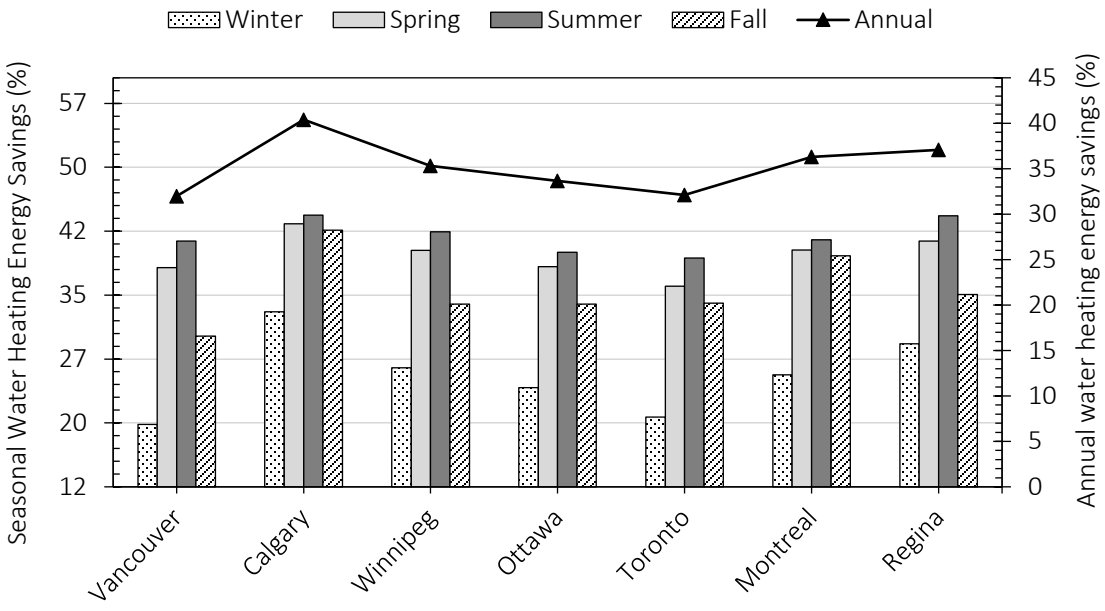


Figure 7-24 - Comparison of the Annual and Seasonal water heating energy savings for the different cities in Canada

Considering the seasonal water heating energy consumption in Figure 7-24, the maximum water heating energy savings during winter attributed to the auxiliary heating provided by the BIPV/T façade is 32.5% for the Calgary climate and the minimum water heating energy savings during winter is 19.3% for the Vancouver climate. The water heating energy savings during winter for Winnipeg, Ottawa, Toronto, Montreal, and Regina are 26.0%, 23.6%, 20.2%, 25.2%, and 28.8% respectively. The water heating energy consumption during winter varied by up to 13.2% between the cities considered (i.e., Calgary and Vancouver). The water heating energy savings during Spring is 37.7%, 42.9%, 39.7%, 37.8%, 35.5%, 39.8%, and 40.6% for Vancouver, Calgary, Winnipeg, Ottawa, Toronto, Montreal, and Regina respectively. The water heating energy savings during Spring are varied by up to 7.32% considering the BIPV/T energy performance in Calgary and Toronto. The water heating energy savings during Summer is 40.8%, 43.9%, 41.9%, 39.5%, 38.8%, 41.0%, and 43.8% for Vancouver, Calgary, Winnipeg, Ottawa, Toronto, Montreal, and Regina respectively. While, the highest water heating energy savings was seen in Calgary and Regina, the energy savings for all the climates is similar. The water heating energy savings during Fall is 29.7%, 42.1%, 33.4%, 33.4%, 33.6%, 39.1%, and 34.5% for

Vancouver, Calgary, Winnipeg, Ottawa, Toronto, Montreal, and Regina respectively. The maximum water heating energy savings during Fall occurred in Calgary while the minimum water heating energy savings during fall occurred in Vancouver. Overall, the annual water heating savings is maximized Calgary. Vancouver showed the lowest annual water heating energy savings.

## 7.7 Conclusion

An airflow enhanced BIPV/T façade concept coupled with heat pump technology was proposed and numerically investigated for the overall energy saving potential when utilized for DHW. The numerical simulation involved four distinct phases: weather data analysis, detailed CFD simulation, Regression analysis, and BES. In the weather data analysis, representative days for each month with varying levels of solar radiation are determined. The determined outdoor conditions were inputted as boundary conditions for the detailed CFD simulation to determine the heat gain and electrical efficiency. In the regression analysis, the heat gain and electrical efficiency are correlated with the outdoor temperature, solar radiation, wind speed and cloud cover. The derived multi-variable polynomial expression is then implemented in EnergyPlus via the Energy Management System to dynamically predict the heat added to the storage tank per hour of operation of the BIPV/T coupled heat pump system. Following, the energy impacts on the DHW energy usage are quantified for different wall orientations and climatic conditions across Canada by considering a typical residential DHW consumption profile.

The simulation methodology was implemented for the mild climate of Vancouver, BC. However, the multivariable polynomial expression was corrected to extend the predictive accuracy to all climates. The energy analysis showed that while the roof integrated BIPV/T façade concept showed the highest energy savings of all the orientations considered, the BIPV/T façade can be implemented on the walls (i.e., South facing walls) without significant loss in energy performance. This is especially important for high-rise residential buildings in an urban settlement where the roof to wall area is relatively small. The results cite the feasibility of the wall integrated BIPV/T façade. Further the performance of the BIPV/T façade coupled with heat pump was investigated for different cities including Vancouver, Calgary, Winnipeg, Ottawa, Toronto, Montreal, and Regina. The DHW

heating energy savings ranged from 40.4% in Calgary to 32.0% in Vancouver for a south oriented BIPV/T façade evaporator. Additional energy analysis showed that the BIPV/T façade significantly reduces the wall heat flux compared with a typical rainscreen assembly. In fact, the peak heat flux was reduced by 69.7%. This implied that the BIPV/T façade has the potential to reduce the overall building energy consumption in addition to the savings in DHW energy usage. While the potential of the BIPV/T coupled heat pump has been demonstrated herein, further experimental analysis is recommended to proof the BIPV/T façade integrated with heat pump concept.

## 7.8 References

Ahmet Cecen (2021). Multivariate Polynomial Regression (https://github.com/ahmetcecen/MultiPolyRegress-MatlabCentral), GitHub. Retrieved November 11, 2021.

Analytics, G. A. R. D. (2004). EnergyPlus Testing with ANSI/ASHRAE Standard 140-2001 (BESTEST).

Incropera, F. P., Lavine, A. S., Bergman, T. L., & DeWitt, D. P. (2007). Fundamentals of heat and mass transfer. Wiley.

ASHRAE. (2017). 2017 ASHRAE Handbook: Fundamentals. ASHRAE.

Bai, Y., Chow, T. T., Menezo, C., & Dupeyrat, P. (2012). Analysis of a hybrid PV/thermal solar-assisted heat pump system for sports center water heating application. International Journal of Photoenergy, 2012.

Chow, T. T., Fong, K. F., Pei, G., Ji, J., & He, M. (2010). Potential use of photovoltaic-integrated solar heat pump system in Hong Kong. Applied Thermal Engineering, 30(8-9), 1066-1072.

Eksioglu, B., Demirer, R., & Capar, I. (2005). Subset selection in multiple linear regression: a new mathematical programming approach. Computers & Industrial Engineering, 49(1), 155-167.

Ji, J., He, H., Chow, T., Pei, G., He, W., & Liu, K. (2009). Distributed dynamic modeling and experimental study of PV evaporator in a PV/T solar-assisted heat pump. International Journal of Heat and Mass Transfer, 52(5-6), 1365-1373.

Ji, J., Liu, K., Chow, T. T., Pei, G., He, W., & He, H. (2008). Performance analysis of a photovoltaic heat pump. Applied Energy, 85(8), 680-693.

Keliang, L., Jie, J., Tin-tai, C., Gang, P., Hanfeng, H., Aiguo, J., & Jichun, Y. (2009). Performance study of a photovoltaic solar assisted heat pump with variable-frequency compressor–a case study in Tibet. Renewable Energy, 34(12), 2680-2687.

Layek, A. (2010). Optimal thermo-hydraulic performance of solar air heater having chamfered rib-groove roughness on absorber plate. International Journal of Energy and Environment, 1(4), 683-696.

Manzolini, G., Colombo, L. P., Romare, S., & Fustinoni, D. (2016). Tiles as solar air heater to support a heat pump for residential air conditioning. Applied Thermal Engineering, 102, 1412-1421.

Müller-Steinhagen, H., & Heck, K. (1986). A simple friction pressure drop correlation for two-phase flow in pipes. Chemical Engineering and Processing: Process Intensification, 20(6), 297-308.

Nghana, B., Tariku, F., & Bitsuamlak, G. (2021). Assessing ventilation cavity design impact on the energy performance of rainscreen wall assemblies: A CFD study. *Building and Environment*, *196*, 107789.

Pei, G., Ji, J., Chow, T. T., He, H., Liu, K., & Yi, H. (2008). Performance of the photovoltaic solar-assisted heat pump system with and without glass cover in winter: a comparative analysis.

Siemens, P. (2018). Simcenter STAR-CCM+ User Guide V13. 04. Siemens PLM.

Urban, R. (2021, June 19). *Solar Energy Maps Canada 2021 (Every Province)*. energyhub.org. Retrieved October 28, 2021, from https://www.energyhub.org/solar-energy-maps-canada/#solar-energy-maps-canada.

Xu, G., Deng, S., Zhang, X., Yang, L., & Zhang, Y. (2009). Simulation of a photovoltaic/thermal heat pump system having a modified collector/evaporator. Solar Energy, 83(11), 1967-1976.

Zhao, X., Zhang, X., Riffat, S. B., & Su, Y. (2011). Theoretical study of the performance of a novel PV/e roof module for heat pump operation. Energy conversion and Management, 52(1), 603-614.

Luyties, W., & Luyties, M. (n.d.). What is the average size of a rooftop solar system? Owoe - solar power - what is the average size of a rooftop solar system? Retrieved December 22, 2021, from https://www.ourworldofenergy.com/vignettes.php?type=solar-power&id=15

# Chapter 8

# 8 Conclusions and further work

## 8.1 Conclusion

A new BIPV/T façade concept as part of a heat pump system for DHW was proposed and numerically investigated to understand the potential for energy improvement in a low-rise residential setting. The BIPV/T concept could be described as an airflow enhanced PV/T evaporator with finely controlled air flow rates and patterns to achieve higher thermodynamic efficiencies. Thus, there exist multiple fluid streams with different heat transfer and flow characteristics. In the airflow stream, the heat exchange with the adjacent collector surface may cause a positive or negative enthalpy change. Similarly, in the refrigerant tubes, the heat exchange between with the collector surface and the airflow stream causes the fluid to evaporate. This posed a multiphase heat transfer problem in the refrigerant tubes.

The airflow and refrigerant flow stream are decoupled and numerically investigated separately to understand the heat transfer and flow characteristics. In the air flow analysis, the refrigerant tubes are treated as roughness elements and their impact on the convective heat transfer coefficients are studied. In chapter 3, the turbulent natural convection heat transfer coefficient was investigated for a roughened air channel. The study investigated the effect of rib cross-sectional shape, rib height, rib spacing, channel inclination, and different asymmetric heating intensities on the natural convection heat transfer coefficient. It was seen that the roughness elements enhanced the convective heat transfer coefficient for all case with channel inclination less than 60 degrees from the vertical. Above 60 degrees, the rib elements were detrimental to the natural convection heat transfer. A new natural convective heat transfer coefficient correlation was derived considering the different geometrical and flow parameters investigated.

In chapter 4, the forced convection heat transfer coefficient was investigated for a roughened air channel. The study investigated the effect of rib cross-sectional shape, rib height, rib spacing, and channel flow rate on the forced convection heat transfer coefficient. The visualization of the velocity contours showed vortices formed in the immediate

upstream and downstream of the roughness elements. The near wall vortex flow structures were categorized into three distinct flow regimes from detailed analysis of the CFD derived wall shear stress. The three flow regimes were named accordingly: Skimming flow, wake interference flow, and isolated roughness flow. The naming convention was consistent with atmospheric boundary layer flow. Following, a parametric analysis is conducted to optimize the thermohydraulic performance of the solar air heater. The optimum rib geometry for the circular and triangular transverse rib was given in Chapter 4 respectively. A new forced convective heat transfer coefficient correlation was derived considering the different geometrical and flow parameters investigated.

In chapter 5 and 6, the multiphase flow in the refrigerant tube is validated with experimental data for the detailed CFD simulation and numerically verified. The air-side and refrigerant side were then coupled based on the assumption that the coupling was intrinsically handled by the governing equations. Then effect of rib height, rib spacing, and flow ratio of the refrigerant tube and air channel on the thermodynamic and electrical yield of the BIPV/T façade concept. The geometrical and flow parameters were investigated under peak solar conditions and off-peak solar conditions. The geometrical and flow parameters that optimized the thermal and electrical efficiency of the BIPV/T façade for the peak and off-peak solar conditions were presented.

Once the BIPV/T façade construct had been optimized, the BIPV/T-HP system was studied. In the system scale, the BIPV/T-HP energy performance is quantified for a scenario when the system is utilized for DHW. To do this, a four-step simulation procedure was proposed and implemented to verify the annual performance. This involved weather analysis to deduce representative days for different solar exposures for each month of the year. The representative days were inputted as boundary conditions to derive the thermal and hydraulic characteristics of the BIPV/T façade. At this stage the energy performance of the BIPV/T façade was compared with the typical rainscreen wall assembly that was presented in Chapter 2. The temperature in the interstitial layers of the wall assembly was compared with the typical rainscreen wall assembly. It was shown that the heat flows in the BIPV/T façade concept was significantly reduced compared with the rainscreen assembly which could translate to a better overall energy performance.

Further, the derived electrical and thermal yield, an analytical model of the BIPV/T façade is derived by employing multi-variable polynomial regression analysis to dynamically predict the overall thermal yield of the BIPV/T-HP system. the dynamic analytical model is then implemented in the building energy simulation platform to quantify the energy impacts for a BIPV/T-HP system for DHW. The implemented model is extended to investigate the potential energy improvements for multiple weather conditions across Canada. It was seen that up to 44.2% of the heat load can be offset with the BIPV/T -HP.

## 8.2 Further work

The potential energy impacts of the BIPV/T façade were demonstrated in this research. However, more work is needed for verification and implementation of the concept. The following recommendations for future work can be made:

- A full-scale experiment to verify the potential energy performance of the BIPV/T façade concept.
- Practical Implementation of the BIPV/T façade concept in the built environment requires consideration for heat, air, and moisture transport in conjunction with whole building simulation including thermal comfort considerations and aesthetics. Further, Integration of the concept in BIM environment can be beneficial to help or aid architects and building designers
- Including urban topography effect on the thermal yield of the BIPV/T is important to represent as built conditions.
- The research was conducted from first lay principles, however, an exegetic analysis is required to account for system losses as well as improve the overall thermodynamic efficiency of the BIPV/T façade concept.

# Curriculum Vitae

**Name**: Barilelo Emmanuel Nghana

| | |
|---|---|
| **Post-secondary Education and Degrees:** | **Western University**<br>London, Ontario Canada<br>2016 – 2022<br>Doctor of Philosophy<br>Civil and Environmental Engineering |
| | **British Columbia Institute of Technology**<br>Burnaby, BC Canada<br>2013 – 2014<br>Master of Engineering<br>Building Science |
| | **University of British Columbia**<br>Vancouver, BC Canada<br>2009 – 2012<br>Bachelor of Applied Science<br>Mechanical Engineering |
| **Honor and Awards** | Western Engineering Scholarship<br>2016 – 2021 |
| **Related works** | Research and Teaching Assistant<br>Western University<br>2016- 2021<br>Research Assistant<br>British Columbia Institute of Technology<br>2013 - 2021 |

**Publications:**

**Journal Articles**

1. Nghana, B., Tariku, F., & Bitsuamlak, G. (2021). Assessing ventilation cavity design impact on the energy performance of rainscreen wall assemblies: A CFD study. Building and Environment, 196, 107789.
2. Nghana, B., & Tariku, F. (2018). Field investigation of moisture buffering potential of american clay and magnesium oxide board in a mild climate. Journal of Architectural Engineering, 24(4), 04018023.
3. Nghana, B., & Tariku, F. (2016). Phase change material's (PCM) impacts on the energy performance and thermal comfort of buildings in a mild climate. Building and Environment, 99, 221-238.